

**A Structural Study of Mercury Adsorbed
on Single Crystal Metal Surfaces**

by

Sarah L. Bastow, BSc.

Thesis submitted to the University of Nottingham for the degree
of Doctor of Philosophy, May 1997.

To Mum and Dad

With Thanks For Everything

O creature sciocche, quanta ignoranza è quella che v'offende?

(O foolish creatures, what ignorance is this which torments you?)

Divina Commedia

Dante Alighieri

Contents

	Page
Abstract	viii
Acknowledgements	ix
Abbreviations and Symbols	xi
Chapter 1 Introduction	1
1.1. Why Study Surface Science?	1
1.2. Why Choose Mercury As An Adsorbate?	2
1.3 Why Use The NIXSW Technique?	6
1.4 Previous Studies of the Hg/Ni(111) Adsorption System	9
1.5 Previous Studies of the Hg/Cu(100) Adsorption System	17
Chapter 2 Theory	22
2.1. Normal Incidence X-Ray Standing Wavefield (NIXSW) Technique	22
2.1.1. Basic Theory of NIXSW	27
2.1.2. Argand Diagram Analysis of NIXSW Data	43

2.1.2.1. Thermal Vibration Effects and Local Disorder	45
2.1.2.2. Multiple Adsorption Sites	47
2.1.2.3. Low Symmetry Adsorption Sites	52
2.1.3. Triangulation of Adsorbate Position	53
2.1.3.1. Hg/Ni(111) System	53
2.1.3.2. Hg/Cu(100) System	55
2.2. Surface Analysis Techniques	58
2.2.1. Auger Electron Spectroscopy (AES)	58
2.2.2. X-Ray Photoelectron Spectroscopy (XPS)	63
2.2.3. Low Energy Electron Diffraction (LEED)	66
Chapter 3 Instrumental and Experimental Details	68
3.1 Description of the Beamline	68
3.2 Description of the Sample Chamber	71
3.3 Crystal Preparation and Alignment	74
3.3.1 Ni(111) Sample	76
3.3.2 Cu(100) Sample	77
3.4 NIXSW Data Acquisition and Preparation	78
3.4.1 Ni(111) Sample	82
3.4.2 Cu(100) Sample	85
3.5 NIXSW Data Analysis	88
3.5.1 NIXSW Fitting Program Outline	89

Chapter 4	Mercury Adsorption on Ni(111) : NIXSW Results	92
4.1	The Ni(111) Substrate	94
4.2	The Ni(111)/Hg- $(\sqrt{3}\times\sqrt{3})R30^\circ$ Structure	96
4.3	The Ni(111)/Hg-p(2x2)-0.5ML Structure	101
4.4	The Ni(111)/Hg- $“c(2\sqrt{3}\times 2\sqrt{3})R30^\circ”$ Structure	105
4.5	Summary of Ni(111)/Hg Structure Results	107
Chapter 5	Mercury Adsorption on Ni(111): Discussion	116
5.1	The Ni(111)/Hg- $(\sqrt{3}\times\sqrt{3})R30^\circ$ 0.33ML Structure - $(\bar{1}11)$ Reflection	119
5.2	The Ni(111)/Hg-p(2x2) 0.5ML Structure - $(\bar{1}11)$ Reflection	130
5.3	The Ni(111)/Hg- $“c(2\sqrt{3}\times 2\sqrt{3})R30^\circ”$ 0.64ML Structure - $(\bar{1}11)$ Reflection	132
5.4	The Ni(111)/Hg (111) Reflection Data For All Structures	134
5.5	The Ni(111)/Hg Data For All Structures And All Reflections	139
5.6	The Ni(111)/Hg Conclusion	140
Chapter 6	Mercury Adsorption on Cu(100) : NIXSW Results	141
6.1	The Cu(100) Substrate	142
6.2	The Cu(100)/Hg-c(2x2)-0.5ML Structure	144
6.3	The Cu(100)/Hg-c(4x4)-0.62ML Structure	149
6.4	The Cu(100)/Hg-(3x3)-0.66ML Structure	153

6.5	The Cu(100)/Hg-c(2x6)-0.83ML Structure	155
6.6	Summary of Cu(100)/Hg Structure Results	157
Chapter 7	Mercury Adsorption on Cu(100) Discussion	164
7.1	The Cu(100)/Hg-c(2x2)-0.50ML Structure	169
7.1.1.	The (200) Reflection NIXSW Data for the c(2x2) Structure	170
7.1.2.	The (111) Reflection NIXSW Data for the c(2x2) Structure	174
7.2	The Cu(100)/Hg-c(4x4)-0.62ML Structure	177
7.3	The Cu(100)/Hg-(3x3)-0.66ML Structure	190
7.4	The Cu(100)/Hg-c(2x6)-0.83ML Structure	196
7.5	The Cu(100)/Hg Conclusion	206
Chapter 8	Summary	208
	References	214

Abstract

The Normal Incidence X-Ray Standing Wavefield technique has been used to study the adsorption of mercury on two single crystal metal surfaces, Ni(111) and Cu(100). The three Hg/Ni(111) structures studied were $(\sqrt{3}\times\sqrt{3})R30^\circ$ -0.33ML, $p(2\times 2)$ -0.5ML and “ $c(2\sqrt{3}\times 2\sqrt{3})R30^\circ$ ”-0.64ML. A well-ordered, commensurate mercury adlayer is postulated, which has a low frequency (or soft) phonon mode parallel to the surface. Such a surface is well ordered and will give good LEED patterns, but the large distribution of distances relative to the $(\bar{1}11)$ set of planes leads to a low coherent fraction, in agreement with the $(\bar{1}11)$ NIXSW data. The Hg/Cu(100) structures studied were two equilibrium structures, $c(2\times 2)$ -0.50ML and $c(4\times 4)$ -0.62ML and two non-equilibrium structures, (3×3) -0.66ML and $c(2\times 6)$ -0.83ML. In agreement with the literature, the NIXSW analysis of the lowest coverage Cu(100)/Hg- $c(2\times 2)$ -0.50ML structure indicated mercury adsorption into the most energetically stable four-fold hollow sites. However, the NIXSW analysis of the Cu(100)/Hg- $c(4\times 4)$ -0.62ML structure appears to disprove the mercury coincidence net proposed by previous authors. Our model proposes that some of the mercury atoms adsorb exactly in energetically favourable four-fold hollow sites whilst some reside in sites slightly off the four-fold hollow position. The Cu(100)/Hg- (3×3) -0.66ML structure is found to consist of two domains, each containing mercury atoms adsorbed equally in both bridge and four-fold hollow sites and differing only in the type of bridge sites occupied by the mercury adsorbate atoms. Finally, the NIXSW data of the highest coverage Cu(100)/Hg- $c(2\times 6)$ -0.83ML structure, was found to indicate a model combining a slightly rumpled overlayer with more than a monolayer of adsorbate atoms to fit the experimental NIXSW data presented here.

Acknowledgements

It has often been said that we live in interesting times and that is how I can best describe my time in Nottingham: “Interesting!” There are many people who have helped make my time interesting and many who have prevented it from becoming too interesting (which isn’t always favourable). I would like to express my thanks to all of these people as without their help and support, I may not have reached this stage.

- ❖ Firstly I would like to acknowledge my supervisor *Rob Jones*, for his support, guidance and many gems of advice. He was most appreciated when seen arriving at Daresbury with beer, orange juice and chocolate brought for the troops...we were always pleased to see him carrying a Sainsbury’s carrier bag!
- ❖ My thanks also go to my *Research Group* especially *Nicky, Roslinda* who have endured all of my jokes and even laughed at some of them. Thanks to *Roslinda* for her help at Daresbury (where she worked extremely hard) and the endless supply of wonderful food!
- ❖ Recognition also goes to all those from Warwick who contributed to the experimental runs at Daresbury: *Ad, Glyn, Jens, Steve, Gavin*. They withstood a great deal of hardship to bring the science contained within this thesis to the reader. I would particularly like to thank *Ad Ettema* for his help and advice in the fitting and analysis of the NIXSW data. Thanks also to *Phil Woodruff* for the use of his beamtime at Daresbury.
- ❖ *Bruce Cowie*, the station scientist on Beamline 6.3. at Daresbury is also greatly appreciated. His infinite talent allowed us to obtain all the experimental data shown here. He was also wonderful for ideas, moral support and above all patience when we broke anything.

- ❖ Thanks to *Katherine, Rob Meehan, June* and *Ivan* for their help and support when I first arrived in Nottingham. I would also like to thank technical and administrative staff (including *Nev, Neil* and *Margaret*) in Nottingham and Daresbury. I am also grateful for *Martin McCoustra*'s help with the computers' temper tantrums.
- ❖ Special thanks also go to *Andrew Chew* and *Austin Chambers* who gave me my first taste of scientific research and subsequent inspiration.
- ❖ I would like to thank the lads for their friendship and moral support over the years. Especially *Richie* for the use of his computer (and patience when it broke!) and *Andy* for providing continuous amusement.
- ❖ Thanks to those people who have made my life interesting, enjoyable and most importantly, not "too" interesting! *Karl, Sean* and *Nick* for their continuous (much appreciated and missed) abuse and camaraderie. *Clare, Gail, Alex C* and *Alexis* for their endless support and friendship. My friends in Nottingham who have been marvellous and suitably abusive: *Helen, Elaine, Alex Wright, Helen Viner, Stuart, Andy, Stan, Quesne, Susan, Anne-Marie* and *Mark A*. Thanks to my proof readers *Helen Viner* and *Elaine* who had an unenviable task...and survived!
- ❖ I would like to acknowledge the EPSRC, BVC, Institute of Physics, SCI and the Commission for the European Communities for their financial support.

Finally and most importantly I would like to thank my family especially *Mum, Dad, Grandma* and *The Hooligans* whose love and support (and nagging!) has helped me every step of the way.

Abbreviations and Symbols

Γ	Parameter = $(e^2/4\pi\epsilon_0 mc^2)\lambda^2/\pi V$
η	Displacement Parameter Related To The Variable Used To Scan Through The Bragg Peak
ν	Frequency Of Photon
σ	Gaussian X-Ray beam energy diffraction peak broadening
θ	Incidence Angle With The Atomic Plane
ϕ	Phase Factor
λ	Wavelength Of The Incident Photon
$\Delta\theta$	Variation Of Incidence Angle θ
ϵ_0	Permittivity Of Free Space
θ_B	Bragg Angle
Δd	Coherent Position
δd	Height Above Extended Substrate Scatterer Planes
ΔE	Variation Of Bragg Energy, E
AES	Auger Electron Spectroscopy
ARPES	Angle Resolved Photoelectron Spectroscopy
B.E.	Binding Energy
c	Speed Of Light
CFS	Constant Final State
CHA	Concentric Hemispherical Analyser

CIS	Constant Initial State
CMA	Cylindrical Mirror Analyser
d_H	Separation Of Atomic Scattering Planes
d_H	Lattice Spacing
d_{hkl}	Separation Of hkl Planes
E	Amplitude Of X-Ray Standing Wavefield
e	Charge Of Electron
E_H/E_0	Amplitude Of The Electromagnetic Field
EPSRC	Engineering and Physical Sciences Research Council
F_0	Structure Factor For The (000) Reflection
FAT	Fixed Analyser Transmission
f_c	Coherent Fraction
FCC	Face Centred Cubic
F_H	Geometrical Structure Factor For H (incident) Reflection
$F_{H'}$	Geometrical Structure Factor For H' (diffracted) Reflection
H	Indices Of The X-Ray Reflection
h	Planck's Constant
\underline{H}	Reciprocal Lattice Vector
HCP	Hexagonal Close Packed
I	Intensity Of X-Ray Standing Wavefield
KE	Kinetic Energy
LEED	Low Energy Electron Diffraction
m	Mass Of Electron

n	Integer
NIXSW	Normal Incidence X-Ray Standing Wavefield
P	Polarisation Factor
R	Reflectivity
\underline{r}	Vector Position Of Absorber
SEXAFS	Surface Extended X-Ray Absorption Fine Structure
SRS	Synchrotron Radiation Source
STM	Scanning Tunneling Microscopy
SXW	Standing X-Ray Wavefield
TEY	Total Electron Yield
UHV	Ultra-High Vacuum
V	Volume Of Unit Cell
x	Height Above Surface Plane
XPS	X-Ray Photoelectron Spectroscopy
XSW	X-Ray Standing Wavefield
z	Perpendicular Distance From The Atomic Scattering Planes

1 Introduction

1.1 Why Study Surface Science?

Surface science is concerned with the chemical composition and atomic arrangements of solid surfaces. These chemical and structural properties are different from those of the bulk material. Over the years many scientists have been driven by a desire to understand why this is so. There are also many processes of technological significance that would benefit from an enlightened and enhanced understanding of surface science, such as the semiconductor (growth of crystals) and chemical industries (heterogeneous catalysts). By developing one's understanding of the simple surface processes (on clean and adsorbate covered surfaces), it is possible to interpret how more complex surface processes occur. Therefore, one of the most fundamental objectives of many areas of surface science research is the quantitative determination of the surface structure, in particular the location of specific adsorbate species. Such an understanding of the structure of a surface can be the basis of a more detailed knowledge of the electronic and chemical characteristics of a surface.

With the advent of modern ultra-high vacuum (UHV) systems and experimental techniques it is possible to maintain and study well ordered, contaminant free surfaces throughout the duration of one's experiments. Such experiments need to be sensitive to the first few atomic layers of a solid surface. There are many techniques now available

(Woodruff and Delchar 1994) to characterise a surface. In spite of the many techniques used to characterise the structure of clean and adsorbate covered surfaces, no specific technique can easily determine the structure of a surface. However, a combination of techniques can provide a detailed description of the adsorption site, and other surface phenomena.

1.2 Why Choose Mercury As An Adsorbate?

Mercury is a model adsorbate for chemisorption studies on metals and semiconductors. It is an easily manageable monatomic vapour at room temperature which can be handled in a gas line or generated from solid state sources in ultra-high vacuum (UHV). The only other monatomic vapours at room temperature are the noble gases. For many substrates the mercury overlayer is relatively weakly chemisorbed ($100\text{-}200\text{ kJ mol}^{-1}$), consequently this chemisorption behaviour is similar to that of physisorbed rare gases (Dowben et al. 1990). Therefore, the study of mercury as an adsorbate has the advantage that it spans the fields covered by both detailed thermodynamic studies of rare gas physisorption on transition metal surfaces and the structural and electronic studies of metal adsorption on metals.

As mercury is monatomic, it can not dissociate when it adsorbs onto metal surfaces. Consequently it is an ideal adsorbate as it should be a less complex to study than dissociating molecules. The resulting chemisorption bonds for mercury adsorption on transition metal surfaces are weak enough to allow lateral adatom-adatom interactions to

transition metal surfaces are weak enough to allow lateral adatom-adatom interactions to play a significant role alongside the adsorbate-substrate interactions. The subtle interplay between these interactions for the adsorption of mercury on transition metal surfaces produces a fascinating set of structures.

Mercury is a large adsorbate (Hg van der Waals diameter = 3.0 Å) which exhibits strong Hg-Hg lateral interactions when chemisorbed. Mercury exists in three forms whilst in the solid state: α -Hg (Heine & Weaire (1966), Weaire (1968a) and Donohue (1974)), β -Hg (Heine & Weaire (1966) and Weaire (1968a)), γ -Hg (Weaire 1968b and Donohue 1974). The two stable forms, α -Hg and β -Hg are respectively low pressure rhombohedral and high pressure body centered tetragonal structures. The γ -Hg form is an unstable structure formed from a stressed α -Hg structure at 4 K and reverts back to the α -Hg structure at 50 K (Donohue 1974). The closed electronic configuration of $(Xe)4f^{14}5d^{10}6s^2$ provides mercury with a high ionisation potential of 10.4 eV (Frost et al. 1967), the highest ionisation potential of any metal. Such a closed shell configuration would lead us to expect non-directional bonding and therefore a weak corrugation in the mercury-substrate interaction energy. Considerable adsorbate-adsorbate interactions are also to be expected when mercury is chemisorbed, as the enthalpy of vaporisation (58.5 kJ mol^{-1}) at its boiling point (630 K) indicates comparatively strong bonding in the pure element (Singh and Jones 1990a). The inert characteristics and low boiling point of mercury are anticipated because of the two tightly bound 6s electrons in the outermost orbital creating a stable free atom

configuration. The above properties indicate that mercury has both rare gas and metallic behaviour when involved in adsorption on metal surfaces, thus creating a very interesting adsorbate to study.

Mercury is an adsorbate of particular interest on some substrate surfaces, such as Ni(111) (Singh and Jones 1989a), Cu(100) (Kime et al. 1992), and W(110) (Zhang et al. 1993) because of its ability to undergo a two-dimensional metallic to non-metallic phase transition. Mercury is also one of the few transition metal adsorbates which can be studied under equilibrium conditions with its own vapour and forms both insulating and metallic overlayers (Zhang et al. 1993, 1994). The ability of mercury to form amalgams with a large proportion of the elements restricts the number of substrate metals for which simple chemisorption is expected. These transition metals include Ni, Fe, and W (Jones & Tong 1987). Mercury can amalgamate with copper at high mercury concentrations, therefore it is essential to monitor the copper surface crystallographic structure to ensure that this does not occur. Under ultra-high vacuum conditions, such amalgamation does not occur.

The adsorbate structures formed when mercury adsorbs onto single crystal surfaces are influenced by the size of the substrate unit mesh relative to the size of the mercury adatom and substrate atoms. The initial growth of a mercury adlayer adsorbed onto clean surface meshes larger than or comparable to the lattice constant of solid α -Hg (2.99 Å) has been found to be pseudomorphic, i.e. the adsorbate forms a structure

similar to that formed by the “next” substrate layer. Such surface meshes include the rather large, open surfaces of the W(100) [Egelhoff et al. (1976) and Jones & Perry (1979)], W(110) [Zhao et al. (1992)], Fe(100) [Jones and Perry (1981)], Cu₃Au(100) [Onellion et al. (1987)] and Ag(100) [Onellion et al. (1986), Varma et al. (1986), Dowben et al. (1987a) and Onellion et al. (1987)] metals. This kind of adsorption results in a (1x1) adsorbate structure dominated by the corrugation of the substrate-adatom interaction. The repulsive, through space lateral interactions of the adsorbed mercury atoms occur because the clean Fe(100) surface unit mesh (2.87 Å) is slightly smaller than the mercury adatoms. However, attractive adsorbate interactions are observed when mercury is adsorbed on the larger W(100) surface (3.16 Å). Such attractive interactions are presumably due to through space orbital overlap at this slightly larger separation. A (1x1) structure still forms (only at low temperatures) when mercury is adsorbed on the (100) faces of silver (2.89 Å) and Cu₃Au (2.72 Å).

In contrast, when mercury is adsorbed on slightly smaller substrate meshes, such as Ni(100) [Jones and Tong (1987), Prince et al. (1989) and Poulsen et al. (1994)] and Cu(100) [Dowben et al. (1990a and 1990b), Kime et al. (1992), Li et al. (1992a) Onellion et al. (1987)], the adsorbed mercury atom is too large to adsorb into adjacent (1x1) sites on the Cu(100) (2.55 Å) and Ni(100) (2.49 Å) surfaces. Consequently, c(2x2) structures are formed at lower coverages (up to 0.5ML) which develop into more complex structures at higher Hg exposure.

Mercury forms a weak chemisorption bond (100-200 kJ mol⁻¹) with many metal surfaces such as Fe(100), W(100), Ni(100), Cu(100) and a particularly weak bond with Ag(100). The chemisorption of mercury on the Si(111) surface at 110 K has also been reported by Li et al. (1992 and 1993). A ($\sqrt{3}\times\sqrt{3}$)R30° structure was formed at low coverage and a (1x1) LEED pattern was observed at higher coverages. The chemisorption of mercury on the Si(111) surface is thought to be much stronger than that for metals due to the presence of mercury atoms after flashing the surface to 1523 K (Li et al. 1993). The presence of these mercury adatoms is also thought to be due to the diffusion of mercury atoms into the bulk Si.

1.3 Why Use The NIXSW Technique?

In the many qualitative structural studies conducted on mercury adsorption on single crystal metal surfaces the mercury adatom was assumed to occupy the highest coordinated hollow site on each structure for the commensurate structures formed. However, it has never been conclusively shown that the mercury adatom always occupies the highest co-ordinated hollow site on each structure. Therefore a structural study which provided quantitative results could produce one of the many missing (or ambiguous) pieces in the search for the true picture of mercury adsorption. It has been shown previously (Prince et al. 1989, Lüdecke et al. 1996) that the X-Ray standing wavefield techniques can possibly find some of these missing pieces due to its ability to

locate the position of the adsorbate atom relative to the extended substrate scattering planes.

The normal incidence X-Ray standing wavefield (NIXSW) technique is relatively new (Woodruff et al. 1987) and involves the measurement of the photoabsorption by atoms on the surface in an X-Ray standing wavefield. The NIXSW technique allows information on the local surface structural environment to be obtained without the need for long range order of the adsorbate layer, by only requiring a well ordered substrate and is therefore of significant use in surface science. Normal incidence to the relevant reflecting planes removes many of the restrictions of instrumentation and crystal perfection (Cowan et al. 1980, Patel et al. 1987, Woodruff et al. 1988 and Kerkar et al. 1992a). The NIXSW experiments can be performed using existing SEXAFS equipment at synchrotron radiation facilities (Bradshaw 1990). The information obtained from the NIXSW method is an adsorbate-substrate layer spacing. Hence, the position of the substrate or the adsorbate atom relative to particular reflecting planes can be determined by measuring the X-Ray absorption of the substrate or adsorbate atom as the wavefield is shifted. By using two or more reflecting planes a real space triangulation of the atomic position into a particular site is possible. Of course, any additional information from LEED and especially chemical bond lengths also aids determination of the adsorption site.

More complex, large surface mesh structures involving multiple site occupation can also be studied by the NIXSW technique, but not so easily. Therefore one can distinguish between the various structural models of adsorbate systems using this technique and complement the large amount of information available from studies using various other surface science techniques.

The (111) and $(\bar{1}11)$ planes are used in the Hg/Ni(111) adsorption system. The $(\bar{1}11)$ plane at an angle of 70.5° to the (111) surface of the substrate makes this reflection highly sensitive to positions parallel to the surface. The (200) and (111) planes are used in the Hg/Cu(100) adsorption system. The (200) reflection is sensitive to distances perpendicular to the surface and the (111) reflection (for which the scattering planes lie at 54.73° to the surface) is sensitive to distances parallel to the surface.

The NIXSW technique has been used to eliminate the possibility of adsorption in the high co-ordinate adsorption sites for several systems, such as the low temperature occupation of the atop site by Rb adsorbed on Al(111) (Kerker et al. in 1992 and Scragg et al. in 1994). For qualitative structural analysis of mercury adsorption, the adatom is implicitly assumed to occupy the high-symmetry hollow sites on each surface in the commensurate structures with one exception. The less well studied adsorption of mercury on Ni(100) (Jones & Tong 1987, Prince et al. 1989, Poulsen et al. 1994) has had two structural investigations applied to the $c(2 \times 2)$ surface. In the first structural study the NIXSW method (Prince et al. 1989) was applied to the $c(2 \times 2)$ structure at

room temperature using just the (200) reflection. Prince et al. (1989) found an apparent occupation of the two-fold bridge sites by the adsorbed atom by the standing X-Ray wavefield analysis of the c(2x2) mercury phase on Ni(100). This adsorption site was derived using the Ni-Hg interlayer distance in conjunction with an assumed Ni-Hg nearest neighbour spacing. However, the second, transmission ion channelling study (Poulsen et al. 1994), carried out at 115 K showed that the mercury was actually adsorbed in the four-fold hollow site and not the 2-fold bridge sites. By studying the mercury adsorption on the Cu(100) surface, we may be able to gain insight into the true adsorption behaviour on a (100) surface. From there it may be possible to obtain an understanding of the mercury behaviour for the c(2x2) Hg/Ni(100) structure.

1.4 Previous Studies of the Hg/Ni(111) Adsorption System

Mercury adsorption on Ni(111) has been extensively studied both experimentally and theoretically (Singh 1989, Singh and Jones 1988, 1989a, 1989b, 1990a, 1990b, and Singh et al. 1993). The Hg/Ni(111) system is thought to be characterised by a combination of weak corrugation and strong lateral interactions. The Ni(111) crystal surface was chosen because of its small unit mesh and hexagonally close packed structure. When mercury is adsorbed on the Ni(111) surface both equilibrium and non-equilibrium structures can be formed (Singh and Jones 1990b). The Hg/Ni(111) structures produce a large number of well-defined LEED patterns. These structures

and hence LEED patterns are dependent on temperature, coverage and whether the surface is under kinetic or thermodynamic control. The Hg/Ni(111) surface structures consist of a two-dimensional monatomic chemisorbed system in which two structural phases can exist. LEED patterns indicate that these are a hexagonal phase and a pseudo-square phase.

The four thermodynamically stable structures of the Hg/Ni(111) adsorption system have been previously investigated using predominantly LEED, Auger Electron Spectroscopy (AES) and Angle Resolved Photoelectron Spectroscopy (ARPES). These structures are the $p(2 \times 2)$ -0.5ML structure, the $(\sqrt{3} \times \sqrt{3})R30^\circ$ -0.33 ML structure, the $p(2 \times 2)$ -0.75ML structure and the " $c(2\sqrt{3} \times 2\sqrt{3})R30^\circ$ "-0.64ML. The following is a summary of the results and conclusions obtained from these various investigations. Such information (LEED patterns and phase diagrams) is necessary for the correct formation of the required adsorbate structures to be studied by the NIXSW technique.

The $(\sqrt{3}\times\sqrt{3})R30^\circ$ -0.33 ML structure was proposed to consist of mercury atoms in the three-fold hollow sites, with one mercury atom per unit mesh (figure 1.4.1). The adlayer shown in figure 5.1.1 can be moved laterally across the nickel surface to atop, or two-fold bridge sites and still preserve the $(\sqrt{3}\times\sqrt{3})R30^\circ$ -0.33 ML structure. The band structure calculations (Singh et al. 1993) could provide no distinction between the two proposed sites (atop or bridge). Another paper (Singh and Jones 1988) suggested that the mercury forms islands, and the mercury atoms reside in three-fold hollow sites. Therefore, the position of the mercury atom in the $(\sqrt{3}\times\sqrt{3})R30^\circ$ -0.33 ML structure still remains conjecture and is therefore to be investigated here. The Hg-Hg distance was shown to be 4.31 Å (Singh and Jones 1988, 1990a) and the adlayers were shown to exhibit attractive Hg-Hg interactions.

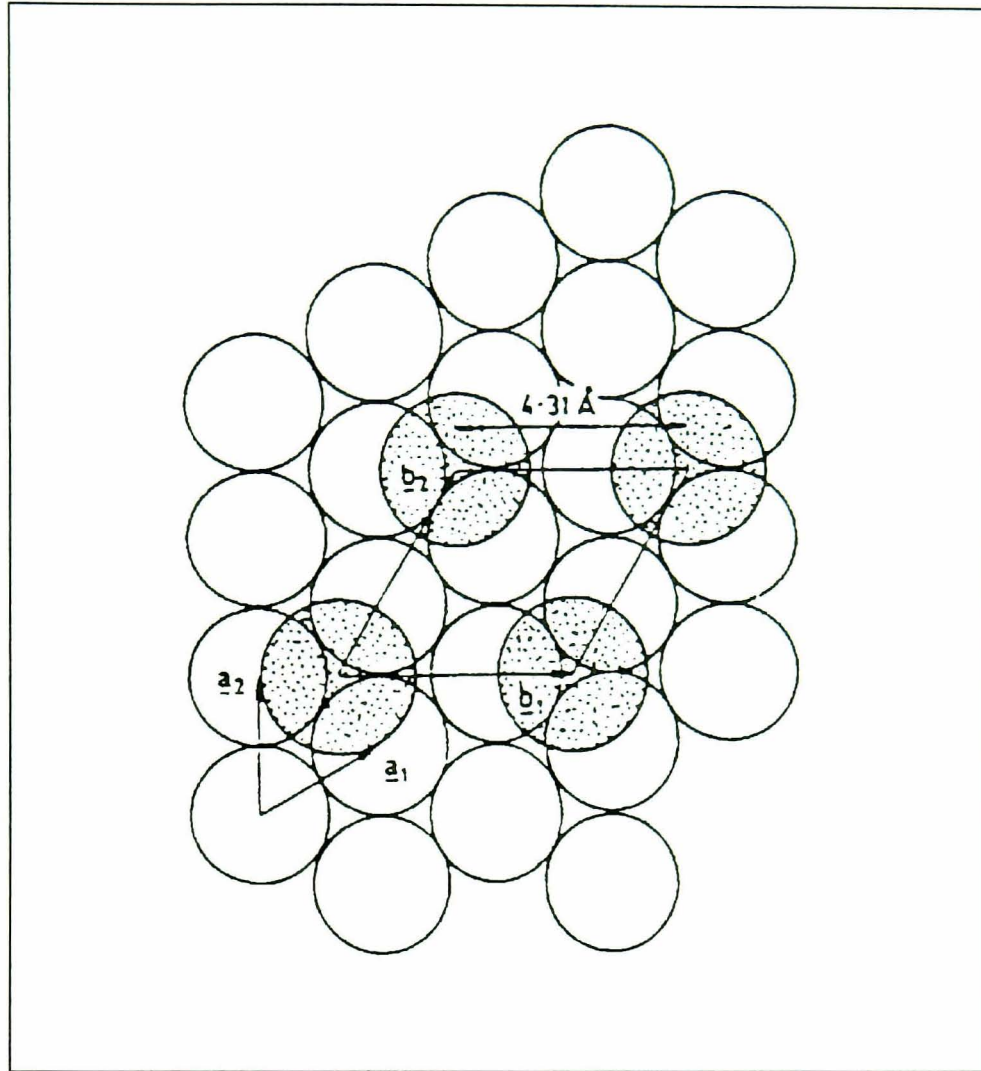


Figure 1.4.1. A possible structure for the Ni(111)- $(\sqrt{3}\times\sqrt{3})R30^\circ$ -Hg structure taken from Singh and Jones (1990a). The stippled circles represent mercury atoms, while a and b refer to the substrate and adlayer nets, respectively.

The $p(2 \times 2)$ -0.5ML structure consisted of open hexagons of mercury sitting in three-fold hollow sites (figure 1.4.2). These hexagons are made up of mercury atoms half in FCC sites and half in HCP sites along with a "hole" in the middle of each hexagon over a one-fold atop site of sufficient size to accommodate another mercury atom. It was also suggested that island structures were formed at a coverage of 0.45 ML prior to the formation of the $p(2 \times 2)$ 0.5ML structure. The structure was also thought to have a Hg-Hg distance of 2.87 Å, and two atoms per unit mesh.

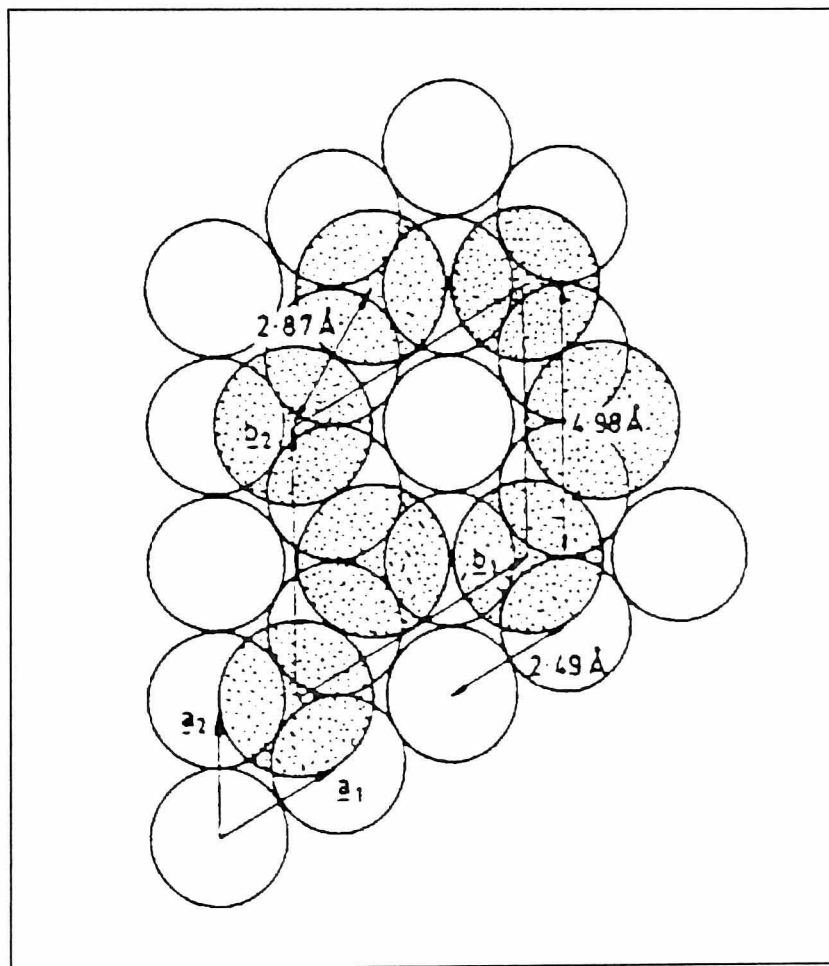


Figure 1.4.2. A possible structure for the Ni(111)- $p(2 \times 2)$, 0.5ML-Hg structure taken from Singh and Jones (1990a). The stippled circles represent mercury atoms, while a and b refer to the substrate and adlayer nets, respectively.

As for the $p(2 \times 2)0.5\text{ML}$ structure, the higher coverage $p(2 \times 2)0.75\text{ML}$ structure was thought to consist of hexagons of mercury sitting in three-fold hollow sites, half in FCC sites and half in HCP sites (figure 1.4.3a). The "hole" in the middle of each hexagon was filled with a mercury atom located in an atop site. The mercury atoms therefore form a hexagonally close packed raft rotated 30° with respect to the substrate, this raft is not flat, but probably slightly buckled (Singh et al. 1993) due to the mercury atom in the atop site. The structure was also thought to have a Hg-Hg distance of 2.87\AA (Singh and Jones 1988, 1989a, 1989b and 1990b) and have metallic behaviour due to the close proximity of the mercury atoms (Singh et al. 1993).

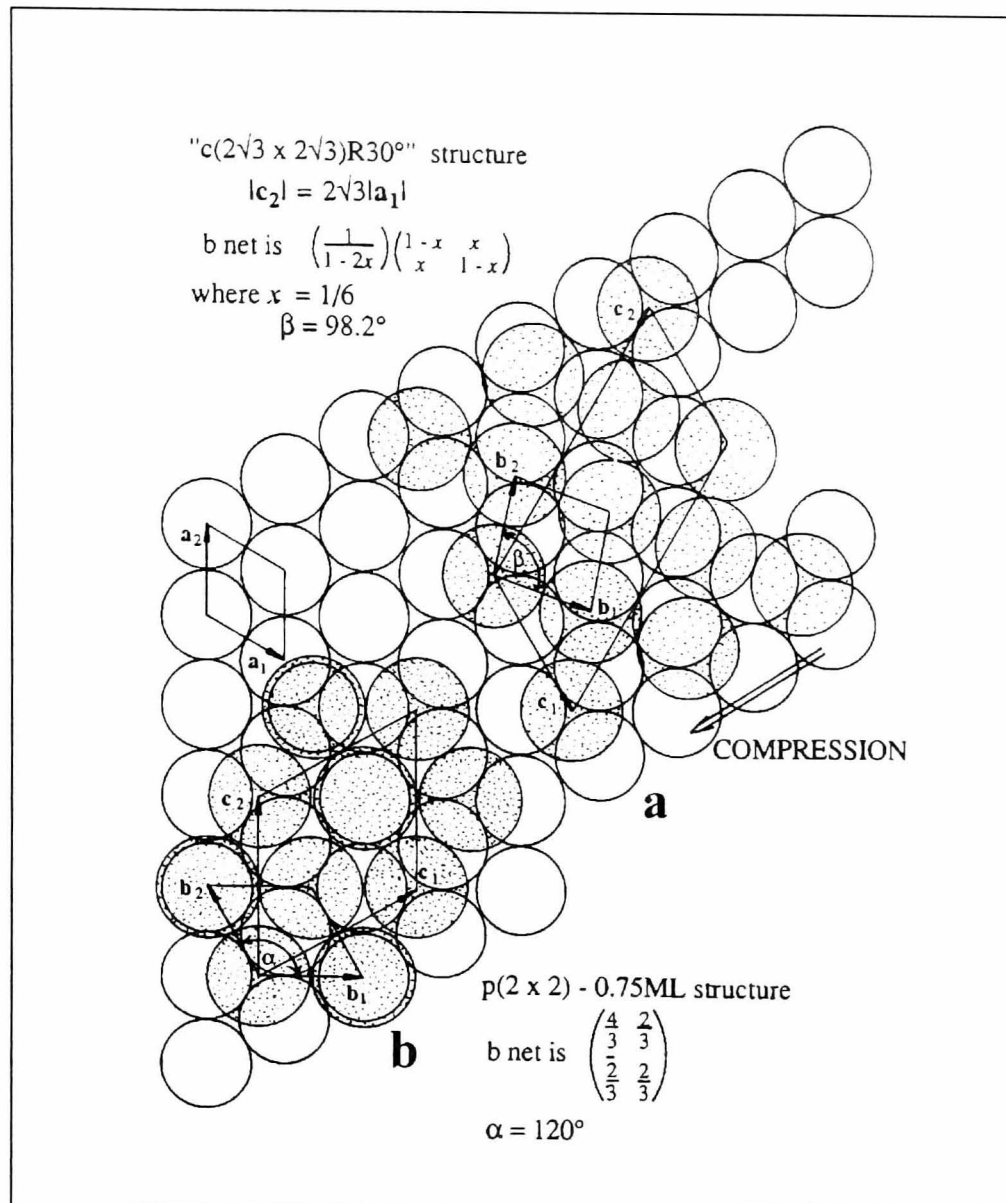


Figure 1.4.3. (a) A real space structure for a perfect Ni(111)- $c(2\sqrt{3} \times 2\sqrt{3})R30^\circ$ -Hg structure taken from Singh and Jones (1989a). The mercury adatom net, b, coincides with the underlying nickel net, a. (b) A real space structure for the Ni(111)- $p(2 \times 2)$, 0.75ML-Hg structure taken from Singh and Jones (1989a). The mercury net, b, is hexagonal and coincides with the nickel net to form the $p(2 \times 2)$. For (a) and (b), the stippled circles represent mercury atoms, while the open circles represent the nickel atoms.

The pseudo-square compression “ $c(2\sqrt{3} \times 2\sqrt{3})R30^\circ$ ” adlayer (figure 1.4.3b) can be described using the real space matrix G , where

$$G = \frac{1}{1-2x} \begin{pmatrix} 1-x & x \\ x & 1-x \end{pmatrix}$$

and $x = 0.18$ (Singh and Jones (1990b)). This $x = 0.18$ structure is referred to as the “ $c(2\sqrt{3} \times 2\sqrt{3})R30^\circ$ ” structure, as it is not quite the true coincident $c(2\sqrt{3} \times 2\sqrt{3})R30^\circ$ structure formed at $x = 1/6$ with a coverage of $2/3$ ML and an internal unit mesh angle of 98° (Singh 1989). The structure was also proposed to have a Hg-Hg distance of 2.87 \AA . It was thought (Singh et al. 1993) that the metallic pseudo-square structure had a better packing geometry, and a larger Hg-Hg spacing than the hexagonal structure.

During adsorption the mercury atoms were thought to travel freely over the pre-adsorbed mercury in the precursor state, but at 323 K the mobility on the clean surface was thought to be restricted. Such restricted behaviour at this temperature would lead one to expect a high diffusion barrier at 323 K to restrict the mobility of the mercury atoms. Therefore the mercury atoms must adsorb into the first available three-fold hollow site available, thus forming the $p(2 \times 2)$ -0.5ML structure. At 351 K, the mobility of the mercury atoms was thought to increase and therefore the mercury atoms were able to form the more thermodynamically stable $(\sqrt{3} \times \sqrt{3})R30^\circ$ structure. Theoretical band structure calculations (Singh et al. 1993) have shown that the phase transitions

were mainly dominated by the Hg-Hg lateral interactions and only slightly affected by the substrate, Ni(111). The higher coverage $p(2 \times 2)$ -0.75ML structure was analysed at 250 K, and the remaining structures were analysed at room temperature, all using AES, LEED, UPS, and work function measurement techniques.

The investigation of mercury adsorption on the Ni(111) surface could possibly provide an insight into whether the adsorbate surface structures are dominated by the lateral Hg-Hg interaction. We describe the NIXSW studies of the $(\sqrt{3} \times \sqrt{3})R30^\circ$ - 0.33ML, $p(2 \times 2)$ - 0.5ML and " $c(2\sqrt{3} \times 2\sqrt{3})R30^\circ$ " - 0.64ML structures (Singh 1989, Singh and Jones 1988, 1989a, 1989b, 1990a, 1990b, and Singh et al. 1993).

1.5 Previous Studies of the Hg/Cu(100) Adsorption System

The studies of mercury adsorption on Cu(100) have been predominantly concerned with the electronic and thermodynamic properties of the adsorbate structure. Consequently, the majority of the structural information presently available regarding this adsorption system has usually been inferred from qualitative information, such as two dimensional LEED patterns. Therefore the adsorption positions of the mercury atoms have been assumed to be high symmetry sites. Hence the NIXSW technique has been applied to the Hg/Cu(100) system in order to identify the adsorption site. The Cu(100) surface has a much greater corrugation (Dowben et al. 1991) than the

hexagonally close packed Ni(111) surface. Consequently, the interaction of the adsorbate with the substrate is likely to be important in determining the adsorbate structure formed. One would anticipate distinctive behaviour from the Hg/Cu(100) adsorption system due to the size of the mercury adatoms combined with the weak chemisorption expected resulting in competition between the adsorbate-adsorbate and adsorbate-substrate interactions.

The mercury adlayer is thought to adopt the square structure of the Cu(100) surface (Onellion et al. 1987). There are two equilibrium structures, $c(2 \times 2)$ and $c(4 \times 4)$, and several non-equilibrium structures, $c(2 \times 2)$ $c(4 \times 4)$, (3×3) and $c(2 \times 6)$ formed when mercury is adsorbed on the Cu(100) surface. The structures have been mainly studied by atom beam scattering (ABS), angle resolved photoemission spectroscopy (ARPES) and LEED techniques (Biham et al. 1993, Dowben et al. 1990a, 1990b, 1991, Hutchings et al. 1990, Kim et al. 1995, Kime et al. 1992, Li et al. 1991a, 1991b, 1992, Li & Vidali 1993, Moses et al. 1992, Onellion et al. 1987, Varma et al. 1990 and Vidali et al. 1990, 1991). There is thought to be a narrow coexistence range between the two equilibrium $c(2 \times 2)$ and $c(4 \times 4)$ phases (Hutchings et al. 1990).

The equilibrium Cu(100)- $c(2 \times 2)$ -Hg-0.50ML structure was thought to consist of mercury atoms in the four-fold hollow sites (Figure 1.5.1). This structure maintained the square geometry of the substrate surface and contained one mercury atom per unit mesh.

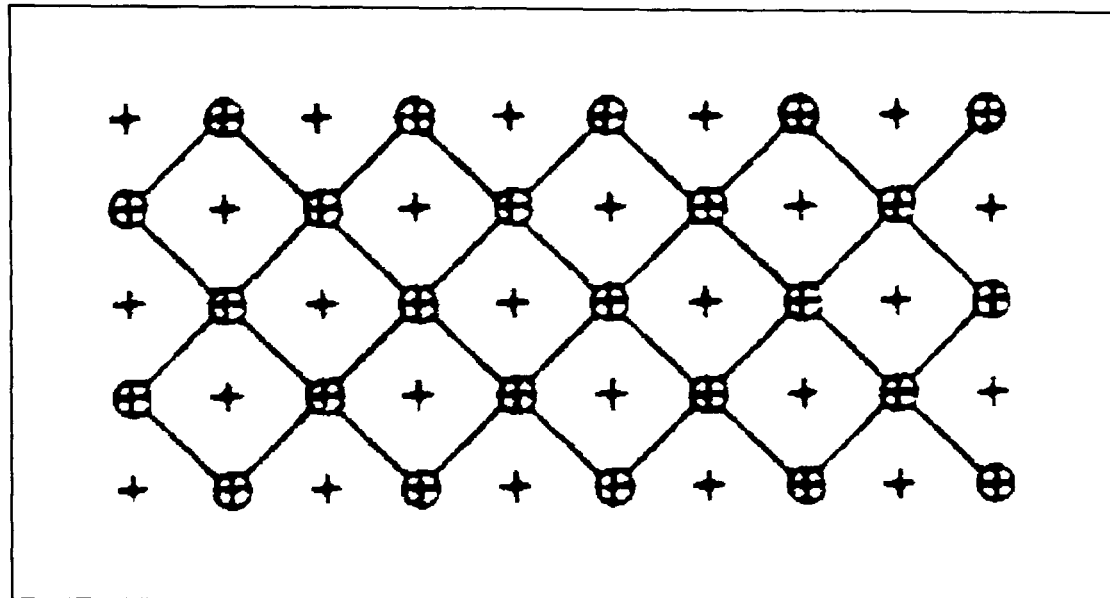


Figure 1.5.1. The equilibrium Cu(100)-c(2x2)-Hg-0.50ML structure taken from Kime et al. (1992). The Cu substrate is denoted by a (+), the Hg atoms sit at the intersections of the overlaying crossed lines. The (\oplus) indicate the coincident net from which the nomenclature is derived.

The equilibrium Cu(100)-c(4x4)-Hg-0.62ML structure was proposed to consist of a real space coincidence net structure with the mercury atoms located in a combination of four-fold hollow and low symmetry sites (Figure 1.5.2). The mercury adlayer was thought to be slightly uneven (i.e. not flat) (Dowben et al. 1991) due to the size of the mercury atom.

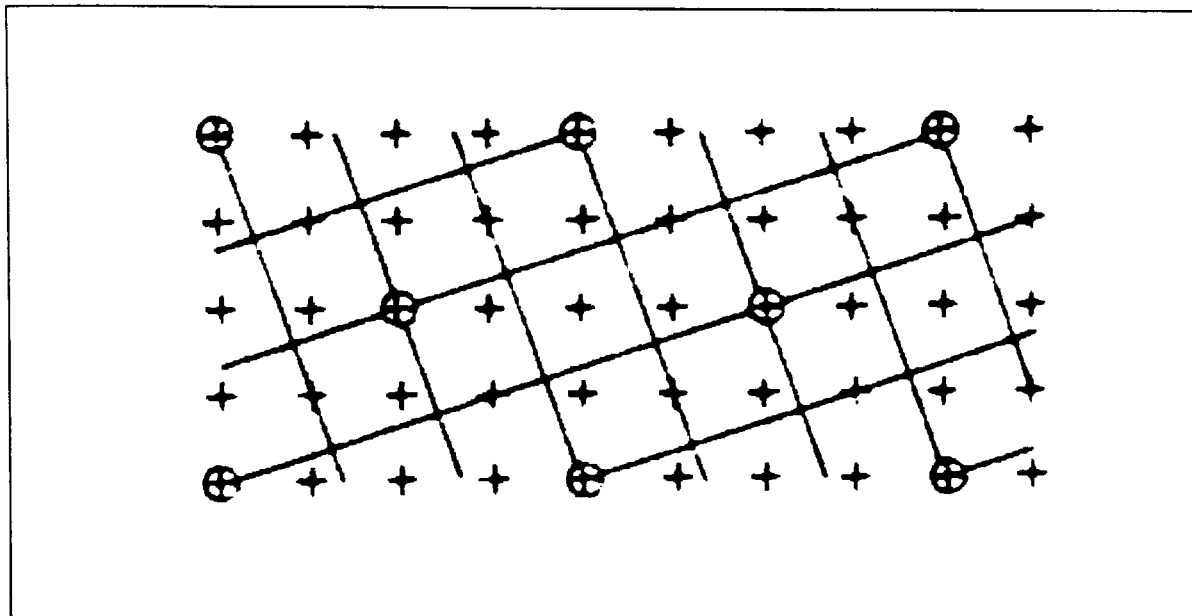


Figure 1.5.2. The equilibrium Cu(100)-c(4x4)-Hg-0.62ML structure taken from Kime et al. (1992). The Cu substrate is denoted by a (+), the Hg atoms sit at the intersections of the overlaying crossed lines. The (⊕) indicate the coincident net from which the nomenclature is derived.

As for the non-equilibrium structures, the Cu(100)-(3x3)-Hg-0.66ML (Figure 1.5.3) and Cu(100)-c(2x6)-Hg-0.83ML (Figure 1.5.4) structures were thought to consist of a combination of high symmetry sites (four-fold or atop) and low symmetry sites. This would therefore produce a 1:1 and 1:4 ratio of high symmetry to low symmetry sites for the (3x3) and c(2x6) structures respectively.

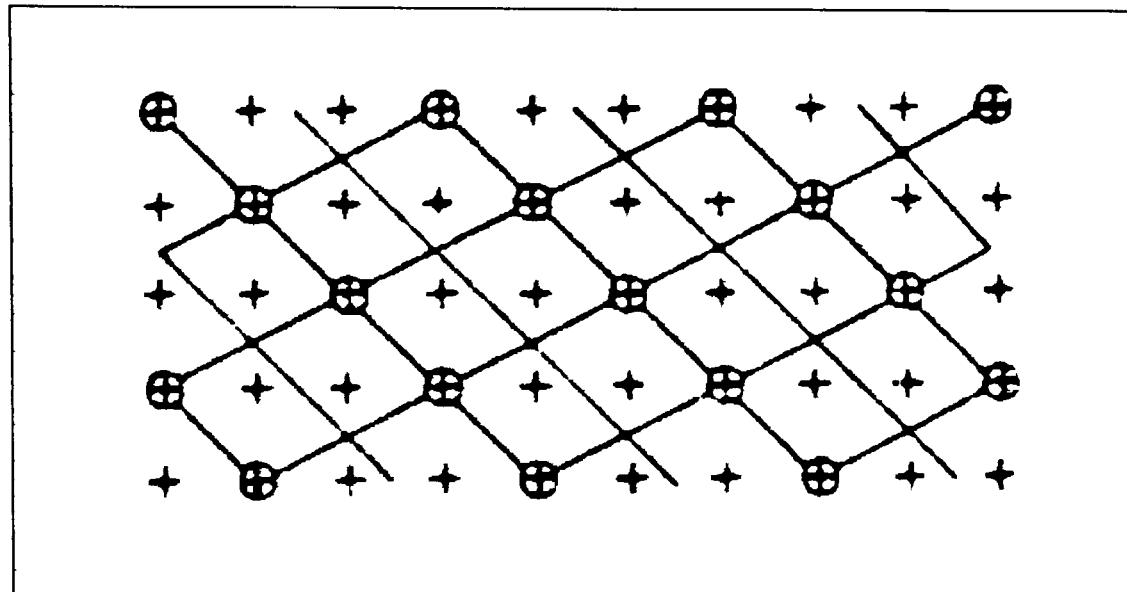


Figure 1.5.3. The non-equilibrium Cu(100)-(3x3)-Hg-0.66ML structure taken from Kime et al. (1992). The Cu substrate is denoted by a (+), the Hg atoms sit at the intersections of the overlaying crossed lines. The (\oplus) indicate the coincident net from which the nomenclature is derived.

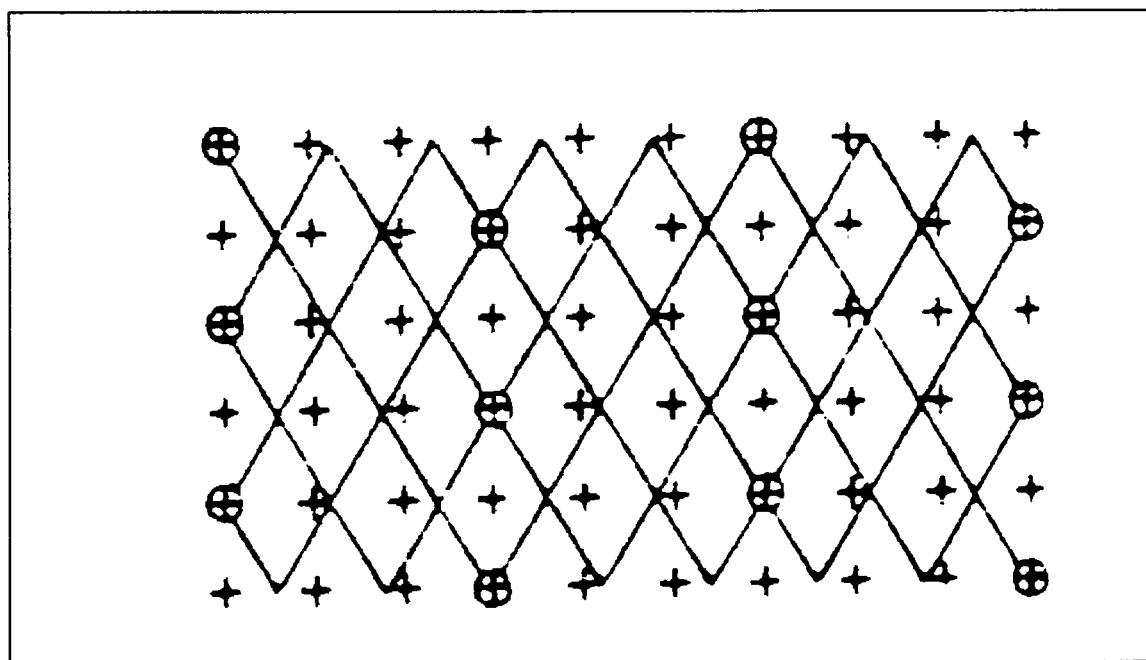


Figure 1.5.4. The non-equilibrium Cu(100)-c(2x6)-Hg-0.83ML structure taken from Kime et al. (1992). The Cu substrate is denoted by a (+), the Hg atoms sit at the intersections of the overlaying crossed lines. The (\oplus) indicate the coincident net from which the nomenclature is derived.

2 Theory

2.1 The Normal Incidence X-Ray Standing Wavefield (NIXSW) Technique

The Normal Incidence X-Ray Standing Wavefield (NIXSW) technique is a powerful tool which allows information on the local surface structural environment to be obtained by monitoring the X-Ray absorption of surface atoms. Such absorption can be monitored by various methods sensitive to surface composition, such as X-Ray Photoelectron Spectroscopy (XPS), thus making this technique sensitive to specific elements on a crystal surface. Consequently, this technique exploits both the advantages X-Ray diffraction for bulk structural analysis and the surface sensitivity of XPS to provide a very distinct method of surface structural determination.

The basis of this technique is an X-Ray standing wave, produced by Bragg reflecting coherent incident and scattered X-Ray waves from a series of lattice planes inside a crystal (figure 2.1). These reflected X-Rays constructively interfere producing an X-Ray standing wavefield (figure 2.3). The intensity of the wavefield produced is parallel to and has the same periodicity as the reflecting lattice planes (for a first order diffraction event) that created it (Cowan et al. 1980 and Patel et al. 1987). The coherent standing wavefield generated extends several thousands of angstroms into the bulk and out of the surface. The total reflectivity of the Bragg scattered beam

observed for the scattering angle or photon energy over which the Bragg condition occurs is limited by the finite penetration (“extinction”) depth of the X-Rays caused by the backscattering of the crystal. Within this range the relative positions of the incoming and outgoing X-Rays determine the phase of the standing wavefield relative to the substrate scatterer planes. Consequently a systematic shift in the phase by half its periodicity would move the nodes and antinodes of the wavefield progressively by half the lattice spacing. Therefore, if one measures the absorption of the X-Ray standing wavefield by specific atoms whilst scanning through the Bragg condition within the range of its existence, it is possible to determine the location of these atoms relative to the extended substrate scatterer planes. The surface specificity of this technique typically comes from monitoring the core level photoemission or Auger electron emission following the X-Ray absorption by the particular surface elemental species in question, i.e. the adsorbed atom.

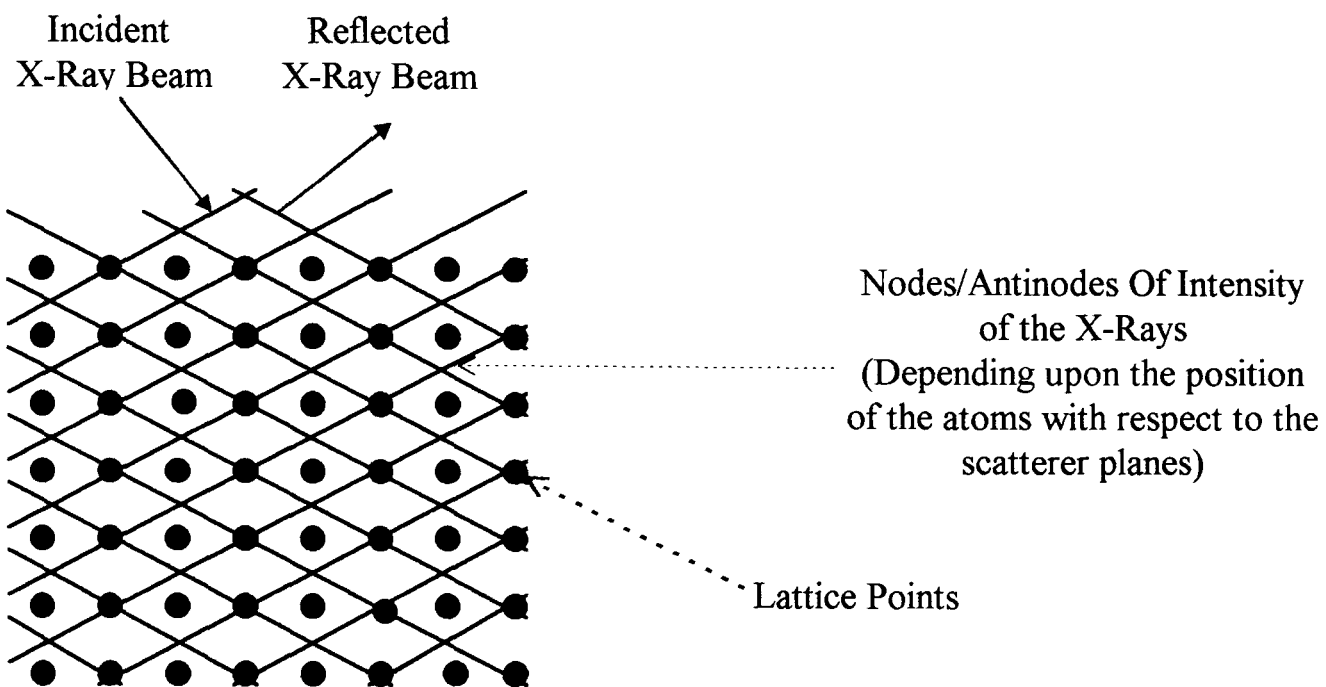


Figure 2.1. The standing X-Ray wavefield, where incident and reflected wavefronts intersect, thus giving regions of maximum and minimum amplitude.

For Bragg reflection to occur, the angle that the incident beam makes with the plane, θ must be equal to the that made by the reflected beam. The reflections from the several Bragg planes must meet in phase, that is they must satisfy the Bragg equation

$$2d_H \sin\theta = n\lambda \quad (2.1.1.)$$

where d_H is the lattice spacing, θ is the incidence angle with the atomic plane, λ is the wavelength of the incident photon, and n is an integer (figure 2.2).

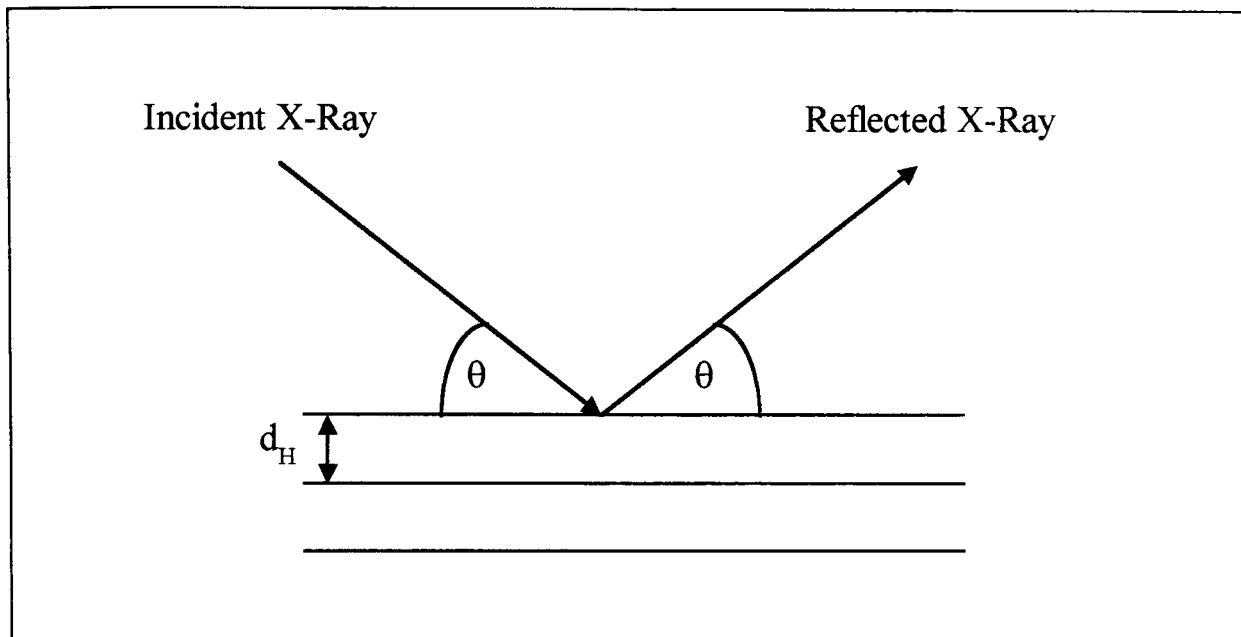


Figure 2.2. A diagram showing the Bragg reflection of an X-Ray at an atomic plane.

Performing the X-Ray standing wavefield experiment at normal incidence (or very close) to the relevant reflecting planes removes many of the restrictions of instrumentation and crystal perfection (Cowan et al. 1980, Patel et al. 1987 and Woodruff et al. 1988a). Therefore, the standing X-Ray wavefield (SXW) technique (Batterman 1964, 1969) was modified by Woodruff and co-workers (Kerkar et al. 1992a, 1992d, 1992f, Prince et al. 1990 and Woodruff et al. 1987, 1988a, 1988b, 1993) to produce the Normal Incidence X-Ray Standing Wavefield technique. The advantage of the NIXSW technique is that it uses softer X-Rays than the SXW technique (Poulsen et al. 1994, Gog et al. 1994, Ohta et al. 1985, Etalaimemi et al. 1993). The higher energy X-Rays used in the SXW technique (e.g. Mo $K\alpha$ X-Ray emission at 17.5 keV) mean that the value of θ (the angle between the beam and the

crystal planes) is small and the angular range of the total reflectivity is only a few arc-seconds. Consequently the X-Ray beam must be highly monochromatic and collimated, and there should only be limited mosaicity in the crystal. The mosaicity of a crystal is determined by how perfectly the atomic layers are positioned relative to one another, so the lowest mosaicity can be obtained for more perfect crystals such as semiconductors.

At normal incidence ($\theta = 90^\circ$) the Bragg condition passes through a turning point in its dependence on the incidence angle, θ . Consequently, because $d\sin\theta/d\theta$ is zero, the Bragg condition becomes very insensitive to the exact value of the incident angle. This makes the technique rather insensitive to limited incident beam collimation (Woodruff et al. 1987 and 1988a), with no significant difference in the NIXSW profile up to a broadening of approximately 0.5 eV. It also allows for an angular range of total reflectivity as much as 1° at $\theta = 90^\circ$ (Woodruff et al. 1988a). The angular dependence of the SXW technique limited it to studying crystals based on semiconductor materials, which have the necessary degree of crystalline perfection. Due to the insensitivity of the technique to angular spread of up to 1° , the mosaic width of the crystal can be of the order of 0.5° and have no significant effect. Therefore metallic substrates can be studied with no significant loss of signal.

For the normal incidence technique, both theory and experiment are made simpler if the Bragg condition is scanned in energy, rather than in angle. This removes the need for a high precision goniometer, and the total reflectivity can be of the order of 1eV. A disadvantage of this technique is that only wavelengths equal to $2d_H$ (from the Bragg equation, $n\lambda = 2d_H \sin\theta$, and $\theta = 90^\circ$ for normal incidence) can be used. Therefore the energy of the light used to scan the Bragg energy is fixed and determined by the crystal used.

2.1.1 Basic Theory of NIXSW

The basic theory of the NIXSW technique is outlined below. A more exhaustive treatment of the theory of both the NIXSW (Woodruff et al. 1988a, 1994) and the SXW (Batterman 1964 and 1969, Hertel et al. 1985, and Zegenhagen 1993b) technique can be found elsewhere. The full dynamical analysis of the diffraction carried out by Batterman (1964) indicated that the finite penetration of the wavefield leads to a finite range (and offset) in the incidence angle (or wavelength) over which total reflectivity can be obtained and the standing wavefield can be produced. Within this range, the phase of the standing wave shifts systematically in relation to the scatterer planes by 180° for half the bulk layer spacing. This analysis took account of the attenuation of the incident X-Ray wavefield as it penetrates the solid.

The location of the absorber atoms in the standing wave-field relative to the reflecting planes determines the absorption of the incident X-Ray flux by the absorber atom in question (see figure 2.3). The intensity of the standing X-Ray wavefield is equal to the square of the amplitude of the wavefield.

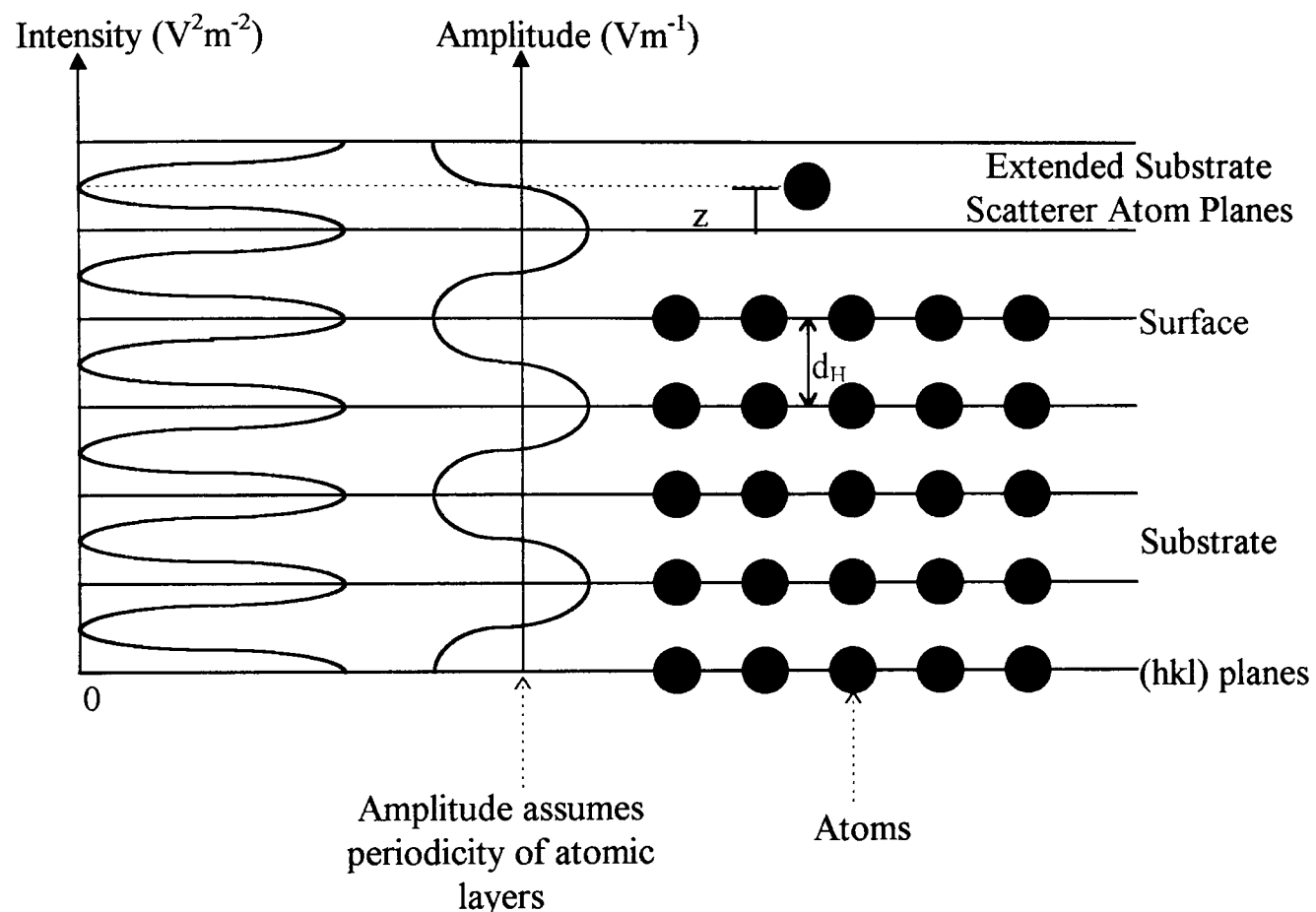


Figure 2.3. A diagram showing the amplitude (E), and the intensity (I) of the X-Ray standing wavefield relative to the periodicity of the atomic layers. The height above the extended scatterer planes is represented by z and the separation of the hkl planes is represented by d_H .

Figure 2.4 shows a schematic diagram for the idealised case of no absorption in the solid (see A in figure 2.4). For absorber atoms located on the scatterer planes, the antinodes of the standing wavefield lie midway between the scatterers causing the absorption to be zero. At the opposite end of the range (i.e. on the other side of the Bragg energy), the antinodes lie on the scatterers causing absorption four times the average absorption (the amplitude is double, and the intensity is equal to the square of the amplitude), (see B in figure 2.4). The profile is inverted for absorber atoms located midway between the scatterer planes, (see C in figure 2.4). This photoabsorption is measured using Auger and photoelectron detection techniques, whereas X-Ray fluorescence has been used in the past to monitor the absorption in SXW experiments.

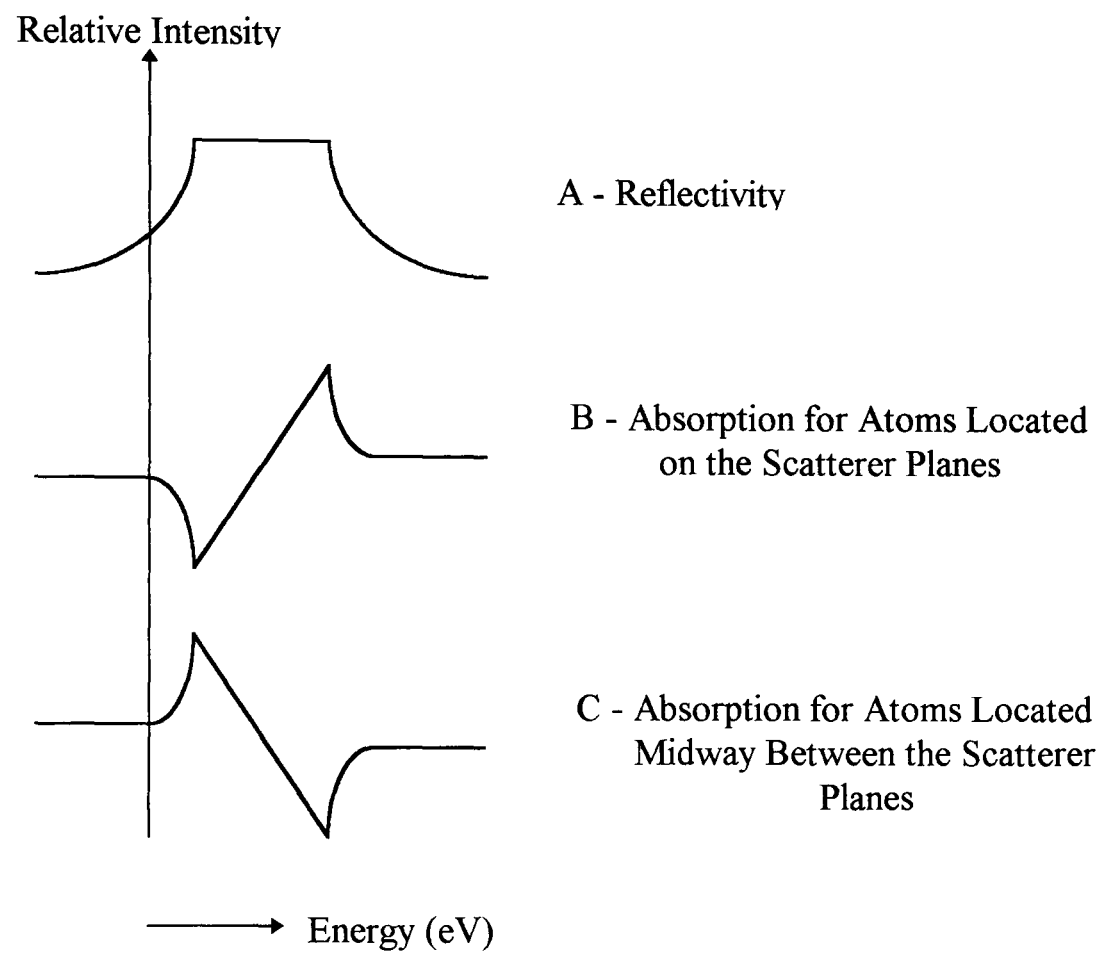


Figure 2.4. A diagram illustrating the Bragg condition for the standing X-Ray wavefield technique, for the idealised case of no absorption in the solid.

For the simple case of a single diffracted beam and a non-absorbing crystal (i.e. the classical two-beam interference problem) the intensity of the diffracted beam will vary spatially between zero and four times that of the incident beam. The intensity of the X-Ray standing wave at a vector position (i.e. absorber location) \underline{r} , is given by

$$I = \left| 1 + (E_H/E_0) \exp(-2\pi i \underline{H} \cdot \underline{r}) \right|^2 \quad (2.1.1.1)$$

where E_H/E_0 is the amplitude of the electromagnetic field and \underline{H} is the reciprocal lattice vector associated with the Bragg reflection being studied (Woodruff et al. 1988a). This can be re-expressed in terms of the perpendicular distance from the atomic scattering planes, z , which are separated by the distance d_H , where H is the indices of the reflection. Therefore,

$$I = \left| 1 + (E_H/E_0) \exp(-2\pi i z/d_H) \right|^2 \quad (2.1.1.2)$$

This is the basic equation governing the normal incidence X-Ray standing wavefield experiments (Woodruff et al. 1988a).

The amplitude (E_H/E_0) of the electromagnetic scattered wavefield relative to the incident one can be expressed in terms of the geometrical structure factors F_H , and $F_{H'}$ for the H (incident) and H' (diffracted) reflections (Woodruff et al. 1988a).

$$E_H/E_0 = -(F_H/F_{H'})^{1/2} [\eta \pm (\eta^2 - 1)^{1/2}] \quad (2.1.1.3)$$

where η is a displacement parameter related to the variable (either angle or energy) which is used to scan through the Bragg peak.

For the original form of the experiment, where the grazing angle θ_B is varied close to the Bragg angle θ_B by a difference $\Delta\theta$, the displacement parameter η is given by,

$$\eta = [\Delta\theta \sin(2\theta_B) + \Gamma F_0] / P \Gamma (F_H F_{H'})^{1/2} \quad (2.1.1.4)$$

where F_0 is the structure factor for the (000) reflection (i.e. the uninterrupted path of the X-Ray beam through the crystal), P is the polarisation factor ($P = 1$ for σ polarisation, and $P = \cos(\theta_B)$ for π polarisation), and

$$\Gamma = (e^2/4\pi\epsilon_0 mc^2) \lambda^2 / \pi V \quad (2.1.1.5)$$

where e and m are the charge and mass of the electron, ϵ_0 is the permittivity of free space, c is the velocity of light, λ is the X-Ray wavelength, and V is the volume of the unit cell.

The centre of this range (where $\eta = 0$) is offset from θ_B by the term ΓF_0 , thus giving an offset in the angle, $\Delta\theta_B$ (equal to $\Gamma F_0/\sin(2\theta_B)$). Equation 2.1.1.6 indicates that the range of $\Delta\theta_B$ over which the total reflectivity condition occurs is

$$\text{range}(\Delta\theta_B) = \pm [P |\Gamma(F_H F_H)^{1/2}/\sin(2\theta_B)] \quad (2.1.1.6)$$

For low atomic number elements, the scattering factors are low, the wavelength is short, or the unit cell is larger. Hence the range of $\Delta\theta_B$ is small, thus giving a narrow rocking curve. This sets constraints on instrumentation as the measurement and control of the incidence angle must be very nearly perfect. The crystal's mosaicity must be smaller than (or comparable to) the rocking curve if the effect is to be monitored.

In order to overcome the mosaicity problem, one can choose to work at (or very close to) normal incidence to the scatterer planes. However, equation 2.1.1.6 cannot apply at $\theta_B = 90^\circ$ ($\sin(2\theta_B) \rightarrow 0$), as ΔE is no longer linear in $\Delta\theta_B$ for $\theta_B \approx 90^\circ$. For θ_B close to 90° , the rocking curve can become quite complex as the two Bragg conditions on

either side of 90° approach one another, therefore the scattering condition is scanned in energy. The range of photon energy over which the standing wave is established is

$$\text{range}(\Delta E) = \pm[E |P| \Gamma(F_H F_H)]^{1/2} / 2\sin^2(2\theta_B) \quad (2.1.1.7)$$

As for equation 2.1.1.7, η is not linear in $\Delta\theta_B$ for $\theta_B \approx 90^\circ$, hence the η parameter is also scanned in energy, thus giving

$$\eta = [-2(\Delta E/E)\sin^2(\theta_B) + \Gamma F_0] / |P| \Gamma(F_H F_H)^{1/2} \quad (2.1.1.8)$$

This is the displacement parameter for our experiment where the energy of the incident X-Ray beam is varied around the Bragg energy, E , by an amount, ΔE (Woodruff et al. 1988a).

Equation 2.1.1.8 shows that η remains linear in ΔE , even at $\theta_B = 90^\circ$. The centre of the reflectivity range is offset from the nominal Bragg energy by $\Gamma F_0 E / (2\sin^2(\theta_B))$.

Thus giving

$$\text{range}(\Delta E) = \pm[E | P | \Gamma(F_H F_H)^{1/2} / 2\sin^2(2\theta_B)] \quad (2.1.1.9)$$

where ΔE is the energy range of the total reflectivity and is only a weak function of θ_B .

The amplitude (E_H/E_0) of the electromagnetic scattered wavefield relative to the incident one can also be expressed as the square root of the reflectivity, R , multiplied by a phase factor (Equation 2.1.1.10).

$$E_H/E_0 = \sqrt{R} \exp(i\phi) \quad (2.1.1.10)$$

This expression can be substituted into equation 2.1.1.2. to give a new expression for the intensity of the wavefield, I (Equation 2.1.1.11)

$$I = | 1 + R + 2\sqrt{R} \cos(\phi - 2\pi z/d_H) |^2 \quad (2.1.1.11)$$

It should be noted that both R and ϕ are functions of the photon wavelength (or incident angle) and therefore vary as the Bragg condition is scanned to provide the X-Ray standing wavefield profile.

Equations 2.1.1.1. to 2.1.1.11. apply to analysis for an absorber sat in a single site on a rigid lattice. For a distribution of possible adsorbate positions (due to several different discrete sites, or vibrational or static disorder, or both) one has to use a distribution of z values with a probability $f(z)dz$ of a given value with a range dz about the value z . Therefore the integral over the total probability incorporates all the adsorbate positions, z from $z=0$ (an adsorbate positioned directly where the surface atoms are situated) to $z=d_H$ (an adsorbate atom positioned exactly where the next layer of substrate atoms would occur). The normalisation of this integral is equal to unity, thus giving

$$\int_0^{d_H} f(z)dz = 1 \quad (2.1.1.12)$$

Thus for the X-Ray standing wavefield absorption profile

$$I = |1 + R + 2\sqrt{R} \int_0^{d_H} f(z) \cos(\phi - 2\pi z/d_H)|^2 dz \quad (2.1.1.13)$$

which can also be written as

$$I = 1 + R + 2f_c \sqrt{R} \cos(\phi - 2\pi D/d_H) \quad (2.1.1.14)$$

where the two parameters that totally define the structural dependence of the measured absorption profile emerge from the analysis of the experimental data. These are the coherent position, D (where the fractional coherent position, $\Delta d = D/d_H$) and the coherent fraction, f_c .

Equation 2.1.1.14. can also be written as

$$I = (1-f_c)(1+R) + f_c[1+R+2\sqrt{R}\cos(\phi-2\pi D/d_H)] \quad (2.1.1.15)$$

Equation 2.1.1.15. illustrates the fact that the absorption profile consists of a coherent part (identical to the equation for the single site 2.1.1.11.) and an incoherent part (the sum of the incident and reflected beam intensities, multiplied by a factor $1-f_c$).

A relationship between the measured quantities and the actual spatial distribution function can be found by comparing equations 2.1.1.13. and 2.1.1.14. This can be seen in equation 2.1.1.16.

$$f_c \cos(\phi-2\pi D/d_H) = \int_0^{d_H} f(D) \cos(\phi-2\pi D/d_H) dD \quad (2.1.1.16)$$

where f_c can be considered as the first component in a Fourier series representation of $f(D)$. Also, f_c contains the coherent position through a phase factor.

In the remainder of this analysis, it is more convenient to use complex numbers. Therefore by expanding the cosine summations in equation 2.1.1.16. one obtains the following

$$\begin{aligned} \cos\phi f_c \cos 2\pi D/d_H + \sin\phi f_c \sin 2\pi D/d_H &= \cos\phi \int_0^{d_H} f(D) \cos(2\pi D/d_H) dD \\ &+ \sin\phi \int_0^{d_H} f(D) \sin(2\pi D/d_H) dD \end{aligned} \quad (2.1.1.17)$$

which must be true for all values of the phase, ϕ (Woodruff et al. 1994). The phase, ϕ varies as the Bragg condition is scanned. Sine and cosine have opposite parity. Hence, equation 2.1.1.17. is only satisfied if both coefficients of sine ϕ and cosine ϕ can be equated, thus giving rise to equations 2.1.1.18. and 2.1.1.19.

$$\cos\phi f_c \cos 2\pi D/d_H = \cos\phi \int_0^{d_H} f(D) \cos(2\pi D/d_H) dD \quad (2.1.1.18)$$

$$\sin\phi f_c \sin 2\pi D/d_H = \sin\phi \int_0^{d_H} f(D) \sin(2\pi D/d_H) dD \quad (2.1.1.19)$$

If equation (2.1.1.19) is multiplied by i (that is $\sqrt{-1}$), this resulting equation is summed with (2.1.1.18) to obtain a complex expression for which both real and imaginary parts must be equal, the following expression is obtained.

$$f_c \exp(2\pi i D/d_H) = \int_0^{d_H} f(D) \exp(2\pi i D/d_H) dD \quad (2.1.1.20)$$

This equation can be used to construct a simple graphical representation of the way in which the measured quantities f_c and D relate to the integral over a real space distribution function (see section 2.1.3). In brief, an Argand diagram can be used to represent each layer spacing in the spatial distribution with a vector whose direction is defined by the phase angle $2\pi D/d_H$ relative to the positive x axis. The length of this vector is equal to the probability of that phase angle, $f(D)$. The resultant (vector summation of the component vectors) has a length equal to the coherent fraction f_c , and a phase angle equal to $2\pi D/d_H$ (or $2\pi \Delta d$).

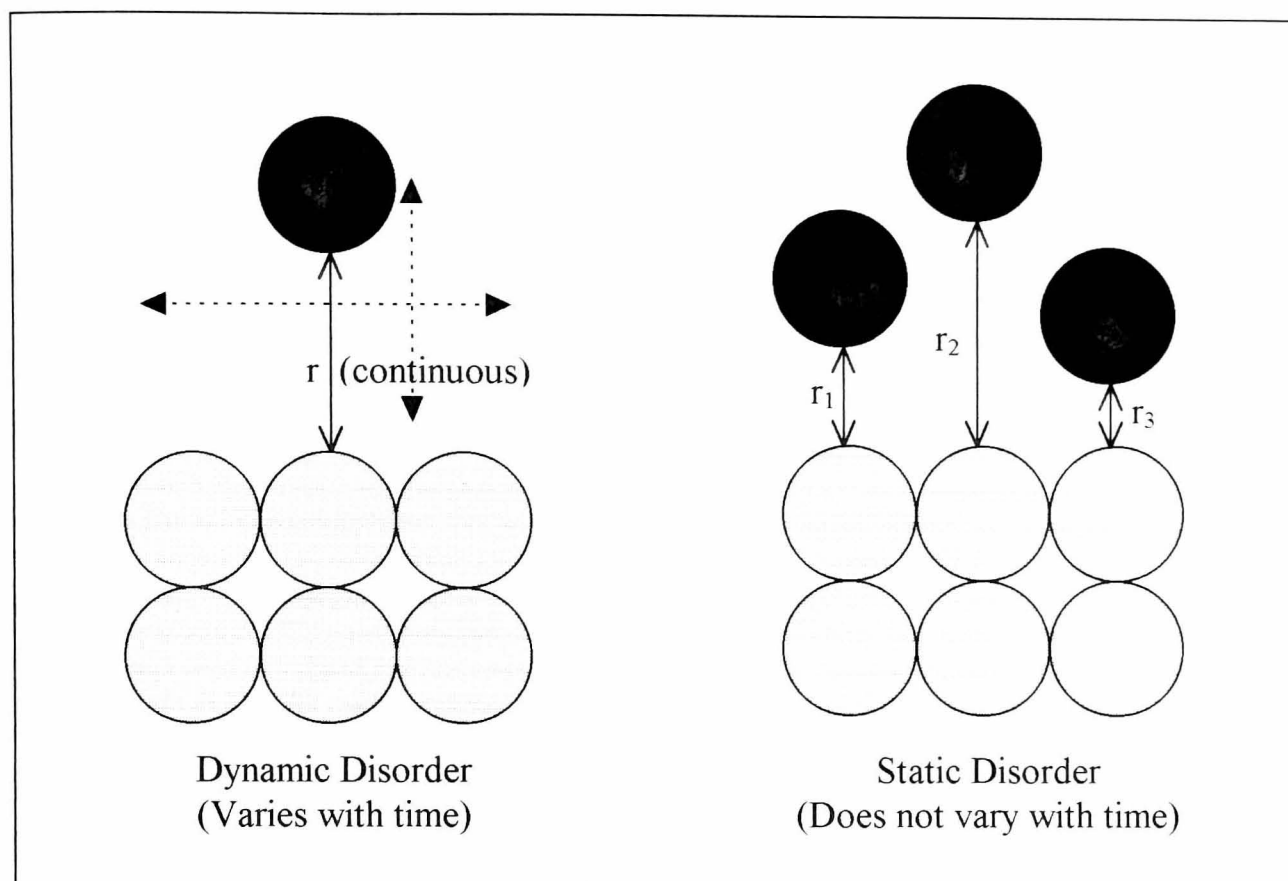


Figure 2.5. A schematic diagram illustrating the two types of disorder that affect the value of the coherent fraction. Dynamic disorder, where the position of the adsorbate, r can be approximately represented by a continuous function, and static disorder, where there are several discrete positions (r_1 , r_2 , and r_3 etc.) for the adsorbate.

The coherent fraction gives an indication of the uncertainty of the adsorbate atom's position relative to a reflecting plane. The value of the coherent fraction is affected by the thermal vibrational motion (dynamic disorder) of the adsorbate, and the range of positions that the adsorbate might have (static disorder) (figure 2.5.). Therefore a coherent fraction of 1 indicates that the adsorbate atom has no thermal vibrational motion, and all the adsorbate atoms are located in one particular type of site.

Calculations for the Cu(100) crystal in the (200) and (111) Bragg reflection planes would produce analogous profiles to those shown in figures 2.6 to 2.9.

Figure 2.6. illustrates how the theoretical NIXSW absorption profiles would change for varying values of the coherent fraction. These absorption profiles were calculated for Ni(111) using a mosaic width of 0.1° , an energy width of 0.8 eV, a lattice spacing of 2.036 Å, a Debye-Waller factor of 1.0 and assuming Δz to be 0.00 Å. The theoretical NIXSW absorption profiles for the (111) and ($\bar{1}11$) reflections are identical for the Ni(111) surface. It can be seen that various values of the coherent fraction produce absorption profiles with significantly different size and shape.

Figure 2.7. shows how the theoretical NIXSW absorption profiles would vary for different values of the perpendicular distance (i.e. the coherent position) of the adsorbate from the atomic scattering planes. These profiles were calculated for Ni(111) in the (111) Bragg reflection plane using a mosaic width of 0.1° , an energy width of 0.8 eV, a Debye-Waller factor of 1.0, a coherent fraction of 1.0 and a lattice spacing of 2.036 Å. The fact that the absorption peak shifts and changes in profile as the absorber location changes, provides the basis of the X-Ray standing wavefield absorption technique.

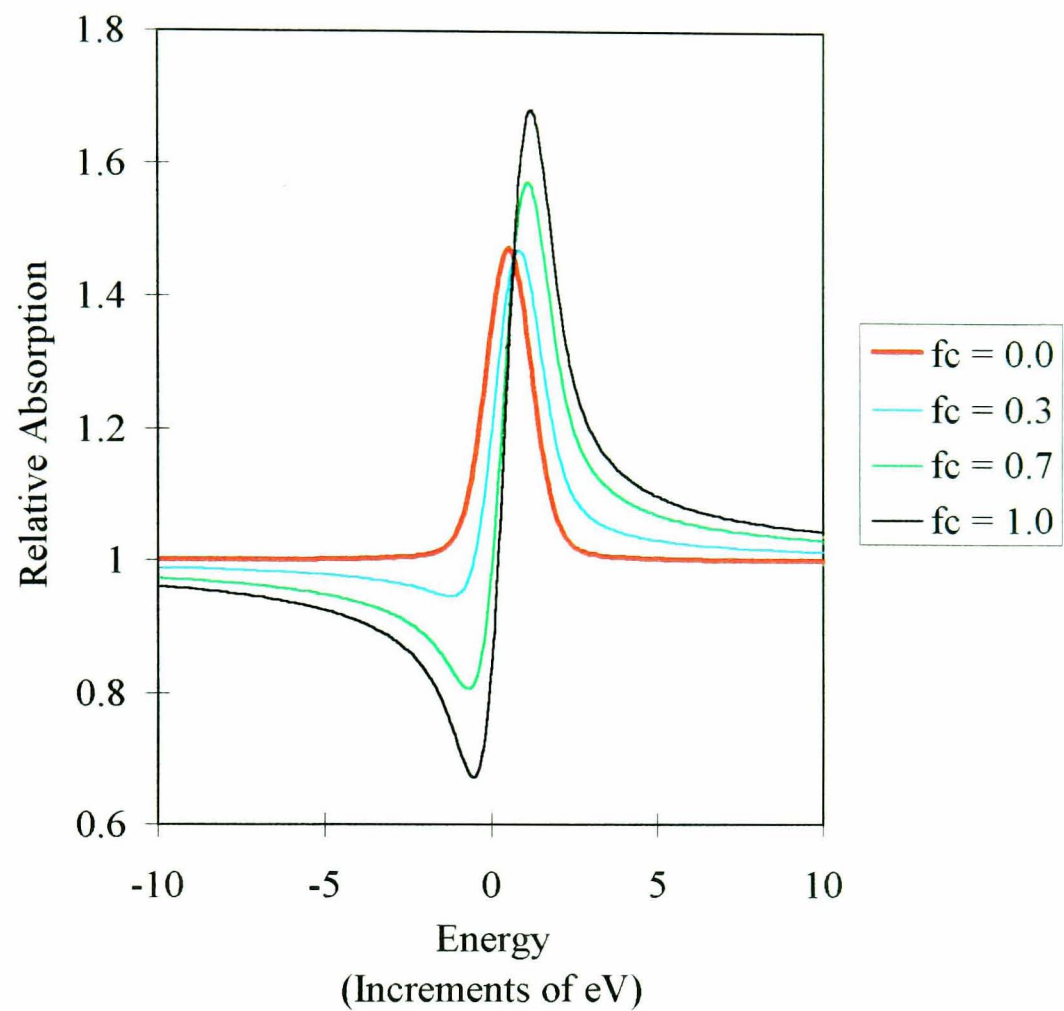


Figure 2.6. The theoretical NIXSW absorption profiles for varying values of the coherent fraction calculated for Ni(111). A mosaic width of 0.1° , an energy width of 0.8 eV, a lattice spacing of 2.036 Å, a Debye-Waller factor of 1.0 and Δz of 0.00 Å were used.

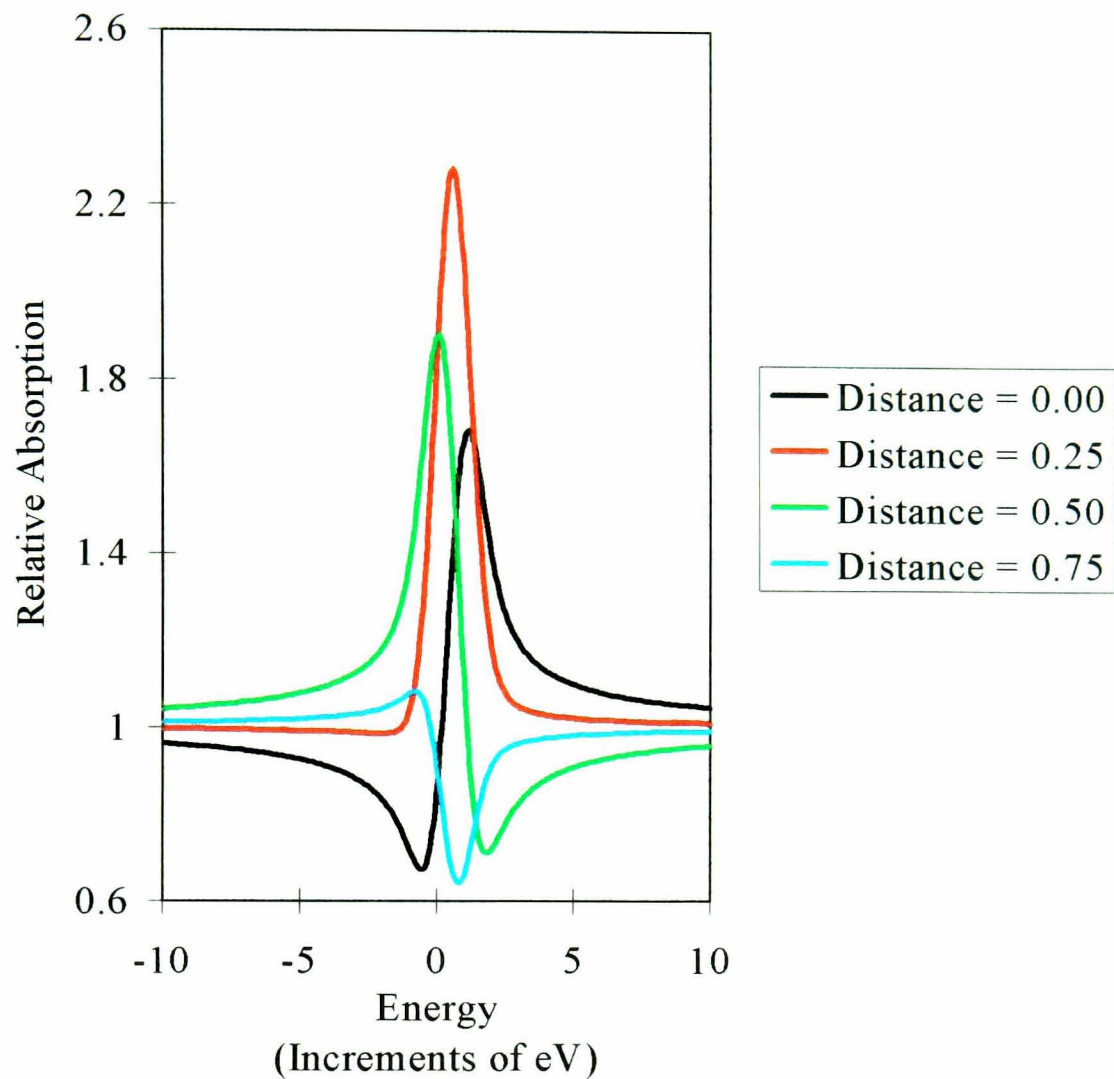


Figure 2.7. The theoretical NIXSW absorption profiles change for varying values of the fractional perpendicular distance of the adsorbate from the atomic scattering planes calculated for Ni(111) in the (111) Bragg reflection plane. A mosaic width of 0.1° , an energy width of 0.8 eV, a Debye-Waller factor of 1.0, a coherent fraction of 1.0 and a lattice spacing of 2.036 Å were used.

Figure 2.8. indicates how the theoretical NIXSW absorption profiles differ for changing values of the mosaic width. These absorption profiles were calculated for Ni(111) in the (111) Bragg reflection plane using an energy width of 0.8eV, a lattice spacing of 2.036 Å, a Debye-Waller factor of 1.0, a coherent fraction of 1.0 and assuming Δz to be 0.00 Å. The similarities in the profiles show the tolerance of the experiment to angular imperfections.

Figure 2.9. displays how the theoretical NIXSW absorption profiles change for different values of the energy broadening of the X-Ray beam. These NIXSW absorption spectra were again calculated for Ni(111) in the (111) Bragg reflection plane using a mosaic width of 0.1°, a lattice spacing of 2.036 Å, a Debye-Waller factor of 1.0, a coherent fraction of 1.0 and Δz of 0.00 Å. It can be seen that the energy broadening (i.e. the energy resolution) of approximately 1eV causes a significant attenuation and broadening of the line shape.

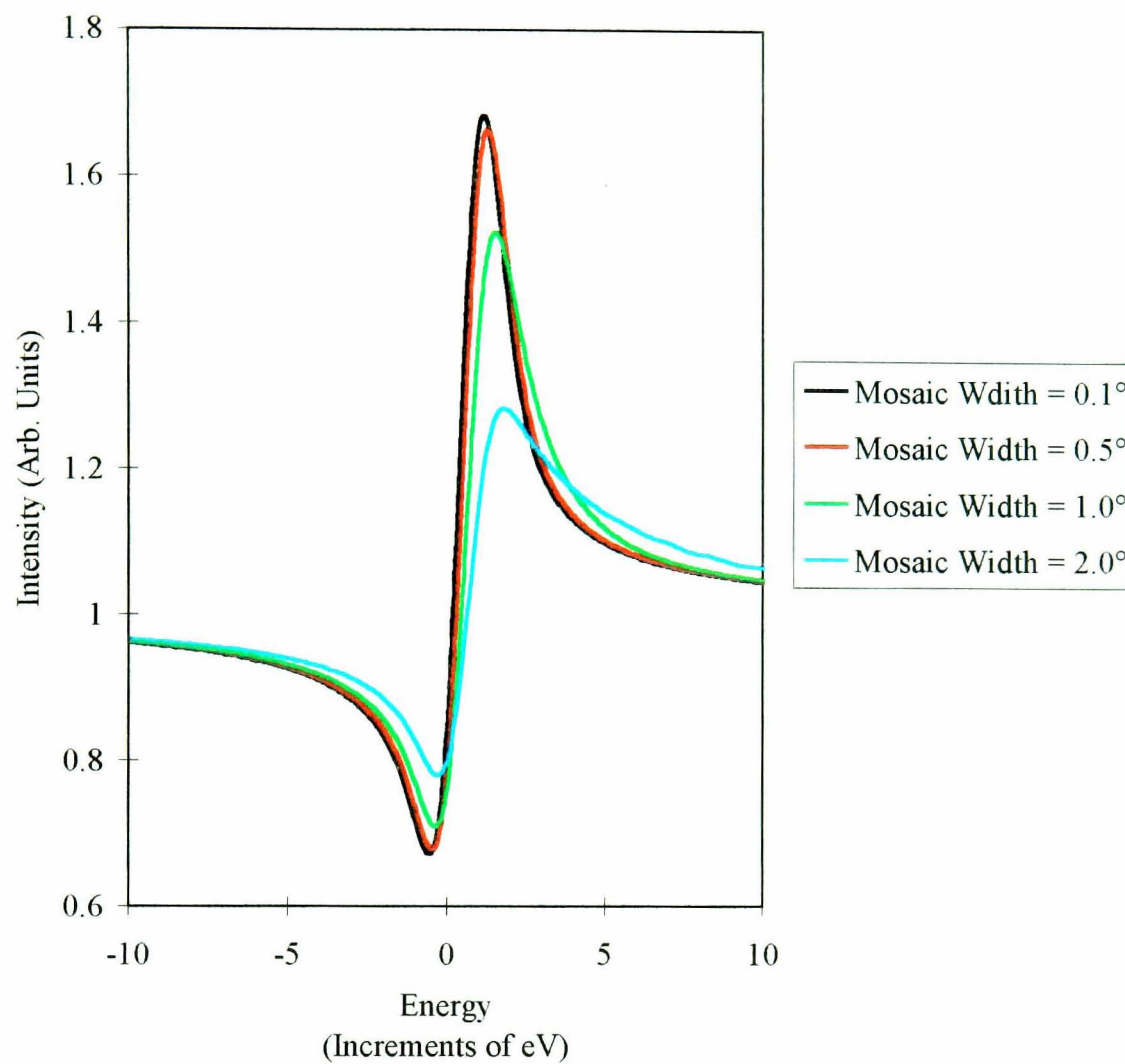


Figure 2.8. The theoretical NIXSW absorption profiles change for varying values of the mosaic width calculated for Ni(111) in the (111) Bragg reflection plane. An energy width of 0.8eV, a lattice spacing of 2.036 Å, a Debye-Waller factor of 1.0, a coherent fraction of 1.0 and Δz of 0.00 Å were used.

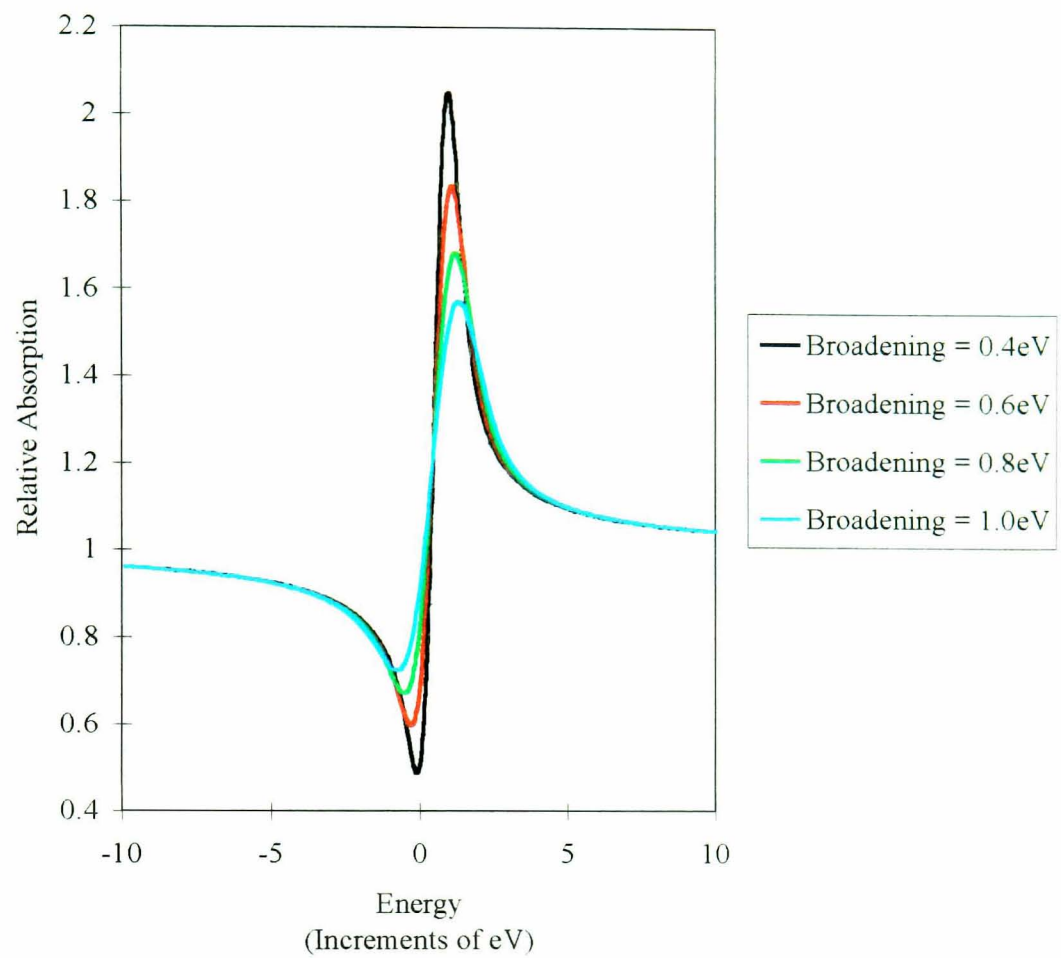


Figure 2.9. The theoretical NIXSW absorption profiles change for varying values of the energy broadening of the X-Ray beam calculated for Ni(111) in the (111) Bragg reflection plane. A mosaic width of 0.1° , a lattice spacing of 2.036 \AA , a Debye-Waller factor of 1.0, a coherent fraction of 1.0 and Δz of 0.00 \AA were used.

2.1.2 Argand Diagram Analysis of NIXSW Data

The theoretical explanation as to how the Argand analysis relates to the NIXSW theory has already been explained in section 2.1.1. In this section, we will discuss how various structural properties of a system can be derived from the Argand diagrams, and therefore facilitate relatively easy analysis through their distinguishability.

The Argand analysis method used to analyse our NIXSW data has already been described by Woodruff et al. (1994). Equation 2.1.1.20 can be used to construct a simple graphical representation of the way in which the measured quantities f_c and z relate to the integral over a real space distribution function.

$$f_c \exp(2\pi D/d_H) = \int_0^{d_H} f(D) \exp(2\pi D/d_H) dD \quad (2.1.1.20)$$

Therefore, an Argand diagram (figure 2.10) can be used to represent the fitting parameters (coherent fraction, f_c and coherent position, $\Delta d = D/d_H$) obtained from each NIXSW scan with a vector in the complex plane. Hence, the adsorbate position can be represented by a vector whose direction is defined by the phase angle $2\pi D/d_H$ relative to the positive x axis. The length of this vector is equal to the probability of the phase angle, $f(D)$ and is therefore multiplied by the formal weighting, f_0 of each of the sites.

Consequently a coherent fraction of 1.0 and coherent position (Δd) of zero (or any multiple of d_{hkl}) is expressed by a unit vector lying along the positive real axis. As Δd is increased continuously from 0 to $d_{(111)}$ (for the (111) reflection data), the vector rotates anti-clockwise until it again lies along the real positive axis when $\Delta d = d_{111}$. The process of increasing Δd continuously from 0 to $d_{(111)}$ is equivalent to raising the adatom above the reflecting planes.

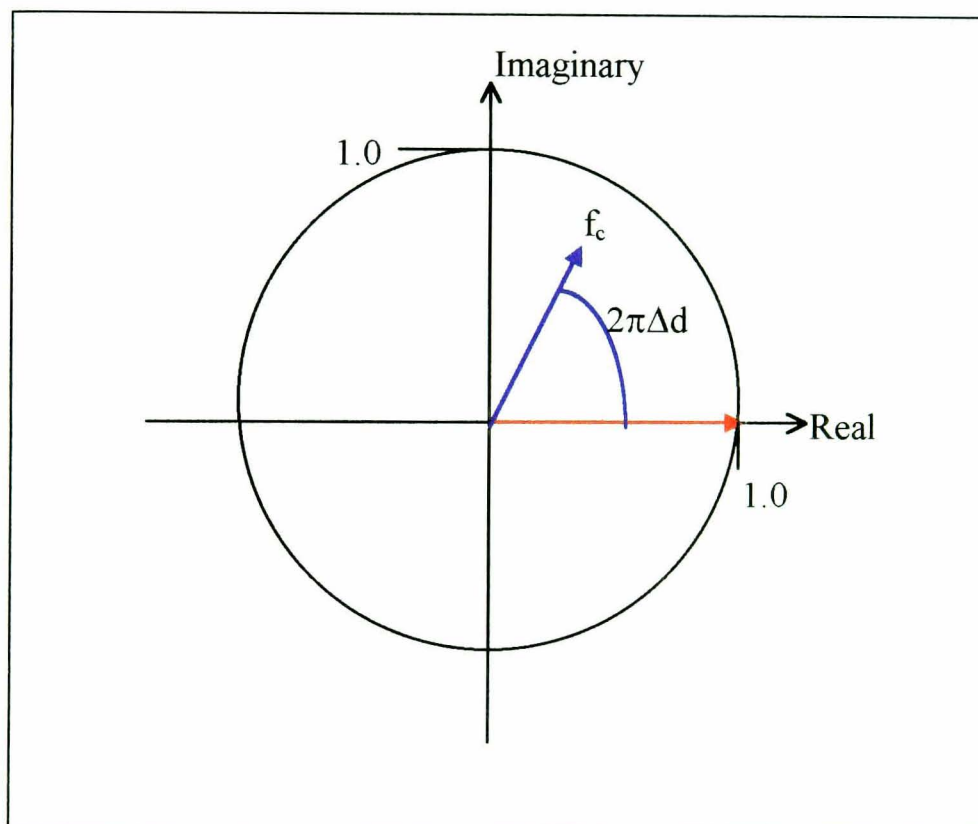


Figure 2.10. An Argand diagram with a vector representation of a coherent fraction, f_c and a fractional coherent position, $2\pi\Delta d = 2\pi D/d_{hkl}$ (blue arrow) for a single rigid adsorption site where d_{hkl} is the periodicity of the bulk scatterer planes. A coherent fraction of 1.0 and a coherent position of zero (or any multiple of d_{hkl}) are represented by the red arrow.

For a single adsorption site, the coherent fraction, f_c is represented by the length of the vector. The coherent position, $2\pi\Delta d$ (i.e. $2\pi D/d_{hkl}$) is the angle of the vector measured anti-clockwise from the positive real axis.

For a distribution of adsorbate positions above the reflecting planes (i.e. static or dynamic disorder), the vector representation is the resultant of the various vector components (vector summation of the component vectors). Such a vector will then have a length equal to the coherent fraction, f_c and a phase angle equal to $2\pi z/d_H$ (or $2\pi\Delta d$) for the adsorbate substrate system (Woodruff et al. 1994).

The resultant vectors obtained from experimental data can then be compared with the vectors (or sums of vectors) produced from the heights of theoretical adsorption sites. We will now discuss several different adsorption effects that occur, how these influence the NIXSW results through equation 2.1.1.20 and how they can be studied using the Argand analysis technique.

2.1.2.1. Thermal Vibration Effects and Local Disorder

Any real adsorbate - substrate system and related structures will experience thermal vibrations. As mentioned earlier, thermal vibrations and local disorder affect the NIXSW fitting parameters.

Vibrations introduce an incoherent component into the X-Ray standing wave, thus reducing the coherent fraction by a Debye-Waller factor. This contribution from the

bulk substrate lattice is predictable and can therefore be distinguished from the unknown spatial distribution function of the absorber atoms.

Thermal vibrations also introduce a finite width in the adatom distribution function $f(D)$, which is normally Gaussian. The resulting dephasing of the absorber layer spacing introduces an incoherent part to the absorption profile. This incoherence increases as the vibrational amplitude and therefore the Gaussian width grows. The thermal vibrations of the adsorbate atoms provide a vector distribution symmetrical about its mean position (figure 2.11), hence the resultant position remains unchanged and only the coherent fraction is affected.

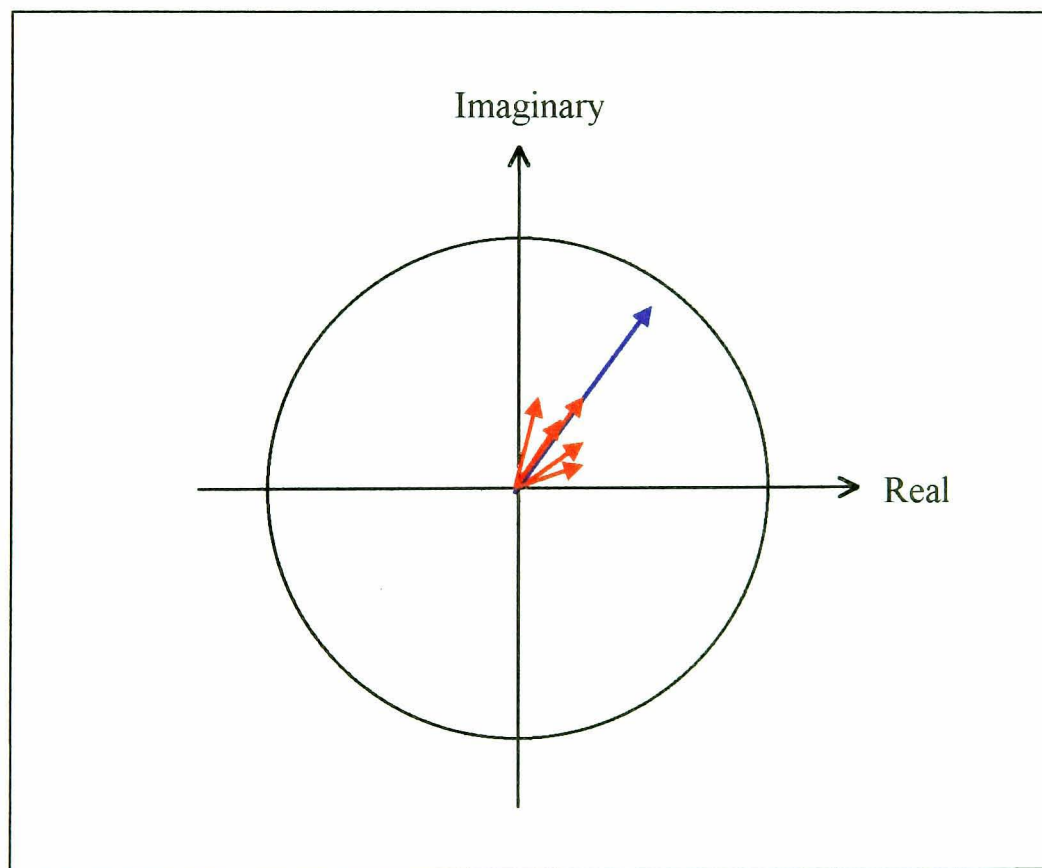


Figure 2.11. Argand vector diagram showing the components (red) and resultant (blue) vectors for a Gaussian distribution of positions due to thermal vibrations.

The X-Ray standing wavefield is sensitive to the component of atomic displacement perpendicular to the scatterer planes (therefore leading to variations in the coherent position, Δd). Consequently, the above considerations can also be applied to static disorder of the adsorbate or substrate atoms. This static disorder will also lead to incoherence in the absorption profile. Therefore the incoherence will again increase as the static disorder and hence the Gaussian width also increases.

2.1.2.2. Multiple Adsorption Sites

It is possible for an adsorbate to occupy at least two distinct adsorption sites on a surface. This could be because the adsorbate is adsorbed in two layers, there are two adsorption sites with similar energies, or because the adsorbed molecule contains two atoms of the same species that adopt inequivalent sites.

The simplest case of multiple adsorption is when two adsorption sites have an equal probability of adsorption. The two adsorbate heights (D_1 and D_2) must be summed for the Argand analysis of this type of adsorption.

If we consider a perfect rigid lattice, with two discrete sites, resultant vector is equal to the vector sum of these two values. The coherent fraction, f_c is multiplied by the formal weighting, f_0 of each of the sites. If we then include the effects of local disorder and thermal vibrations (as in section 2.1.2.1.), there are two peaks in the distribution function $f(D)$. However, the integral over the full distribution function can

be written as the integral sum of all the peaks. If both sites have identical vibrational and static disorder, the individual peaks can then be assigned the same formal weightings, f_0 (0.5 each for two equally weighted sites). Therefore the coherent fraction for the two adsorption sites combined is the value of the coherent fraction, f_c if only one of these sites were occupied, multiplied by the weighting of each site (figure 2.12.). The resulting NIXSW absorption profile would be characterised by

$$D = (D_1 + D_2)/2 \quad f_c = f_0 |\cos [\pi(D_1 - D_2)/d_H]| \quad (2.1.2.2.1)$$

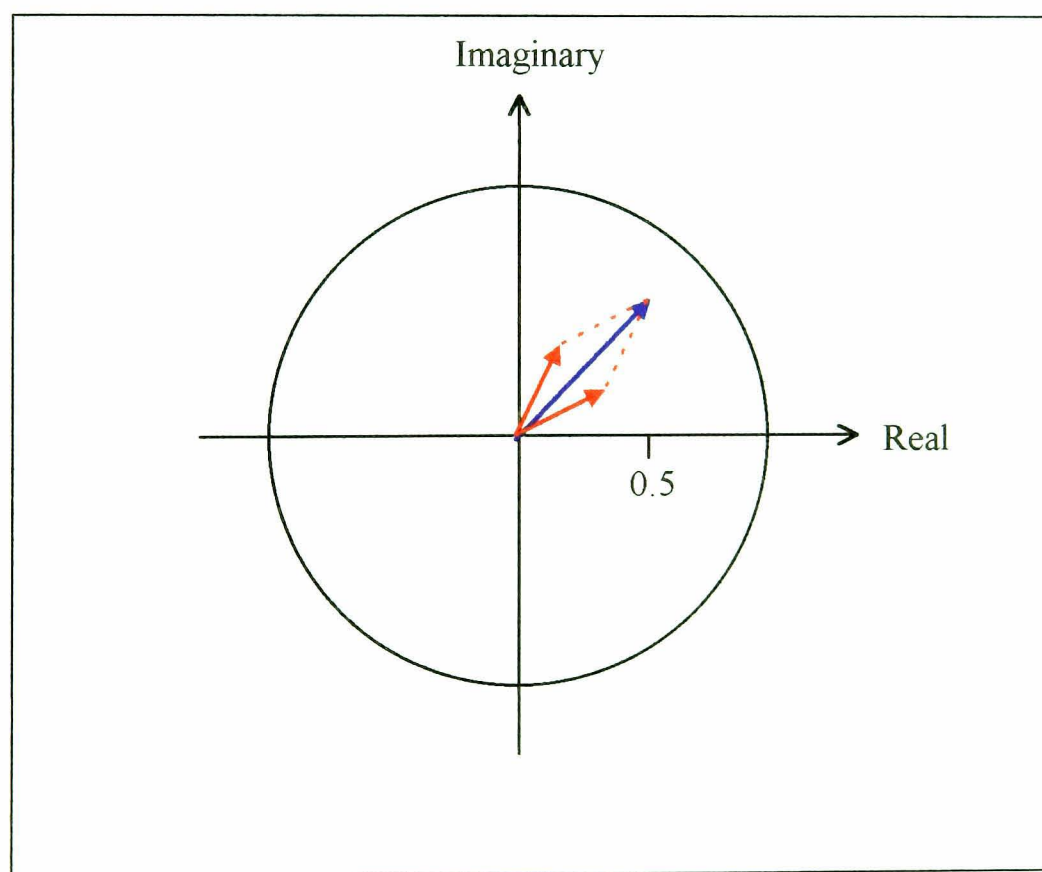


Figure 2.12. Argand vector diagram showing the summation of contributions of two equally weighted adsorbate height layer spacings. The components and the resultant are represented red and blue vectors respectively. It is assumed that there is no disorder or vibrations for the individual contributions.

Equation 2.1.2.2.1. indicates that if the 2 layer spacings differ by half the reflecting plane layer spacing, $d_{hkl}/2$, the resultant coherent fraction, f_c will be zero. This is because the two vectors are equal and opposite, and therefore cancel (figure 2.13.). For a coherent fraction of zero, the NIXSW absorption profile is always Gaussian as the monochromator has a Gaussian output.

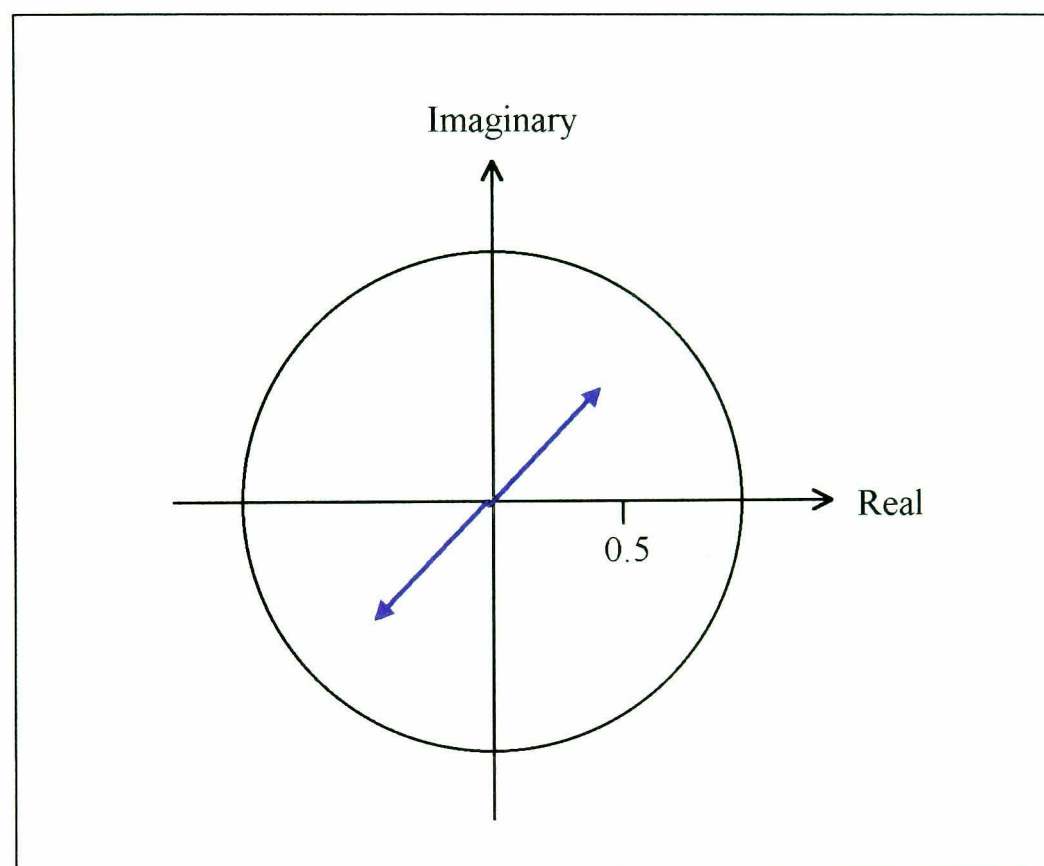


Figure 2.13. Argand vector diagram showing the vector components of two equally weighted adsorbate height layer spacings differing by half the bulk layer spacing. It is assumed that there is no disorder or vibrations for the individual contributions.

It should be noted that the simplicity of equation 2.1.2.2.1. is lost if the two adsorption sites have different weightings, f_0 because of the various occupation weightings or different local disorder (Kadodwala et al. 1996).

For a coincidence lattice adsorbate structure, the individual layer spacings of the different adsorption sites will involve regular increments that are rational fractions of the bulk layer spacing for specific reflections. Such reflections are from experiments involving scatterer planes that are not parallel to the surface (e.g. the (111) plane for the Cu(100) surface). Therefore, as seen in figure 2.14, the vector representation of five equally spaced layer spacings for the different adsorption sites cancels exactly (Woodruff et al. 1994). Consequently, for a coincidence adsorbate lattice studied using any X-Ray standing wavefield in which the reflecting planes are not parallel to the surface, the vector sum of each adatom's contribution leads to a coherent fraction of zero and a Gaussian absorption profile.

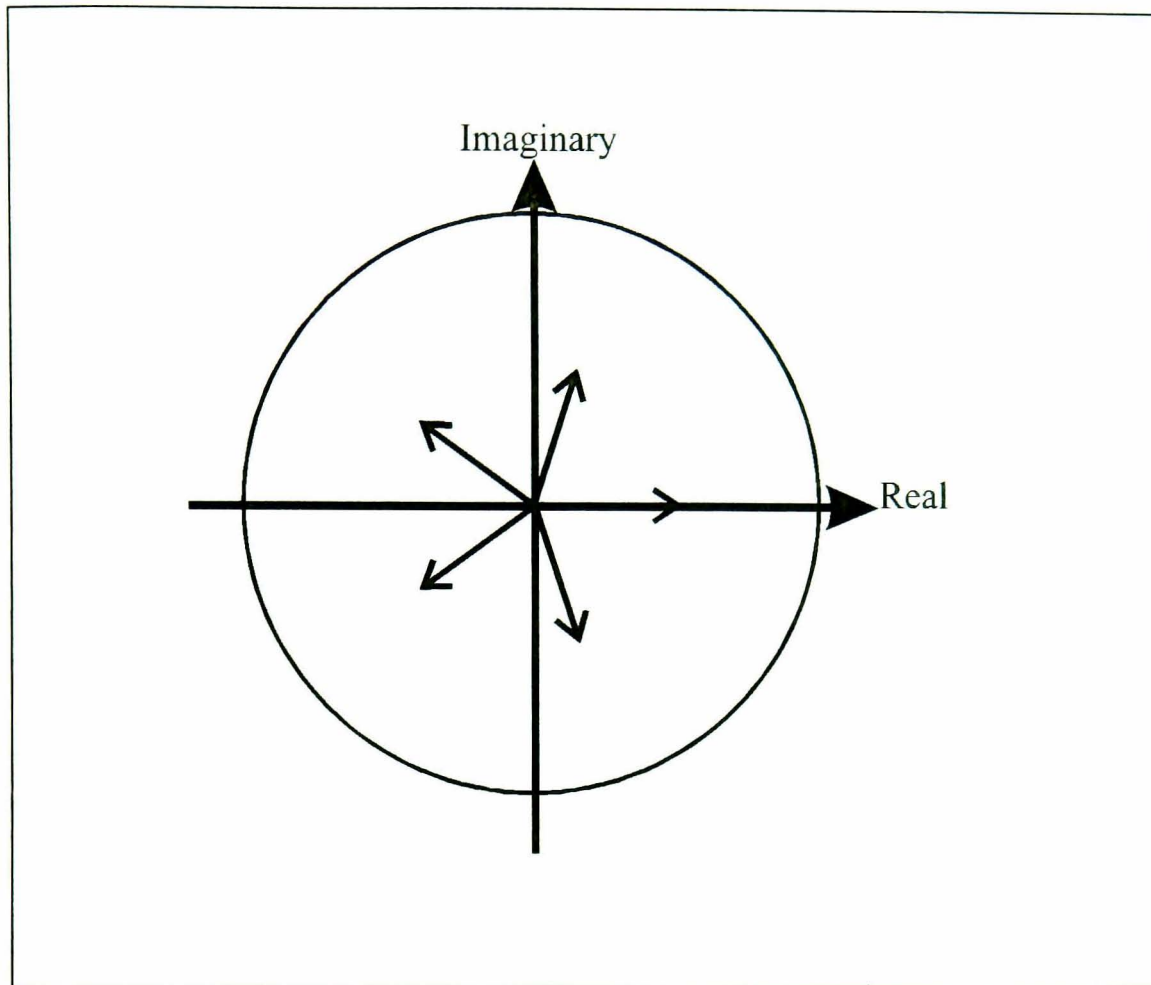


Figure 2.14. An Argand vector diagram showing the adsorbate layer component contribution of five individual adsorbate atoms of a coincident net for which the vectors cancel exactly.

2.1.2.3. Low Symmetry Adsorption Sites

If the local structure of any adsorbate surface has a lower symmetry than the substrate, several different structures must have an equal probability of occurring (Woodruff et al. 1994). For example, if an atom adsorbs onto a 2-fold bridge site of a (111) face centered cubic surface, there are three types of bridge site relative to the substrate surface (see section 1.1.3.1). Two of these bridge sites are essentially identical and therefore have twice the weighting of the other 2-fold bridge site. Consequently, we would expect the surface to be covered by small domains of adsorbates in these different sites, which will be equally occupied on average. Hence, there will be contributions of several adsorbate heights (that is z-values) to any reflection involving scatterer planes not parallel to the surface from each low symmetry site on the surface. This type of domain averaging will also introduce another reduction in the coherent fraction, f_c .

2.1.3 Triangulation of the Adsorbate Position

2.1.3.1 Hg/Ni(111) System

The NIXSW data sets only provided information about the adsorbate-substrate layer spacing in one direction. Therefore, the experiments were performed in both the (111) and $(\bar{1}11)$ directions. A process of real space triangulation is then carried out (Frost et al. 1967 and Kerkar et al. 1992e & 1992f). Each adsorption position has a different distance from each reflecting plane. Hence sites with the same distance from one plane will have a different distance from another plane. The heights of an adsorbate above the (111) reflection plane can be calculated using the mercury atomic radius and the nickel metallic radius. It can be seen from figure 2.15, that an adsorbate in a high symmetry site (on an FCC metal such as the Ni(111) crystal), with a height, x above the (111) plane has a different height with respect to the $(\bar{1}11)$ planes for each particular site. Therefore the height of the adsorbate above the $(\bar{1}11)$ reflection plane can be calculated using simple geometry as illustrated in figure 2.15. For an adsorbate in a three-fold hollow site on a (111) FCC surface there are two types of adsorption site relative to the $(\bar{1}11)$ reflection plane, face centered cubic (FCC) and hexagonally close packed (HCP). The FCC and HCP three-fold hollow sites have different heights above the $(\bar{1}11)$ reflection plane, as illustrated in figure 2.15.

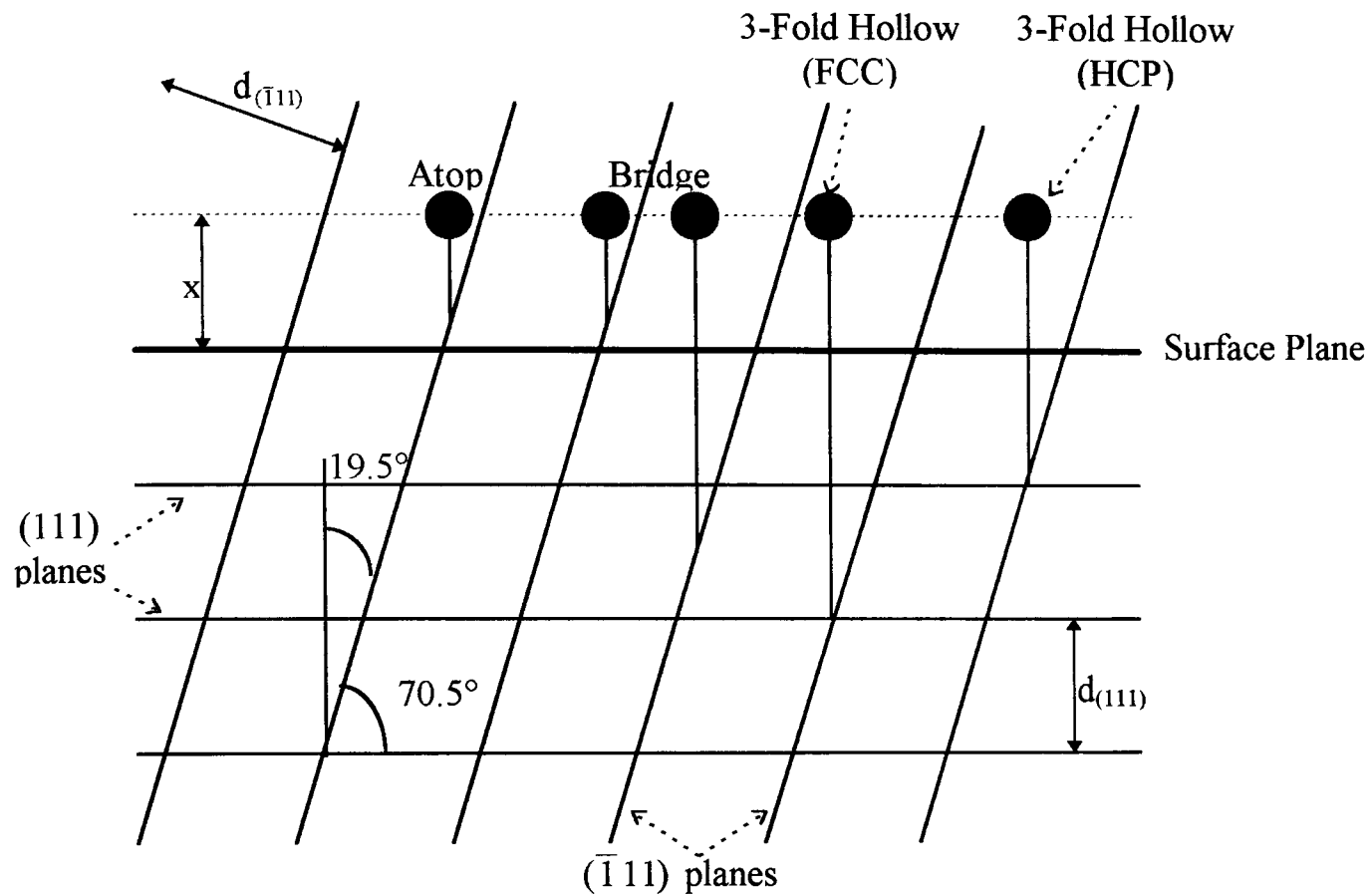


Figure 2.15. A diagram indicating the various high symmetry sites and their differing distances from the $(\bar{1}11)$ reflection plane. $d_{(\bar{1}11)}$ is the distance of the various sites above the $(\bar{1}11)$ reflection plane, and x is the distance of the various sites from the (111) reflection plane. The dimensions indicated in this diagram are arbitrary.

There are three types of bridge site relative to the 3-fold symmetry of the substrate surface, however two of these bridge sites are essentially identical and therefore have twice the weighting of the other 2-fold bridge site. The two different types of 2-fold bridge site on a (111) face centered cubic surface, such as the $\text{Ni}(111)$ surface are illustrated in figure 2.16. Consequently, 2-fold bridge sites have two possible distances with respect to the $(\bar{1}11)$ plane (see figure 2.15.). Type A uses the same

height equation for the height above the $(\bar{1}11)$ plane as the atop site, but has a different height above the (111) plane to the atop site and therefore has a different height above the $(\bar{1}11)$ plane to the atop site.

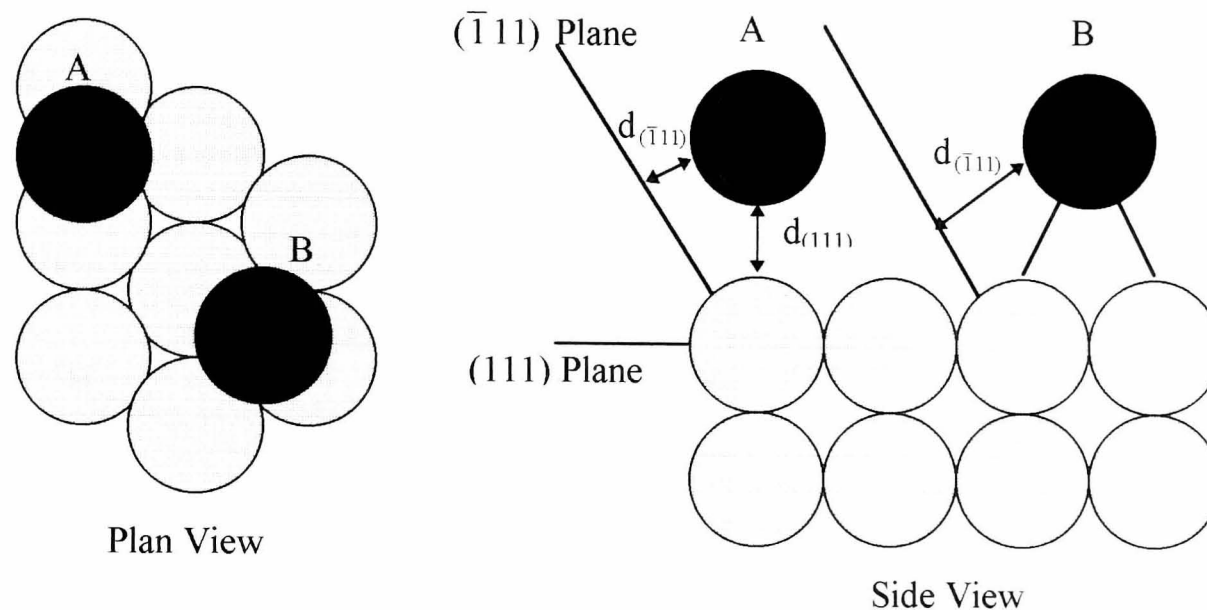


Figure 2.16. A schematic diagram illustrating the two types of bridging sites for a face centered cubic surface, and their different heights with respect to the $(\bar{1}11)$ plane.

2.1.3.2 Hg/Cu(100) System

Again the NIXSW data sets only provide information about the adsorbate-substrate layer spacing in one direction. Therefore, the experiments for the Hg/Cu(100) system were performed in both the (200) and (111) directions. The (200) reflection was used as the (100) reflection was forbidden. For an FCC crystal, the reflections for the (hkl) values which are not all even or all odd are systematically absent (Kittel 1986). Once more a process of real space triangulation is then carried out (Frost et al. 1967 and

Kerkar et al. 1992e & 1992f). Figure 2.17. demonstrates that an adsorbate in a high symmetry site on a Cu(100) crystal with a height, x , above the (200) plane has a different height with respect to the (111) planes for each particular site.

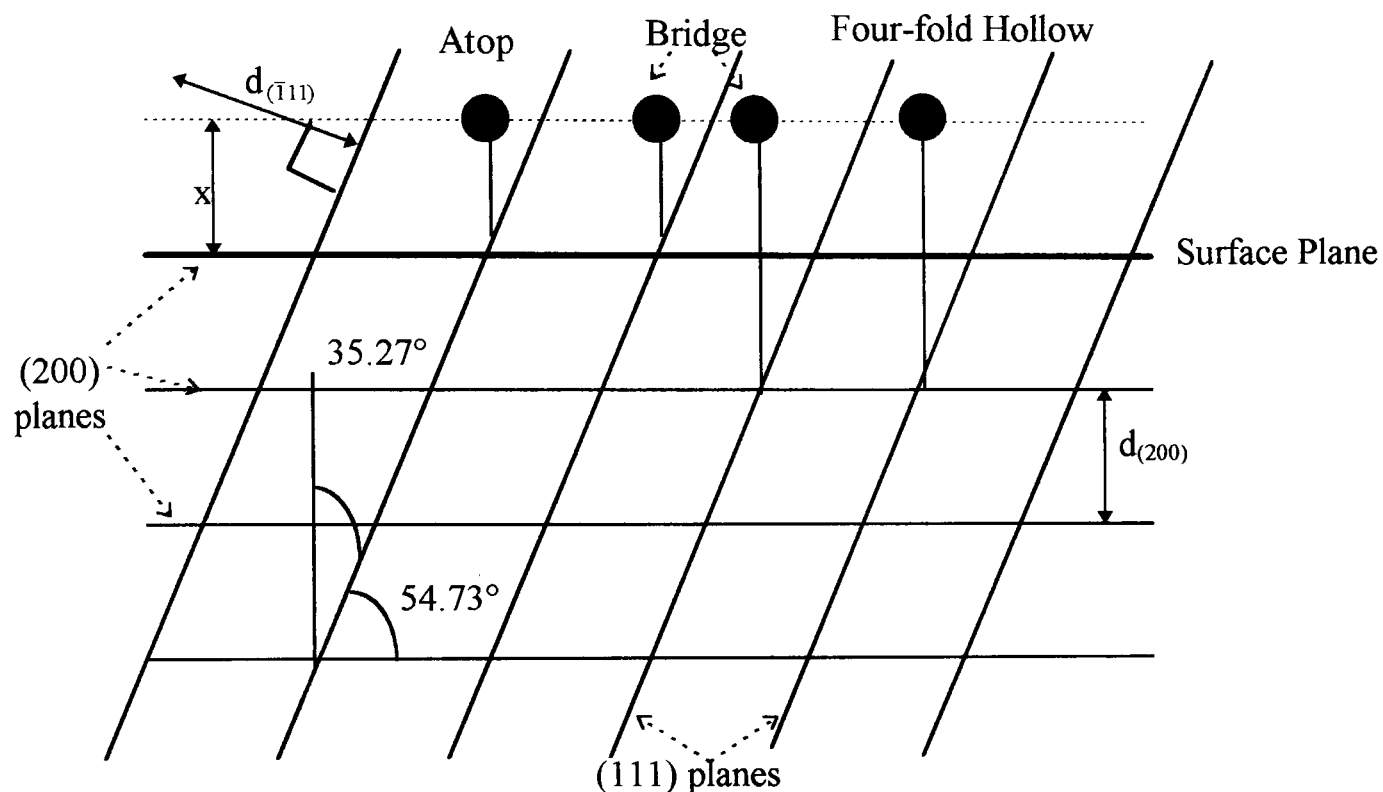


Figure 2.17. A diagram indicating the various high symmetry sites and their differing distances from the (111) reflection plane. $d_{(111)}$ is the distance of the various sites above the (111) reflection plane, and x is the distance of the various sites from the (200) reflection plane. The dimensions indicated in this diagram are arbitrary.

There are two types of bridge site relative to the 4-fold symmetry of the Cu(100) substrate surface, as illustrated in figure 2.18. Consequently, 2-fold bridge sites have two possible distances with respect to the (111) plane (see figure 2.17.). Type A uses the same height equation for the height above the (11) plane as the atop site, but has a different height above the (200) plane to the atop site and therefore has a different height above the (111) plane to the atop site.

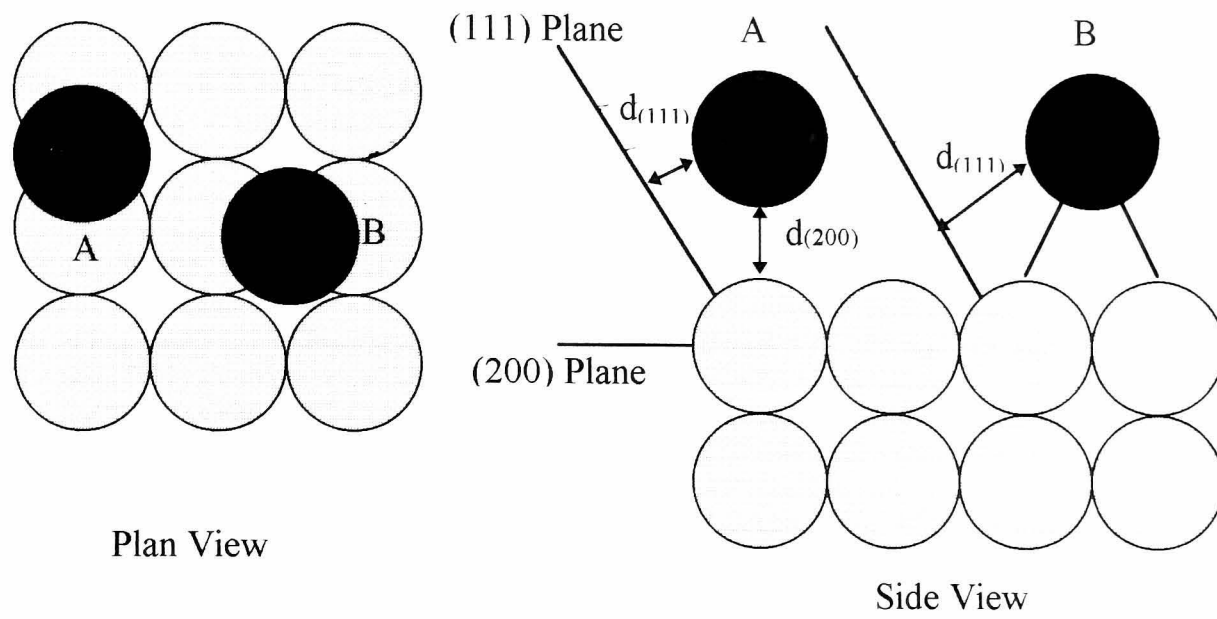


Figure 2.18. A schematic diagram illustrating the two types of bridging sites for a face centered cubic surface, and their different heights with respect to the (111) plane. Type A uses the same height equation for the height above the (111) plane as the atop site, but has a different height above the Cu(100) surface to the atop site and therefore has a different height above the (111) plane to the atop site.

2.2 Surface Analysis Techniques

2.2.1. Auger Electron Spectroscopy (AES)

Auger electron spectroscopy (AES) is perhaps one of the most common electron-based elemental analysis techniques. Its most useful role is in the determination of surface composition (Davis et al. 1976 and Woodruff & Delchar 1994). We have made use of Auger electron emission to monitor the cleanness of the substrate crystals (AES) and the coverage of mercury on the substrate surfaces (AES, XPS). The Auger electron emission is also monitored when using the Normal Incidence X-Ray Standing Wavefield (NIXSW) technique, however this investigation only monitored the photoemission of the relevant elements (section 3.4).

The basic principle of AES can be understood by reference to figure 2.19. When an atom is ionised with the production of a core hole in level A (by either a photon or an electron of sufficient energy $\approx 1.5-5\text{keV}$ the ion eventually loses some of its potential energy by filling the core hole with an electron from a shallower level (B) together with the emission of energy. The energy emitted may appear either as a photon (fluorescence) (fig 2.19.a.) or as kinetic energy given to another electron from a shallower level (C) (fig 2.19.b). These competing processes are dominated by the photon emission only when the initial core hole is deeper than approximately 10keV . It should be noted that the Auger energies are independent of the energy of the incident

radiation. Figure 2.19. is an energy level diagram showing the filling of a core hole in level A, giving rise to (a.) X-Ray photoemission or (b.) Auger electron emission. The levels are labelled with their one-electron binding energies.

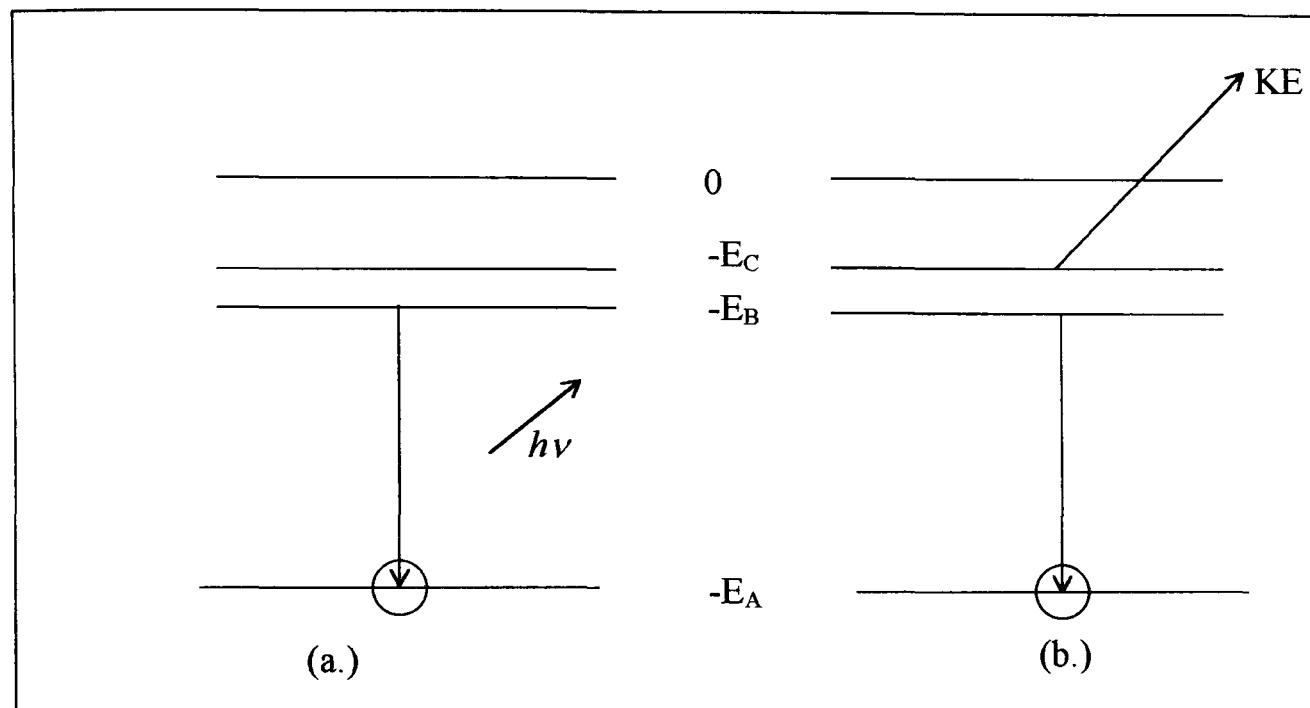


Figure 2.19. An energy level diagram showing the filling of a core hole in level A, giving rise to (a.) X-Ray photoemission or (b.) Auger electron emission. The levels are labelled with their one-electron binding energies.

For the photon emission

$$h\nu = E_A - E_B \quad 2.2.1.1.$$

The Auger effect is allowed energetically provided $E_A \geq E_B + E_C$. For Auger electron emission the kinetic energy

$$KE = E_A - E_B - E_C \quad 2.2.1.2.$$

is characteristic of the atom from which it originates. Equation 2.2.1.2. provides an approximate formula for the kinetic energy of an Auger electron based on the one electron binding energies of the core levels involved.

Therefore, the transition shown in figure 2.2.1.1. is an ABC transition, where A, B, and C are the X-Ray level notations K, L₁, L₂, etc. Where:

$$K \rightarrow 1s$$

$$L_1 \rightarrow 2s$$

$$L_2, L_3 \rightarrow 2p$$

$$M_1 \rightarrow 3s$$

$$M_2, M_3 \rightarrow 3p$$

$$M_4, M_5 \rightarrow 3d \text{ etc}$$

K, L, M etc. represent the principle quantum numbers 1, 2, 3, etc. The subscripts L₁, L₂, L₃, etc. represent the multiplicity, j where $j (= l+s)$ is a vector sum of the orbital angular momentum l and the spin quantum number, s .

A specific sequence of events leading to the production of an Auger electron is:

- (i) ejection of an electron from the K shell of an atom
- (ii) the filling of the vacancy or hole by an electron from the L₁ shell
- (iii) transference of the energy released to an electron in the L₃ shell and its consequent emission. Such a sequence is denoted as a KL₁L₃ process, or the Auger electron is referred to as a KL₁L₃ electron (Figure 2.20.).

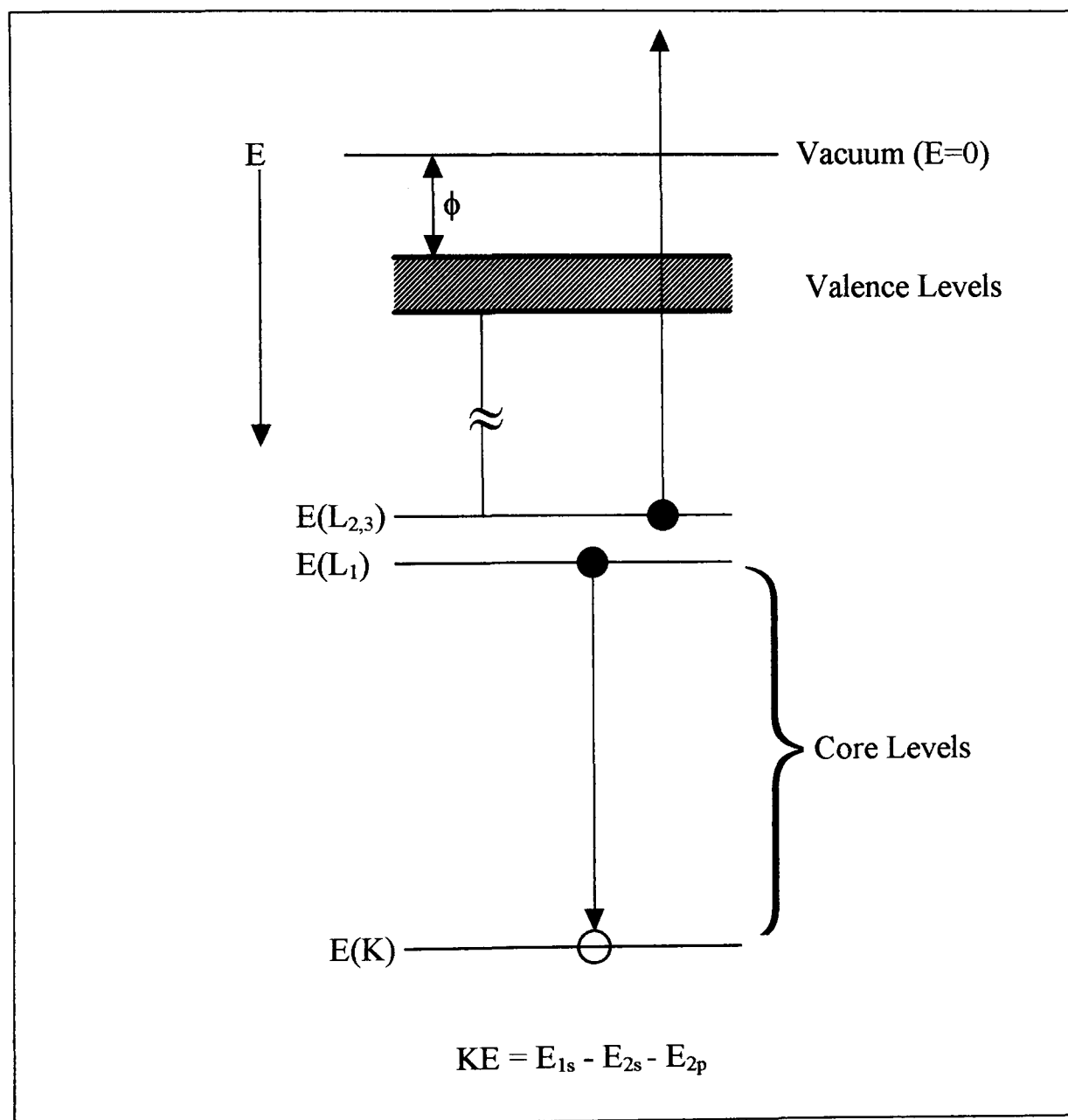


Figure 2.20. The KL₁L₃ process - KLL Auger decay of a 1s core hole. Where E_{2s} and E_{2p} are the binding energies of the 2s and 2p atomic levels respectively in the presence of the 1s core hole, and ϕ is the workfunction.

Figure 2.20. shows a 1s electron is filled preferentially by a radiationless Auger transition i.e. a 2s electron fills the hole and the transition energy ejects a second Auger electron from the 2p level. Notice that the emitted electron's kinetic energy is dependant only on the properties of the atom.

The detected intensity of Auger emission for a given element is dependant upon the following: the incident flux of electrons; the ionisation cross-section of the element at that energy; the backscattering of electrons which could also cause ionisation; the probability of decay through the Auger channel; the solid angle of acceptance of the analyser and the instrumental detection efficiency (Woodruff & Delchar 1994). Either the peak to peak height $dN(E)/dE$ or the peak area is proportional to coverage if all the above conditions are kept constant.

Both the photon and electron emission are characteristic of some combination of the atomic energy levels of the emitter and therefore form the basis of a core level spectroscopy. The Auger electrons have a short mean-free-path and so their detection outside the sample provides a surface sensitive probe of chemical composition. In surface science, the Auger electrons are normally monitored as the photons emitted have a long mean-free-path in solids thus making them less surface sensitive. AES is usually performed with incident electron beams because of the relative ease of producing sufficiently energetic ($\approx 1.5-5\text{keV}$) electron beams of high intensity (1-100 μA) (Woodruff & Delchar 1994).

The AES spectrum has a characteristic elastic peak due to electrons that pass undisturbed through the solid and a long seemingly featureless tail of electrons that have lost energy to the solid. Two type of electrons contribute to this tail. These are primary and secondary electrons. Primary electrons exit the sample after losing energy in single well defined inelastic event. These show up as tiny squiggles in $N(E)$ that reveal their origin in the derivative signal $dN(E)/dE$. Secondary electrons lose their energy through multiple inelastic collisions. The experimental signal from these electrons is truly structureless. The elemental signature of the surface is found in the precise energy positions of the sharp structures in the derivative spectrum.

2.2.2. X-Ray Photoelectron Spectroscopy (XPS)

The principle of photoelectron spectroscopy is the excitation of electrons in an atom or molecule by bombarding a surface with X-Ray photons of sufficient energy to ionise an electronic shell so that an electron is ejected into the vacuum (Woodruff & Delchar 1994). The emission energies of these electrons are characteristic of the surface atoms and the angular dependence provides information about the surface structure. The phenomenon of X-Ray photoemission has been used to monitor the coverage of mercury on the substrate surfaces for the energy distribution curves (EDCs) described in section 3.4. The X-Ray photoemission of relevant elements was also monitored when using the Normal Incidence X-Ray Standing Wavefield (NIXSW) technique (section 3.4). Consequently XPS is a vital part of the Normal Incidence X-Ray Standing Wavefield technique.

If an atom on a surface is ionised by an X-Ray photon a core level electron is ejected with an amount of kinetic energy given by

$$KE = h\nu - E_A + E_R \quad 2.2.2.1.$$

where $h\nu$ is the photon energy, E_A is the core level binding energy in the absence of E_R and E_R is a relaxation term.

When an atom is ionised a positive hole is left. The relaxation term is due to the electrons relaxing to lower energy states to partially screen this positive hole and therefore make more energy available for the outgoing photoelectron. The relaxation term consists of two components. One component is due to the relaxation of states within the atom (intra-atomic relaxation) and the other to the relaxation of states on neighbouring atoms, either adsorbate or substrate (inter-atomic relaxation).

XPS is a surface analysis technique that takes advantage of the short mean free path of electrons in matter and the elemental specificity of core-hole binding energies. It can be used for elemental analysis because the energy of the photoelectron depends on E_A and is therefore characteristic of the atom. The atomic species present can be determined by matching the inferred values of E_B to the table of elemental core binding energies. XPS can also provide some information about the chemical environment of an element. This is because both E_A and E_R may exhibit a chemical shift (range of a few eV or less) dependant on the chemical environment of the element in question.

Therefore XPS can also be used to provide information about elemental surface composition. The surface sensitivity of XPS can also be increased by monitoring the electrons emitted at small angles to the surface. These electrons travel a longer distance in the solid, and are therefore more likely to be absorbed unless they are generated at or in the near surface region.

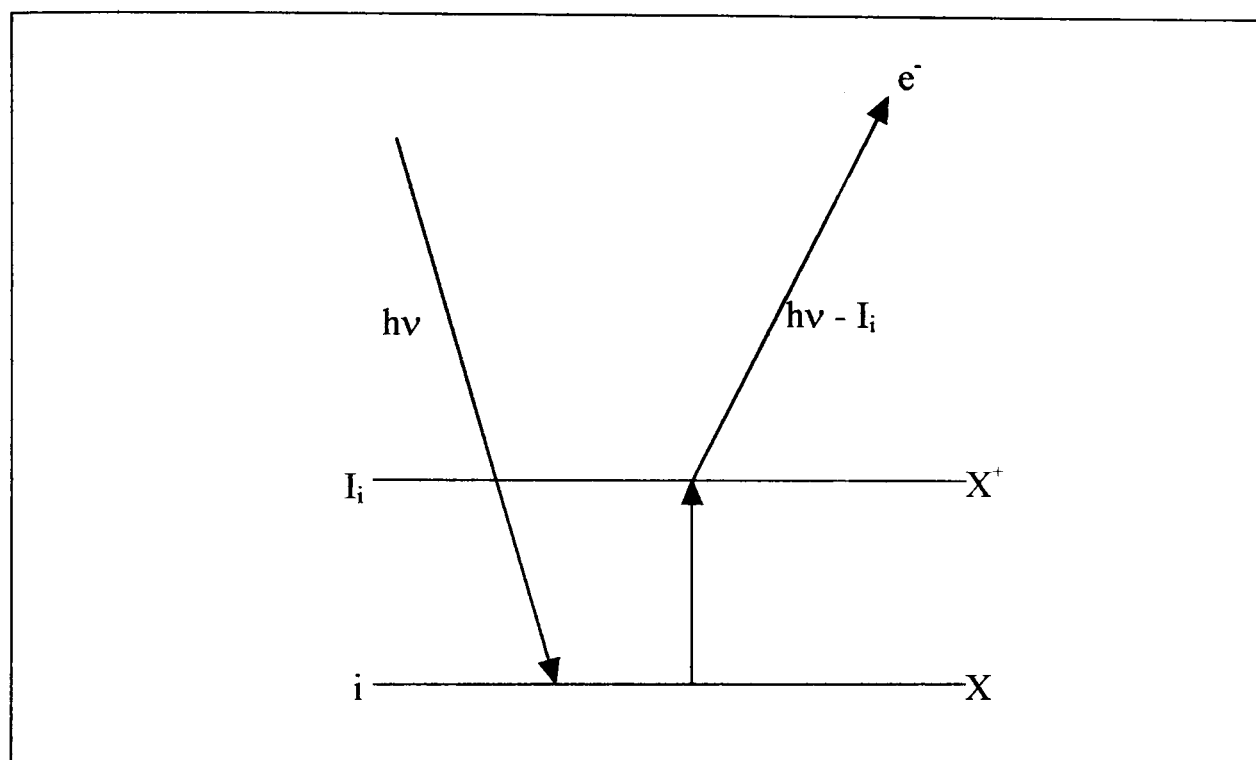


Figure 2.21. An incoming photon of energy $h\nu$ means that an energy I_i is needed to remove an electron from an orbital i , and the difference appears as the kinetic energy of the electron.

2.2.3. Low Energy Electron Diffraction (LEED)

Low energy electron diffraction can supply a simple and convenient characterisation of the long range order of a surface, thus providing an accurate determination of the crystallography of a surface (Woodruff & Delchar 1994, Zangwill 1992). In LEED a beam of monoenergetic electrons (typically with energies 10-500 eV) is backscattered from the surface of a sample under ultra-high vacuum (UHV) conditions. The elastically scattered electrons (figure 2.22.) (about 1% of the total yield) are separated from the inelastically scattered electrons by retarding grids held at appropriate potentials and then accelerated to strike a fluorescent screen held at a large positive potential thus creating a diffraction pattern.

LEED is extremely sensitive to surface atomic arrangements (the penetration depth is typically less than 1 nm) due to the high atomic scattering cross sections for electrons in this energy range (10-500 eV). A sharp spot LEED pattern implies the presence of a well-ordered surface and provides direct information about the symmetry of the substrate. The surface atom arrangement can have symmetry no greater than that indicated by the LEED pattern. The true surface structure could possibly have a lower symmetry than that indicated by LEED.

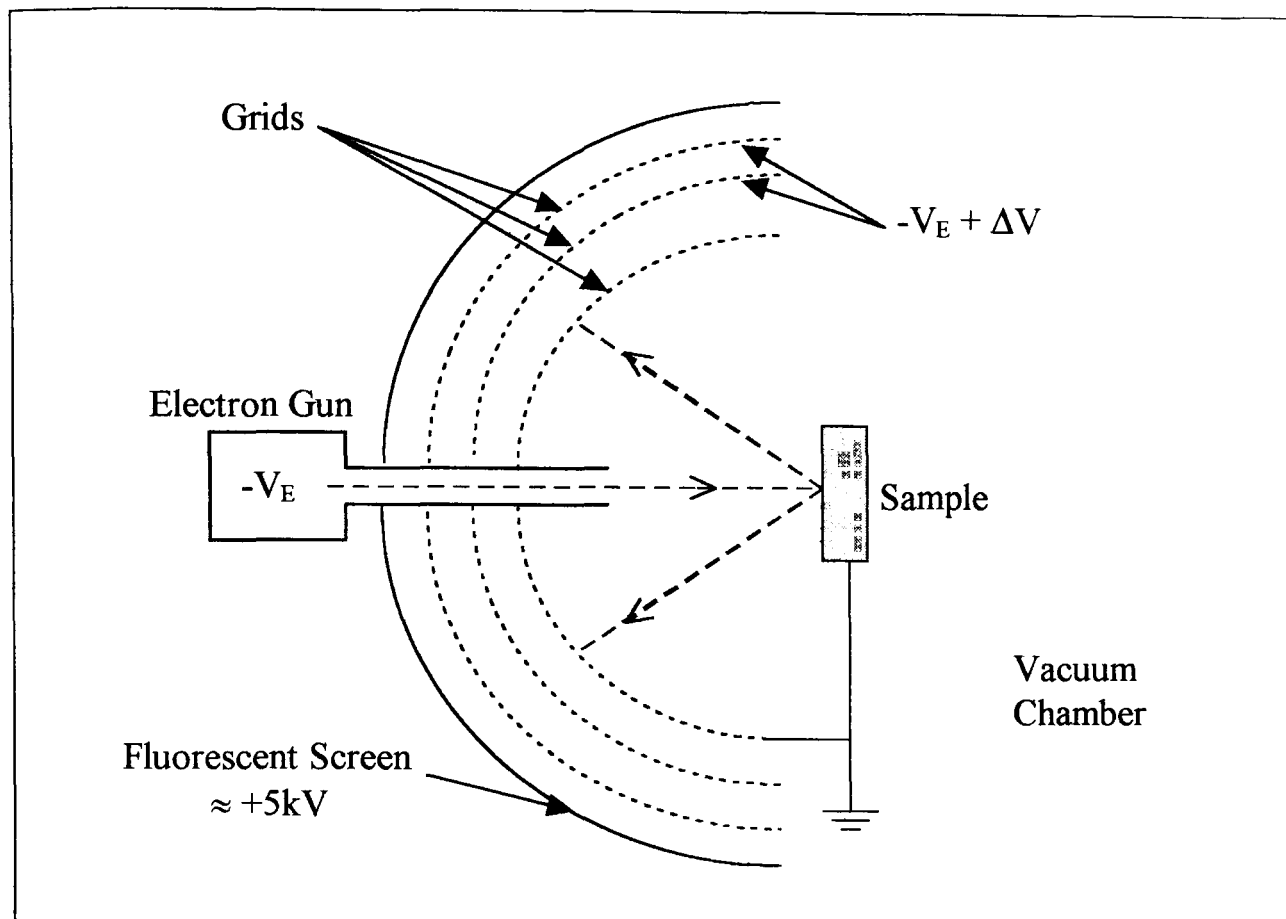


Figure 2.22. A schematic diagram of the “optics” used for LEED experiments. The potential V_E defines the electron energy as eV_E .

3 Instrumental and Experimental Details

This chapter gives a description of the experimental procedures and details of the equipment used in the NIXSW data acquisition.

3.1 Description of the Beamline

All the experiments reported here were carried out on the SEXAFS beamline (6.3) of the Synchrotron Radiation Source (SRS) at the Engineering and Physical Sciences Research Councils (EPSRC) Daresbury Laboratory, U.K. The SEXAFS beamline is equipped with a grazing incidence toroidal prefocussing mirror and an ultra-high vacuum (UHV) two crystal monochromator.

The experiments used synchrotron radiation, which is produced when high energy electrons (2 GeV) are constrained to a circular orbit by the strong magnetic fields (bending magnets of 1.2 T) in a storage ring (circumference of 96 m). Electrons placed in this type of confinement emit a high flux of photons in a continuous spectrum at a tangent to the storage ring. This radiation is highly polarised in the plane of the synchrotron with the electric vector (\underline{E}) parallel to the ring.

Figure 3.1.1 shows a schematic diagram of beamline 6.3. More details of the beamline can be found in McDowell et al (1986). The beam originates from bending magnet 6 and then passes through a rack of ten carbon filters, each 1000 Å thick to remove the ultraviolet component of the beam. The photon beam then strikes a gold coated toroidal quartz premirror at an angle of 0.5°, which provides a high energy cut-off of

11.1 keV and a demagnification of 2:1 at the sample. The beam then enters a double crystal monochromator that has been described in more detail by McDowell et al (1986) from which a single photon energy can be selected in the range 2000-8430 eV. Germanium (111) crystals were used in the X-Ray monochromator. The monochromating crystals are fitted with water cooling to largely eliminate thermal effects.

After the monochromator, the X-Ray beam passes through the I_0 section as shown in figure 3.1.2. The monochromator contains a copper mesh to monitor the beam intensity (I'_0) of the incident light by adjusting the incident beam monitors and beam monitor slits, installed between the exit slit of the monochromator and the surface science end-station. When the X-Ray beam collides with the copper, it causes electrons to be produced; this photoemission allows the intensity of the beam to be monitored and the remainder of the beam is able to pass through the open parts of the mesh. Copper is favoured as it is a convenient metal to work with. The X-Ray beam's position on the copper mesh changes due to the decay of the beam, consequently different amounts of the beam will collide with the mesh. This causes oscillations in the beam current. A fine aluminium foil beam monitor is used to observe the beam intensity (I_0 current) so that glitches from the monochromator and beam decay can be detected and therefore the experimental signal can be compensated. This beam monitor observes both the incident beam and the Bragg reflected beam at nominal normal incidence from the sample. It was therefore possible to normalise the data with respect to the X-Ray intensity using I'_0 and the measurement of the Bragg reflected beam intensity versus the energy with I_0 . The apertures define the beam size so that it falls only on the crystal and not on the back plate or mounting clips.

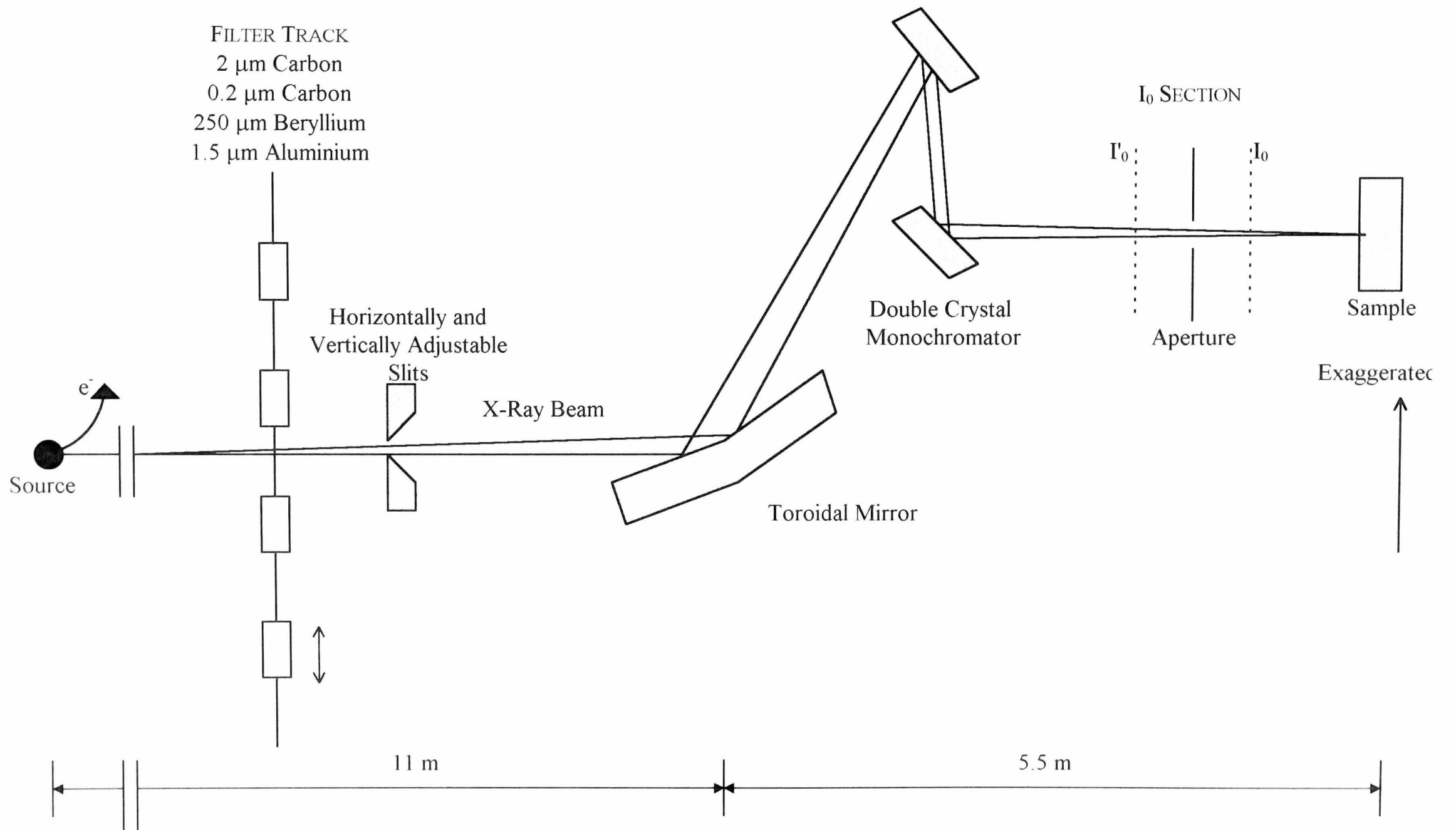


Figure 3.1.1 Schematic diagram of beamline 6.3 at Daresbury SRS Laboratory.

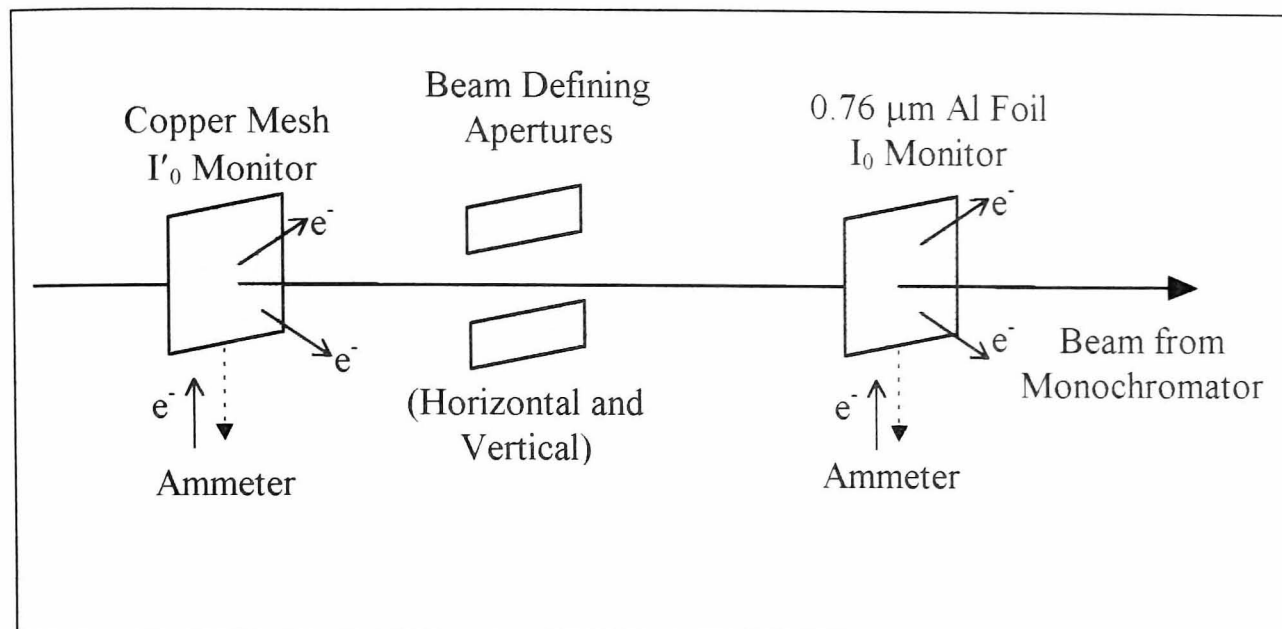


Figure 3.1.2. Schematic Diagram of how the beam's intensity is monitored before it enters the sample chamber. The electrons caused by the impact of the beam on the monitors are illustrated.

3.2 Description of the Sample Chamber

The beam passes from the I_0 section into the sample chamber, which is illustrated schematically in figure 3.2.1. The chamber consists of a sample preparation level and an analysis level.

A rotary backed turbo pump and a titanium sublimation pump were used to maintain the sample chamber at a working pressure of 3×10^{-10} mbar. The gas line was also pumped by a rotary backed turbo pump. The total pressure of the chamber was monitored using several ion gauges. A VG quadrupole mass spectrometer (mass range = 1-200) was used to measure the partial pressures of the individual component gases of the vacuum and for leak testing.

The sample holder was mounted on a VG manipulator equipped with liquid nitrogen cooling and filaments to heat the sample by electron bombardment. The liquid nitrogen cooling allowed the sample to be cooled to 150 K. The temperature of the surface was monitored using a chromel-alumel thermocouple spot welded to the sample holder. The sample was equipped with three degrees of linear motion (x, y and z), which enabled it to be moved between the sample preparation and analysis levels. It also had two degrees of rotational motion to allow the azimuth (ϕ) of the crystal and the photon incidence angle on the crystal (θ) to be changed.

A VG cold cathode argon ion sputter gun was used to clean the sample. VG low energy electron diffraction (LEED) optics (3 grid) were used to monitor the surface order of the clean sample. They were also used to check that the expected structures were formed when dosing the mercury onto the nickel and copper crystals.

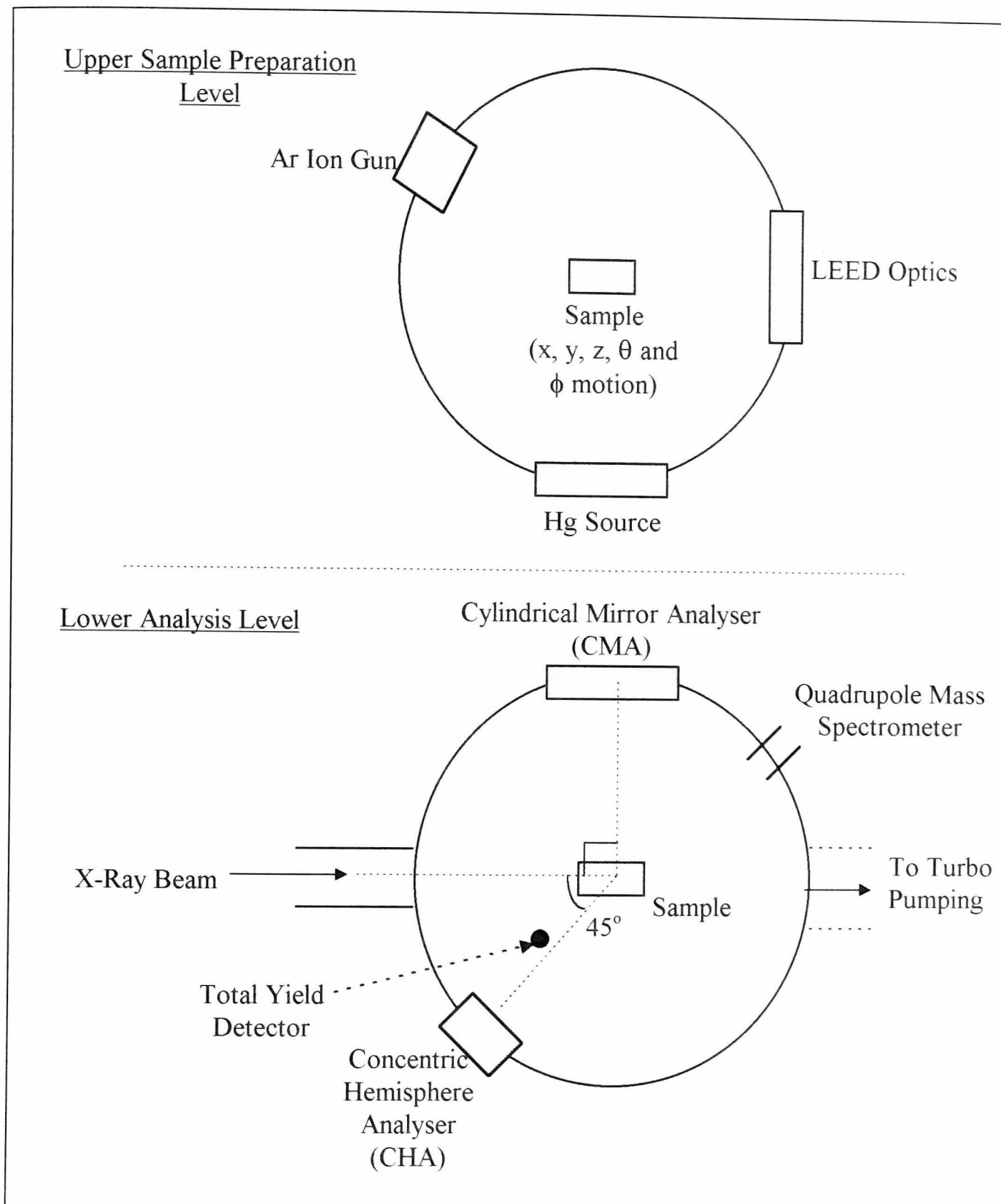


Figure 3.2.1. Schematic diagram of the sample chamber.

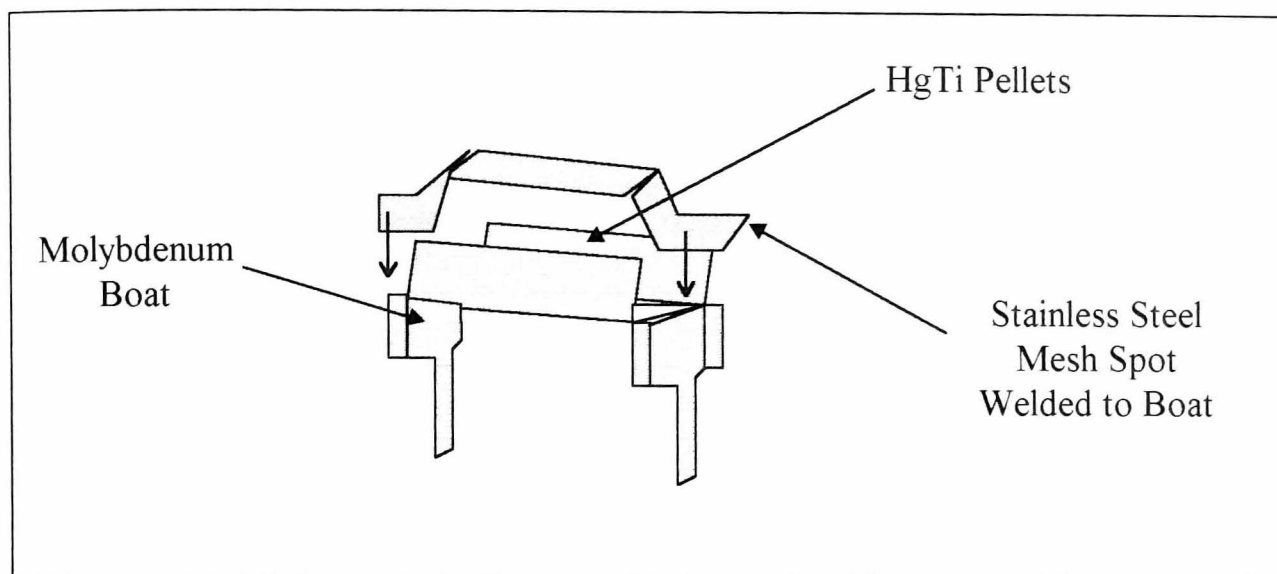


Figure 3.2.2. A schematic diagram of the mercury vapour source, showing the molybdenum boat and the stainless steel mesh spot welded to the molybdenum.

The mercury vapour source used to emit mercury vapour into the chamber and consisted of between 7 and 9 HgTi intermetallic pellets (SAES Getters) mounted on a molybdenum boat, with a stainless steel mesh spotwelded onto the mount to hold the pellets in place. (Figure 3.2.2.) The molybdenum boat was heated resistively and consequently the pellets were heated conductively and radiatively to approximately 870 K and would decompose to generate mercury vapour at a pressure of approximately 2×10^{-8} mbar in the chamber. The mercury vapour source was mounted at the same level as the argon ion gun and the LEED optics. This source was degassed at approximately 870 K with the crystal surface turned 180° away from the source before forming the adsorbate structures.

The analysis level consisted of a Perkin-Elmer double pass cylindrical mirror analyser (CMA) (Singh 1989a) and a 100 mm mean radius concentric hemispherical electrostatic electron energy analyser (CHA) (VSW Ltd. HA100). The CMA contained an integral electron gun, to enable Auger electron spectroscopy (AES) (Carlson 1975) to be performed, in order to monitor the cleanness of the sample. The CMA was operated in analogue mode for electron stimulated Auger analysis of the surface. The CHA, at an angle of 45° to the X-Ray beam and in the horizontal plane, was used to measure energy distribution curves (EDC's) of the electrons leaving the sample under X-Ray irradiation during the experiments. The analyser was operated in pulse counting mode during NIXSW experiments and a fixed analyser transmission (FAT) of 44 eV which provided maximum signal to noise after background subtraction.

A total yield detector (known as the spoon) was mounted in front of the sample under the incoming photon beam. This probe was biased at +9 V and was used to measure the total electron yield (TEY) leaving the crystal surface.

3.3 Crystal Preparation and Alignment

Both the Ni(111) and Cu(100) samples were prepared by a combination of X-Ray Laue alignment, spark machining, mechanical polishing (performed at Warwick University). The sample was cleaned by *in situ* argon ion bombardment (2 keV, 12 $\mu\text{A cm}^{-2}$, ≈ 2000 s) with annealing to approximately 780 K (Ni) and 820 K (Cu). LEED and Auger electron spectroscopy were used to determine when a clean and well-ordered surface was obtained. This process was repeated until a sharp (1x1) LEED pattern was observed. Both electron stimulated AES and synchrotron radiation X-Ray photoelectron spectra (XPS) were taken after cleaning which showed that the crystal was free from contamination.

Both samples were aligned for the NIXSW scans by monitoring the value of I_0 . As the wavelength of the radiation was scanned through the Bragg condition, a Gaussian peak in I_0 due to the diffracted beam passing back down the beamline could be seen (figure 3.4.1.). Alignment was achieved by altering the position of the crystal to optimise the intensity of the peak in I_0 . The I_0 signal was optimised for both reflections: the (111) and (-111) Bragg reflection planes for the Ni crystal; the (200) and (111) Bragg reflection planes for the Cu crystal. Further optimisation was obtained by also maximising the drain current from the sample. The NIXSW scans taken at low temperatures were carried out to reduce the Debye-Waller factor (i.e. reduce thermal effects).

The procedures for forming the adsorbate structures both crystals were attained by referring to phase diagrams detailed in previous work (Singh & Jones 1990a, Kime et al 1992). All the adsorbate structures were checked by comparing previous LEED patterns (Singh & Jones 1990a and 1990b, Dowben et al 1990) and AES spectra (Davis et al 1976).

Where possible (for equilibrium structures) NIXSW data was taken at both room temperature (≈ 298 K) and low temperature (≈ 150 K) to determine whether temperature affected the position of the adsorbate relative to the reflecting planes. For all the structures that needed cooling before data collection, a short period of time was allowed to elapse between forming the structure and cooling the surface to ensure that all the mercury vapour in the chamber had been pumped away in the chamber. This was done to prevent the mercury vapour from condensing on the surface and forming new structures. This procedure was followed for all the structures where cooling was required before data collection. All the structures were checked before cooling using LEED and AES techniques, LEED was also used after cooling to verify the surface structure.

3.3.1 Ni(111) Sample

The Ni(111)/Hg-p(2x2)0.5ML structure (Singh & Jones 1988 & 1990a) was formed with the sample at room temperature, by saturating the clean surface with mercury at about 2×10^{-8} mbar. A sharp p(2x2) LEED pattern was observed, which remained unaltered after turning off the mercury source and pumping away the vapour before taking the NIXSW data at 298 K.

The Ni(111)/Hg- $(\sqrt{3} \times \sqrt{3})R30^\circ$ structure (Singh & Jones 1988 & 1990a) was formed from the p(2x2)0.5ML structure, by heating to ≈ 350 K in vacuo and observing the LEED pattern until the $(\sqrt{3} \times \sqrt{3})R30^\circ$ structure had formed. The sample was then immediately cooled to room temperature (≈ 298 K) to avoid any further desorption and the NIXSW scans taken.

The “ $c(2\sqrt{3} \times 2\sqrt{3})R30^\circ$ ” structure (Singh & Jones 1989a & 1990b) was generated by first forming the multilayers at ≤ 240 K and heating the sample to 273 K to desorb first the multilayers and then part of the chemisorbed layer to form the distinctive “ $c(2\sqrt{3} \times 2\sqrt{3})R30^\circ$ ” LEED pattern. The sample was then rapidly cooled to 185 K to avoid any further desorption and the NIXSW scans were performed at this temperature. The “ $c(2\sqrt{3} \times 2\sqrt{3})R30^\circ$ ” structure is written in inverted commas as the structure is not quite perfectly coincident.

3.3.2 Cu(100) Sample

The Cu(100)/Hg-(3x3) structure (Li et al 1991, Kime et al 1992) was formed by dosing the clean surface with mercury at about 3×10^{-8} mbar with the copper sample at ≈ 170 K (to ensure formation of an acceptable (3x3) structure). The LEED pattern was observed to determine when a sharp (3x3) pattern had formed. The sample was then cooled to 150 K (to reduce the Debye Waller factor) to take the NIXSW data.

The Cu(100)/Hg-c(2x2) structure (Li et al 1991, Kime et al 1992, Dowben et al 1990a, b) that was analysed at room temperature was formed by gently heating in vacuo (i.e. removal of cooling) to approximately 300 K, of the (3x3) structure, through the c(4x4) structure until a sharp c(2x2) LEED pattern was observed. When the structure had formed, the sample was cooled to approx 263 K to avoid any further desorption. The sample temperature was then allowed to rise to approximately 298 K to enable room temperature NIXSW data to be taken.

The Cu(100)/Hg-c(2x2) structure (Li et al 1991, Kime et al 1992, Dowben et al 1990a, b) that was analysed at 175 K was formed with the sample at room temperature (≈ 300 K), by dosing the clean surface with mercury at about 8×10^{-8} mbar to give the c(2x2) structure (indicated by the LEED pattern). The NIXSW data was taken with the sample cooled to 175 K to reduce the Debye Waller factor. Therefore, using either of the above methods we were able to produce identical Cu(100)/Hg-c(2x2) structures.

The Cu(100)/Hg-c(2x6) structure (Li et al 1991, Kime et al 1992) was formed by dosing the clean surface with mercury at about 5×10^{-8} mbar with the copper sample at 167 K (to ensure the generation of a satisfactory c(2x6) structure). Again the LEED

pattern was studied to determine when sharp $c(2 \times 6)$ LEED pattern could be seen. The sample was then cooled to 150 K at which the NIXSW data was taken.

The Cu(100)/Hg- $c(4 \times 4)$ structure (Li et al 1991, Kime et al 1992, Dowben et al 1990a, b) that was analysed at 160 K was formed by dosing the clean surface with mercury at about 5×10^{-8} mbar with the copper sample at approximately 280 K and observing the LEED pattern until a sharp $c(4 \times 4)$ pattern was seen. The NIXSW data was then taken with the sample cooled to 160 K, thus reducing thermal effects.

The Cu(100)/Hg- $c(4 \times 4)$ structure (Li et al 1991, Kime et al 1992, Dowben et al 1990a, b) that was analysed at room temperature was formed by slowly heating in vacuo (i.e. removal of cooling) the $c(2 \times 6)$ structure to give the $c(4 \times 4)$ structure. The structure determination was done by observing the LEED pattern until the $c(4 \times 4)$ structure had formed. The NIXSW data was taken with sample temperature maintained at 290 K. Again, by using two different adsorption techniques we were able to produce identical Cu(100)/Hg- $c(4 \times 4)$ structures.

3.4 NIXSW Data Acquisition, Preparation

In order to record the (111) and (200) NIXSW adsorption profiles (for the Ni(111) and Cu(100) crystals respectively), the crystal was first adjusted for normal X-Ray incidence, checking the alignment by monitoring the 180° backscattered reflectivity profile which was superimposed on the I_0 beam monitor when this condition was achieved to within about 0.5° (figure 3.4.1). This symmetrical reflectivity profile is only dependant on the non-structural absolute energy and energy broadening parameters.

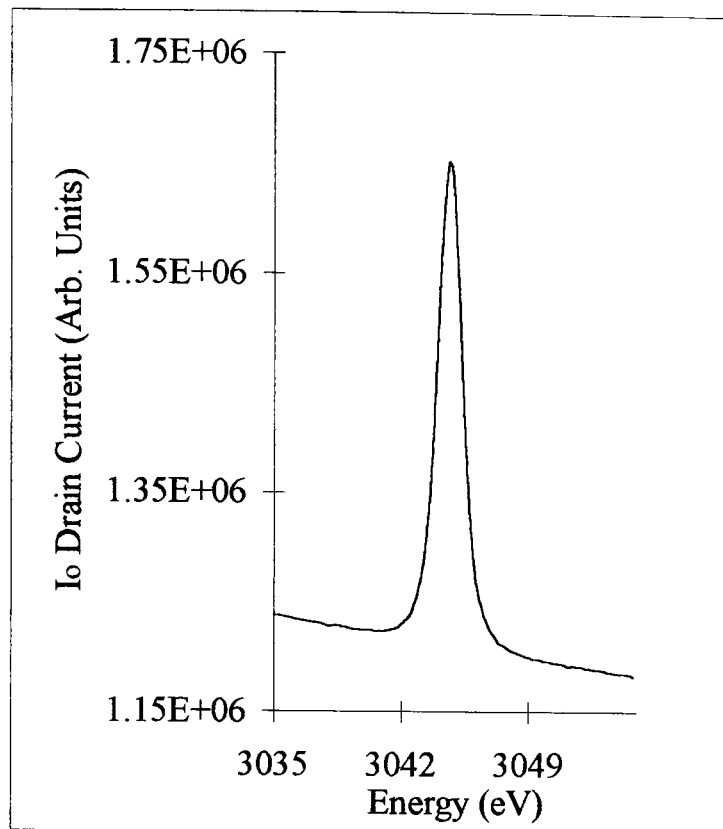


Figure 3.4.1 A spectrum showing the peak in I_0 as the Bragg energy is scanned for the Ni(111) sample. The slope in the base line of this spectrum is due to the decay of the X-Ray beam over the scan time of 75 minutes.

Figure 3.4.1. shows the signal from this monitor as a function of photon energy around the Bragg peak value of 3044 eV (for both (111) and $(\bar{1}11)$ reflections) for the Ni(111) sample (3435 eV (for the (200) reflection) and 2975 eV (for the (111) reflection) for the Cu(100) sample). The absolute photon energy (the energy scale shown in figure 3.4.1.) is related to the nominal kinematical Bragg energy (chapter 2) which is at the centre of the scanned energy range (where the peak in I_0 is at the maximum). A similar procedure was used to establish normal incidence to the $(\bar{1}11)$ Bragg planes for the Ni(111) crystal (polar angle of 70.53° to the (111) surface normal) and for the (111) plane of the Cu(100) crystal (polar angle of 54.73° to the (100) surface).

The energy distribution curves (EDC's) were taken by scanning the binding energy at a nominal photon energy of 3000 eV (Ni(111) sample both reflections and Cu(100) sample (111) reflection) and 3450 eV (Cu(100) sample (200) reflection). One complete NIXSW experiment (repeated several times for each sample preparation) was performed by measuring the intensity of an Auger or photoelectron peak as the wavelength of the light was scanned through the Bragg condition (i.e. 10 eV either side of the Bragg energy). These experiments consisted of four incident photon energy scans (an "on-off" pair for both the substrate and adsorbate) through the appropriate Bragg peak, measuring the four different emitted electron energy yields sequentially. Cold NIXSW profiles were obtained to minimise effects of thermal vibrations (through a Debye-Waller factor) and adatom mobility. In this study the intensity of the photoelectron peaks was measured, therefore as the photon energy was scanned across the Bragg condition, the kinetic energy was also scanned across the Bragg peak. Consequently, the CHA is operated in different modes depending on the type of peak being monitored. The Constant Initial State (CIS) mode is used to monitor photoelectron peaks and the Constant Final State (CFS) mode is used for Auger peaks that are of a fixed kinetic energy. The CIS mode enables the CHA to scan the electron energy as the photon energy is scanned and the CFS mode enables the CHA to detect electrons at a fixed energy. The CHA was operated in the constant initial state mode, so that the kinetic energy of the CHA increased as the X-Ray energy increased.

The peak being monitored rests on a background of secondary electrons and the intensity of this background varies during a scan. To compensate for this, "on" and "off" scans were made to monitor the background intensity therefore enabling the true intensity of the electrons to be obtained. The "on" scan was taken at the energy of the peak of interest and the "off" scan was taken several eV to the high kinetic energy side

of the peak (figure 3.4.2.). Along with the data from monitoring the photoabsorption, the signals from the total yield detector and the I_0 and I'_0 mesh were recorded.

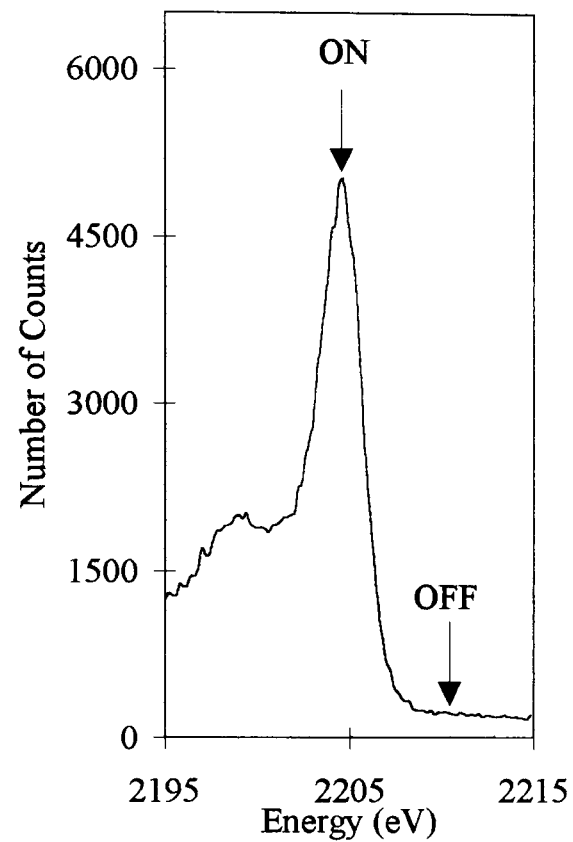


Figure 3.4.2. A diagram indicating the positions of the “on” and “off” positions on an EDC (Ni(111)-Hg-p(2x2)-0.5ML data) to enable monitoring of the background intensity of the scan.

3.4.1 Ni(111) Sample

The NIXSW experiments were performed using the (111) Bragg reflection plane, (with the X-Ray beam normal to the sample surface) and the $(\bar{1}11)$ Bragg reflection plane (with the X-Ray beam at 70.5° to the surface normal, in the appropriate azimuth and normal to the $(\bar{1}11)$ reflection plane). (figure 3.4.1.1.) NIXSW experiments are performed using the (111) and $(\bar{1}11)$ planes to enable determination of the positions of the atoms being studied by real space triangulation. Both planes have a layer spacing of $d_{111}=d_{\bar{1}11}=2.036 \text{ \AA}$, giving normal incidence Bragg reflections at a nominal photon energy of 3044 eV. NIXSW scans were taken in the X-Ray energy range from 3035-3055 eV.

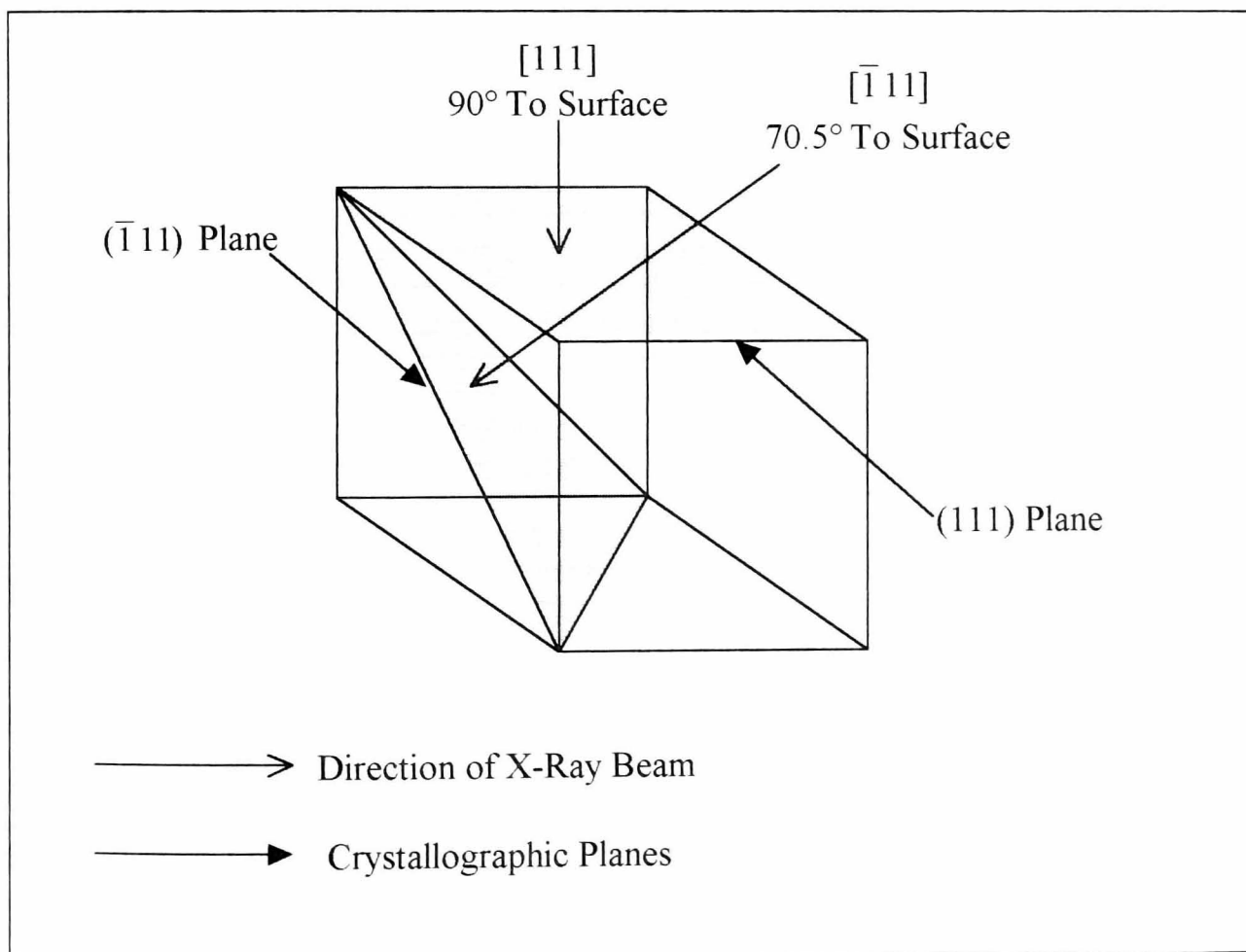


Figure 3.4.1.1. Schematic of the Ni(111) single crystal, showing the direction of the X-Ray beam for the [111] and $[\bar{1}11]$ NIXSW profiles.

The photoabsorption signals of the substrate nickel atoms and the adsorbate mercury atoms were measured by monitoring the nickel $2p_{3/2}$ photoelectron peak (binding energy, B.E. = 852 eV) and the mercury $3d_{3/2}$ photoelectron peak (B.E. = 2385 eV). The positions of these peaks and their respective binding energies were obtained from a wide (0-3000 eV) EDC using a photon energy of 3000 eV (figure 3.4.1.2.). High resolution (650-690 eV for mercury, 2195-2215 eV for nickel) EDC's were performed using a photon energy of 3000 eV to obtain a more accurate position for the photoelectron peaks (figure 3.4.1.3.).

Due to a problem with the CHA (it was unable to jump from the adsorbate energy to the substrate energy quickly enough to permit simultaneous NIXSW scans), some of the mercury adsorbate (NIXSW) scans and the nickel substrate (NIXSW) scans were performed separately. The monochromator was set to scan through the Bragg condition over an energy range of 10 eV (i.e. 2379-2389 eV on the EDC) for the first experimental run and 8 eV (i.e. 2382-2390 eV on the EDC) for the second experimental run, where the Bragg energy is in the centre of this range. An increment of 0.2 eV, a 5 second-per-point (for the first run) and 10 second-per-point (for the second run) count time was used for the mercury $3d_{3/2}$ (B.E. = 2385 eV) scans. An energy range of 5 eV (i.e. 850-855 eV) with an increment of 0.2 eV and a 5 second-per-point (for the first run) and 10 second-per-point (for the second run) count time was used for the nickel $2p_{3/2}$ (B.E. = 852.7 eV) substrate scans. The photoelectron intensities of these peaks (“on” positions), together with background levels ≈ 10 eV to higher kinetic energies of these peaks (“off” positions) and the total electron yield, were monitored simultaneously during each NIXSW scan (Kadodwala et al 1995).

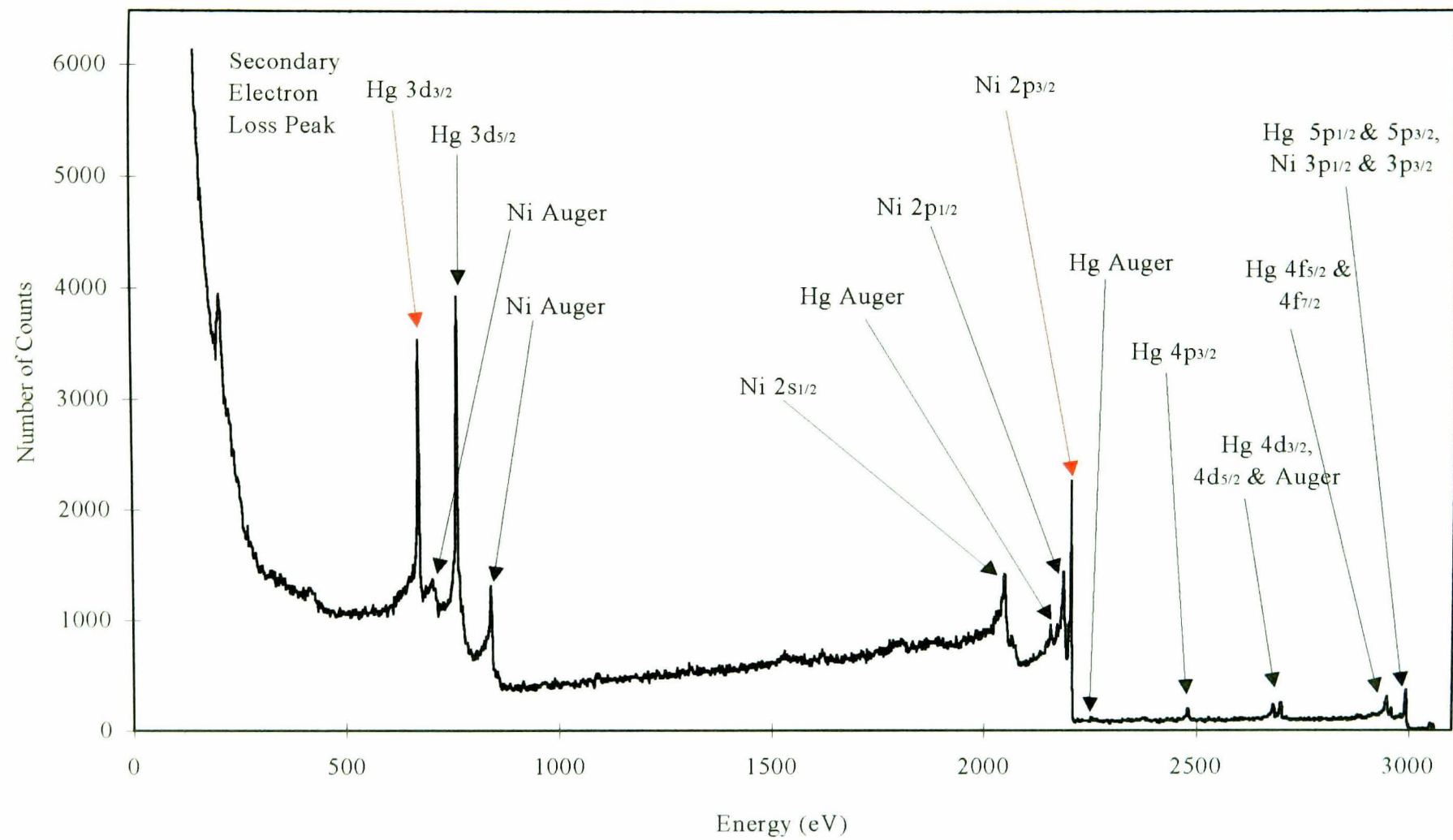


Figure 3.4.1.2. A wide energy distribution curve from the Ni(111)-Hg-p(2x2)-0.5ML [111] data, with an incident photon energy of 3060 eV, an increment of 2 eV and a 0.5 second-per-point count time. The spectrum shows the Hg 3d_{3/2} and Ni 2p_{3/2} photoelectron peaks in red and other distinguishable Auger and photoelectron peaks.

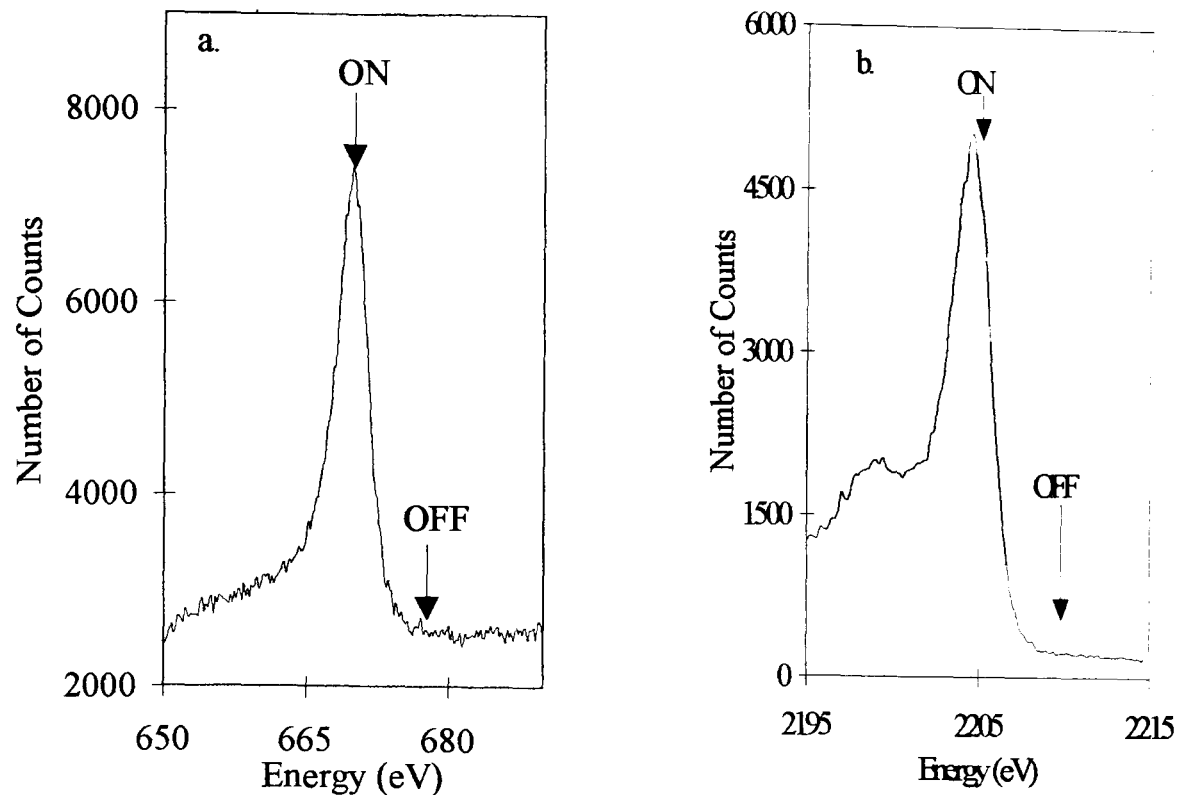


Figure 3.4.1.3. Fine energy distribution curves from the Ni(111)-Hg-p(2x2)-0.5ML [111] data with an incident photon energy of 3060 eV, an increment of 0.2 eV and a 1 second-per-point count time. The spectra show the (a.) Hg 3d_{3/2} and (b.) Ni 2p_{3/2} photoelectron peaks.

Although the 3d_{5/2} photoelectron peak is slightly larger than the 3d_{3/2} and the Auger peaks remain fixed in kinetic energy during the scans, either the Hg 3d_{5/2} photoelectron peak or the Hg Auger peaks at 2078 and 2167 eV could have been used in principle for monitoring the NIXSW of mercury. However, at the photon energies used, the Hg 3d_{5/2} photoelectron peak coincided with a sizeable Ni Auger peak, making background subtraction difficult. The Hg 3d_{3/2} could be used as it always lies to lower kinetic energies than the fixed energy Ni Auger peaks for the scans described here, allowing accurate background subtraction. LEED structures and the intensity of the Hg 3d_{3/2} photoelectron peak relative to the substrate Ni 848 eV Auger peak, were monitored before and after each NIXSW scan.

3.4.2 Cu(100) Sample

The EDC's for the Cu(100) sample were taken by scanning the kinetic energy at a nominal photon energy of 3450 eV for the (200) direction and 3000 eV for the (111) direction. Also, the NIXSW experiment was performed by measuring the intensity of an Auger or photoelectron peak as the wavelength of the light was scanned through the Bragg condition (i.e. 10 eV either side of the photon energy at the Bragg condition). For the (200) Bragg reflection plane, the X-Ray beam is normal to the surface, and for the (111) Bragg reflection plane, the X-Ray beam is at 54.73° to the surface.

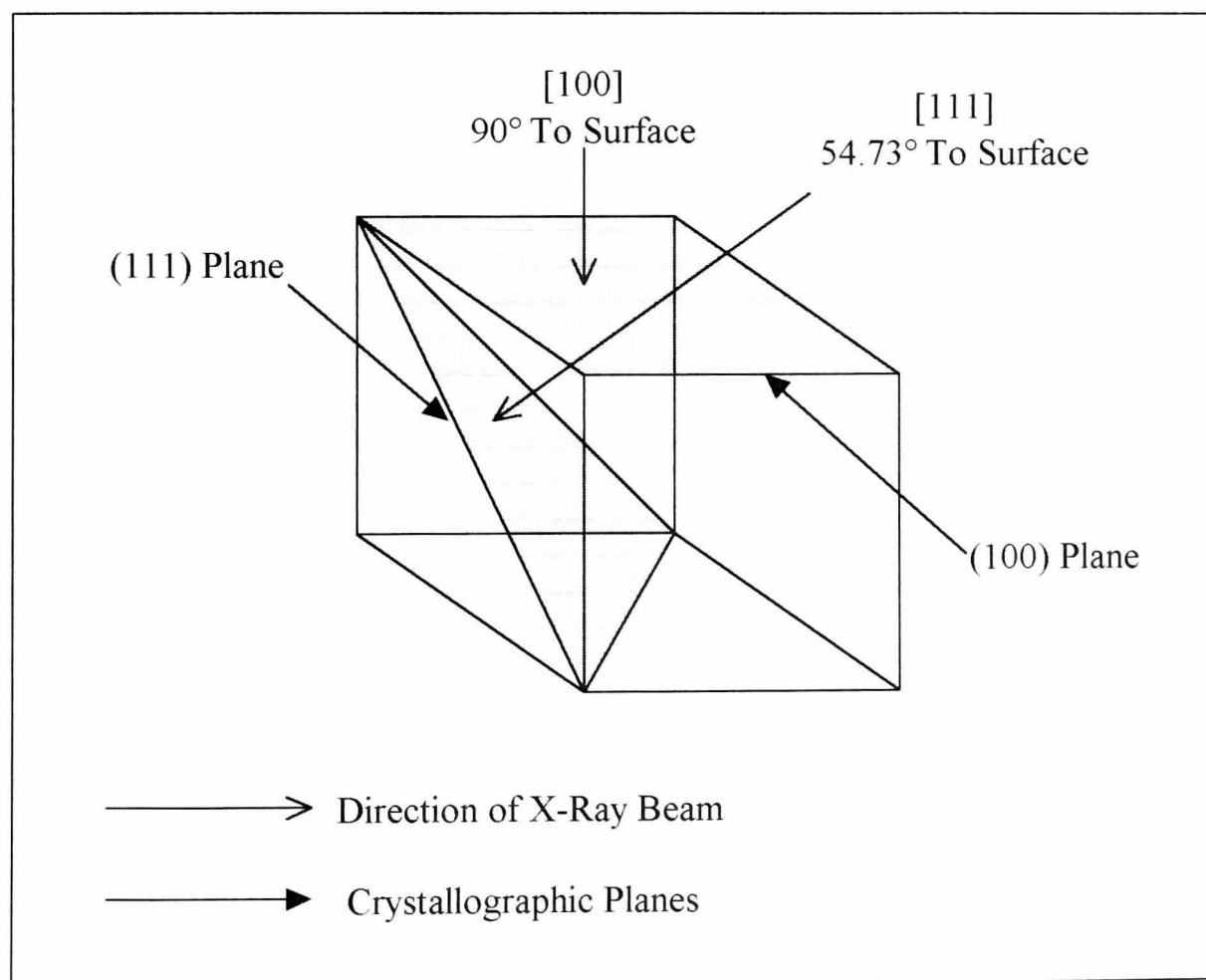


Figure 3.4.2.1. Schematic of the cross section of the Cu(100) single crystal, showing the direction of the X-Ray beam for the [100] and [111] NIXSW profiles.

The photoabsorption signals of the substrate copper atoms and the adsorbate mercury atoms were measured by monitoring the copper $2p_{3/2}$ photoelectron peak (binding energy, B.E. = 932 eV) and the mercury $3d_{5/2}$ photoelectron peak (B.E. = 2291 eV). The positions of these peaks and their respective binding energies were obtained from the positions of photoelectron peaks on a wide EDC (150-3500 eV for (200) direction and 150-3000 eV for (111) direction) using a photon energy of 3450 eV (figure 3.4.2.2) for the [200] reflection and 3000 eV (figure 3.4.2.3.) for the [111] reflection. High resolution (1040-1075 eV mercury, 2500-2520 eV copper for the [200] reflection (figure 3.4.2.4.) and 685-710 eV mercury, 2040-2065 eV copper for the [111] reflection (figure 3.4.2.5.)) EDC's were performed using a photon energy of 3450 eV for the [200] reflection and 3000 eV for the [111] reflection to obtain a more accurate position for the photoelectron peaks.

The monochromator was set to scan through the Bragg condition over an energy range of 11 eV (i.e. 2290-2301 eV on the EDC, where the Bragg energy is in the centre of this range), with an increment of 0.2 eV, a 15 second-per-point count time for the mercury scans. An energy range of 6 eV (i.e. 932-938 eV, where the Bragg energy is in the centre of this range) with an increment of 0.2 eV, and a 10 second-per-point count time for the copper substrate scans.

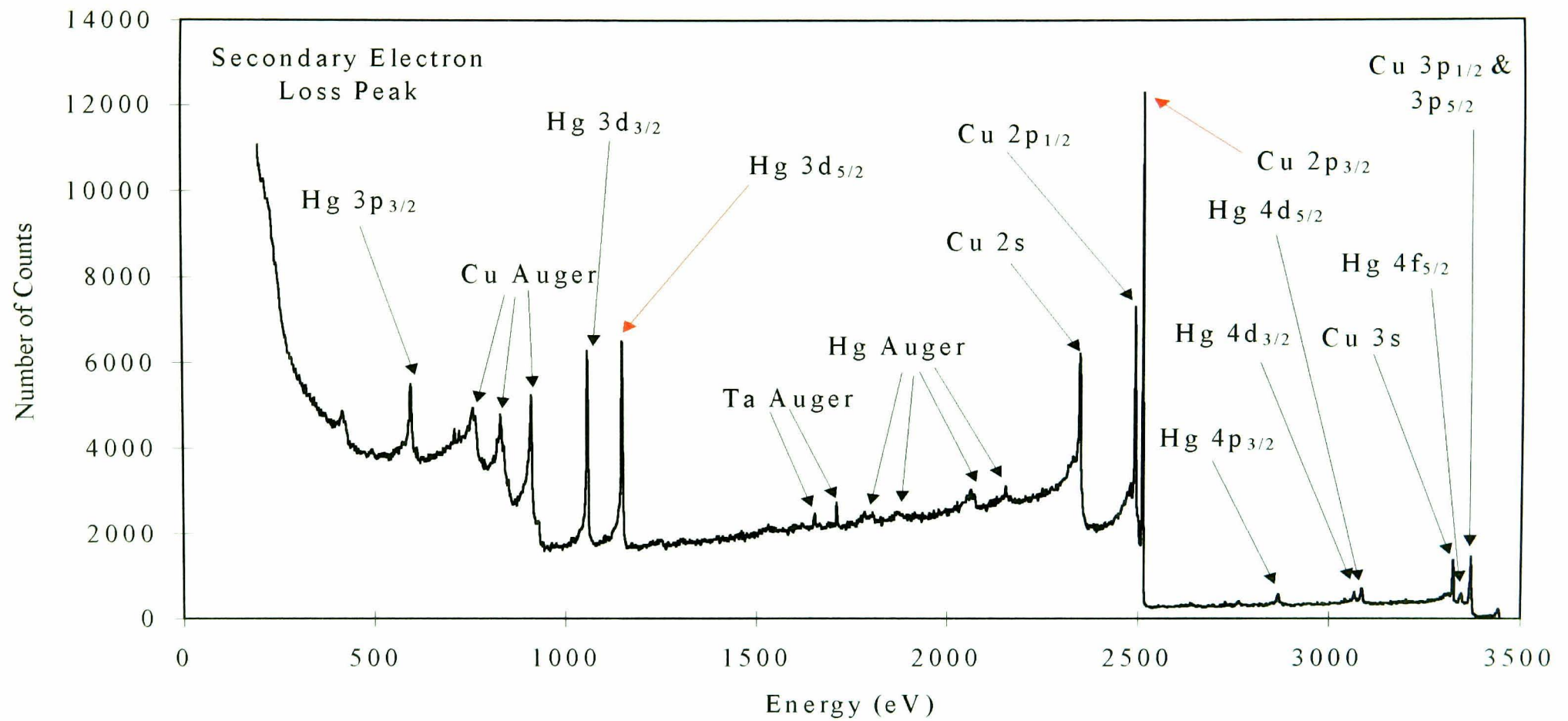


Figure 3.4.2.2. A wide energy distribution curve from the Cu(100)-Hg-c(2x2)-0.5ML [200] data, showing the Hg 3d_{5/2} and Cu 2p_{3/2} photoelectron peaks, with an incident photon energy of 3450 eV, an increment of 2 eV, and a 1 second-per-point count time. The spectrum shows the Hg 3d_{5/2} and Cu 2p_{3/2} photoelectron peaks in red and other distinguishable Auger and photoelectron peaks. Tantalum Auger peaks from the sample mount can also be seen.

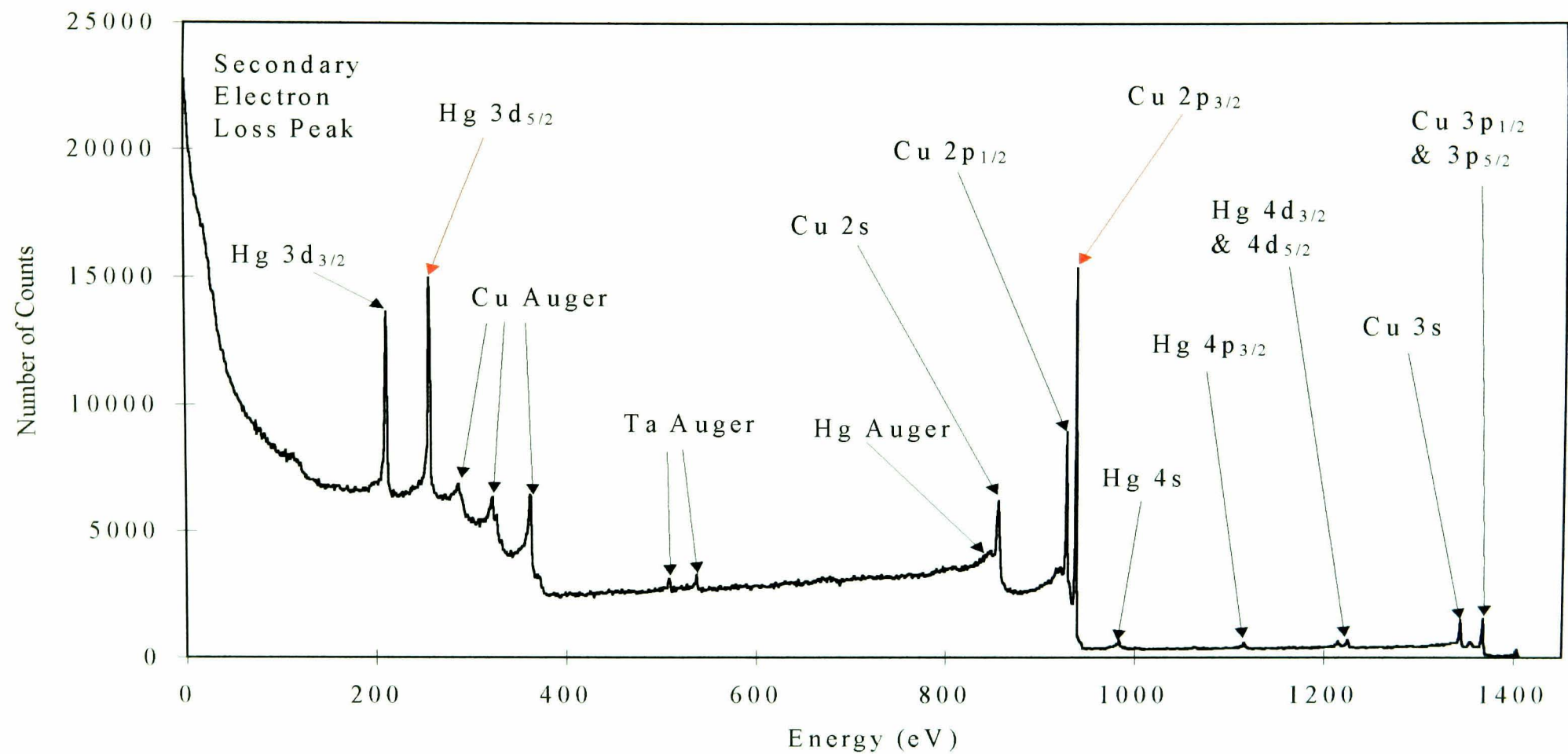


Figure 3.4.2.3. A wide energy distribution curve from the Cu(100)-Hg-c(2x2)-0.5ML [111] data, showing the Hg 3d_{5/2} and Cu 2p_{3/2} photoelectron peaks, with an incident photon energy of 3000 eV, an increment of 2 eV, and a 1 second-per-point count time. The spectrum shows the Hg 3d_{5/2} and Cu 2p_{3/2} photoelectron peaks in red and other distinguishable Auger and photoelectron peaks. Tantalum Auger peaks from the sample mount can also be seen.

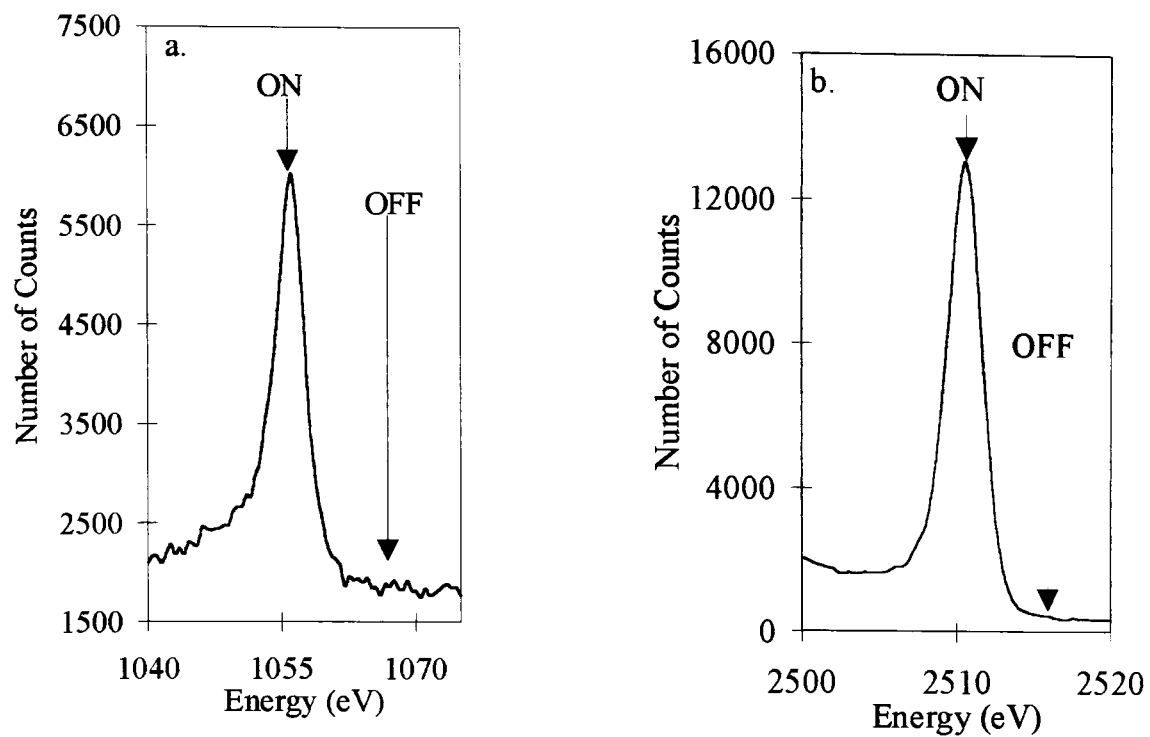


Figure 3.4.2.4. Fine energy distribution curves from the Cu(100)-Hg-c(2x2)-0.5ML [200] data, showing the (a.) Hg 3d_{5/2} and (b.) Cu 2p_{3/2} photoelectron peaks, with an incident photon energy of 3450 eV, an increment of 0.2 eV, and a 1 second-per-point count time.

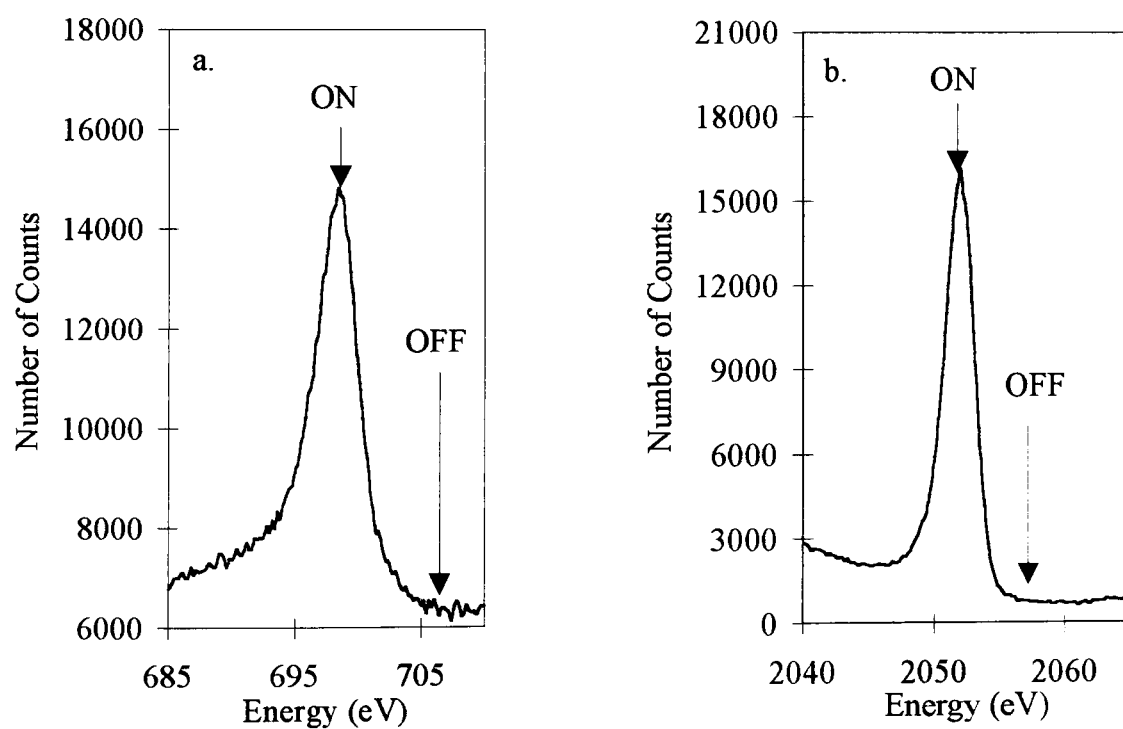


Figure 3.4.2.5. Fine energy distribution curves from the Cu(100)-Hg-c(2x2)-0.5ML [111] data, showing the (a.) Hg 3d_{5/2} and (b.) Cu 2p_{3/2} photoelectron peaks, with an incident photon energy of 3000 eV, an increment of 0.2 eV, and a 1 second-per-point count time.

3.5. NIXSW Data Analysis

The fitting of data was performed using combination of two FORTRAN programs, one written by D.P. Woodruff (program 1) and one written by A.R.H.F. Ettema (program 2). Program 1 uses the equations outlined in section 2.1.1. allowing the user to input the various parameters for the fits the NIXSW spectra to provide theoretical profiles to compare with the normalised experimental NIXSW spectra. Program 2 uses the aforementioned equations to calculate the photoabsorption profile around the Bragg energy, the coherent position, coherent fraction, and the X-Ray beam energy broadening values for each data set. Both programs follow the basic steps below. Program 1 allows the user to view each fit and the spectra and determine the fit by eye, while program 2 compares the fits with the experimental spectra, and increments the fitting parameters until the best fit is found. Program 2 was used to determine a general value for the fitting parameters, and program 1 was then used to fit the spectra more accurately. The following section outlines the steps that the computer program executes in order to fit each of the data sets.

To compensate for the decay in intensity of the radiation with time from the storage ring, the intensities were normalised with the I_0 beam monitor signal which does not display the reflectivity peak. The resulting absorption profiles were normalised by further being divided by the average of the intensities at the extremes of the energy range beyond the conditions needed for the coherent X-Ray standing wave to a value of 1.0 on the left and right sides of the spectra. The above procedures are detailed in section 3.5.1. below.

3.5.1. NIXSW Fitting Program Outline

1. The peak in the I_0 signal due to the incoherent reflection from the standing wave extending back into the I_0 Al foil is removed (figure 3.5.1.1.).

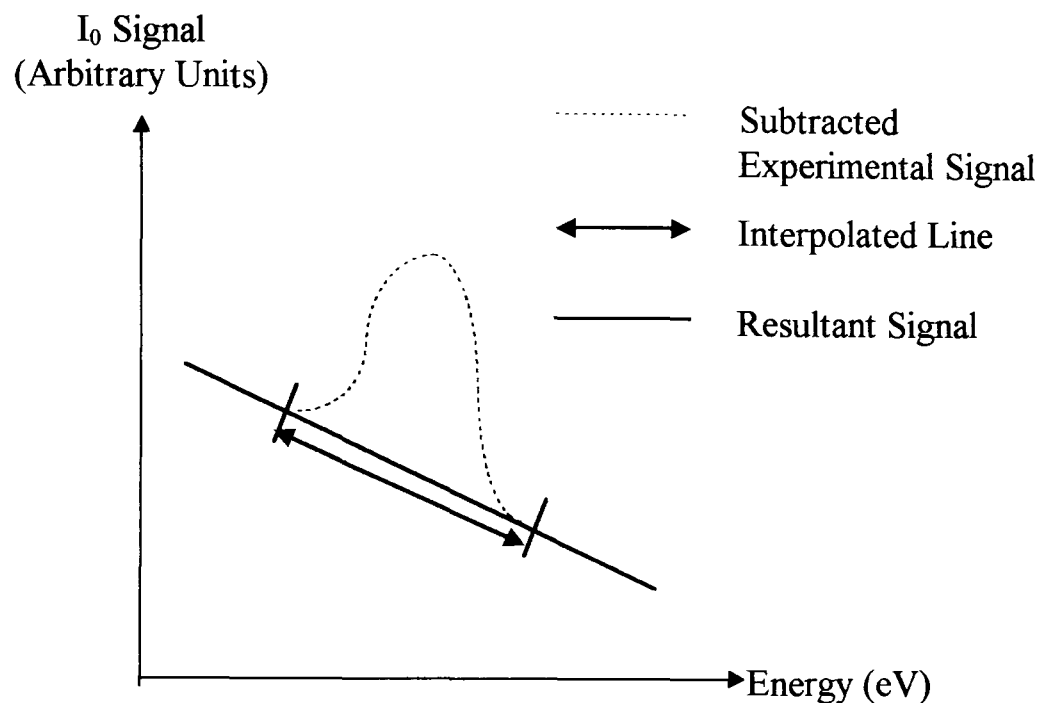


Figure 3.5.1.1. Subtraction of the peak from the I_0 signal.

2. The converted CHA signal (i.e. the value from step 2) is divided by the I_0 signal, which monitors the beam intensity variations of the monochromator. This is to compensate for the decay of the synchrotron current, along with removing any monochromator related variations in the CHA signal.
3. The spectra resulting from step 2 are normalised to unity by dividing them by the value of the peak outside the total reflection region (point A or B on figure 3.5.1.2.). A sloping background on the NIXSW profile was not observed because of the large number of counts obtained for the various signals.

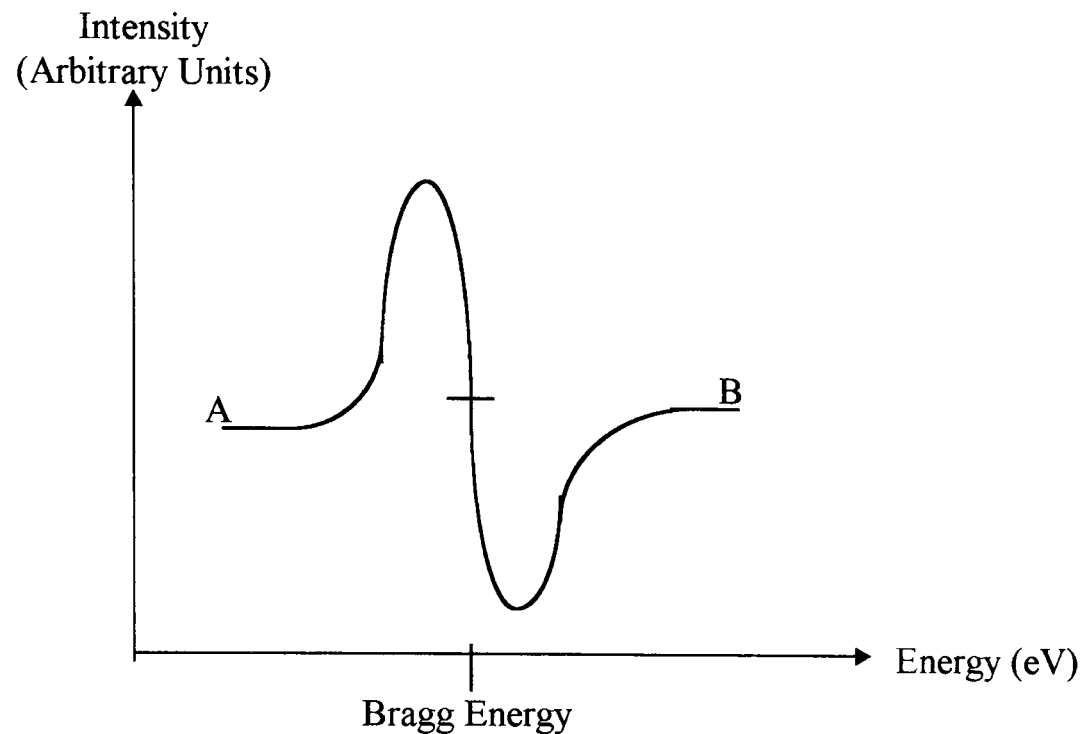


Figure 3.5.1.2. A spectrum indicating the points (A and B) at which the values for the normalisation of spectra can be taken.

4. The data sets are fitted using an iterative process optimising the energy broadening width (for one substrate scan initially to determine the value to fit the remaining spectra), the coherent fraction, and the coherent position, D .

To account for the effect of thermal vibrations and the incoherent fraction of absorbers, equation 2.1.1.2. is replaced in the program by equation 3.5.1.1.

$$I = \left| 1 + f_c(E_H/E_0) \exp(-2\pi i D/d_H) \right|^2 + (1 - f_c)^2 \left| E_H/E_0 \right|^2 \quad (3.5.1.1)$$

where I is the intensity of the X-Ray standing wave, f_c is a product of the absorber Debye-Waller factor and the coherent fraction of the absorbers and E_H/E_0 is the amplitude of the electromagnetic field. For this study, the Debye-Waller factor was assumed to be 1.000.

Initially the fitting was carried out on a substrate scan to find the optimum fit for a particular energy broadening of the X-Ray beam, which was assumed to have a Gaussian line width. This value of energy broadening was then used throughout the remainder of the fitting process.

The program required the input of the fixed structural parameters F_0 , F_H (real and imaginary values), d_H , and V . The structural parameters for Ni(111) and Cu(100) from crystallographic tables (MacGillavry 1968) are shown in table 3.5.1. The program also takes into account the angular mosaic width of the crystal, which was assumed to be 0.100° for both crystals.

Structural Parameters	Ni(111) Crystal Both Reflections	Cu(100) Crystal [200] Reflection	Cu(100) Crystal [111] Reflection
F_0 real	111.5873	115.6126	116.1488
F_0 imaginary	11.2660	10.7276	13.6456
F_H real	81.9321	82.6273	88.7084
F_H imaginary	11.2660	10.7276	13.6456
d_H (Å)	2.036	1.8075	2.0871
V (Å ³)	43.5847	47.242	47.242

Table 3.5.1. Values of the structural fitting parameters for the crystals and planes indicated taken from crystallographic tables (MacGillavry 1968).

4 Mercury Adsorption on Ni(111) : NIXSW Results

The following sections contain details of the Normal Incidence X-Ray Standing Wavefield (NIXSW) results obtained for the various Ni(111)/Hg structures. The photoelectron peak intensities were normalised to a value of 1.0 as outlined in section 3.5 at the extremes of the energy range, well away from the Bragg condition. The substrate NIXSW profile obtained using the Ni 2p_{3/2} photoelectrons was then fitted by varying the coherent fraction (f_c), coherent position (Δd) and instrumental diffraction peak broadening width.

The coherent fraction for a particular direction describes the order of the surface (adsorbate or substrate) perpendicular to that plane. A value of 1.0 corresponds to complete order with no vibrations. A value of zero corresponds to complete disorder with an even distribution of absorber atoms, or a small number of well-defined adsorption sites which combine together to give a coherent fraction of zero. (Woodruff et al. 1994). It should be noted that both static disorder and the Debye-Waller factor (dynamic disorder, which is temperature dependent) contribute to the coherent fraction. The coherent position is the perpendicular distance of the absorber atoms from the extended bulk scatterer planes.

For a perfect structure with a rigid lattice and fixed absorbers in identical sites, the only parameter determining the NIXSW absorption profile is the absorber-scatterer layer spacing. If the absorber-scatterer layer spacing changes by one half of the bulk layer

spacing the lineshape is essentially inverted. Therefore sensitivity to this parameter is rather high and the fit is primarily determined by the relative amplitudes of the positive and negative excursions of the profile, and by the peak energy. In reality, the lattice is not rigid and the absorbers can be expected to show both static and dynamic disorder. This disorder therefore attenuates the amplitude of the “coherent” absorption profile by a Debye-Waller factor. The incoherent part appears as a balancing fraction of absorption profile which has the lineshape of the reflectivity curve. This reflectivity has a much lower amplitude, and in our case, in which the instrumental energy resolution is comparable to the natural absorption width, is essentially symmetric (figure 3.4.1.). Therefore the dominant effect of lowering the coherent fraction reduces the absolute magnitude of the absorption profile. A small shift of the peak towards the midpoint energy of the NIXSW range also occurs. For this reason, at least for reasonably large coherent fractions (about 0.75 or larger), there is relatively little coupling between the layers spacing and coherent fraction parameters in the fitting process. However, as the coherent fraction can be described by a Debye-Waller factor (i.e. a mean square atomic displacement) it can be seen that any reduced coherent fraction can be equally well fitted by some combination of layer spacings which approximately simulates the required atomic displacement distribution. Consequently, a pair of symmetrically displaced layer spacings will provide a very similar fit to that of the two component layer spacings. Therefore, it is difficult to establish error limits on the alternative fits as the layer spacings and coherent fractions are coupled.

All the NIXSW profiles (both substrate and adsorbate) were fitted using a Gaussian X-Ray beam energy diffraction peak (instrumental) broadening σ , where $\sigma = 0.615, 0.880 \pm 0.1$ eV for the two different experimental runs carried out. The adsorbate NIXSW profiles were then fitted by varying the coherent position, Δd and coherent fraction, f_c . The distances (obtained from the NIXSW best fits) of the mercury adsorbate atoms from the Ni substrate layers are relative to the nearest extended scatterer plane. The adsorption sites were calculated using the triangulation method (Frost et al. 1967, Kerkar et al. 1992a, 1992b) outlined in section 2.1.3.1. The peak-to-peak height ratios of the mercury and nickel peaks in the Auger and photoelectron scans were calculated for the various adsorbate structures formed. Their values corresponded with those expected for the coverage of each adsorbate structure produced. This provided yet another indication that the correct adsorbate structures had been formed. All the spectra for the $p(2 \times 2)$ -0.5ML and $(\sqrt{3} \times \sqrt{3})R30^\circ$ -0.33ML structures were taken at both 298 K and 138 K. The " $c(2\sqrt{3} \times 2\sqrt{3})R30^\circ$ "-0.64ML structures were scanned at 185 K.

4.1 The Ni(111) Substrate

Representative NIXSW results for the Ni(111) substrate (from the $p(2 \times 2)$ 0.5ML - Hg structure results) are shown in figure 4.1.1. The NIXSW spectra for all the other structures ($(\sqrt{3} \times \sqrt{3})R30^\circ$ -0.33ML and " $c(2\sqrt{3} \times 2\sqrt{3})R30^\circ$ "-0.64ML) are identical to the ones shown here for the $p(2 \times 2)$ 0.5ML - Hg structure. Hence the crystal surface can be assumed to be of good crystallographic order and the different mercury structures do

not affect the structure of the nickel substrate. The substrate NIXSW spectra were fitted with a broadening width, $\sigma = 0.615$ eV. It can be seen that the representative spectra along with their best fits shown in figure 4.1.1. differ slightly in shape indicating that the (111) and $(\bar{1}11)$ will give different fitting parameters. The (111) profile has a negative excursion of approximately 0.65 and a positive excursion of 1.95 at the higher energy side of the profile. Whereas the $(\bar{1}11)$ profile has a negative excursion (again at the lower energy side of the positive excursion) of 0.75 coupled with a positive excursion of approximately 1.75. All the substrate NIXSW profiles were fitted with a coherent position of 0 or 2.03 \AA ($= d_{111}$) for both the (111) and $(\bar{1}11)$ reflections. Hence, the coherent position obtained from the substrate absorption signal is consistent with the absorbers being coincident with the scatterer planes, as expected (Kadodwala et al. 1995). The substrate NIXSW profiles also produced a coherent fraction of 0.9 ± 0.1 for the (111) and 0.8 ± 0.1 for the $(\bar{1}11)$ reflections (figure 4.1.1.). The slightly smaller nickel coherent fraction for the $(\bar{1}11)$ reflections indicates that there is more substrate disorder parallel to the surface, than perpendicular to it. This also indicates that the (111) NIXSW fits will be of better quality compared with the $(\bar{1}11)$ fits.

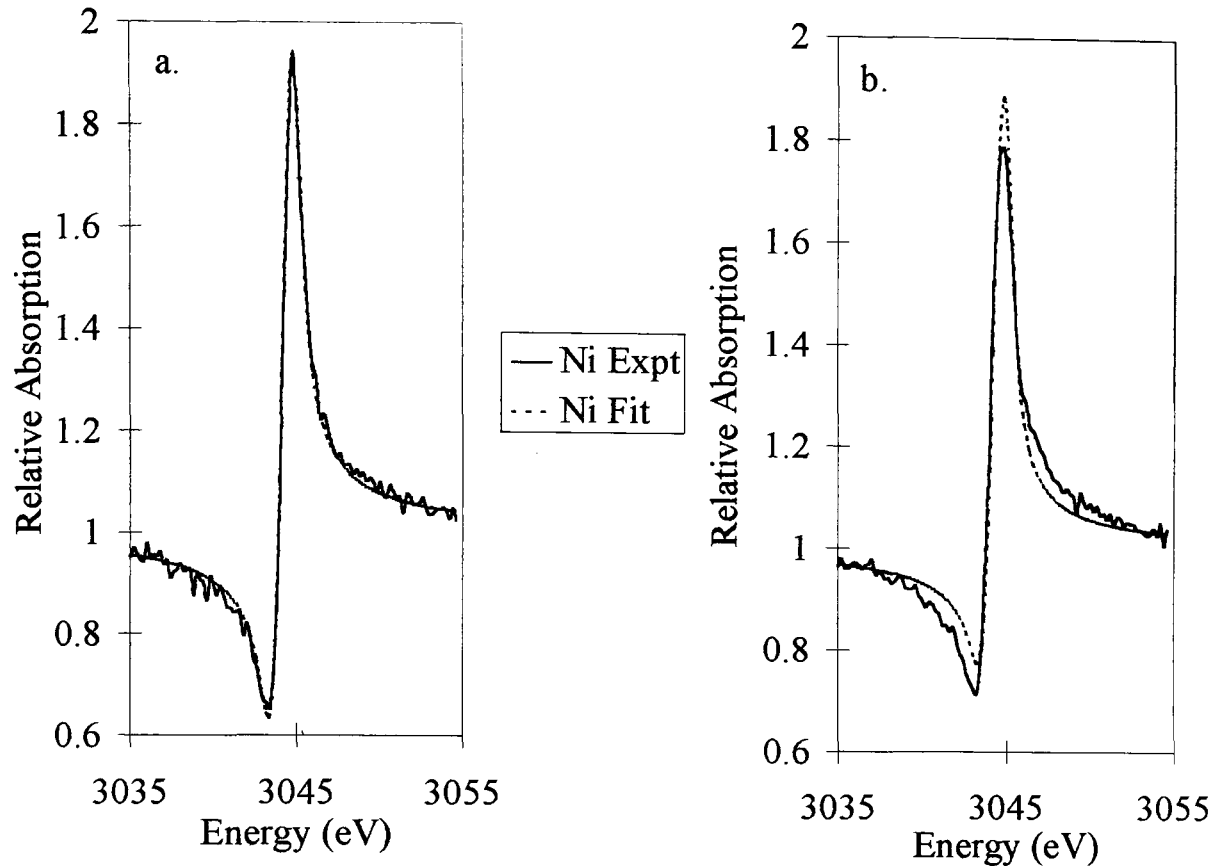


Figure 4.1.1. Ni(111)/Hg-p(2x2)-0.5ML structure (111) (a.) and $(\bar{1}11)$ (b.) NIXSW scans and best fits for Ni ($2p_{3/2}$ photoelectron peaks) for the sample at $T=298$ K.

4.2 The Ni(111)/Hg- $(\sqrt{3}\times\sqrt{3})R30^\circ$ Structure

For the $(\sqrt{3}\times\sqrt{3})R30^\circ$ -0.33ML structure several NIXSW adsorbate absorption profiles were taken for the (111) and $(\bar{1}11)$ reflections at the two temperatures of 298 K (six (111) scans and five $(\bar{1}11)$ scans) and 138 K (two scans of both (111) and $(\bar{1}11)$ reflections). The observed LEED patterns were consistent with that of a $(\sqrt{3}\times\sqrt{3})R30^\circ$ structure. These LEED patterns were still visible after the NIXSW experiment and

became sharper on cooling to 138 K. The Hg:Ni peak-to-peak ratios of the Auger, EDC and NIXSW profiles gave an average coverage value of 0.33 ± 0.05 and 0.31 ± 0.04 for the 138 K and 298 K structures respectively. These values are in close agreement with the anticipated coverage of 0.33ML for the $(\sqrt{3} \times \sqrt{3})R30^\circ$ structure. Representative NIXSW results for the Ni(111)/Hg- $(\sqrt{3} \times \sqrt{3})R30^\circ$ structures are shown in figures 4.2.1. and 4.2.2. along with their best fits. The spectra are identical to the other spectra and fits obtained for the Ni(111)/Hg- $(\sqrt{3} \times \sqrt{3})R30^\circ$ structure. These NIXSW spectra were fitted with a broadening width, $\sigma = 0.880\text{eV}$. The results of these fits are detailed in table 4.2.1.

It can be seen that spectra taken at the two different temperatures, figures 4.2.1. and 4.2.2., differ slightly in shape. The Ni(111)/Hg- $(\sqrt{3} \times \sqrt{3})R30^\circ$ -0.33ML adsorbate NIXSW spectra also have a different size and shape compared with those of the Ni substrate scans, thus indicating that the fitting parameters will be different compared with those for the Ni substrate. This indicates, as expected, that the mercury atoms will reside at a different distance from the extended scatterer planes than the substrate atoms and these adsorbate atoms will also produce different coherent fractions from best fits of the NIXSW profiles.

The (111) profiles for both temperatures are similar in shape, with almost no negative excursion. However, the positive excursion of 2.1 for the low temperature profile is higher than that of the room temperature profile (positive excursion ≈ 1.9), thus

indicating a higher coherent fraction for the low temperature profile and consequently the cold structure.

The $(\bar{1}11)$ scans at 298 K (figure 4.2.1. (b.) shows a typical example) were slightly different to the cold, 138 K scans. The room temperature profile is almost Gaussian with a positive excursion of 1.5 and no negative excursion, indicating a coherent fraction close to zero. However, the low temperature profile has a noticeable dip (to approximately 0.925) on the low energy side of the scan and a positive excursion of 1.55, thus indicating a higher coherent fraction than the higher temperature spectra.

Reflection	Temperature	Coherent Position	Coherent Fraction
(111)	298 K	2.46 (± 0.2) Å	0.68 (± 0.10)
(111)	138 K	2.40 (± 0.2) Å	0.78 (± 0.10)
$(\bar{1}11)$	298 K	0.40 (± 1.00) Å	0.05 (± 0.05)
$(\bar{1}11)$	138 K	0.10 (± 1.00) Å	0.35 (± 0.05)

Table 4.2.1. The fitting parameters obtained from the Ni(111)/Hg- $(\sqrt{3}\times\sqrt{3})R30^\circ$ structure NIXSW profiles for both (111) and $(\bar{1}11)$ reflections at room temperature (298 K) and 138 K.

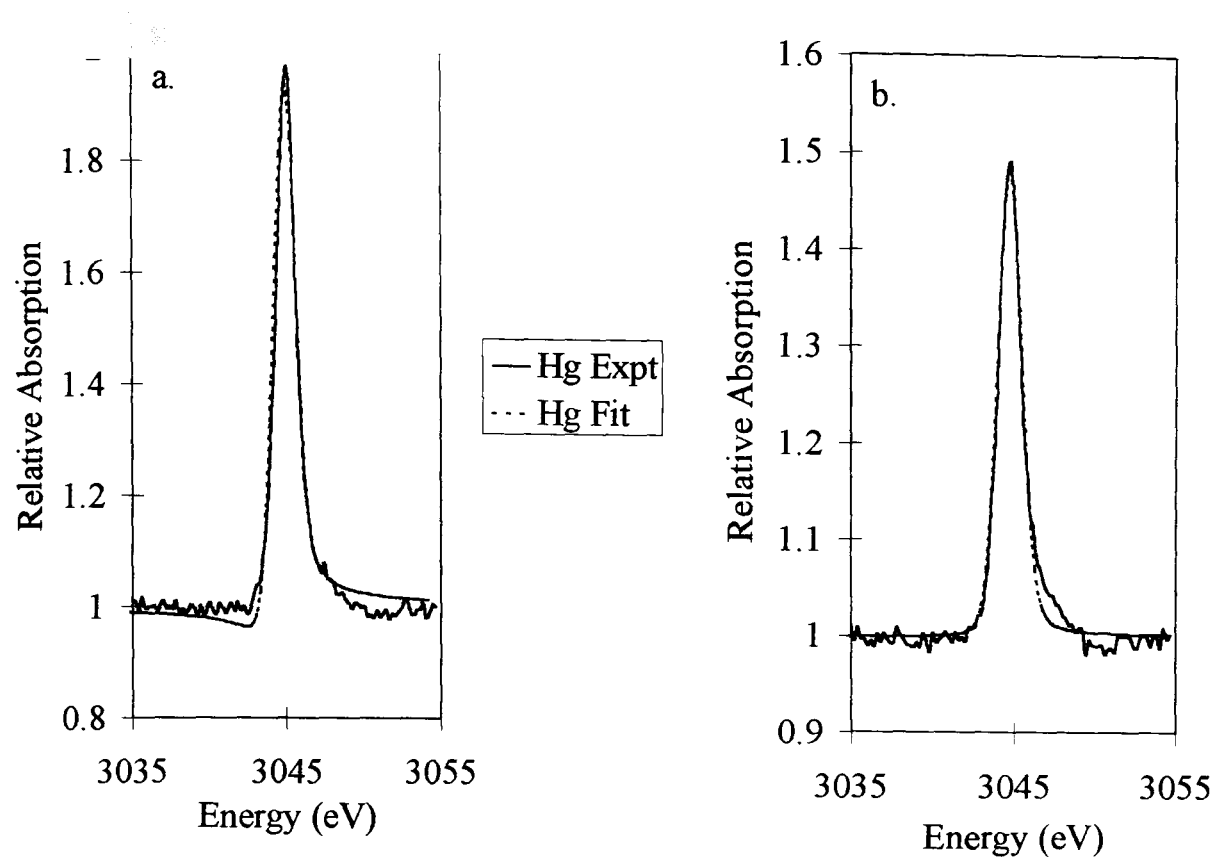


Figure 4.2.1. Ni(111)/Hg-($\sqrt{3}\times\sqrt{3}$)R30°-0.33ML structure (111) (a.) and ($\bar{1}\bar{1}1$) (b.) NIXSW scans and best fits for Hg ($3d_{3/2}$ photoelectron peaks) for the sample at T = 298 K.

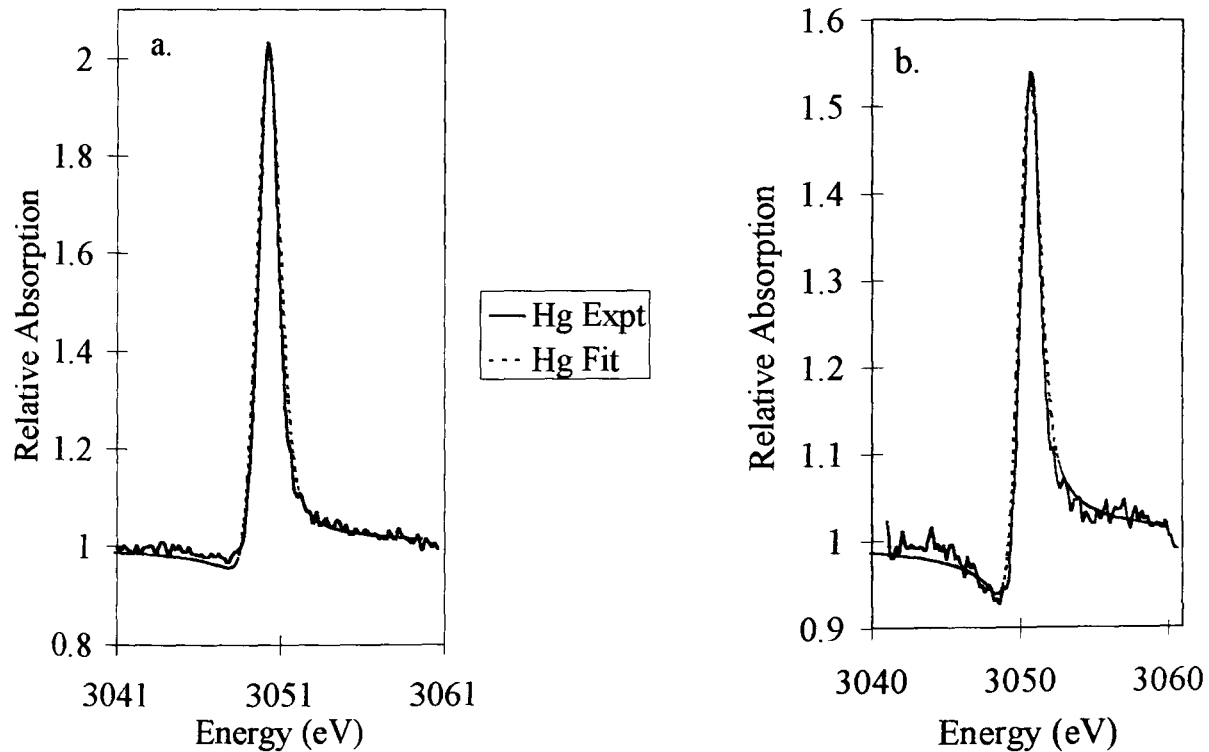


Figure 4.2.2. Ni(111)/Hg-($\sqrt{3}\times\sqrt{3}$)R30°-0.33ML structure (111) (a.) and ($\bar{1}\bar{1}1$) (b.) NIXSW scans and best fits for Hg ($3d_{3/2}$ photoelectron peaks) for the sample at T = 138 K.

These data values shown in table 4.2.1. were calculated as an average of the fitting parameters obtained from the best fits of all the NIXSW profiles taken for each structure at the different temperatures. The errors in the fitting parameters are obtained by determining the range of possible fits that acceptably match the experimental profiles and using this range as an agreeable error margin. It can be seen that the (111) distances agree quite well within the error margins, but the $(\bar{1}11)$ distances are different. However, the $(\bar{1}11)$ results have very low coherent fractions, thus producing the difference in adsorbate distances. The high coherent fractions of the (111) fits imply a rather well defined height above the (111) planes. However, the coherent fractions for the $(\bar{1}11)$ reflections suggest several different contributing heights above the angled $(\bar{1}11)$ planes. The results shown in table 4.2.1. also indicate by the larger coherent fraction for both reflections at the lower temperature that there could be thermal motion present as the order of the surface has increased by “freezing” the surface structure.

4.3 The Ni(111)/Hg-p(2x2)0.5ML Structure

Several Ni(111)/Hg-p(2x2)0.5ML structure adsorbate absorption profiles were taken for the (111) and $(\bar{1}11)$ reflections at 298 K (five (111) scans and five $(\bar{1}11)$ scans) and 138 K (two scans of both (111) and $(\bar{1}11)$ reflections). The observed LEED patterns were consistent with those expected for a p(2x2)0.5ML structure and were visible after the NIXSW experiment. These LEED patterns became sharper when cooling to 138 K. The Hg:Ni ratios of the Auger, EDC and NIXSW profiles gave an average value of 0.50 ± 0.09 and 0.50 ± 0.05 for the 138 K and 298 K structures respectively. Representative individual NIXSW scans together with their best fits for the Ni(111)/Hg-p(2x2)0.5ML structure are shown in figures 4.3.1. and 4.3.2. A Gaussian broadening width of 0.615 ± 0.1 eV was used to fit spectrum 4.3.1.a. and a width of 0.880 ± 0.1 eV was used to fit spectra 4.3.1.b. and 4.3.2. The results of these fits are detailed in table 4.3.1.

As for the Ni(111)/Hg- $(\sqrt{3} \times \sqrt{3})R30^\circ$ structure, the (111) profiles for both temperatures are quite similar in shape, with only a small negative excursion (to 0.975). However, the low temperature profile had a lower positive excursion of 2.0 compared with that of the room temperature (positive excursion of approximately 2.05) indicating a higher coherent fraction for the cold structure (see below). The fairly high coherent fraction of the (111) reflection again implies a rather well defined height above the (111) planes. These (111) scans (Figure 4.3.1. (a.) and 4.3.2. (a.)) were the

same, to within noise level, as those for the $(\sqrt{3}\times\sqrt{3})R30^\circ$ structure, see figures 4.2.1. and 4.2.2.

Again, the $(\bar{1}11)$ scans at 138 K were slightly different to the room temperature scans. Furthermore, the $(\bar{1}11)$ scans were similar to the profile for the $(\sqrt{3}\times\sqrt{3})R30^\circ$ -Hg structure (figure 4.3.2.) taken at 298 K and would therefore be expected to provide similar fitting parameters to those for the $(\sqrt{3}\times\sqrt{3})R30^\circ$ structure. Both the $(\bar{1}11)$ reflections (figures 4.3.1. (b.) and 4.3.2. (b.) show typical examples), taken at room temperature gave a much smaller peak ≈ 1.4 in height and were approximately Gaussian in shape. Therefore, lowering the temperature of the surface to 138 K seemed to have no effect on the $(\bar{1}11)$ data (figure 4.3.2.b.) apart from a very small effect in the form of a small dip on the low energy side of the scan, on the shape of the 138 K data. The low peak height of the $(\bar{1}11)$ data suggests a coherent fraction close to zero, which would imply several contributing heights along the $[\bar{1}11]$ direction.

It can be seen that the coherent fraction of the $(\bar{1}11)$ scans is quite small in comparison with the (111) value and that the errors in the adsorbate position are relatively large for both reflections. The coherent fraction for the (111) scan taken at 138 K is comparable to that for the room temperature scan, which therefore does not indicate an elimination of thermal motion by cooling the structure and effectively “freezing” the structure on the surface in contrast to the Ni(111)/Hg- $(\sqrt{3}\times\sqrt{3})R30^\circ$ -0.33ML results.

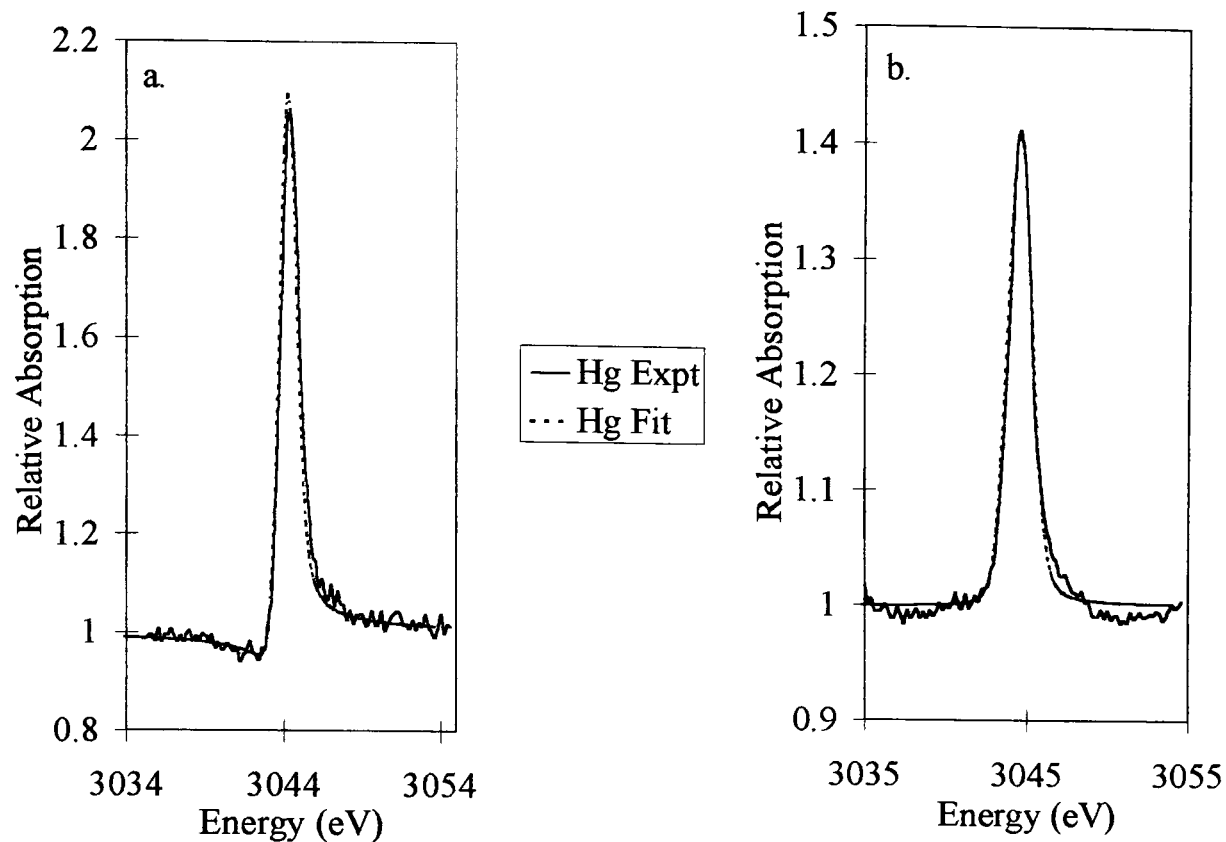


Figure 4.3.1. Ni(111)/Hg-p(2x2)-0.5ML structure (111) (a.) and $(\bar{1}11)$ (b.) NIXSW scans and best fits for Hg ($3d_{3/2}$ photoelectron peaks) for the sample at $T = 298$ K

The table of results also shows that both the (111) and $(\bar{1}11)$ distances agree within the error margins. The high coherent fractions of the (111) fits again indicate a rather well defined height above the (111) planes, unlike the coherent fractions for the $(\bar{1}11)$ reflections, which suggest several different contributing heights above the angled $(\bar{1}11)$ planes. The marginally higher coherent fraction of the (111) cold NIXSW profile could suggest a possible “freezing” of the structure, but this is not substantiated by the $(\bar{1}11)$ 138 K scan’s coherent fraction. The low coherent fraction of the $(\bar{1}11)$ data renders the NIXSW profiles insensitive to the position of the adsorbate relative to

the extended scatterer planes, as any adsorbate height combined with a coherent fraction of approximately zero would produce a Gaussian profile.

Reflection	Temperature	Coherent Position	Coherent Fraction
(111)	298 K	2.43 (± 0.25) Å	0.58 (± 0.10)
(111)	138 K	2.43 (± 0.25) Å	0.78 (± 0.10)
($\bar{1}11$)	298 K	1.69 (± 1.00) Å	0.05 (± 0.05)
($\bar{1}11$)	138 K	1.81 (± 1.00) Å	0.05 (± 0.05)

Table 4.3.1. The fitting parameters obtained from the Ni(111)/Hg-p(2x2)-0.5ML structure NIXSW profiles for both (111) and ($\bar{1}11$) reflections at room temperature (298 K) and 138 K.

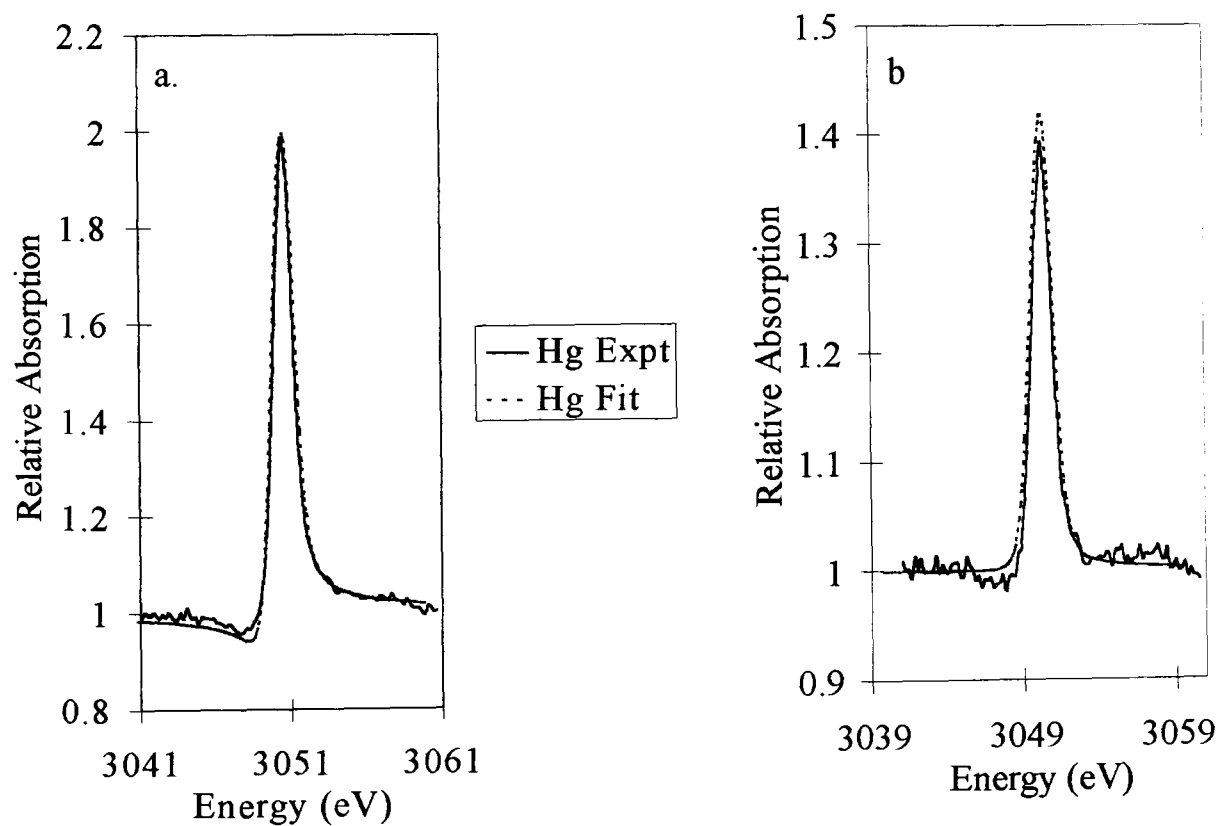


Figure 4.3.2. Ni(111)/Hg-p(2x2)-0.5ML structure (111) (a.) and ($\bar{1}11$) (b.) NIXSW scans and best fits for Hg ($3d_{3/2}$ photoelectron peaks) for the sample at $T = 138$ K

4.4 The Ni(111)/Hg–“ $c(2\sqrt{3}\times 2\sqrt{3})R30^\circ$ ” structure

One profile was taken for the “ $c(2\sqrt{3}\times 2\sqrt{3})R30^\circ$ ”-0.64ML structure for each reflection at 185 K. The Hg:Ni peak to peak ratios of the Auger, EDC and NIXSW profiles gave an average value of 0.66 ± 0.16 , concordant with a coverage of 0.64ML expected for the “ $c(2\sqrt{3}\times 2\sqrt{3})R30^\circ$ ”-0.64ML structure. The LEED pattern observed both before and after the NIXSW experiment was consistent with that of the “ $c(2\sqrt{3}\times 2\sqrt{3})R30^\circ$ ”-0.64ML ($x=0.18$) structure. The NIXSW spectra for the Ni(111)/Hg–“ $c(2\sqrt{3}\times 2\sqrt{3})R30^\circ$ ”-0.64ML structure are shown in figure 4.4.1. along with their best fits. These spectra were fitted with a Gaussian energy broadening width of 0.615 ± 0.1 eV. The results of these fits are shown in table 4.4.1.

The (111) scan (figure 4.4.1. a.) was similar to the (111) scans for the other structures, with a positive excursion of approximately 1.95, and a negative excursion of 0.95 at the lower energy side of the profile. Therefore, the coherent fraction and coherent position obtained from the fit of the (111) NIXSW profile was similar to those obtained for the other structures.

The ($\bar{1}11$) scan (figure 4.4.1.) had a peak with a positive excursion of approximately 1.28, which was smaller than that for the $p(2\times 2)$ -0.5ML and $(\sqrt{3}\times\sqrt{3})R30^\circ$ structures. Also, the negative excursion of approximately 0.98 was on the higher energy side of the profile relative to the positive excursions. The fit of the ($\bar{1}11$) profile, gave a

higher coherent fraction of $0.29 (\pm 0.05)$. Consequently, this higher coherent fraction indicates that there may be a decrease in the disorder and number of contributing heights relative to the $(\bar{1}11)$ plane than for the previous NIXSW profiles.

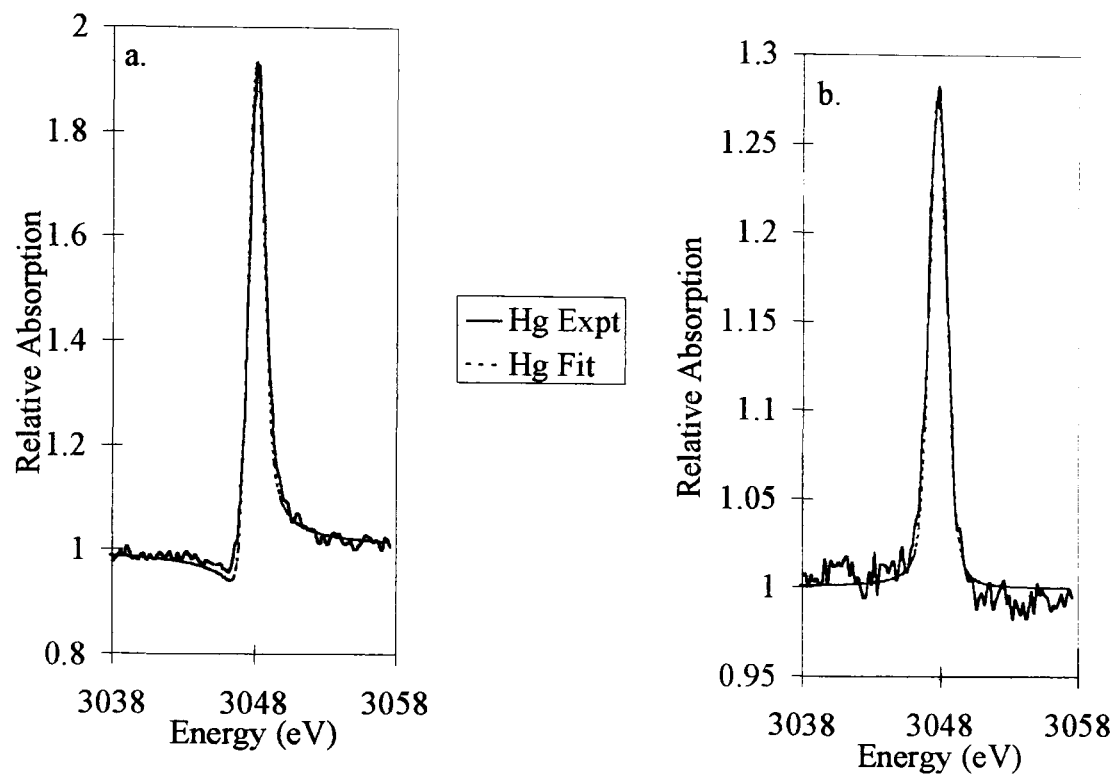


Figure 4.4.1. Ni(111)/Hg- $\sqrt{3}\times\sqrt{3}$ R30 $^\circ$ -0.64ML structure (111) (a.) and $(\bar{1}11)$ (b.) NIXSW scans and best fits for Hg ($3d_{3/2}$ photoelectron peak) for the sample at $T = 185$ K.

Reflection	Temperature	Coherent Position	Coherent Fraction
(111)	185 K	$2.35 (\pm 0.20)$ Å	$0.76 (\pm 0.05)$
$(\bar{1}11)$	185 K	$1.56 (\pm 0.85)$ Å	$0.29 (\pm 0.05)$

Table 4.4.1. The fitting parameters obtained from the Ni(111)/Hg- $\sqrt{3}\times\sqrt{3}$ R30 $^\circ$ -0.64ML structure NIXSW profiles for both (111) and $(\bar{1}11)$ reflections 185 K.

It can be seen that the coherent fraction of the $(\bar{1}11)$ scans compared with the (111) value is larger than the coherent fraction for the other Hg/Ni(111) structures. It should also be noted that the errors in the adsorbate position are relatively large. The lower coherent fraction of the (111) fits indicate a less well defined height above the $[111]$ planes, unlike the coherent fractions for the $(\bar{1}11)$ reflections, for which the reverse is true.

4.5 Summary of Ni(111)/Hg Structure Results

The coherent position is given as the height above the extended scatterer planes, plus an integral number of layer spacings appropriate to the adsorbate-substrate bond distance. If one considers the (111) reflection distance, Δd (Å), it can be seen that this adsorbate height above the (111) substrate scatterer planes indicates a Hg-Ni separation much smaller than the Hg-Ni bond length (2.63 Å) in the NiHg amalgam (Puselj and Ban 1997). Therefore, the mercury adatom is assumed to be located at a height of $(\Delta d + 2.03)$ Å above the (111) substrate planes. However, for the $(\bar{1}11)$ distance, the Δd (Å) value does not create an unfeasibly small Hg-Ni bond distance above the $(\bar{1}11)$ substrate scatterer planes.

The remainder of this section provides a brief comparison of the experimentally observed adsorbate positions with those expected for various adsorption geometries and Hg-Ni bond distances.

Structure	(111) Reflection		$(\bar{1}11)$ Reflection		Temp (K)
	$(\Delta d + 2.03)$ Å	f_c	Δd (Å)	f_c	
$(\sqrt{3} \times \sqrt{3})R30^\circ$	2.46 ± 0.20	0.68 ± 0.10	0.40 ± 1.00	0.05 ± 0.05	298
	2.46 ± 0.20	0.78 ± 0.10	0.10 ± 1.00	0.35 ± 0.05	138
$p(2 \times 2)-0.5ML$	2.43 ± 0.25	0.58 ± 0.10	1.69 ± 1.00	0.05 ± 0.05	298
	2.43 ± 0.25	0.78 ± 0.10	1.81 ± 1.00	0.05 ± 0.05	138
“ $c(2\sqrt{3} \times 2\sqrt{3})R30^\circ$ ”	2.35 ± 0.20	0.76 ± 0.05	1.56 ± 0.85	0.29 ± 0.05	185

Table 4.5.1 Summary of the experimentally determined coherent positions (Δd) and coherent fractions (f_c) for the Hg adsorbate NIXSW profiles obtained from the (111) and $(\bar{1}11)$ reflections for the Ni(111)/Hg structures.

Poulsen et al. 1994 determined the Ni-Hg bond length to be 2.86 Å for mercury on Ni(100) at 115 K, with adsorption in the four fold hollow, while NIXSW data for the same surface at 300 K (Prince et al. 1989), gave a bond length of 2.95 Å (Poulsen et al. 1994) after recalculation for adsorption in the four fold hollow. The mean of these two distances (2.91 Å) can be used as a Hg-Ni bond length for the Ni(111) surface. We can therefore calculate the layer spacing expected for mercury adsorption in the atop, 2-fold bridge and 3-fold hollow sites on the Ni(111) surface using the equations obtained from figure 4.5.1. (see table 4.5.2.). The nickel metallic radius is 1.25 Å (MacGillavry 1968), therefore the Ni-Ni bond length is assumed to be 2.50 Å.

Alternatively, the radius for atomic mercury (1.48Å) (MacGillavry 1968) can be used along with the nickel metallic radius (1.25Å) (MacGillavry 1968) to give a Hg-Ni separation of 2.73 Å. If this value can be substituted into the equations obtained in figure 4.5.1. to provide yet another set of adsorption heights (Table 4.5.2.). Also, the Ni-Hg bond distance (2.63Å) (Puselj & Ban 1977) can be used to provide a third set of adsorption heights using the equations used for the previous theoretical values (Table 4.5.2.)

Adsorption Site	(111) Refl.			$(\bar{1}11)$ Refl.		
	(Δd)	d_{111}	(Å)	Δd (Å)		
	A	B	C	A	B	C
Atop	2.91	2.73	2.63	0.97	0.91	0.88
2-fold bridge (a)	2.63	2.43	2.31	0.87	0.81	0.77
2-fold bridge (b)	2.63	2.43	2.31	1.89	1.83	1.79
3-fold hollow (FCC)	2.53	2.39	2.20	0.17	0.12	0.06
3-fold hollow (HCP)	2.53	2.39	2.20	1.52	1.48	1.41

Table 4.5.2. Calculated heights of mercury above the (111) and $(\bar{1}11)$ planes for A) Fixed Ni-Hg bond distance of 2.905 Å, B) A Hg-Ni separation of 2.73 Å obtained for the mercury atomic radius (1.48Å), and the nickel metallic radius (1.25 Å) and C) The Hg-Ni bond distance (2.63 Å) (Puselj & Ban 1977).

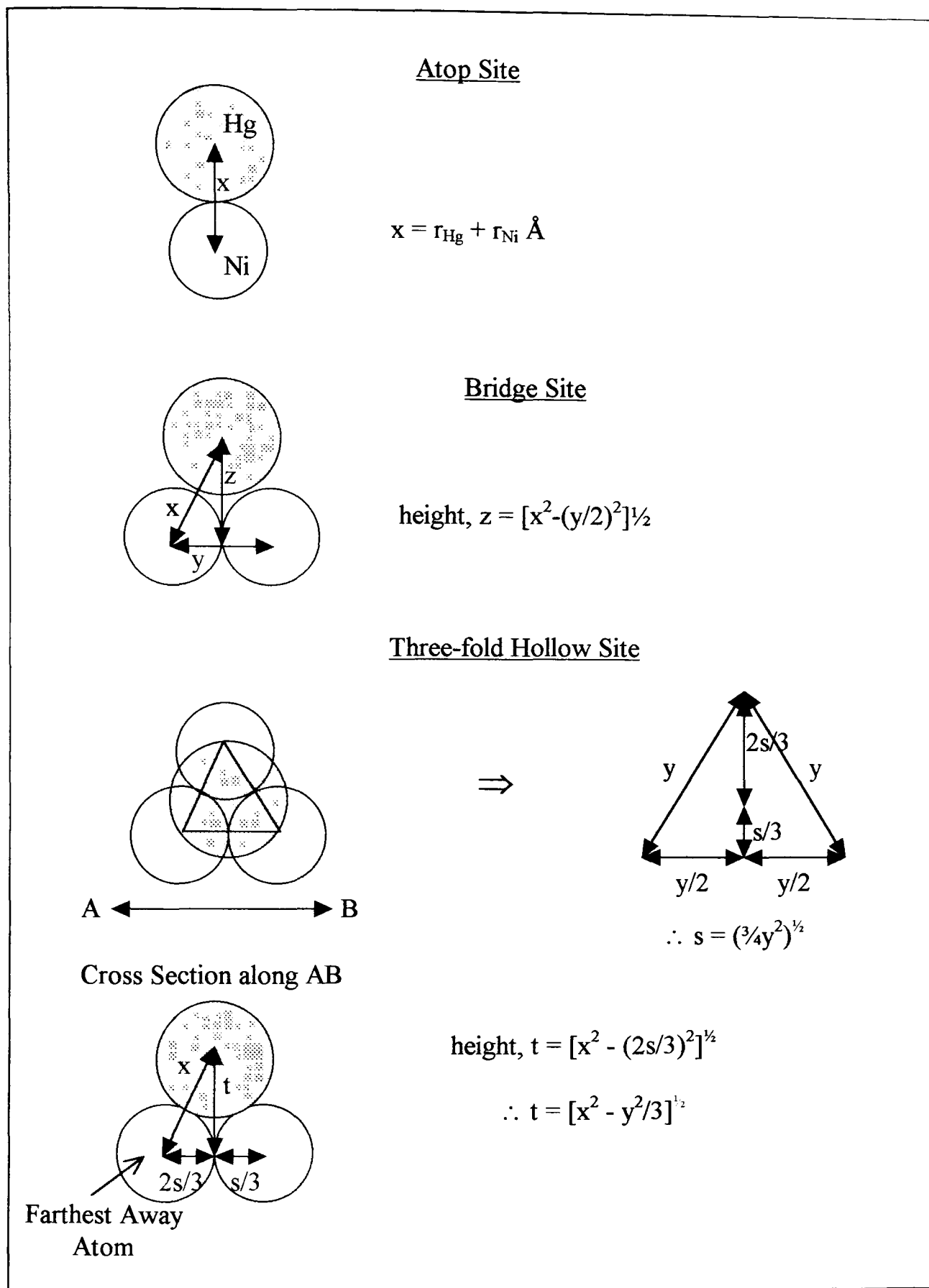


Figure 4.5.1. A schematic diagram showing how the theoretical [111] adsorbate heights were calculated.

The 298 K and 138 K (111) reflection profiles for the $(\sqrt{3}\times\sqrt{3})R30^\circ$ structure gave coherent positions of 2.46 ± 0.20 Å consistent with adsorption in either a 2-fold bridge site, or a 3-fold hollow (face centered cubic (FCC) and hexagonal close packed (HCP)) site (only for B and C calculations). The (111) NIXSW fitting parameters cannot distinguish between the different types of bridge (case a. and b.) and 3-fold hollow (HCP and FCC) sites (see chapter 2). The face centered cubic sites are where the next layer of nickel atoms would have occurred and the hexagonal close packed are where there is a nickel atom sat directly below the three-fold site. Therefore, the $(\bar{1}11)$ results are also needed to enable one to distinguish these different adsorption sites from the fitting parameters. Neither (111) reflection profiles gave a coherent position indicating adsorption in an atop site. Unlike the (111) profiles, the NIXSW scans for the $(\bar{1}11)$ profiles are able distinguish between the two possible bridge sites and the FCC and HCP sites. However, it is difficult to make any comparison of the $(\bar{1}11)$ reflection values without the Argand diagram analysis discussed in the next chapter.

Both the 298 K and 138 K (111) reflection profiles (table 4.5.1.) for the $p(2\times 2)-0.5\text{ML}$ structure gave coherent positions of 2.43 ± 0.25 Å. This coherent position indicates adsorption possible in either an atop site (for calculation A), a 2-fold bridge site (for A, B, or C calculations), or a 3-fold hollow (HCP or FCC) site (for A, B, or C calculations). Again, it is difficult to compare theoretical values obtained for the $(\bar{1}11)$ profile.

The experimental (111) adsorption height of 2.35 ± 0.20 Å obtained for the “ $c(2\sqrt{3} \times 2\sqrt{3})R30^\circ$ ” structure placed the mercury atoms in bridge (for B or C calculations) or 3-fold (FCC or HCP) hollow sites (for A, B, or C calculations).

It is worth noting that the $(\bar{1}11)$ reflection is established at relatively grazing incidence (19.5°) to the surface compared with the (111) reflection (90°). Consequently, the area of surface illuminated by the X-Ray beam is larger for the $(\bar{1}11)$ reflection, and not precisely coincident with that illuminated for normal incidence. This difference could affect the coherent fraction observed for the two different reflections as the beams could be illuminating slightly different areas on the crystal surface. The high coherent fraction of the substrate NIXSW profiles (0.9 ± 0.1 for the (111) and 0.8 ± 0.1 for the $(\bar{1}11)$ reflections) is consistent with a well ordered substrate surface and does not account for the comparatively low coherent fractions of the adsorbate NIXSW profiles. The coherent fractions for the (111) profiles obtained from the fits of the $(\sqrt{3} \times \sqrt{3})R30^\circ$ and the $p(2 \times 2)-0.5\text{ML}$ structures indicate that the coherent position for both sets of data could be ascribed to a single adsorbate-substrate layer spacing of the same value. The relatively high (111) coherent fraction of the “ $c(2\sqrt{3} \times 2\sqrt{3})R30^\circ$ ” structure could have a similar effect. The low coherent fractions for the $(\bar{1}11)$ profiles (which are lower than the value of ≈ 0.5 (Kadodwala et al 1995) that one would expect) suggest that there is a large amount of static or dynamic disorder about the mean position with respect to the $(\bar{1}11)$ planes. This information combined with the relatively high (111) coherent fraction suggests that there is little motion perpendicular

to the surface, but a large amount of disorder parallel to the surface. Such disorder would have no effect on the (111) NIXSW results, but would lead to displacements quite close to perpendicular to the $(\bar{1}11)$ planes. The low $(\bar{1}11)$ coherent fractions and large errors in the coherent positions for the various structures also indicates that there is a large amount of uncertainty in the Δd values. If the nearest neighbour Hg-Hg interactions were sufficiently strong, they could lead to static random displacements of the adsorbate atoms off the exact high symmetry sites. It has often been postulated that mercury atoms are a very mobile adsorbate (Swanson et al 1968, Jones & Perry 1978, Singh & Jones 1988 and 1990a and Kime et al 1992) and are expected to form island structures when adsorbed on metal single crystal surfaces (Jones & Perry 1978, Singh & Jones 1989a and 1989b, Li et al 1992a and Li et al 1992b). The atomically smooth, close packed surface of the Ni(111) crystal (Singh & Jones 1989a, 1989b) does possess quite small geometrical corrugations. These corrugations would offer little resistance to lateral movements of an adsorbate and will be discussed in more detail in the next chapter.

Another explanation of the low $(\bar{1}11)$ coherent fraction could be that there is more than one layer spacing involved, that is, more than one site may be occupied. Due to the high coherent fractions obtained for the (111) NIXSW profiles, this interpretation would require that these various sites have essentially indistinguishable (111) layer spacings. When one considers the various heights above the (111) planes for the different adsorption sites, in comparison to the large mercury diameter (2.96 Å) (MacGillavry 1968), the different sites do appear to have very similar values (figure 4.5.1.). The calculated (111) heights for the 2-fold bridge and 3-fold hollow sites differ only by 0.1 Å, which is a direct consequence of the large size of the mercury atom relative to the unit mesh of the Ni(111) surface. Again, this will be discussed in greater detail in the next chapter.

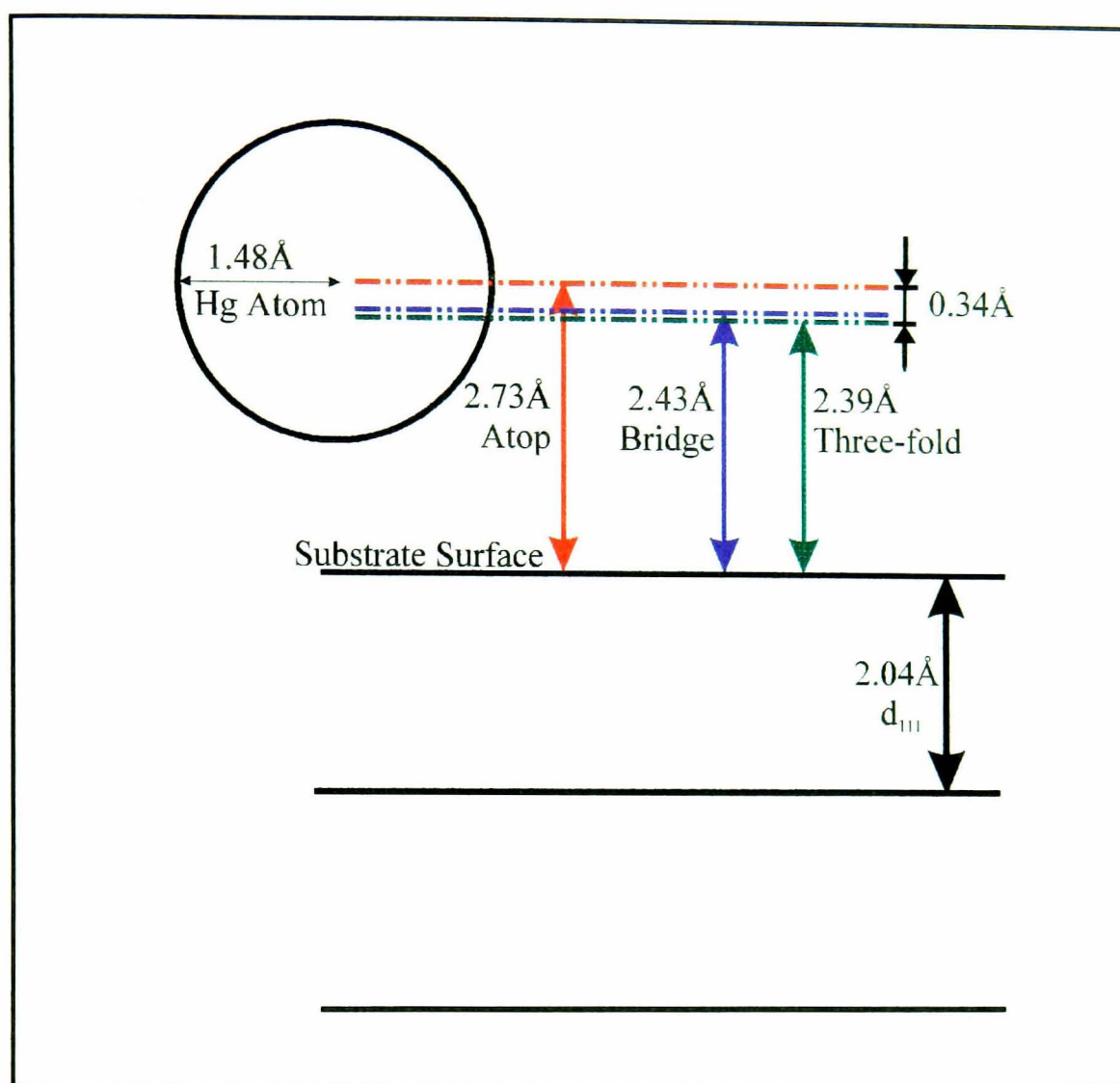


Figure 4.5.1. A scale diagram showing the small difference in adsorbate heights for the various high symmetry sites (atop, bridge, 3-fold) with respect to Hg atomic diameter (2.96 \AA) and the nickel substrate layer spacing (2.04 \AA).

5 Mercury Adsorption on Ni(111) Discussion

Island formation (patches of adsorbate separated by patches of adsorbate free substrate) of the adsorbate species requires that the adsorbate is able to diffuse across the surface. In response to attractive adsorbate-adsorbate interactions, adsorption only occurs at the perimeter of the islands (Evans 1989). These types of adsorbate-adsorbate attractive lateral interactions have been seen to produce two-dimensional ideal gas behaviour at low coverages for mercury adsorbed on the more corrugated (100) surface of nickel (Jones and Tong 1987). Swanson et al. (1968) also stated that mercury behaved more like a common gaseous adsorbate (CO_2 , N_2 , O_2 , etc.) rather than an electropositive metallic adsorbate.

As the heat of chemisorption usually decreases with increasing coverage, the mobility of adspecies tends to be more possible at higher coverages. The mobility of an adatom will vary for different crystallographic planes of the same metal substrate and possibly different areas of the surface if surface heterogeneity is suspected (King and Woodruff 1983). Hence, for a more close packed surface (i.e. the smaller the corrugation), the adsorbate is more able to migrate across the surface (Tompkins 1978). A weak corrugation in the mercury-substrate interaction energy as a function of lateral position on the surface is expected. This is due to the large mercury size (relative to the small Ni(111) unit mesh size) and non-directional bonding (due to the closed shell configuration).

The Argand diagram analysis method (Woodruff et al. 1994) outlined below (described in detail in section 2.1.2.) is the technique used to analyse our NIXSW data. The fitting parameters obtained from each NIXSW scan, f_c (coherent fraction) and Δd (coherent position) can be represented as vectors on an Argand diagram. The length of the vector represents the coherent fraction, f_c and the angle of the vector measured anti-clockwise from the positive real axis represents the value $2\pi\Delta d/d_{hkl}$, where Δd is the coherent position (Å) and d_{hkl} is the distance between the (hkl) reflecting planes. For the Ni(111) surface, this is the (111) and $(\bar{1}11)$ layer spacing depending on which reflection is used. A coherent fraction, f_c of 1.0 and a coherent position, Δd of zero (or any multiple of d_{111}) is expressed as a unit vector lying along the positive real axis (figure 2.10).

As described in section 2.1.3.1. a single layer spacing relative to the $(\bar{1}11)$ planes only occurs for those adsorption sites which retain the full three-fold symmetry of the substrate (FCC, HCP and atop sites). Once these symmetrically equivalent sites have been taken into account, any adsorption site having less than 3-fold symmetry will lead to two or more different $(\bar{1}11)$ layer spacings (Woodruff et al. 1994). Consequently, an experimental $(\bar{1}11)$ adsorption profile produced by adsorption sites with less than 3-fold rotational symmetry would yield a very low coherent fraction (typically 0.5 or less) or would not be fitted by a single layer spacing.

A low coherent fraction for the substrate absorption profile can be attributed to non-uniform regions of the surface which are therefore incoherent with the underlying bulk layers in which the standing wavefield is established. Hence, the adsorbate coherent fraction cannot usually be of a greater value than that of the substrate.

Specifically, a pair of symmetrically displaced layer spacings will provide a very similar fit to that of the mean layer spacing along with a reduced coherent fraction. This reduced coherent fraction corresponds to an average displacement similar to that of the 2-component layer spacings. Hence, as described in the experimental chapter, it is difficult to set error limits on the alternative fits since the layer spacing and coherent fraction are coupled. The coherent fractions and positions resulting from the nickel substrate scans have similar values to those expected for a well-ordered crystal surface, thus indicating that the adsorbate coherent fraction results can be compared with the substrate coherent fraction of 0.9 ± 0.1 . For the $(\bar{1}11)$ data, the steep angle these planes make to the sample surface (70.5°) ensure that the Δd values (which are 19.5° to the surface, figure 2.15.) have a large component (94%) parallel to the surface. Consequently, any NIXSW experimental data obtained for the $(\bar{1}11)$ direction will provide information about the adsorbate's behaviour parallel to the surface.

The NIXSW method determines the adsorption site relative to the continuation of the underlying bulk substrate in which the standing wave is established (section 2). Therefore, a change in the top one or two layer spacings of the substrate will mean that the coherent position will be the true Hg-Ni layer spacing plus the amount by which

the top layer of the substrate has expanded and not the spacing of the adsorbate layer from the substrate layer (Prince et al. 1989).

Sizeable adsorbate-adsorbate interactions are expected for mercury, as its boiling point of 630 K (Lide 1992) is indicative of strong bonding in the pure element. Atomic mercury has a full set of 5d and 6s valence orbitals and its chemical behaviour is therefore fairly inert. Consequently the mercury adatom only bonds weakly through its s-orbitals to the nickel substrate surface. The combination of the small Ni(111) surface corrugation (due to small surface unit mesh) and weak Hg-Ni surface bonding allows the Hg s-orbitals to overlap. Such an s-orbital overlap allows lateral Hg-Hg interactions which influence the adsorbate surface structure (Singh et al. 1993). Over a range of Hg-Hg separations for different mercury sub-monolayer films, the smaller the separation, the smaller the attractive pairwise interaction. For a sufficiently small Hg-Hg separation, the lateral interaction becomes repulsive.

5.1 The Ni(111)/Hg-($\sqrt{3}\times\sqrt{3}$)R30° 0.33ML Structure - ($\bar{1}11$) Reflection

The behaviour of the isosteric heat of adsorption, q_{st} for mercury adsorbed on Ni(111) has indicated strong attractive lateral interactions between the mercury atoms sites [Varma et al. (1986) and Singh & Jones (1988 and 1989b)]. Singh (1989) also stated that the Hg-Hg separation of 4.31Å, which is greater than that for the low pressure α -Hg (2.99 Å, Donohue 1974) indicates a high probability of attractive lateral interactions. Therefore, when adsorbate-adsorbate lateral interactions are strong and

attractive and the adsorbate-substrate interaction is weak, island formation is thought highly probable (Morrison 1977). This is because the weak adsorbate-substrate interaction allows the adsorbate to diffuse across the surface and the strong adsorbate-adsorbate interaction causes the adsorbate atoms to form islands. These adsorbate-adsorbate lateral interactions are thought to be responsible for the formation of rafts of Hg adatoms on the Ni(111) surface which can compress and alter in response to coverage changes (Singh & Jones 1988). The formation of mercury rafts (Singh & Jones (1988 and 1989b)) has also been implied by LEED observations. Dowben et al. (1987) also found that mercury formed islands when adsorbed on a Ag(100) surface. Island structure has also been observed when mercury adsorbs on the Cu(100) (Dowben et al. 1990b), W(100) (Jones and Perry 1978) and W(110) (Zhang et al. 1993 and 1994a) surfaces. The mercury adatoms in these islands are expected to be subject to two conflicting forces as proposed for the mobility of Pt clusters on Pt(111) by Li et al. (1994). They stated that the adsorbate atoms would be pulled into the adsorption sites by the binding energy of the surface. The distance between the two adjacent adatoms would then be forced to equal the distance between the sites. However, the binding energy between the two adjacent atoms in the island compels them to occupy a separation compatible with the bond length. If the bond length is different from the site-to-site distance, the atoms in the island have to compromise between these two tendencies. Consequently, as the cluster is displaced some of the atoms will find less stable (higher energy) positions and therefore the clusters' ability to slide as a whole will increase.

Using a hard sphere model, consideration of the large size of the Hg atom (2.99 Å van der Waals diameter (Singh 1989)) and the small Ni(111) hexagonally close packed surface net (unit mesh size of 2.49 Å (Singh 1989)) indicates that the Hg could move from the 3-fold hollow site via the 2-fold bridge site to the atop site with relative ease. Band structure calculations (Singh et al. 1993) have shown that the change in work function for these three sites is approximately 0.1 eV with a work function of 4.99 eV for the $(\sqrt{3}\times\sqrt{3})R30^\circ$ structure. Singh and Jones (1989b) have already stated that the surface structure formation on the particularly smooth corrugation of the Ni(111) surface (small unit mesh and hexagonally close packed structure) is dominated by the large mercury adsorbate exhibiting strong Hg-Hg lateral interactions.

Despite the strong adsorbate-adsorbate interactions and the weak corrugation of the adsorbate substrate potential for a single adsorbed atom, it is clear from the observation of the commensurate LEED patterns that commensurate structures are formed. Dowben et al. (1988) have also observed mercury adsorbate structures which are largely coincident with their substrate ($\text{Cu}_3\text{Au}(100)$, $\text{Ag}(100)$, $\text{Fe}(100)$ and $\text{W}(100)$). However, an overlayer of this type should be unstable to low frequency (“soft”) phonon modes involving substantial local displacements parallel to the surface. The local displacements parallel to the surface in such a (long wavelength) mode can be much larger than the changes in the local adsorbate-adsorbate nearest neighbour distances which can be expected to be constrained by the long adsorbate-adsorbate interactions. The LEED pattern from such a layer would remain that of a rigid commensurate overlayer, as the orientation and spacing of the adlayer net remains

fixed, but the large amplitude of the vibration across the surface would produce a large distribution of distances parallel to the surface and hence a large distribution of Δd with respect to the $(\bar{1}11)$ planes. For the above postulate all possible positions with respect to the $(\bar{1}11)$ planes would be equally probable and we would attain the homogeneous distribution of adsorbate heights essential for a coherent fraction of zero. This creates an apparent paradox where the $(\bar{1}11)$ NIXSW data with $f_c \approx 0.2$ is consistent with a rather disordered surface, but in contrast the sharp LEED patterns observed are consistent with a high degree of crystallinity in the adlayer.

It is proposed that the Hg rafts mentioned above, as a whole and at constant coverage, can translate across the substrate surface. This agrees with the weakly chemisorbed mercury adlayers described in previous studies (Ag(100)-Onellion et al. 1986, Ni(111)-Singh and Jones 1989b). Translations in all directions across the surface would produce an even distribution of distances parallel to the surface and therefore an even distribution of Δd relative to the $(\bar{1}11)$ planes. It should be noted that in any domain, translations parallel to the $(\bar{1}11)$ planes will generate a definite coherent position, Δd . Hence, any departure away from $f_c = 0$ may be due to either translation parallel to the $(\bar{1}11)$ planes or to some preference to a specific adsorption site. If the Hg adatoms were able to translate freely across the Ni(111) surface, the adsorption would be entirely disordered, therefore the Hg atoms would be randomly adsorbed at an “xy” position on the Ni surface. The $(\bar{1}11)$ NIXSW results would therefore have very low coherent fractions indicative of several different contributing heights above the angled

$(\bar{1}11)$ planes. Such low coherent fractions for the $(\bar{1}11)$ NIXSW results have been observed. In the absence of a more conclusive explanation, the $(\bar{1}11)$ NIXSW spectra indicate that the Ni(111)/Hg- $(\sqrt{3}\times\sqrt{3})R30^\circ$ -0.33ML structure consists of islands that are able to translate in all directions across the surface. These translations subsequently produce an even distribution of distances parallel to the surface and therefore an even distribution of Δd relative to the $(\bar{1}11)$ planes.

It has been shown (Wright and Chrzan 1993) that the surface of K(110) has a (1x1) structure with a large fluctuating displacement ($\approx 0.45 \text{ \AA}$ root mean squared at $T = 25 \text{ K}$) of the surface layer along the $[\bar{1}10]$ direction rather than a static lateral shear displacement reconstruction as originally proposed (Itchkawitz et al. 1992). The magnitudes of these fluctuations are said to increase with temperature. This is the type of motion we postulate for our Hg adlayers. The two systems are similar in that both mercury and potassium are low melting point metals, 234 K and 336 K respectively and interact primarily via their non-directional s-orbitals. Therefore, one might expect the mercury, which is bonded relatively weakly (isosteric heat of adsorption = 110-200 kJ mol^{-1} Singh and Jones 1990a), compared with the lateral interactions, to the hexagonal Ni(111) to behave similarly to potassium on the pseudo-hexagonal (110) face of potassium (ΔH° sublimation $\approx 80 \text{ kJ mol}^{-1}$). The temperature used for the potassium LEED study was 25 K, which is much lower than the 138 K used in this study. However, the root mean squared displacement of 0.45 \AA for the surface layer of potassium was still appreciable. Consequently we would not expect to significantly

reduce the motion of the Hg surface by merely cooling it from 298 K to 138 K and indeed the NIXSW spectra only changed very slightly on cooling.

The Hg-Hg adsorbate interaction has previously been thought induce mercury adatoms to move with coverage dependent vibration amplitudes ($0.1 \pm 0.03 \text{ \AA}$ at 115 K for low coverage of $\theta \approx 0.18 \text{ ML}$ and higher for $\theta \approx 0.45 \text{ ML}$) on nickel surfaces (Poulsen et al. 1994). This adlayer would create a LEED pattern consistent with our observations, as the orientation and spacing of the adlayer net remains fixed. The mercury adlayer rafts may be unable to rotate freely and forced to translate across the surface due to the following: steps (Barber and Loudon 1989 and Günther et al. 1993) on the surface may inhibit the rotation of the semi-rigid rafts; or the adsorption energy corrugation of the raft and substrate combination is channelled in the low miller indices directions with significant barriers between the channels. Therefore, the raft can move bodily in the directions of the channels but not rotate.

Singh and Jones (1990a) proposed that the mercury islands observed in their study were able to rotate freely on the Ni(111) surface. In contrast, the rafts postulated here would not be able to rotate on the substrate surface, as this would not produce the sharp LEED spots observed in our experiments. This is in agreement with the lack of LEED structure observed at higher temperatures ($310 \text{ K} < T < 351 \text{ K}$) by Singh and Jones (1989b) which was attributed to a combination of the smooth corrugation of the Ni(111) surface and the Hg adatom interactions allowing the mercury islands to rotate

freely to any orientation (Singh 1989). Therefore the adlayer rafts would be free to rotate across the Ni(111) surface, thus creating blurred or even no LEED structure.

In previous studies (Varma et al. (1986) and Singh & Jones (1989b)), the mercury atoms for the $(\sqrt{3}\times\sqrt{3})R30^\circ$ -0.33ML structure were arbitrarily placed in the more energetically favoured three-fold hollow sites on the Ni(111) surface (figure 5.1.1.). This hypothesis would place the mercury atoms in either face centred cubic (FCC) sites where the next layer of nickel atoms would have occurred, or in hexagonal close packed (HCP) sites where there is a nickel atom directly below the three-fold site (Figure 5.1.2.). However, mercury adatoms have also been thought to reside in bridge sites on the Ni(100) surface (Prince et al. 1989 and 1990) rather than the more energetically favourable four-fold hollow sites (Poulsen et al. 1994 for Ni(100) and Jones & Perry 1981 for Fe(100)). Consequently, the adsorption sites suggested for the $(\sqrt{3}\times\sqrt{3})R30^\circ$ -0.33ML structure by previous studies have all been arbitrary and it is therefore reasonable to say that the Hg adatoms could be located in any of the high symmetry sites.

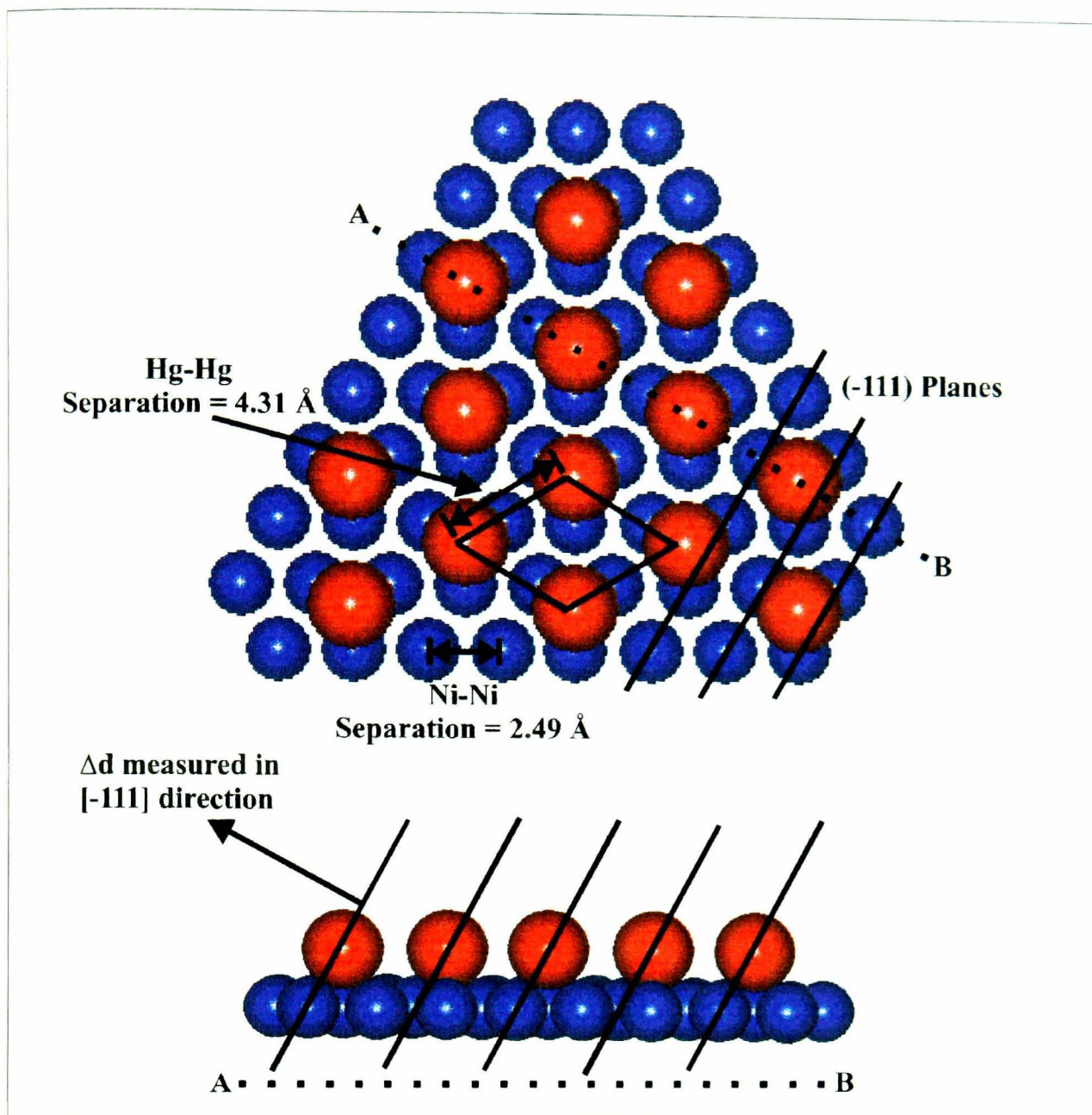


Figure 5.1.1. A schematic diagram of the possible Ni(111)- $(\sqrt{3}\times\sqrt{3})R30^\circ$ -Hg-0.33ML real space structure (plan and side views) containing one mercury atom per unit mesh, with the mercury atoms arbitrarily located in three-fold hollow sites. The mercury adatom surface net, Hg-Hg adsorbate and Ni-Ni substrate separation are also shown. The adlayer is not puckered in this diagram. The $(\bar{1}11)$ planes are schematically illustrated on the side view of the structure indicating how these planes relate to the mercury adsorbate atoms' position. The blue and red atoms represent nickel and mercury respectively. The diameters of the atoms are relative to each other.

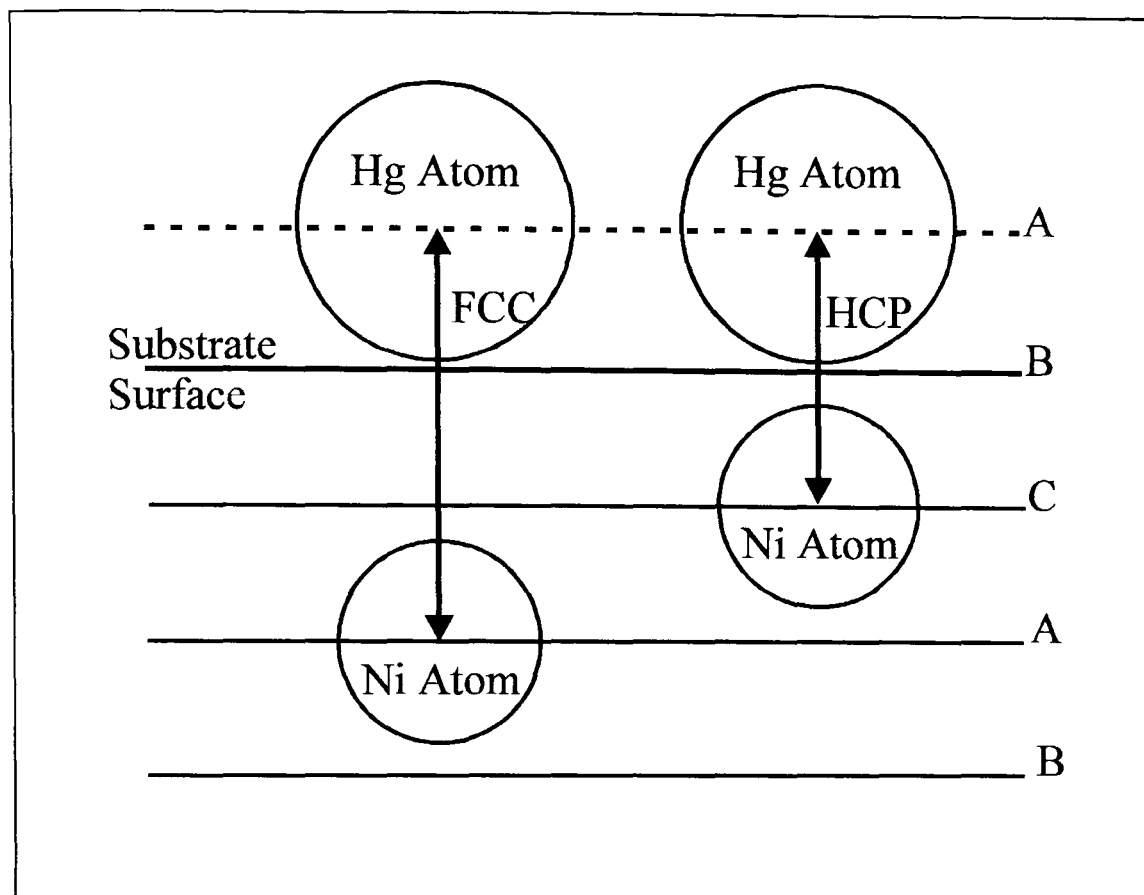


Figure 5.1.2. A diagram illustrating the difference between a three-fold FCC (Hg atom directly above a Ni atom in the next substrate layer would have occurred) and a three-fold HCP site (where a Ni atom is sat directly below the three-fold site).

The partial occupation of both HCP and FCC hollows can only be reconciled with separate domains of FCC and HCP occupation if all the adsorbate atoms lie on regular mesh domains, rather than a mixture of single sites in the domains. The difference in the binding energies of the adsorbates at the FCC and HCP two sites could be very small. At low coverages occupation of both sites due to the small energetic differences is possible for adsorption of isolated atoms. High coverage occupation of both sites would involve adsorbate-adsorbate interactions and possibly force some adsorbates into less favourable sites. As mentioned at the beginning of this chapter, the high coherent fraction for the (111) reflection data excludes the possibility of low symmetry sites. There are adsorption systems in which the adsorbate appears to occupy both sites

on an equal basis (Kerker et al. 1992a and references therein). For single hollow site adsorption in the few cases which have been studied using methods which permit the examination of structures with no long-range order, adsorption is found to be invariably in the FCC site (Kerker et al. 1992a).

It is conceivable that a coherent fraction close to zero can also be attained using several equally populated adsorption sites. For example, a combination of atop, 3-fold FCC and 3-fold HCP sites, equally populated and measured using the $(\bar{1}11)$ planes will yield an NIXSW spectrum with a coherent fraction, f_c very close to zero. The three vectors for these particular sites are approximately 120° apart from each other (figure 5.1.3.). Therefore using simple vector addition, these vectors should almost cancel each other out, thus producing a Gaussian NIXSW spectrum and a coherent fraction close to zero. This type of combined adsorption is close to that of the raft/domain idea suggested in this thesis.

The large errors in coherent position, of the $(\bar{1}11)$ reflection data make it impossible to discuss the experimental data as vectors on an Argand diagram. The very low coherent fraction (0.05 ± 0.05) of the room temperature data implies an even distribution of adsorbate heights from zero to $d_{(\bar{1}11)}$ relative to the $(\bar{1}11)$ reflecting planes. The marginally higher coherent fraction of the low temperature data (0.35 ± 0.05) could be due to a reduction in the thermal motion perpendicular to the $(\bar{1}11)$ reflecting planes as the mercury surface structure is “frozen” to the Ni surface. If the

mercury atoms were in several well-defined high symmetry adsorption sites, then cooling would still cause very little or no change, as the mercury atoms would be “frozen” into their respective sites. As we observe very little change on cooling the adsorbate structures, this idea must also be considered.

If the mercury atoms do not reside wholly in FCC or HCP sites, then the only other combinations of high symmetry sites available are wholly atop, bridge (case a) or bridge (case b) sites. At this point, the reader is reminded that there are twice as many type “b” bridge sites than there are type “a” (section 2.1.3.1.). The Argand diagram representation for these theoretical values of the possible sites is shown in figure 5.1.3.

Onellion et al. (1988) found that mercury adsorbed into a variety of adsorption sites on the Ag(100) surface rather than purely in the most thermodynamically stable sites. It is difficult to justify why different parts of these structures would have domains consisting wholly of atop, bridge (case a), bridge (case b), 3-fold HCP, or 3-fold FCC occupied sites. It is therefore logical to presume that the low coherent fractions in the $(\bar{1}11)$ data are due to a genuine distribution of adsorbate coherent positions, Δd . Alternatively, the data could have contributions from both disordered and ordered structure, which has previously been proposed for the $(\sqrt{3}\times\sqrt{3})R30^\circ$ structure (Zhao & Gomer 1992).

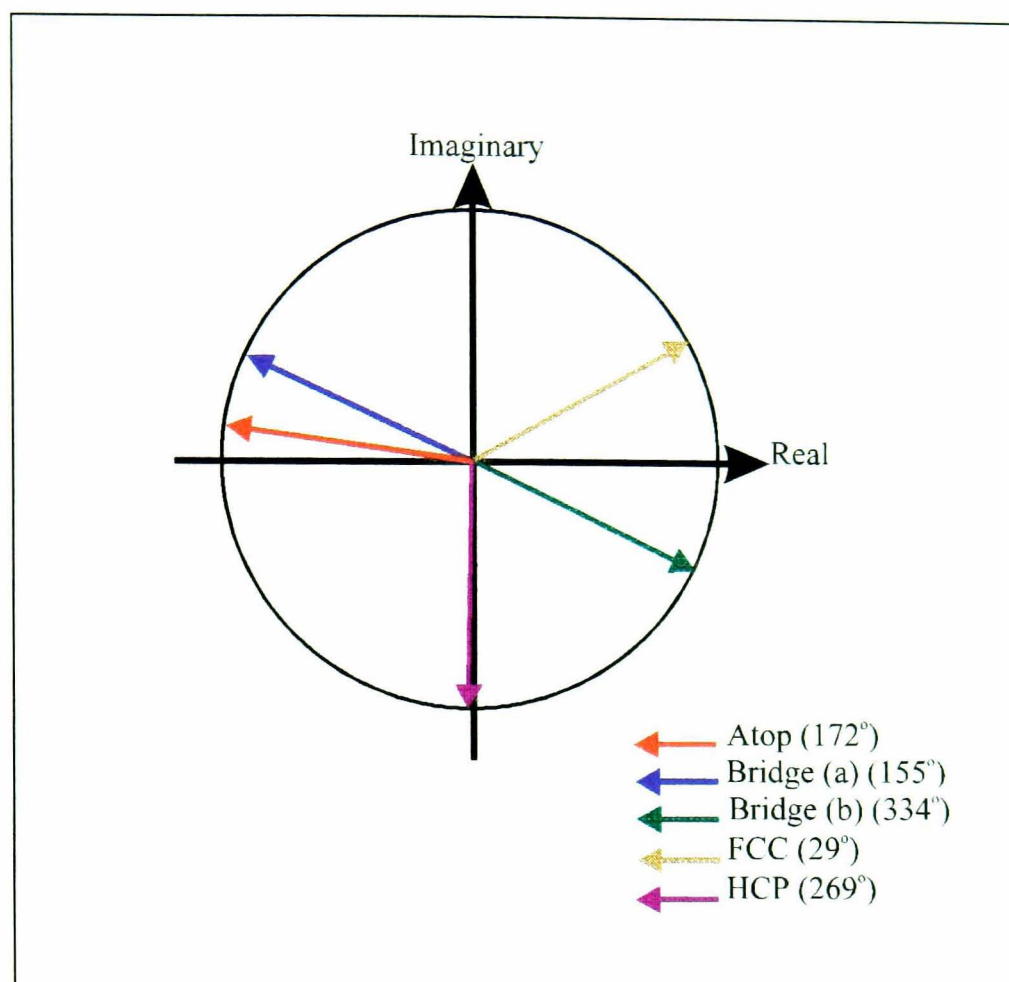


Figure 5.1.3. Argand vector diagram showing the vectors for the $(\bar{1}11)$ illustrating the theoretical vectors (coloured arrows) of the atop, bridge (case a and b), FCC and HCP sites.

Static random lateral displacements of the adsorbate atoms off the exact high symmetry sites are caused if the nearest neighbour adsorbate-adsorbate interactions are sufficiently strong. However it seems unlikely that these displacements would be, on average as large as 0.34 \AA (vertical distance between the high symmetry sites, section 4.5). The Ni-Ni separation is 2.50 \AA , therefore the displacements would need to be as large as 14% of the Ni atom separation. Dynamic disorder can really only be reconciled with such large displacements if the adsorbed atoms are assumed to be extremely mobile on the surface.

5.2 The Ni(111)/Hg-p(2x2)0.5ML Structure - $(\bar{1}11)$ Reflection

The p(2x2)0.5ML structure also exhibits a sharp LEED pattern with no suggestions of any disordered component on the surface (Singh, 1989 and Singh & Jones 1990b), so the translating adlayer model is again appropriate to account for the low coherent fraction relative to the $(\bar{1}11)$ reflection plane. Therefore, our hypothesis for the p(2x2)0.5ML structure also agrees with that proposed for the $(\sqrt{3}\times\sqrt{3})R30^\circ$ structure in section 5.1.

The model postulated for the Ni(111)/Hg-p(2x2) - 0.5ML structure (Singh (1989) and Singh & Jones (1988)) suggests that the mercury atoms form islands and adsorb into three-fold hollow sites, half in FCC and half in HCP sites. Such adsorption would construct open hexagons of mercury atoms (figure 5.2.1.) separated by 2.87 Å, slightly less than the van der Waal radius of the Hg (3.0 Å) with a maximum coverage of 0.5ML. This is in close agreement with nearest neighbour distances found for mercury adsorbed on other surfaces (2.87 Å - Hg/Fe(100) Jones & Perry (1981), ≈ 2.8 Å - Hg/Ni(100) Jones & Tong (1987), 2.72 Å - Hg/Cu₃Au(100) Onellion et al. (1987) and 2.89 Å Hg/Ag(100) Dowben et al. (1987a & b) and Onellion et al. (1986)). At a coverage of approximately 0.45 ML it is more energetically favourable for the islands to rearrange into a hexagonal mesh to form the p(2x2)-0.5ML structure (Singh and Jones 1990a). Such a structure would display repulsive interactions due to the direct overlap of the mercury s and possibly even d orbitals (Singh 1989). This is in agreement with the decrease of the isosteric heat of adsorption characteristic of

repulsive lateral interactions between the adsorbate atoms (Singh and Jones 1990a). Singh et al. (1993) also observed d band splitting in UPS spectra of the $p(2 \times 2)$ -0.5ML surface that was predominantly the effect of lateral interactions between nearest neighbour mercury atoms.

The coherent fractions for the $(\bar{1}11)$ NIXSW data are very low, with both the 298 K and 138 K data producing a coherent fraction of 0.05 ± 0.05 . Therefore, as for the $(\sqrt{3} \times \sqrt{3})R30^\circ$ structure, it is impossible to compare the $(\bar{1}11)$ NIXSW data on an Argand diagram due to the large errors in coherent position.

Figure 5.2.2. shows an Argand diagram illustrating the theoretical vectors for adsorption half in 3-fold HCP sites and half in 3-fold FCC sites. The coherent fraction, $f_c \approx 0.42$ obtained by the 50:50 HCP:FCC model is obviously a great deal higher than that obtained by the experiment. Hence, it appears that the mercury atoms do not adsorb equally onto FCC and HCP sites, without adsorption elsewhere. By moving the $p(2 \times 2)$ -0.5ML mercury adatom net laterally, the mercury atoms could be positioned in 50% atop, 50% HCP sites or 50% atop, 50% FCC sites surfaces (figure 5.2.3.) (Singh 1989 and Singh & Jones 1990a). It was also argued (Varma et al. 1986 and Singh & Jones 1990a) that the $p(2 \times 2)$ -0.5ML mercury adatom net could be translated laterally and relocated in 2-fold bridge sites. This translation would place the lattice points in bridge sites (Varma et al. 1986), but not all Hg atoms would be in bridge sites, some would not be in any high symmetry site (Figure 5.2.4.).

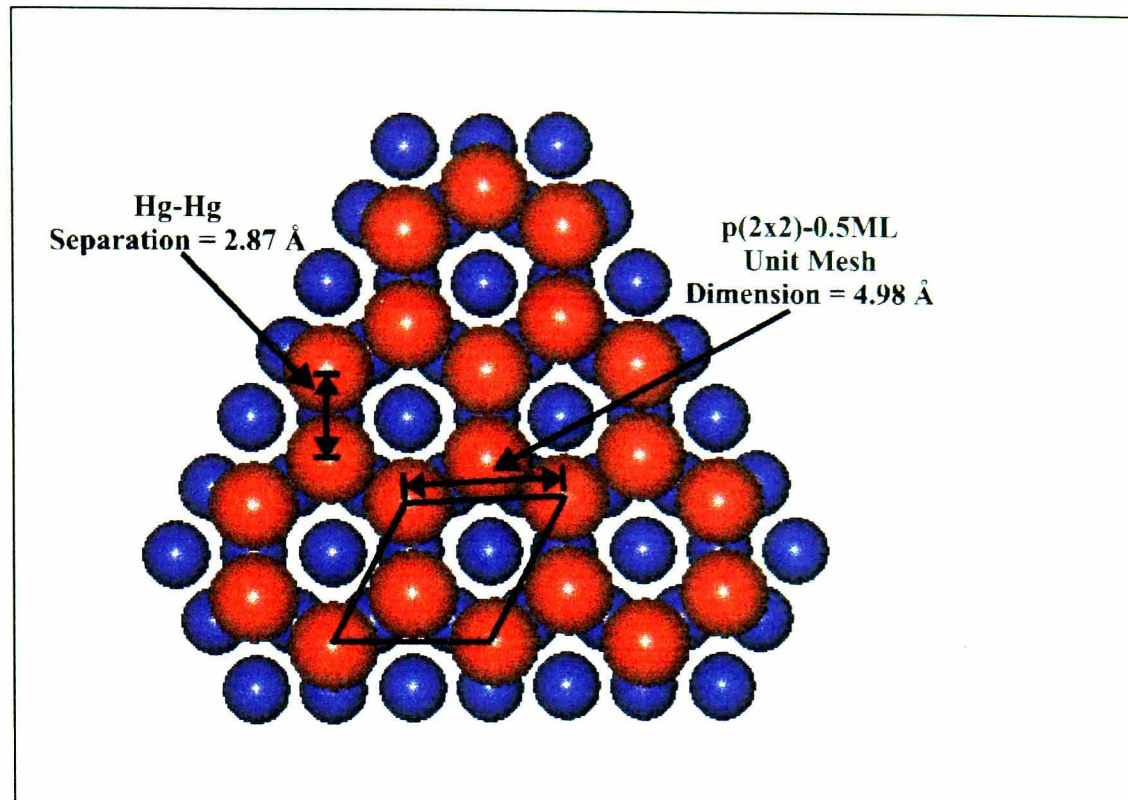


Figure 5.2.1. A schematic diagram of the possible Ni(111)-p(2x2)-Hg-0.50ML real space structure containing two mercury atoms per unit mesh, with the mercury atoms arbitrarily located in three-fold hollow sites (half in HCP and half in FCC). The mercury adatom surface net and Hg-Hg adsorbate separation are also shown. The adlayer is not puckered in this diagram. The blue and red atoms represent nickel and mercury respectively. The diameters of the atoms are relative to each other.

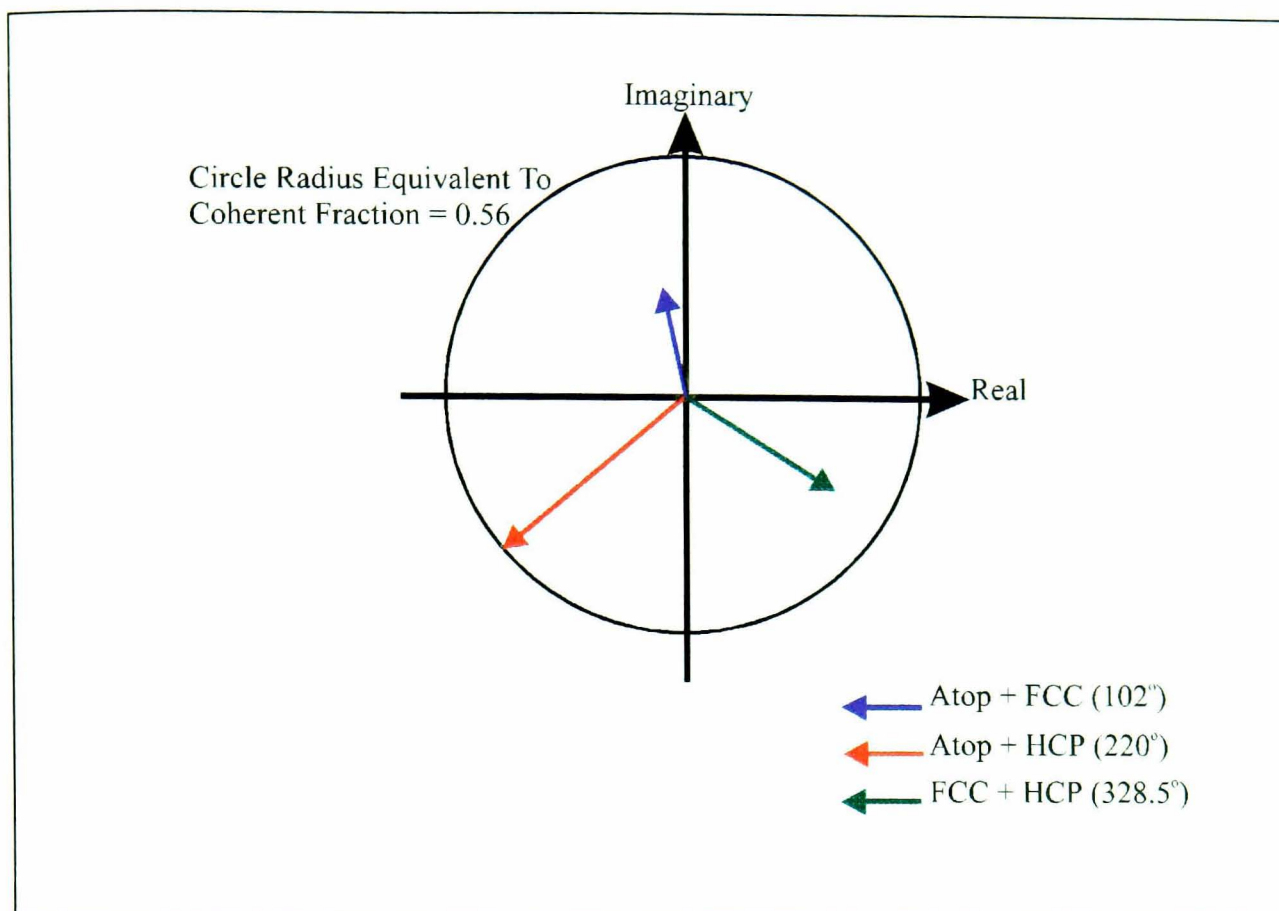


Figure 5.2.2. Argand vector diagram showing the $(\bar{1}11)$ theoretical vectors (coloured arrows) for adsorption half in 3-fold HCP sites and half in 3-fold FCC sites (also 50% atop + 50% FCC, 50% atop + 50% HCP).

The above discussion indicates that any particular type of high symmetry site adsorption would produce coherent fractions well outside the errors for our low $(\bar{1}11)$ experimental values, so again, one would have to postulate many domains with different adsorption sites to achieved low value of f_c .

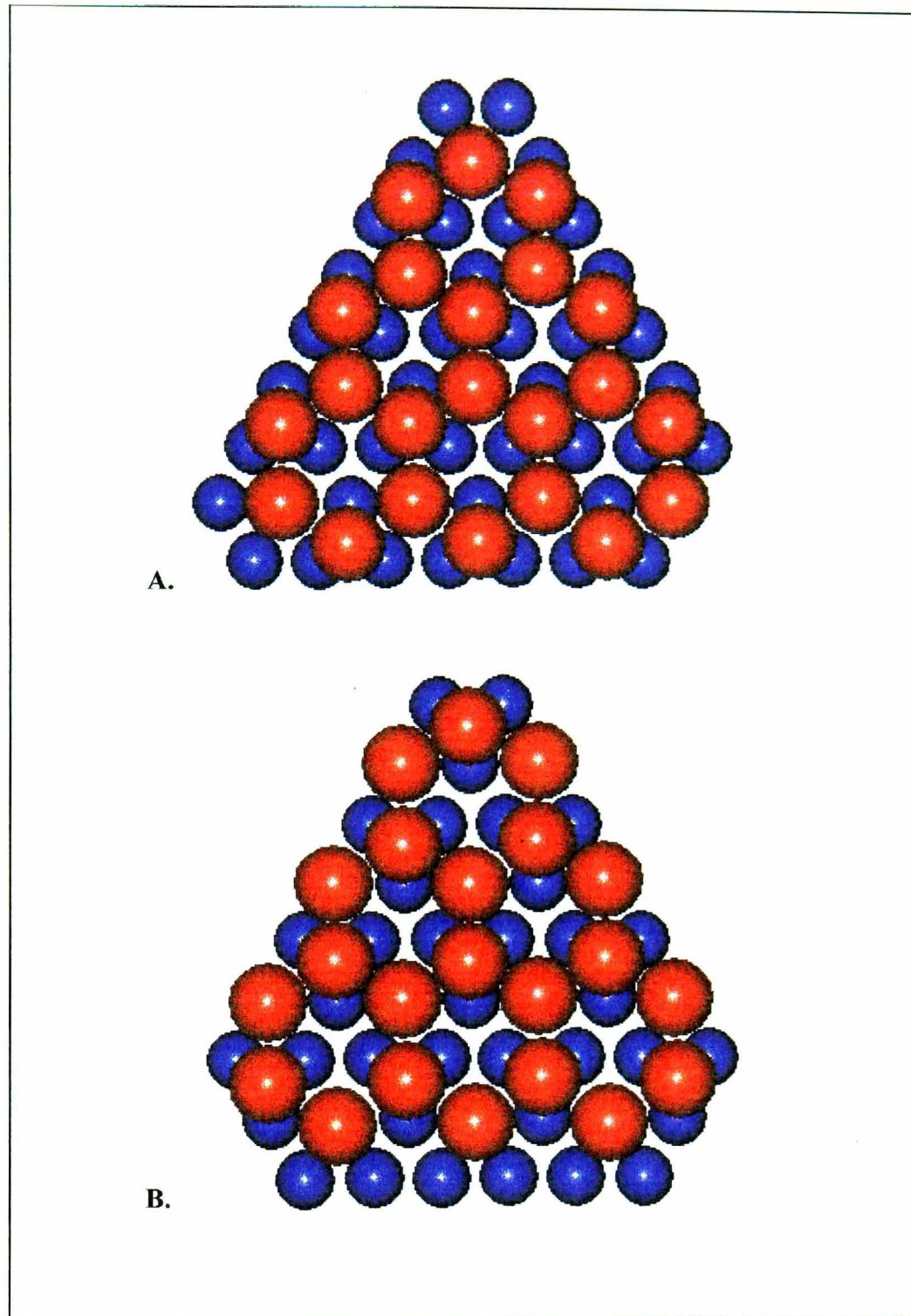


Figure 5.2.3. A schematic diagram of the possible Ni(111)-p(2x2)-Hg-0.50ML real space structure containing two mercury atoms per unit mesh, with the mercury atoms arbitrarily located in A) half in atop and half in three-fold hollow sites (HCP) and B) half in atop and half in three-fold hollow sites (FCC). The adlayer is not puckered in this diagram. The blue and red atoms represent nickel and mercury respectively. The diameters of the atoms are relative to each other.

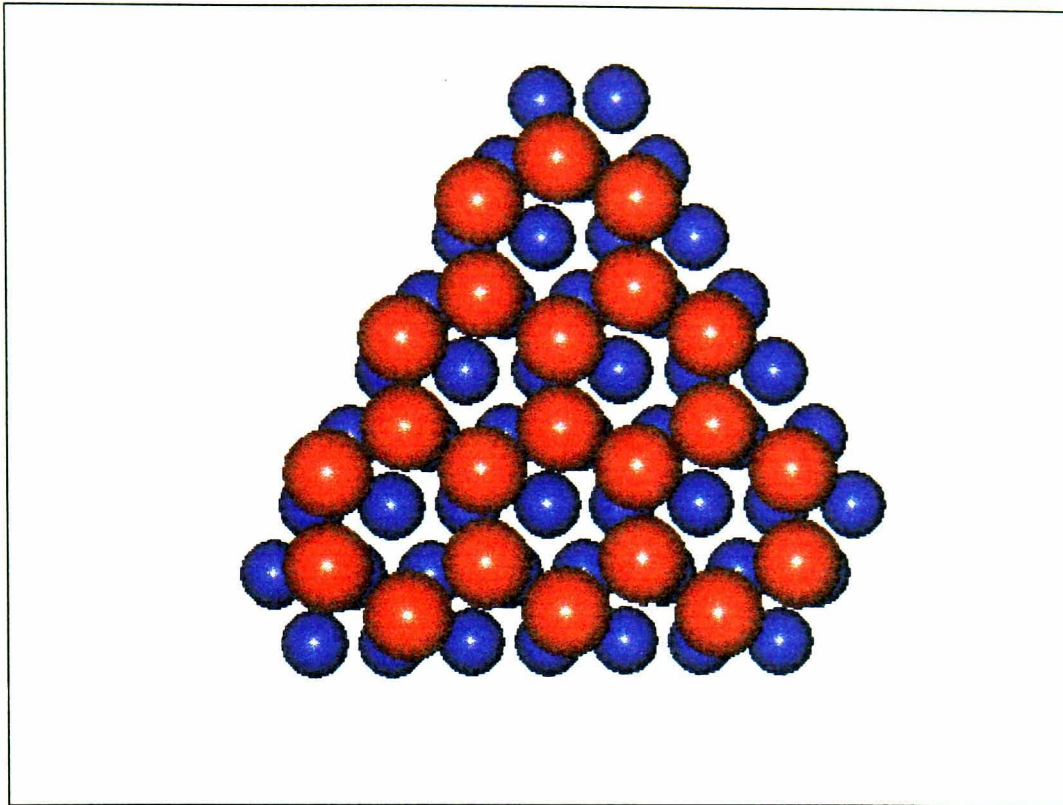


Figure 5.2.4. A schematic diagram of the possible Ni(111)-p(2x2)-Hg-0.50ML real space structure containing two mercury atoms per unit mesh, with the mercury atoms arbitrarily located in bridge sites and off bridge sites. The adlayer is not puckered in this diagram. The blue and red atoms represent nickel and mercury respectively. The diameters of the atoms are relative to each other.

5.3 The Ni(111)/Hg-“ $c(2\sqrt{3}\times 2\sqrt{3})R30^\circ$ ”- 0.64ML Structure - $(\bar{1}11)$ Reflection

The coherent fraction of 0.29 ± 0.05 for the $(\bar{1}11)$ NIXSW data at 185 K is quite low, and so the errors on the coherent position are high. Therefore, as for the $p(2\times 2)$ -0.5ML and $(\sqrt{3}\times\sqrt{3})R30^\circ$ structures, it is impossible to compare the $(\bar{1}11)$ NIXSW data on an Argand diagram due to the large errors in coherent position. The low coherent fraction obtained from the fitting of the NIXSW scans indicates that there is either static or dynamic disorder present. Consequently, one would expect the mercury adatoms to behave similarly to the other structures studied. Therefore a translating semi-rigid raft of mercury adatoms is also proposed for the “ $c(2\sqrt{3}\times 2\sqrt{3})R30^\circ$ ” 0.64ML structure.

It should be noted that even though the temperature of 185K was higher than the 138K for the $p(2\times 2)$ -0.5ML and $(\sqrt{3}\times\sqrt{3})R30^\circ$ structure and its structure is inherently more heterogeneous in terms of site adsorption than the other two structures. The “ $c(2\sqrt{3}\times 2\sqrt{3})R30^\circ$ ” structure showed the second largest f_c (0.29) of any of the $(\bar{1}11)$ reflection data. This would imply that the increased surface density has reduced the root mean squared surface displacement of the Hg adlayer such that the f_c value has increased, possibly to the value characteristic of its static heterogeneity of adsorption sites. Additionally, such a relatively high coherent fraction for this structure might be expected for low temperature data, as the adatoms will tend to reside in the shallow energy minima which must be present as the thermal motions decrease.

At a coverage of 0.64ML, the “ $c(2\sqrt{3} \times 2\sqrt{3})R30^\circ$ ” structure (Singh 1989, Singh and Jones 1989a, 1989b, 1990b and Singh et al. 1993) was the highest coverage Hg/Ni(111) structure studied. This adlayer can be described using the matrix G, where

$$G = \frac{1}{1-2x} \begin{pmatrix} 1-x & x \\ x & 1-x \end{pmatrix}$$

and $x = 0.18$ (Singh and Jones (1990b). For a non-equilibrium coverage of 0.6ML to 0.64ML, the “ $c(2\sqrt{3} \times 2\sqrt{3})R30^\circ$ ” structure is formed when the pseudo-square adlayer becomes periodic and compresses from the $x = 0.2$ to the $x = 0.18$ structure along a direction parallel to the substrate direction of closest packing (Singh and Jones 1989b). This “ $c(2\sqrt{3} \times 2\sqrt{3})R30^\circ$ ”-structure is a slightly distorted square adlayer of mercury atoms with an internal unit mesh angle of approximately 96° and four mercury atoms per unit mesh (Singh et al. 1993) (figure 5.3.1.). The same pseudo-square arrangement would be somewhat distorted by site adsorption. The Hg-Hg separation of 2.90 Å is less than the mercury atomic diameter (3.0 Å) and the Hg-Hg separation in the solid (2.99 Å in α Hg), thus indicating possible repulsive lateral interactions between the mercury adatoms in this metallic pseudo square adlayer (Singh 1989). For the mercury structures formed in non-thermodynamic equilibrium at $T < 290$ K, the mercury was said to form islands over a wide range of coverages (0.2 - 0.6 ML) consisting of coincident pseudo-square adlayers of mercury (Singh and Jones 1989b). This island formation and the pseudo-square structure were attributed to attractive adatom-adatom interactions. For the “ $c(2\sqrt{3} \times 2\sqrt{3})R30^\circ$ ” structure, it is possible to locate one

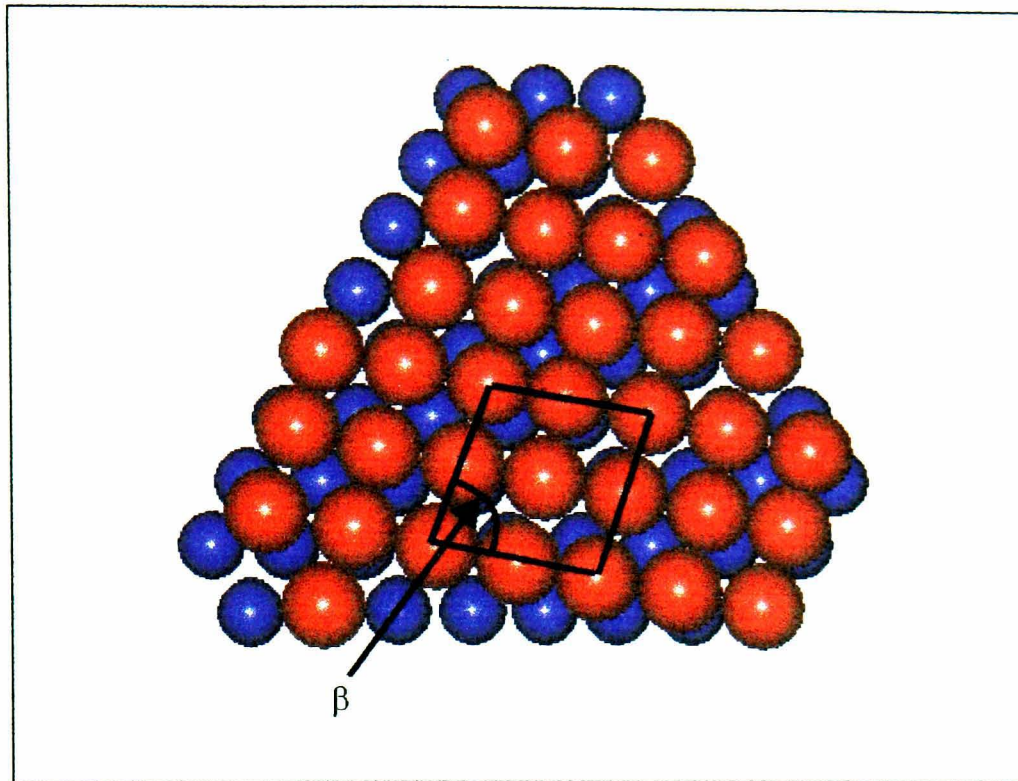


Figure 5.3.1. A schematic diagram of the possible Ni(111)-c($2\sqrt{3}\times 2\sqrt{3}$)R30°-Hg-0.64ML real space structure containing one mercury atoms per unit mesh. The mercury adatom surface net with an angle $\beta = 96^\circ$ is also shown. The adlayer is not puckered in this diagram. The blue and red atoms represent nickel and mercury respectively. The diameters of the atoms are relative to each other.

Hg atom in say, a 3-fold hollow HCP site, which then positions two Hg atoms approximately in bridge sites and a 4th in an approx 3-fold hollow FCC site. With the three possible orientations of this structure relative to the fixed $(\bar{1}11)$ planes, there are then a large number of vectors which need to be summed leading to a small value for f_c . Clearly, when one considers that this situation is for just one set of possible adsorption sites, the large number of possible adsorption sites for this structure prevents us from making any further deductions.

5.4 The Ni(111)/Hg (111) Reflection Data For All Structures

We are now in a position to discuss the (111) reflection data. Figures 5.4.1 to 5.4.3. illustrate the Argand diagrams for experimental (111) NIXSW scans of all three structures formed by mercury adsorption on the Ni(111) surface. These Argand diagrams illustrate the mercury adsorption heights relative to the (111) reflection planes. The vectors in the Argand diagram show that the experimental data can be fitted by adsorption of the mercury atoms in the bridge or three-fold hollow site. However, the low coherent fraction and the large errors in the angle (coherent position) cause one to doubt this possibility.

For all three structures using the (111) reflections, the root mean squared displacement of the coherent position is found to be approximately 0.39 Å. We return to the hard sphere model and assume that the mercury adlayer is flexible, such that the Hg adatoms remain in contact with the substrate. This will cause the adlayer to pucker

with some Hg atoms in three-fold hollows and others in bridge or atop sites, as well as other heights in between. The total range from the 3-fold hollows to the atop is approximately 0.34 Å (figure 4.5.1.), which is identical to the value of 0.39 ± 0.25 Å derived from the experimental coherent position values (within error margins). The coherent fraction, f_c is related to the Debye-Waller factor, M , by $f_c = \exp(-M)$. The Debye-Waller factor does not distinguish between static and dynamic contributions. Therefore we suggest that the lowering of the coherent fraction in the (111) data for all three surfaces is primarily due to puckering of the mercury adlayer with some contribution from the vibration of the mercury perpendicular to the surface at each site.

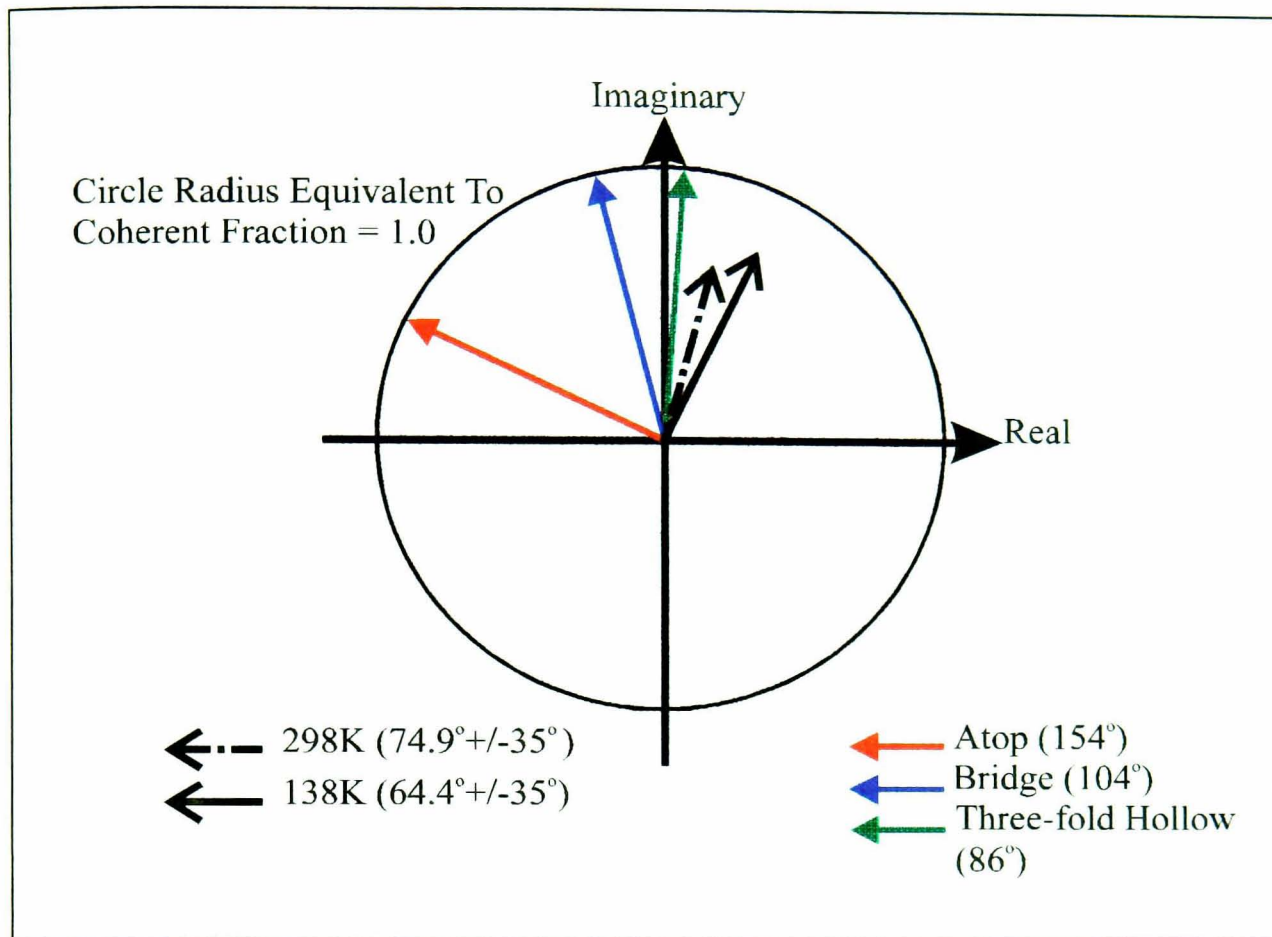


Figure 5.4.1. Argand vector diagram showing the vectors for the (111) illustrating the theoretical vectors (coloured arrows) of the atop, bridge and three-fold hollow sites along with the experimental vectors (black arrows) obtained for the Ni(111)/Hg-($\sqrt{3} \times \sqrt{3}$)R30°- 0.33ML structure at T = 138 K and T = 298 K.

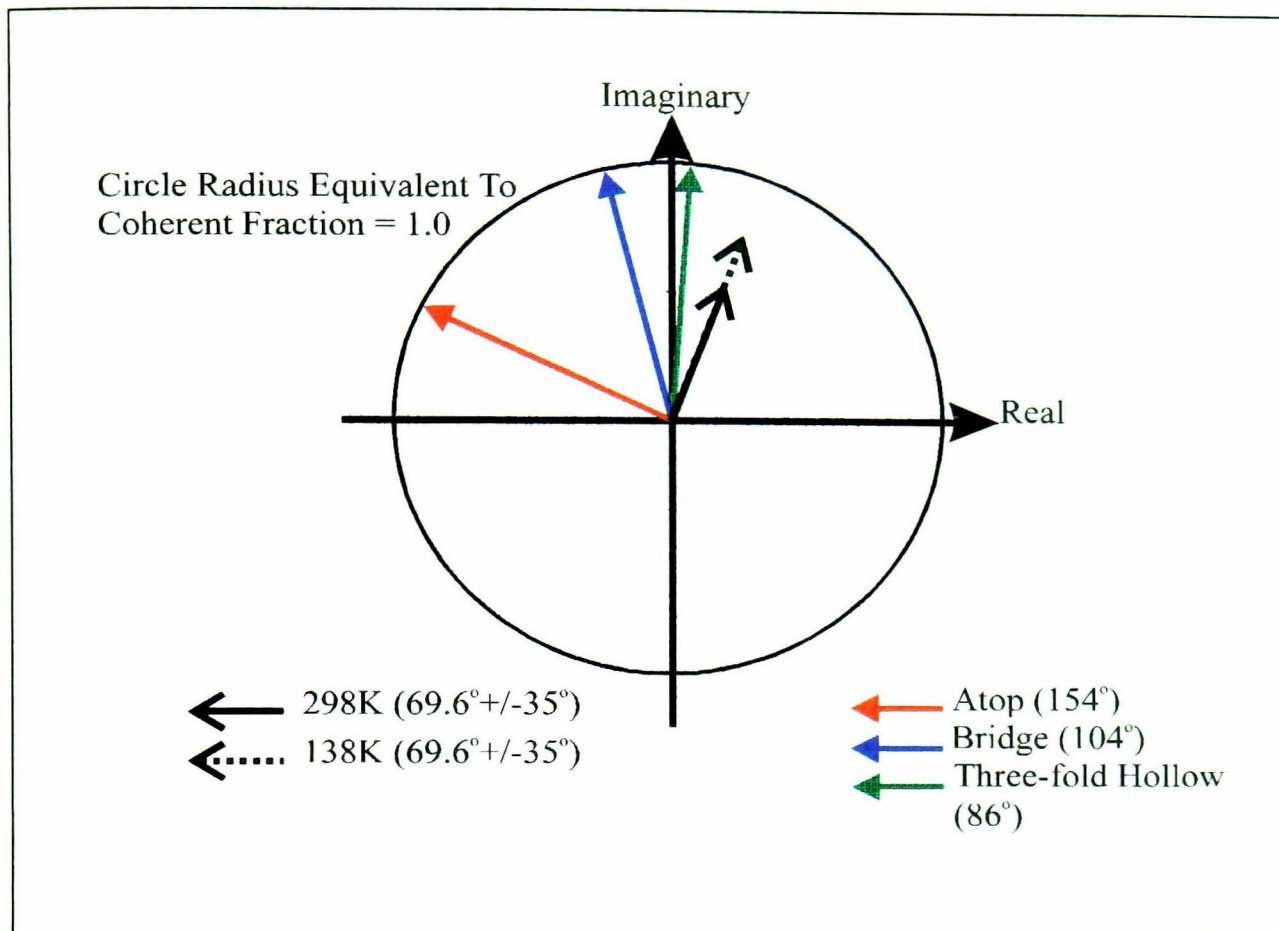


Figure 5.4.2. Argand vector diagram showing the vectors for the (111) illustrating the theoretical vectors (coloured arrows) of the atop, bridge and three-fold hollow sites along with the experimental vectors (black arrows) obtained for the Ni(111)/Hg-p(2x2)-0.5ML structure at $T = 138$ K and $T = 298$ K.

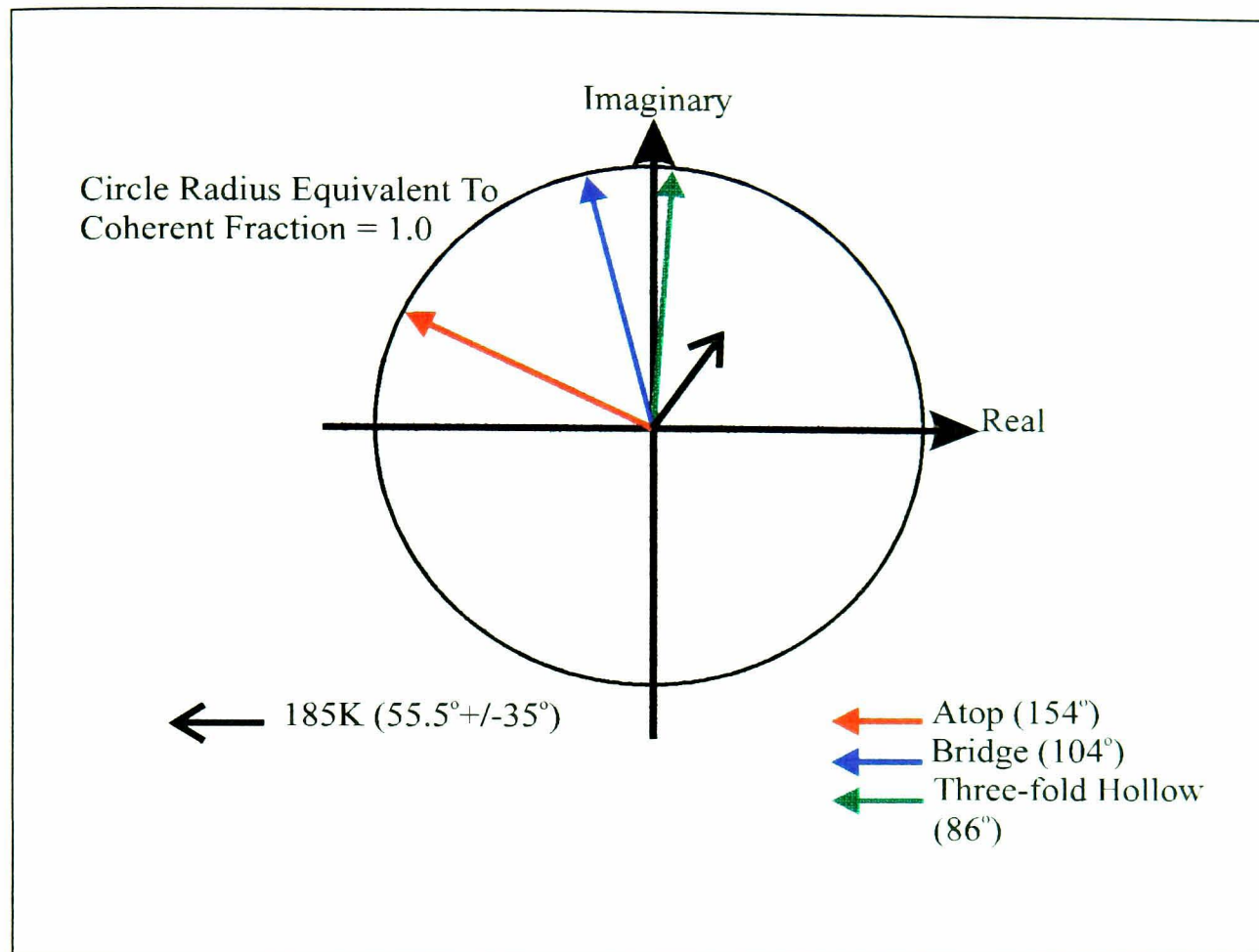


Figure 5.4.3. Argand vector diagram showing the vectors for the (111) illustrating the theoretical vectors (coloured arrows) of the atop, bridge and three-fold hollow sites along with the experimental vectors (black arrows) obtained for the Ni(111)/Hg - $c(2\sqrt{3} \times 2\sqrt{3})R30^\circ$ - 0.64ML structure at T = 185 K.

5.5 The Ni(111)/Hg Data For All Structures And All Reflections

The coherent fractions of the NIXSW scans indicate that although there is excellent order in the substrate and in the adsorbate atoms perpendicular to the surface, there is significant disorder parallel to the surface for all phases, including the low coverage phases. Static disorder parallel to the surface (i.e. displacement from ideal high symmetry sites) might well result from strong adsorbate-adsorbate repulsion which has been observed for mercury adsorption on Ni(111) (Singh 1989, Singh and Jones 1990a and Singh et al. 1993) and many other surfaces (Fe(100) - Jones & Perry (1981) and Dowben et al. (1988), Ni(100) - Jones & Tong (1987), Hg/Cu₃Au(100) and W(100) - Dowben et al. 1988 and Ag(100) - Dowben et al. (1988) and Kime et al. (1992)). This type of adsorbate-adsorbate repulsion is generally thought to occur at short distances in alkali adsorption, but this could not easily account for the low coverage phase. However, large vibrational amplitudes parallel to the surface (dynamic disorder) might reasonably explain the lower coherent fractions parallel to the surface and would be consistent with the high mobility expected of alkali adsorption on such a surface.

One must question why the mercury rafts can translate freely, but not rotate, on the surface. We suggest that steps (Barber and Loudon 1989 and Günther et al. 1993) on the surface may hinder rotation of the semi-rigid rafts. Alternatively, the adsorption energy corrugation of the raft and substrate combination could be channelled in low Miller index directions (also proposed adsorption for Hg/Ni(100) by Poulsen et al.

1994) with considerable energy barriers between the channels. Consequently the raft can translate in the direction of the channels, but cannot rotate.

5.6 The Ni(111)/Hg Conclusion

The application of the NIXSW to three mercury adlayers which exhibit sharp, bright LEED patterns, yields results which appear to imply a disordered adsorbate surface. This apparent paradox is resolved by proposing that the mercury adlayer undergoes a low frequency, large amplitude vibration parallel to the surface. This would allow the crystallinity of the adlayer to be maintained for LEED analysis. Yet the continuous variation of the coherent position of the mercury adsorbate atoms relative to the $(\bar{1}11)$ planes would account for the very low coherent fractions observed for this reflection.

Given the ambiguity of the Ni(111)/Hg NIXSW data, only a qualitative argument is possible. The conclusion reached from the NIXSW data is therefore the best explanation the data presented.

The combination of a large atom on a close packed metal surface produces a situation in which the degree of geometrical corrugation of the surface is very small. Therefore the factors governing the optimum adsorption site may be more subtle than in a system having larger corrugation. This idea will be further investigated in chapters six and seven where mercury adsorption on a more open substrate surface such as Cu(100) was studied.

6 Mercury Adsorption on Cu(100) : NIXSW Results

This chapter describes the results obtained for the four Cu(100)/Hg structures investigated using the NIXSW technique. As for the Ni(111) profiles, the photoelectron peak intensities were normalised to a value of 1.0 at the extremes of the energy range, well away from the Bragg condition. The substrate NIXSW profiles obtained using the Cu $2p_{3/2}$ photoelectrons were fitted in the same manner as the Ni(111) substrate spectra using the coherent position (Δd), coherent fraction (f_c) and instrumental broadening width as variables.

To recapitulate, the coherent position is the perpendicular distance of the absorber atoms from the extended bulk scatterer planes. The coherent fraction for a particular reflection describes the order of the surface (adsorbate or substrate) in that plane (a value of 1.0 indicating complete order with no vibrations and a value of zero indicating complete disorder). The distances of the mercury adsorbate atoms from the Cu substrate layers are relative to the nearest extended scatterer plane. Hence, as for the Ni(111) data the ambiguity of these distances relative to the number of substrate layer spacings can be removed when the chemical bond distances are known.

All the NIXSW profiles were fitted using an X-Ray beam energy broadening, $\sigma = 1.550 \pm 0.025$ eV for the (200) reflection and $\sigma = 0.95 \pm 0.05$ eV for the (111) reflection. For the adsorbate NIXSW profiles, the broadening width was fixed at

$\sigma = 1.55$ eV (for the (200) reflection) and $\sigma = 0.95$ eV (for the (111) reflection), with the data being fitted by varying the coherent position, Δd and the coherent fraction, f_c . The adsorption sites were again calculated as in chapter 4 using the triangulation method (Frost et al. 1967, Kerkar et al. 1992a, 1992d) outlined in section 2.1.3.

As for the Ni(111) data, the peak-to-peak height ratios of the mercury and copper peaks in the Auger and photoelectron scans were calculated for the various adsorbate structures formed. Again, these values corresponded with those expected for the coverage of each adsorbate structure formed. This provided an additional indication that the correct adsorbate structures had been formed. The NIXSW fits are again decided by the relative amplitudes of the positive and negative excursions of the profiles and by the peak energy.

6.1 The Cu(100) Substrate

Representative (200) and (111) reflection NIXSW results taken for the Cu(100) substrate are shown in figures 6.1.a. (from the cold c(4x4) structure) and 6.1.b. (from the warm c(4x4) structure). All the Cu(100) substrate NIXSW spectra for the c(2x2)-0.5ML, c(4x4)-0.62ML, (3x3)-0.66ML and c(2x6)-0.83ML structures were identical to those in figure 6.1. It can be seen that the spectra shown in figure 6.1 differ slightly in shape indicating that the (200) and (111) will give different fitting parameters. The (200) profile has a negative excursion of 0.88 and a positive excursion of 1.44 at the higher energy side of the profile. Whereas the (111) profile has a negative

excursion (also at the lower energy side of the positive excursion) of 0.70 along with a positive excursion of approximately 1.78.

The fitting procedure gave perfect coherent positions of 0 or 1.81 Å (= d_{100}) for the (200) reflection, and 0 or 2.09 Å (= d_{111}) for the (111) reflection. Therefore the coherent position obtained from the fitting of the substrate absorption signal is consistent with the substrate absorbers being coincident with the extended scatterer planes, as anticipated. A coherent fraction of 0.9 ± 0.1 for both the (200) and (111) (figure 2.14.) reflections was also obtained from the above fitting procedure. Therefore the Cu(100) crystal surface can be assumed to be of good crystallographic order and that the different mercury adsorbate structures do not affect the copper surface. The NIXSW absorption profile fit for the (111) reflection data is not as good as the fit for the (200) data. This may be due to the greater amount of substrate disorder parallel to the surface rather than perpendicular to it, along with possible thermally induced disorder due to the higher temperature (298 K) of the sample for the (111) reflection data. However, the positive excursion height of the (111) fit is approximately 0.2 higher than that of the experimental data, producing an increase in the coherent fraction of almost 0.05 for the theoretical fit.

All the NIXSW spectra for the $c(2 \times 2)$ -0.5ML and $c(4 \times 4)$ -0.62ML structures were taken at room temperature (298 K) and 155 K. The NIXSW spectra for the (3×3) -0.66ML and $c(2 \times 6)$ -0.83ML structures were taken at 155 K as they only exist at this temperature. As for the NIXSW spectra in chapter 5, the experimental noise level can

be observed on the absorption profile wings. The errors for the NIXSW- fitting parameters were obtained from the range of possible fits that acceptably matched the experimental profiles.

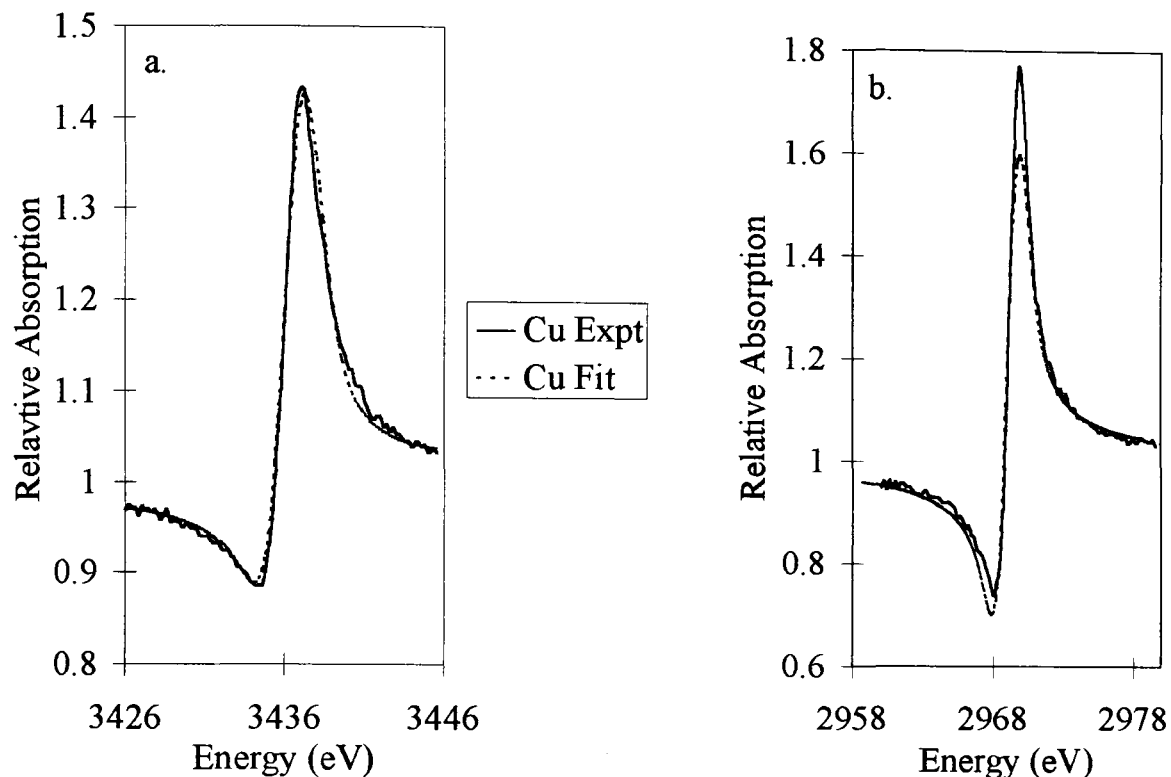


Figure 6.1. Cu(100)/Hg-c(4x4)-0.62ML structure (200) (a.) and (111) (b.) NIXSW scans and best fits for Cu ($2p_{3/2}$ photoelectron peaks) for the sample at $T = 155$ K (a.) and $T = 298$ K (b.).

6.2 The Cu(100)/Hg-c(2x2)-0.5ML Structure

For the c(2x2)-0.5ML structure two reproducible NIXSW profiles were taken for the (200) and (111) reflections at each of the two temperatures (298 K and 155 K). The observed LEED patterns were consistent with that of a c(2x2) structure. These LEED patterns were still visible after the NIXSW experiment and became sharper on cooling. The Hg:Cu peak to peak ratios of the Auger, EDC and NIXSW profiles gave an

average value of 0.54 ± 0.02 and 0.50 ± 0.05 for the 155 K and 298 K structures respectively. These values are in close agreement with the anticipated coverage of 0.50ML for the $c(2 \times 2)$ structure. Representative NIXSW results for the Cu(100)/Hg- $c(2 \times 2)$ -0.5ML structures are shown in figures 6.2. and 6.3. along with their best fits. The NIXSW spectra are identical to the other spectra and fits obtained for the $c(2 \times 2)$ -0.5ML structure. It can be seen that the spectra shown in figure 6.2. differ quite distinctly in shape indicating that the (200) and (111) spectra will produce different fitting parameters, this is also the case for the lower temperature scans (figure 6.3.).

The (200) scans for both temperatures were similar, within noise level (figure 6.2.a. and 6.3.a.). The positive excursion of both the low and room temperature data is identical at approximately 1.57. However, the NIXSW profile taken at 155 K has a lower negative excursion of 1.0 compared with that of the room temperature profile (0.98). Therefore the low temperature data would have a higher coherent fraction (approximately 0.05) than that obtained from the fit of the room temperature data.

The (111) scans at 155 K were slightly different to the room temperature scans, having a slightly larger dip on the low energy side of the scan (figure 6.3.b. shows a typical example). The positive excursion of both the low and room temperature data is again identical at approximately 1.62. Yet, the NIXSW profile taken at 298 K has a higher negative excursion of 0.90 compared with that of the low temperature profile (0.88). Again, the coherent fraction of the room temperature data would have a lower coherent fraction than that obtained from the fit of the low temperature data.

The fitting parameters obtained for the best fits of the NIXSW spectra are shown in table 6.2. These fitting parameters were again calculated as an average of the parameters obtained from the best fits of all the NIXSW profiles taken for each of the various structures at the particular temperatures studied. Two experimental spectra were taken for each structure, using both the (200) and (111) reflections at both room temperature and low temperature (155 K).

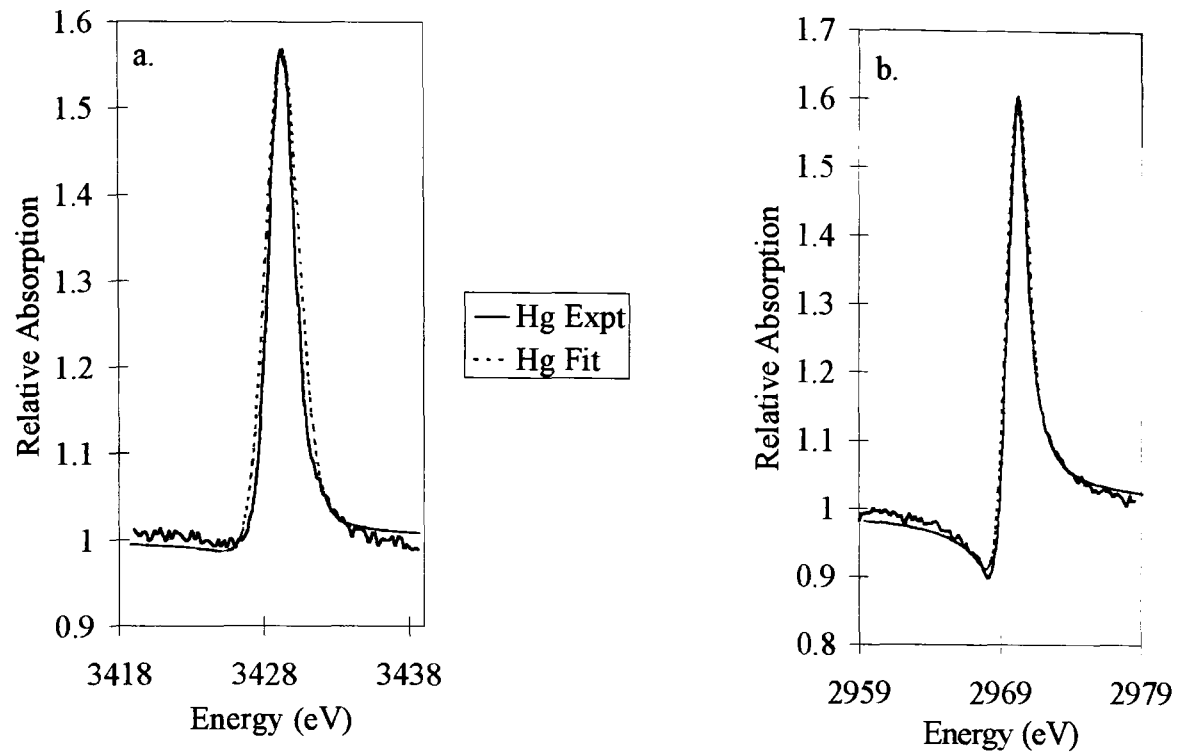


Figure 6.2. Cu(100)/Hg-c(2x2)-0.5ML structure (200) (a.) and (111) (b.) NIXSW scans and best fits for Hg (3d_{5/2} photoelectron peaks) for the sample at T = 298 K.

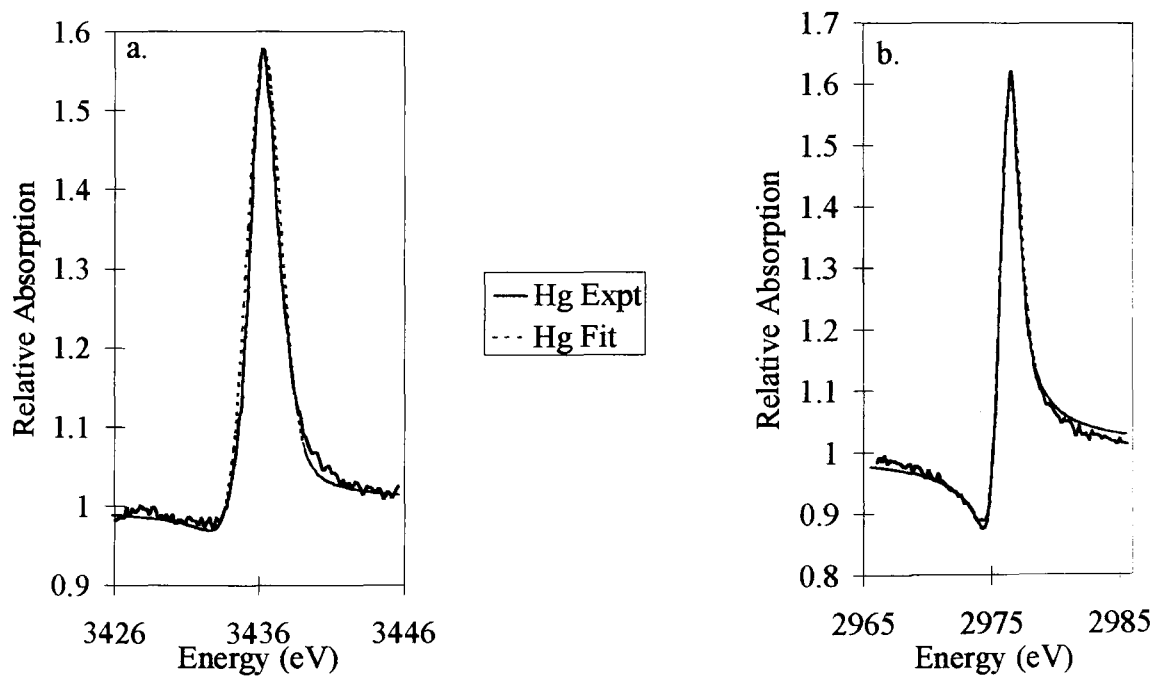


Figure 6.3. Cu(100)/Hg-c(2x2)-0.5ML structure (200) (a.) and (111) (b.) NIXSW scans and best fits for Hg (3d_{5/2} photoelectron peaks) for the sample at T = 155 K.

From table 6.2.1. it can be seen that the coherent positions agree within the error margins for both the (200) and (111) reflections taken at 155 K and 298 K. The high coherent fractions of the (200) reflection profiles at both temperatures imply a very well defined height of the adsorbate above the (200) planes. The higher coherent fraction of the low temperature data shows a possible increase in order perpendicular to the surface because of the reduction of thermal disorder due to the cooling of the sample. However, both coherent fractions for the room temperature data and low temperature data for the (200) data agree within error limits. The coherent fraction of the (111) reflection data also indicates a degree of order of the adsorbate atoms relative to the (111) planes. Again the lower temperature data having a higher coherent fraction than the room temperature data indicates a possible reduction of thermal disorder by cooling of the sample.

Reflection	Temperature	Coherent Position	Coherent Fraction
(200)	298 K	$0.388 \pm 0.020 \text{ \AA}$	0.85 ± 0.05
(200)	155 K	$0.375 \pm 0.030 \text{ \AA}$	0.90 ± 0.05
(111)	298 K	$0.200 \pm 0.040 \text{ \AA}$	0.50 ± 0.10
(111)	155 K	$0.125 \pm 0.050 \text{ \AA}$	0.60 ± 0.10

Table 6.2.1. Results of the fittings of the Hg adsorbate NIXSW profiles obtained from the (200) and (111) reflections at room temperature and 155 K for the Cu(100)/Hg-c(2x2)-0.5ML structure.

6.3 The Cu(100)/Hg-c(4x4)-0.62ML Structure

For the c(4x4)-0.5ML structure two reproducible NIXSW profiles were again taken each for the (200) and (111) reflections at the two temperatures of 298 K and 155 K. The observed LEED patterns were consistent with that of a c(4x4) structure all over the sample surface. These LEED patterns were still visible after the NIXSW experiment and also became sharper on cooling. The Hg:Cu peak to peak ratios of the Auger, EDC and NIXSW profiles gave an average value of 0.86 ± 0.23 and 0.62 ± 0.02 for the 155 K and 298 K structures respectively. These values are in close agreement with the expected coverage of 0.62ML for the c(4x4) structure. Representative NIXSW results for the Cu(100)/Hg-c(4x4)-0.62ML structures are shown in figures 6.4. and 6.5.

As for the c(2x2)-0.5ML spectra, the (200) scans for both temperatures were the same, to within noise level (figure 6.4.a. and 6.5.a.). Both the (200) profiles have a negative excursion of approximately 0.99 and a positive excursion of 1.55 at the higher energy side of the profile. Consequently one can assume that the low and room temperature data would have similar coherent fractions.

The (111) scans at room temperature and 155 K were the same within the experimental noise level (figures 6.4.b. and 6.3.b. show typical examples). Both (111) profiles have a negative excursion (also at the lower energy side of the positive excursion) of approximately 0.90 along with a positive excursion of approximately 1.66. From this

one can once more assume that the coherent fraction of both the low and room temperature data would have identical coherent fractions.

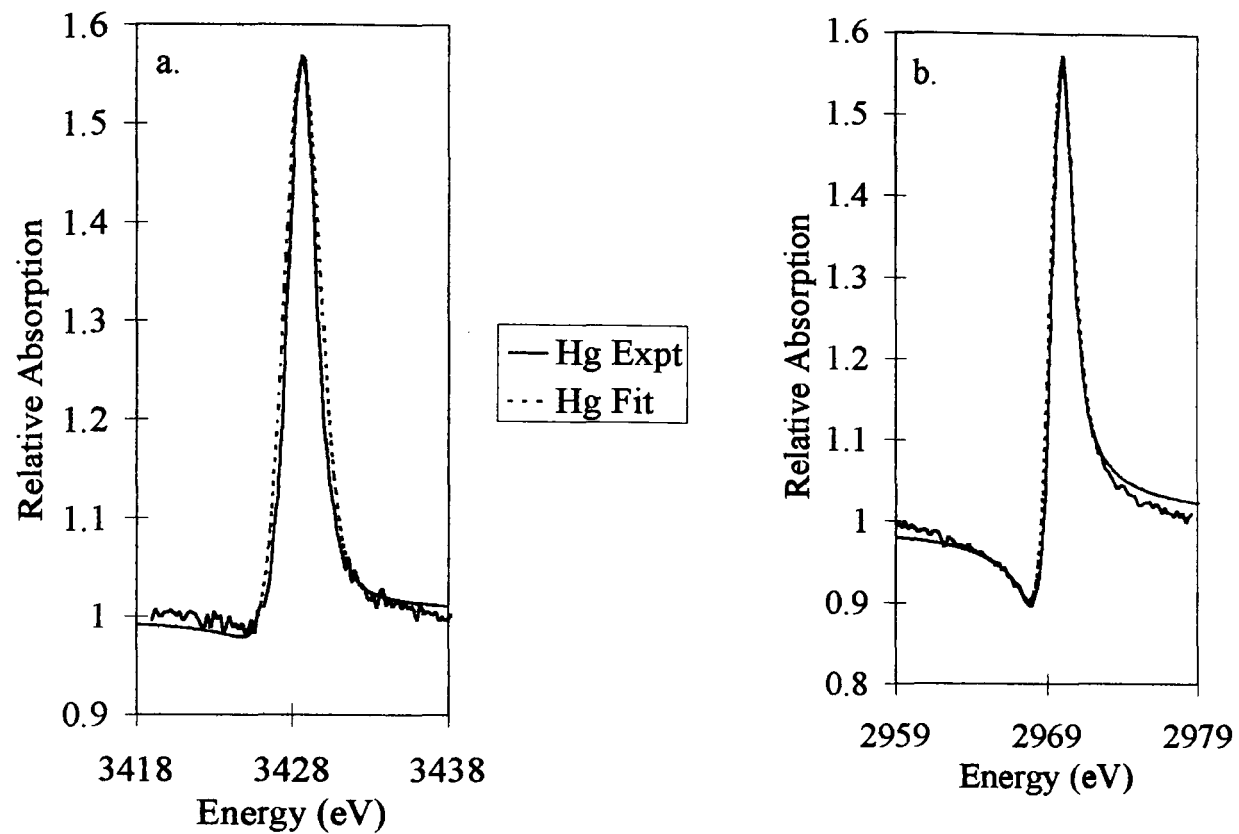


Figure 6.4. Cu(100)/Hg-c(4x4)-0.62ML structure (200) (a.) and (111) (b.) NIXSW scans and best fits for Hg (3d_{5/2} photoelectron peaks) for the sample at T = 298 K.

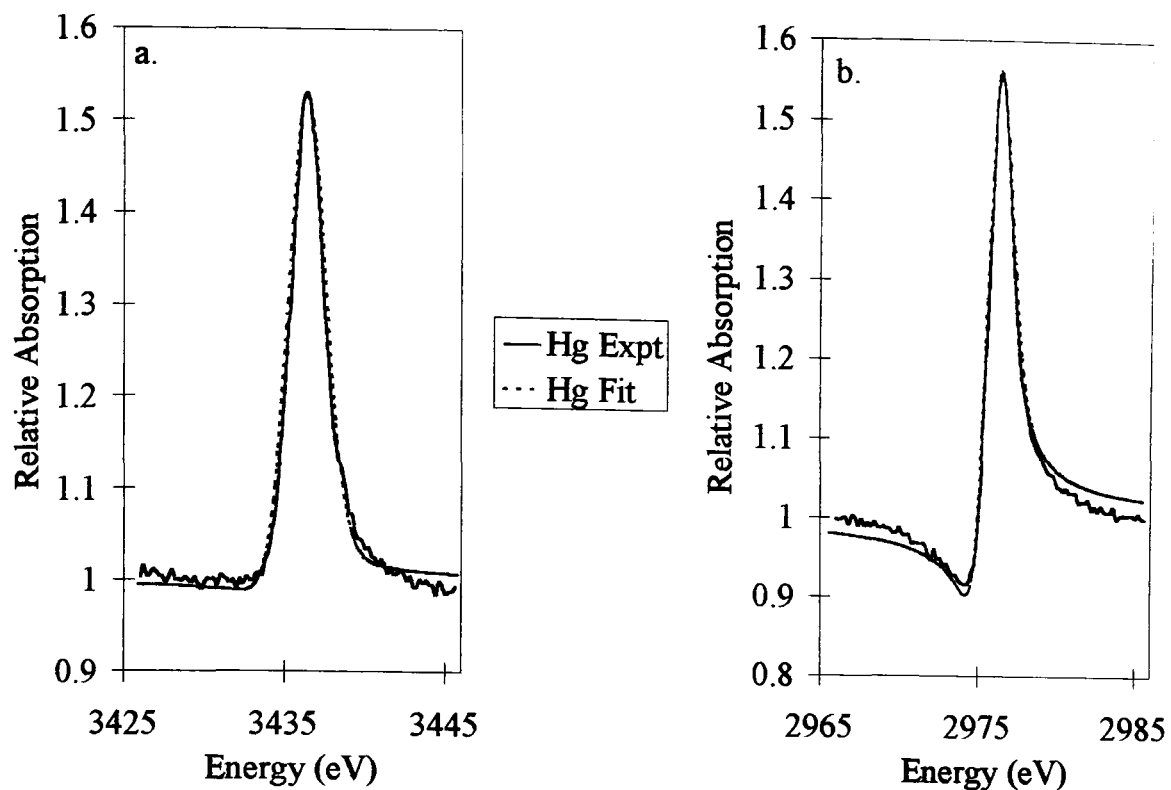


Figure 6.5. Cu(100)/Hg-c(4x4)-0.62ML structure (200) (a.) and (111) (b.) NIXSW scans and best fits for Hg ($3d_{5/2}$ photoelectron peaks) for the sample at $T = 155$ K.

Both the (200) and (111) room temperature spectra are also of a similar size and shape to those of the c(2x2)-0.5ML room temperature spectra (with the c(2x2) (111) profile having a slightly larger positive excursion than the c(4x4) profile). It can therefore be expected that these spectra will provide similar fitting parameters. Also the NIXSW profiles taken at lower temperatures (both (200) and (111) profiles) have a similar shape to those of the c(2x2)-0.5ML NIXSW profiles, but the positive and negative excursions are smaller in the c(2x2)-0.5ML profiles, thus indicating similar, but slightly different fitting parameters for these spectra.

The results of these fits are shown in table 6.3.1. The coherent positions obtained from the fits of the (200) NIXSW profiles taken at 155 K and 298 K agree within experimental error margins. The coherent positions for the (111) profiles also agree within error margins for the two temperatures. Likewise, the coherent fractions for the (200) reflection at 155 K and 298 K agree. The high coherent fractions of the (200) reflection profiles at both temperatures imply a very well defined height of the adsorbate above the (200) planes. The coherent fractions of the (111) reflection profiles imply quite a well-ordered surface with respect to the (111) planes, but this order is less than that of the (200) reflection planes.

Reflection	Temperature	Coherent Position	Coherent Fraction
(200)	298 K	$0.388 \pm 0.020 \text{ \AA}$	0.80 ± 0.04
(200)	155 K	$0.425 \pm 0.030 \text{ \AA}$	0.75 ± 0.05
(111)	298 K	$0.175 \pm 0.040 \text{ \AA}$	0.50 ± 0.10
(111)	155 K	$0.125 \pm 0.050 \text{ \AA}$	0.50 ± 0.10

Table 6.3.1. Results of the fittings of the Hg adsorbate NIXSW profiles obtained from the (200) and (111) reflections at room temperature and 155 K for the Cu(100)/Hg-c(4x4)-0.62ML structure.

6.4 The Cu(100)/Hg-(3x3)-0.66ML Structure

For the (3x3)-0.66ML structure two reproducible NIXSW profiles were again taken each for the (200) and (111) reflections at 155 K. The observed LEED patterns still visible after the NIXSW experiment and were consistent with that of a (3x3) structure. The Hg:Cu peak to peak ratios of the Auger, EDC and NIXSW profiles gave an average value of 0.59 ± 0.11 , which closely agrees with the predicted coverage of 0.66ML for the (3x3) structure. Representative NIXSW results for the Cu(100)/Hg-(3x3)-0.66ML structures are shown in figure 6.6.

The (3x3)-0.66ML low temperature (200) NIXSW profile has a positive excursion of 1.58 and a negative excursion of 0.98 on the lower energy side of the scan. The (200) low temperature spectra are identical to those of the c(2x2)-0.5ML and c(4x4)-0.62ML low temperature (200) profiles. Consequently the fitting parameters for the (3x3)-0.66ML NIXSW scans are expected to be identical to those for the c(2x2)-0.5ML and c(4x4)-0.62ML profiles.

The (3x3)-0.66ML (111) NIXSW profile is of similar shape to those of both the c(2x2)-0.5ML and c(4x4)-0.62ML spectra. However, the (3x3) profile for the (111) reflection has positive and negative excursions of 1.59 and 0.9 respectively. They are therefore of similar magnitude to the positive and negative excursions of the (111) reflection c(4x4)-0.62ML spectra taken at 155 K, and slightly different to those of the (111) reflection c(2x2)-0.5ML spectra. Hence, it would be expected that the fitting

parameters of the (3x3)-0.66ML NIXSW profiles would be more like those of the c(4x4)-0.62ML spectra than the c(2x2)-0.5ML spectra.

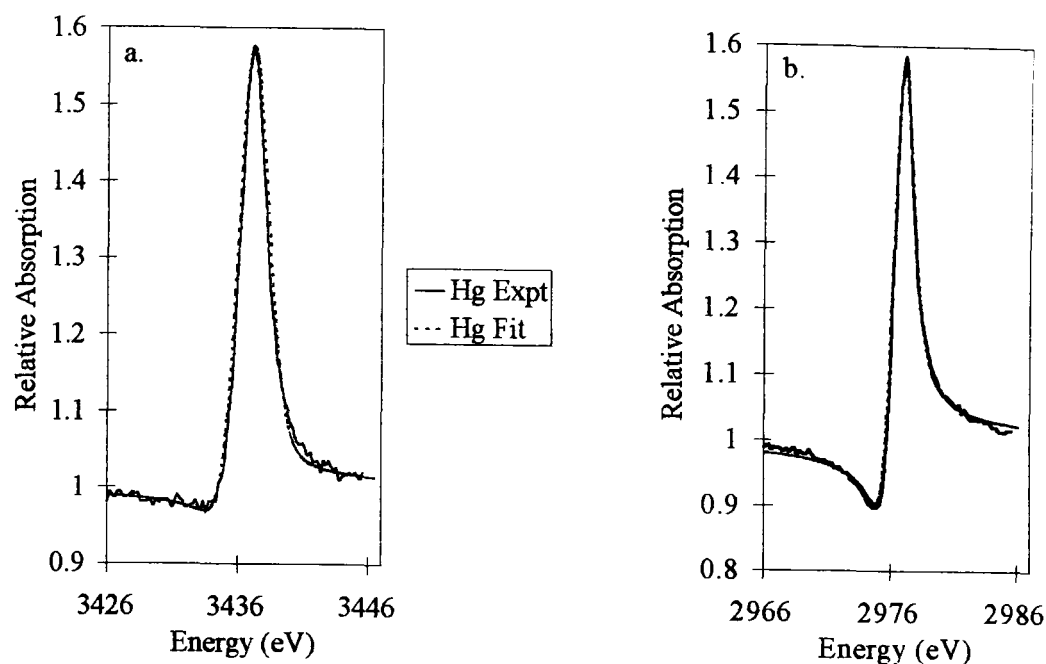


Figure 6.6. Cu(100)/Hg-(3x3)-0.66ML structure (200) (a.) and (111) (b.) NIXSW scans and best fits for Hg ($3d_{5/2}$ photoelectron peaks) for the sample at $T = 155$ K.

The results of the above NIXSW fits are shown in table 6.4.1. The high coherent fraction of the (200) reflection profiles implies a very well defined height of the adsorbate above the (200) planes. The coherent fraction of the (111) reflection profile implies a well-ordered surface with respect to the (111) planes, but this order is not as good as that of the (200) reflection planes.

Reflection	Temperature	Coherent Position	Coherent Fraction
(200)	155 K	$0.375 \pm 0.025 \text{ \AA}$	0.90 ± 0.05
(111)	155 K	$0.150 \pm 0.035 \text{ \AA}$	0.55 ± 0.07

Table 6.4.1. Results of the fittings of the Hg adsorbate NIXSW profiles obtained from the (200) and (111) reflections at 155 K for the Cu(100)/Hg-(3x3)-0.66ML structure.

6.5 The Cu(100)/Hg-c(2x6)-0.83ML Structure

For the c(2x6)-0.83ML structure two reproducible NIXSW profiles were again taken for the (200) and (111) reflections at 155 K as they only exist at such a low temperature. The Hg:Cu peak to peak ratios of the Auger, EDC and NIXSW profiles gave an average value of 1.70 ± 0.26 . The anticipated coverage for the c(2x6) structure is 0.83ML, consequently there appears to be evidence of multilayer formation. The observed LEED patterns were consistent with that of a c(2x6) structure all over the sample surface and were still visible after the NIXSW experiment. Therefore there is also evidence of a c(2x6) structure on the copper surface. Representative NIXSW results for the Cu(100)/Hg-c(2x6)-0.83ML structures are shown in figure 6.7.

Both the low temperature NIXSW profiles for the (200) and (111) structures are noticeably different from those presented in the previous sections. The (200) NIXSW scan has an almost Gaussian profile with a positive excursion of approximately 1.42 and almost no negative excursion. The (111) NIXSW profile is still almost Gaussian in shape with a positive excursion of 1.46 and a slight negative excursion (0.99) on the lower energy side of the scan. It should be noted that a Gaussian NIXSW profile indicates a coherent fraction of zero and therefore complete disorder for the particular reflection being used. All the NIXSW spectra for the previous structure have negative excursions of at most 0.98, whereas a “Gaussian” NIXSW profile has no negative excursion on either side of the profile’s positive excursion.

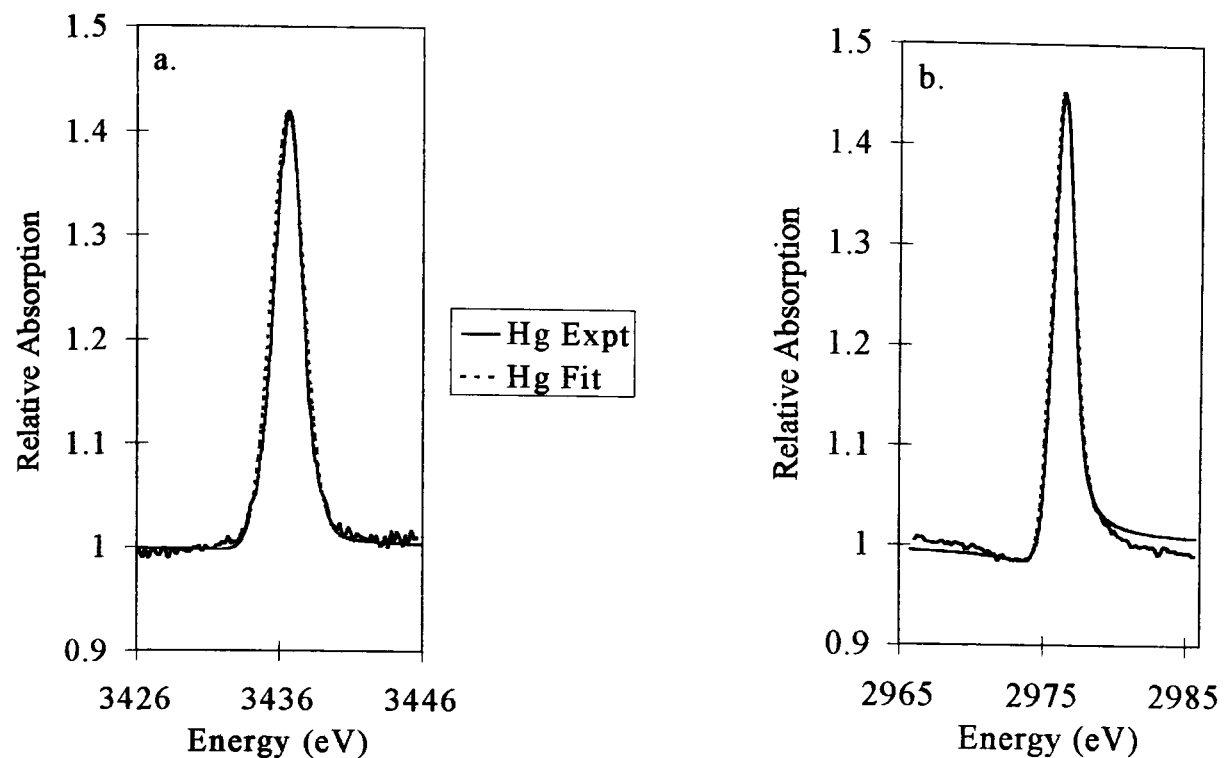


Figure 6.7. Cu(100)/Hg-c(2x6)-0.5ML structure (200) (a.) and (111) (b.) NIXSW scans and best fits for Hg ($3d_{5/2}$ photoelectron peaks) for the sample at $T = 155$ K.

The results of the above NIXSW fits are shown in table 6.5.1. The low coherent fractions of both the (200) and (111) reflection profiles imply a poorly defined height of the adsorbate above the (200) and (111) planes. Such a poorly defined adsorbate height would be consistent with multilayer formation.

Reflection	Temperature	Coherent Position	Coherent Fraction
(200)	155 K	$0.450 \pm 0.025 \text{ \AA}$	0.39 ± 0.10
(111)	155 K	$0.150 \pm 0.050 \text{ \AA}$	0.25 ± 0.15

Table 6.5.1. Results of the fittings of the Hg adsorbate NIXSW profiles obtained from the (200) and (111) reflections at 155 K for the Cu(100)/Hg-c(2x6)-0.83ML structure.

6.6 Summary of the Hg/Cu(100) Structure Results

As described previously in chapter 4, the coherent position is given as the height above the extended scatterer planes, plus an integral number of layer spacings appropriate to the adsorbate-substrate bond distance. These values are compiled in table 6.6.1. The errors for each adsorbate height are with respect to the relevant reflecting planes, and were determined by observing the quality of the fits for various displacements of the adsorbates.

The separation of the mercury and copper atoms can be calculated using the copper metallic (1.28 Å) and mercury atomic (1.48 Å) radii (MacGillavry 1968), thus giving a Hg-Cu bond length equal to 2.76 Å. If the mercury atoms were to adsorb at the separation, Δd (Å), for the (200) reflection distance, this would lead to an unreasonably small Hg-Cu bond distance compared with the Hg-Cu separation of 2.76 Å. Therefore the mercury adsorbate atoms must be positioned at a distance, $(\Delta d + d_{200})$ (Å) from the (200) reflection planes. Similarly, the mercury atoms must be located at a distance of $(\Delta d + d_{111})$ (Å) from the (111) reflection planes as a adsorbate height of (Δd) (Å) created an unfeasibly small Hg-Cu bond length. The (200) layer spacing, d_{200} is 1.8075 Å and the (111) layer spacing, d_{111} is 2.083 Å.

From table 6.6.1. it can be seen that the fits for both the c(2x2)-0.5ML, c(4x4)-0.62ML and (3x3)-0.66ML structures gave an adsorbate height of ≈ 2.20 Å above the (200) planes. The coherent fraction of ≈ 0.85 for the c(2x2)-0.5ML fits is slightly higher than that of ≈ 0.75 for the less densely packed c(4x4)-0.62ML. The adsorbate height of ≈ 2.26 Å above the (200) planes for the c(2x6)-0.83ML structure is slightly higher, but within error limits, than those for the previous structures. The coherent fraction of ≈ 0.39 for the c(2x6)-0.83ML structure in the [200] direction is somewhat different to those of all the previous structures.

Structure	(200)	Reflection	(111)	Reflection	Temp (K)
	$\Delta d + 1.8075$ (Å)	f_c	$\Delta d + 2.083$ (Å)	f_c	
c(2x2)-0.5ML	2.183 ± 0.030	0.90 ± 0.05	2.208 ± 0.050	0.60 ± 0.10	155
	2.196 ± 0.020	0.85 ± 0.05	2.283 ± 0.040	0.50 ± 0.10	298
c(4x4)-0.62ML	2.233 ± 0.030	0.75 ± 0.05	2.208 ± 0.050	0.50 ± 0.10	155
	2.196 ± 0.020	0.80 ± 0.04	2.233 ± 0.040	0.50 ± 0.10	298
(3x3)-0.66ML	2.183 ± 0.025	0.90 ± 0.05	2.233 ± 0.035	0.55 ± 0.07	155
c(2x6)-0.83ML	2.258 ± 0.025	0.39 ± 0.03	2.458 ± 0.050	0.25 ± 0.15	155

Table 6.6.1. Summary of the experimentally determined coherent positions ($\Delta d + d_{hkl}$) and coherent fractions (f_c) for the Hg adsorbate NIXSW profiles obtained from the (200) and (111) reflections for the Cu(100)/Hg structures.

As for the (200) reflection scans, the (3x3)-0.66ML structure gave a similar coherent position ($\approx 2.18 \text{ \AA}$), and coherent fraction (≈ 0.55) to the c(2x2), and c(4x4) fitting parameters ($\approx 2.24 \text{ \AA}$ and ≈ 0.55 respectively) for the (111) reflection. Additionally, the (111) fitting parameters of $\approx 2.46 \text{ \AA}$ for the coherent position, and ≈ 0.20 for the coherent fraction of the c(2x6)-0.83ML structure are dissimilar to those of the other structures.

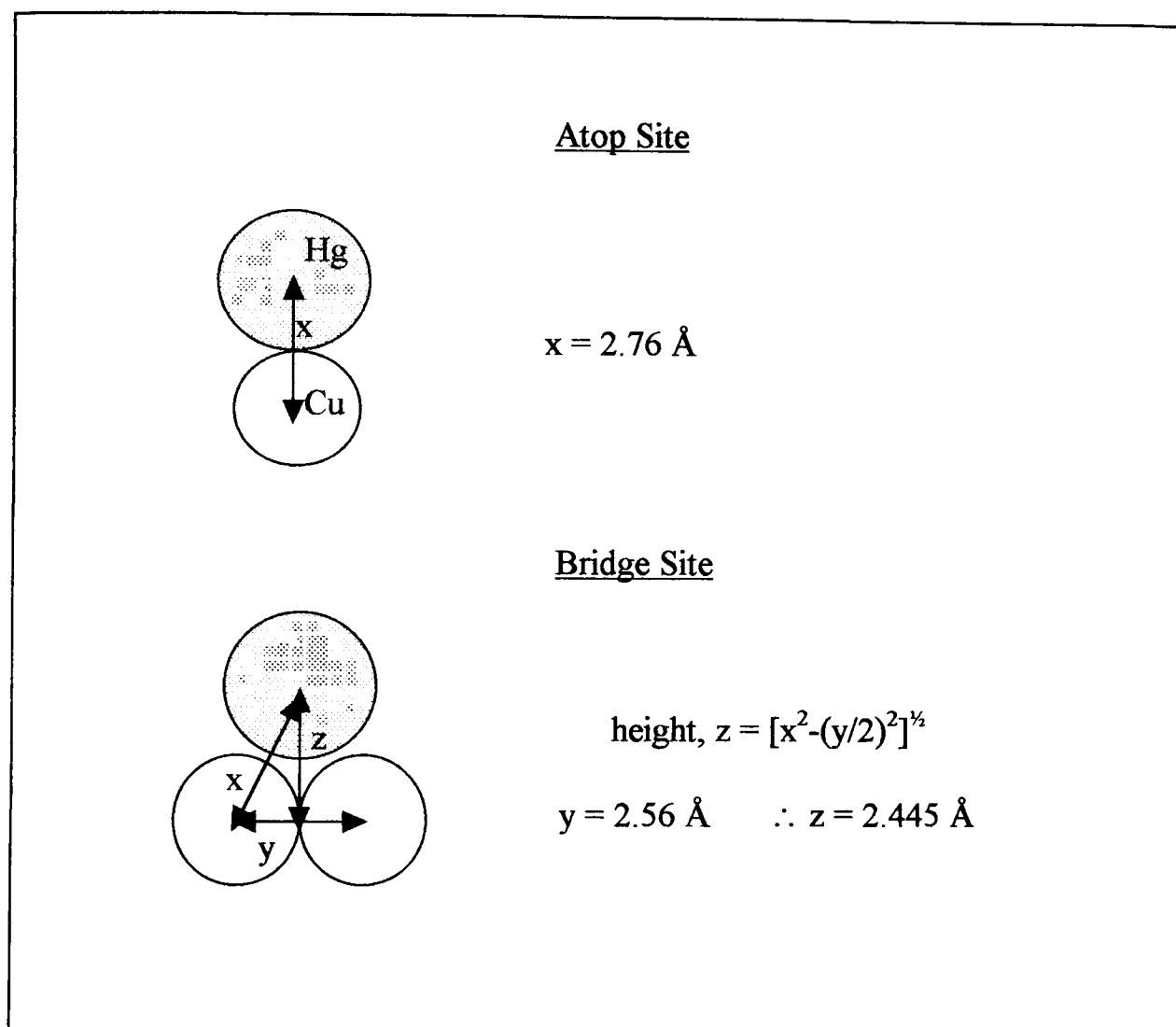
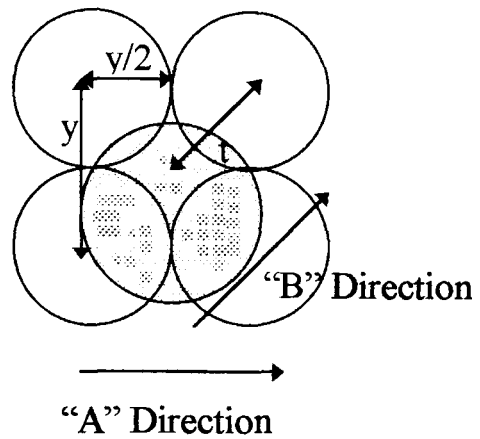


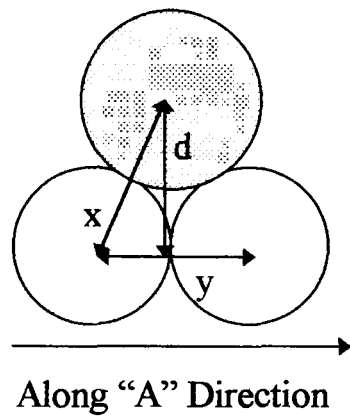
Figure 6.8. A schematic diagram showing how the theoretical (200) reflection adsorbate heights for the atop and bridge sites were calculated.

Four-fold Hollow Site



$$t = [(y/2)^2 + (y/2)^2]^{1/2}$$

$$y = 2.56 \text{ \AA} \therefore t = 1.810$$



$$x = \text{Hg-Cu distance} = 2.76 \text{ \AA (from atop)}$$

$$\therefore f = [s^2 - t^2]^{1/2}$$

$$\therefore f = 2.083 \text{ \AA}$$

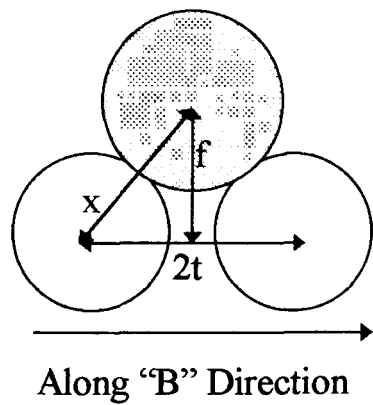


Figure 6.9. A schematic diagram showing how the theoretical (200) reflection adsorbate height for the four-fold hollow site was calculated.

The coherent fractions for the quite open Cu(100) substrate NIXSW profiles are consistently higher than those for the flatter, more densely packed Ni(111) surface, as one would have expected purely from the corrugation of the surface. Using the copper metallic (1.28 Å) and mercury atomic (1.48 Å) radii (MacGillavry 1968), one can calculate the layer spacing expected for mercury adsorption in the atop, 2-fold bridge and 4-fold hollow sites (figures 6.8. and 6.9.) on Cu(100) (see table 6.6.2.). The copper metallic radius is 1.28 Å, therefore the Cu-Cu bond length is assumed to be 2.56 Å.

Adsorption Site	(200) Reflection		(111) Reflection	
	Δd (Å)	$\Delta d + d_{200}$ (Å)	Δd (Å)	$\Delta d + d_{111}$ (Å)
atop	0.953	2.761	1.594	3.677
2-fold bridge (a)	0.638	2.446	1.412	3.495
2-fold bridge (b)	0.638	2.446	0.368	2.451
4-fold hollow	0.276	2.084	0.159	2.246

Table 6.6.2. Calculated heights of mercury above the (200) and (111) planes for a fixed Cu-Hg bond distance of 2.76 Å. The (200) layer spacing, $d_{200} = 1.8075$ Å and the (111) layer spacing, $d_{111} = 2.083$ Å. The mercury atomic radius (1.48 Å) and copper metallic radius (1.28 Å) values were used (MacGillavry 1968).

The 155 K and 298 K (200) reflection profiles for the c(2x2)-0.5ML and c(4x4)-0.62ML structures gave coherent positions of approximately 2.2 Å which is halfway between the adsorption heights for 2-fold bridge site or four-fold hollow site adsorption. The 155 K (200) reflection coherent positions obtained for the (3x3)-0.66ML (2.19 Å) and c(2x6)-0.83ML (2.26 Å) structures are also halfway between the adsorption heights for 2-fold bridge site or four-fold hollow site adsorption. The high coherent fractions obtained from the fits of the (200) NIXSW profiles for the c(2x2)-0.5ML, c(4x4)-0.62ML and (3x3)-0.66ML structures indicate that single site adsorption is occurring. This single site adsorption would be consistent with adsorption of the mercury atoms into four-fold hollow sites. However, the coherent fraction obtained from the fit of the (200) NIXSW profile for the c(2x6)-0.83ML structure is comparatively small (≈ 0.388). Such a low coherent fraction would be inconsistent with single site adsorption and would be indicative of some static or dynamic disorder of the adsorbate adlayer with respect to the (200) planes.

The 155 K and 298 K (111) reflection profiles for the c(2x2)-0.5ML and c(4x4)-0.62ML structures gave coherent positions of approximately 2.23 Å. This adsorbate height above the (111) planes is very close to that of adsorption in a four-fold hollow site (2.246 Å). The 155 K (111) reflection coherent positions obtained for the (3x3)-0.66ML (2.18 Å) is also close to the height consistent with four-fold hollow site adsorption. The relatively high coherent fractions obtained from the fits of the (111) NIXSW profiles for the c(2x2)-0.5ML, c(4x4)-0.62ML and (3x3)-0.66ML structures also indicate that single site adsorption could be occurring. This single site adsorption

would be consistent with adsorption of the mercury atoms into four-fold hollow sites, as for the (200) reflection data for these structures.

The adsorbate height above the (111) planes found for the $c(2 \times 6)$ -0.83ML ($\approx 2.46 \text{ \AA}$) indicates that the mercury atoms could be residing in either the bridge (case b) or the four-fold hollow site. However, the coherent fraction obtained from the fit of the (111) NIXSW profile for the $c(2 \times 6)$ -0.83ML structure is also relatively small (≈ 0.20). This low coherent fraction would also be inconsistent with single site adsorption. We would therefore expect some static or dynamic disorder of the adsorbate adlayer with respect to the (111) planes. Such disorder could be an indication of multilayer formation which will be discussed further in chapter 7.

Adsorption of the mercury atoms into four-fold hollow sites for the $c(2 \times 2)$ -0.5ML, $c(4 \times 4)$ -0.62ML and (3×3) -0.66ML structures has been proposed in previous studies of the Hg/Cu(100) adsorption system (Dowben et al. 1991, Li, W. et al. 1991a and 1992 and Kime et al. 1992). The above ideas will be discussed along with other possibilities in chapter 7.

7 Mercury Adsorption on Cu(100) Discussion

As for the mercury adsorption structures formed on Ni(111), there are two types of mercury adsorption on the Cu(100) surface. We have studied the equilibrium $c(2 \times 2)$ - 0.50ML and $c(4 \times 4)$ - 0.62ML structures, along with the non-equilibrium (3×3) - 0.66ML and $c(2 \times 6)$ - 0.83ML structures. Both structures are also described in Onellion et al. 1987, Hutchings et al. 1990, Varma et al. 1990, Dowben et al. 1990a. and 1990b., Vidali et al. 1990, Dowben et al. 1991, Li et al. 1991a. and 1991b., Vidali et al. 1991, Kime et al. 1992, Moses et al. 1992 and Li et al. 1992a.. The (200) reflection was used as the (100) reflection is forbidden.

The Argand diagram analysis method (Woodruff et al. 1994) outlined in chapters 2 and 5 and below (described in detail in section 2.1.3.) was again the technique used to analyse our NIXSW data. The fitting parameters obtained from each NIXSW scan, f_c (coherent fraction) and Δd (coherent position) can be represented as vectors on an Argand diagram. The length of the vector represents the coherent fraction, f_c and the angle of the vector measured anti-clockwise from the positive real axis represents the value $2\pi\Delta d/d_{hkl}$, where Δd is the coherent position (\AA) and d_{hkl} is the distance between the (hkl) reflecting planes (for the Cu(100) surface, this is the (200) and (111) layer spacing). A coherent fraction, f_c of 1.0 and a coherent position, Δd of zero (or any multiple of d_{111}) is expressed as a unit vector lying along the positive real axis.

The (111) reflections emerge at 54.73° to the (200) plane (figure 2.17.). The line of intersection of the two planes lies along the edge of the square unit mesh of the clean surface. There are four (111) type reflections emerging from the (100) surface corresponding to the four sides of the clean surface unit mesh. The angle that the (111) planes make to the sample surface (54.73°) ensures that there is a relatively large component of the Δd values (which are 35.27° to the surface, figure 2.17.) parallel to the surface. The measured (200) layer spacing can be used to calculate the anticipated (111) layer spacing for each of the different high symmetry adsorption sites.

A single layer spacing relative to the (111) planes only occurs for those adsorption sites which retain the full four-fold symmetry of the substrate, these are the four-fold hollow site and the atop site. Once the symmetrically equivalent sites created by the substrate (with four-fold symmetry) have been taken into account, any adsorption site having less than four-fold rotational symmetry (Hollas 1992) will lead to two or more different (111) layer spacings (Woodruff et al. 1994). An experimental (111) adsorption profile produced by adsorption sites with less than 4-fold rotational symmetry would yield a very low coherent fraction (typically 0.5 or less) or would not be fitted by a single layer spacing. The two-fold bridge sites have a lower symmetry and consequently two different layer spacings with respect to the (111) planes (figure 2.18.). As seen in section 2.1.3.2. one bridge site (type a) has the same theoretical (111) layer spacing as the atop site and a weighting of half of all the bridge sites. In reality, the type “a” bridge site has a different (111) adsorption height to the atop site, as the (200) adsorption heights for the atop and bridge sites (from which the

theoretical (111) can be derived) are different. The other bridge site (type b) has an entirely different (111) layer spacing to the type “b” site with a weighting of half the bridge sites. A combination of these bridge sites equally populated and measured using the (111) planes will yield a Gaussian NIXSW spectrum with a baseline normalised to a value of 1.0. Such a Gaussian NIXSW spectrum would produce a coherent fraction, f_c , very close to zero (Woodruff et al. 1994) for the bridge sites. The two vectors in an Argand diagram for these particular sites are 180° apart from each other (Figure 7.1.). Therefore using simple vector addition, these vectors will cancel exactly. None of the NIXSW profiles obtained using the (111) reflection for any of the four Hg/Cu(100) structures studied were Gaussian in shape. Consequently, the coherent fraction obtained from fitting the experimental NIXSW spectra was not zero and thus did not indicate complete disorder in either the (200) or (111) direction. Therefore equal population of the mercury adsorbate atoms in the bridge sites can be eliminated for all four of the adsorbate structures studied in this chapter.

The coherent fractions and positions resulting from the copper substrate scans are of similar values to those expected for a well-ordered crystal surface. Therefore the adsorbate coherent fraction results can be compared with the substrate coherent fractions of 0.9 ± 0.1 .

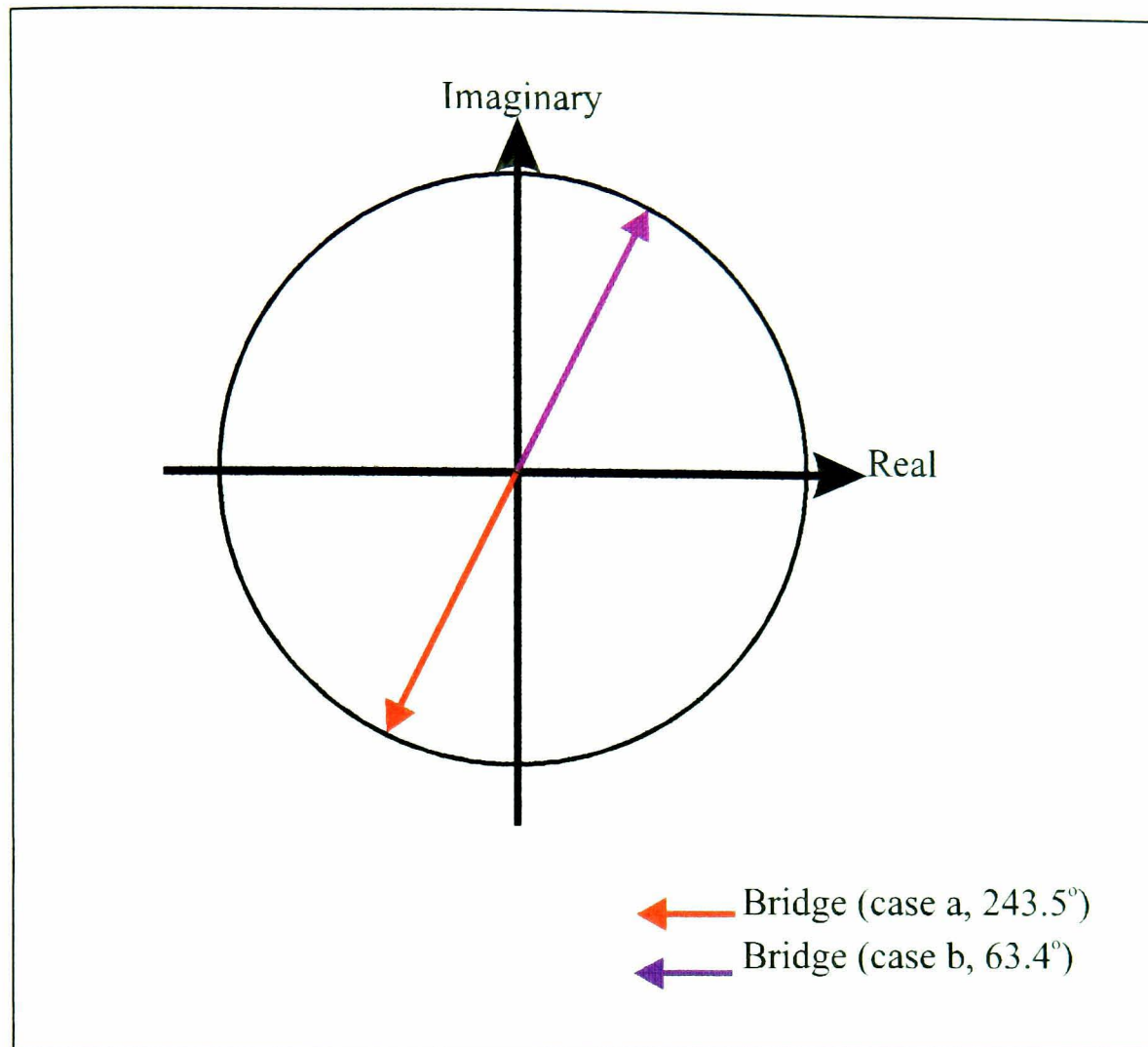


Figure 7.1. Argand vector diagram showing the vectors for the (111) reflection illustrating the theoretical vectors of the bridge (case a and b) sites. Equal weighting of these two vectors (i.e. equal population of the two bridge sites) would produce a coherent fraction of zero for a (100) surface.

The mobility of an adatom is expected to vary for different crystallographic planes of the same metal substrate (Tompkins 1978), and possibly different areas of the surface if surface heterogeneity is suspected (King and Woodruff 1983). Therefore the more close packed a surface (i.e. the smaller the corrugation), the more the adsorbate is able to migrate across the surface (Tompkins 1978). The Cu(100) surface is a more

corrugated surface compared with the closely packed Ni(111) surface studied in chapters 4 and 5. Consequently, one would expect that the adsorption of an atomic adsorbate such as mercury would be more localised on Cu(100) than on the Ni(111) surface. A previous study (Hutchings et al. 1990) has assumed that the substrate potential is strong enough to force the mercury adatoms into well defined adsorption sites, thus imposing its square symmetry onto the adsorbate overlayer. The previous studies of mercury as an adsorbate on transition metal surfaces (Ni(100) surface: Prince et al. 1989) have indicated that there is a weak corrugation in the mercury-substrate interaction energy as a function of lateral position on the surface. Therefore one would expect that this would also be the case for the Cu(100) surface (Vidali et al. 1990). The relatively low heat of adsorption ($70 \pm 4 \text{ kJ mol}^{-1}$) observed by Dowben et al. (1990b) and Kime et al. (1992) suggests that the chemisorption bond of the mercury with the Cu(100) surface is not as strong as with other substrates such as Ag(100) (Dowben et al. 1987 and Onellion et al. 1986), Fe(100) (Jones & Perry 1981), Ni(100) (Jones & Tong 1987) and W(100) (Egelhoff et al. 1976 and Jones & Perry 1978), Si(100) (Li et al. 1992) and Si(111) (Li et al. 1993).

7.1 The Cu(100)/Hg-c(2x2)-0.50ML Structure

The c(2x2)-0.50ML structure has one mercury atom per unit mesh, a maximum coverage of 0.50ML and a Hg-Hg square unit mesh dimension of 3.62 Å (Onellion et al. 1987, Dowben et al. 1990b). Two mercury atoms per unit mesh would result in unrealistically short Hg-Hg lateral distances (Donohue 1974).

The mercury atoms in the c(2x2)-0.50ML structure are at a distance of 3.62 Å apart (Onellion et al. 1987, Dowben et al. 1990b and Hutchings et al. 1990) which is greater than the Hg-Hg separation in the low pressure α -Hg form (2.99Å, Donohue 1974) possibly indicating strong lateral attractive interactions between the mercury adatoms (Dowben et al. 1990b).

The mercury atoms for the c(2x2)-0.5ML structure were placed in the more energetically favoured four-fold hollow sites (Dowben et al. 1990b) on the Cu(100) surface (figure 7.1.1.). The alternative sites available are the two types of bridge site (case a and b) and the atop site. The formation of c(2x2) structures for various other adsorbates on the (100) surfaces of single crystals has also shown single site adsorption in the four-fold hollow site (Cu(100)/Li Mizuno et al. 1993, Al(100)/Na Berndt et al. 1995, Ni(100)/Na Nielsen et al. 1994, W(100)/Ag Chen et al. 1995 and W(100)/Au Chen et al. 1995).

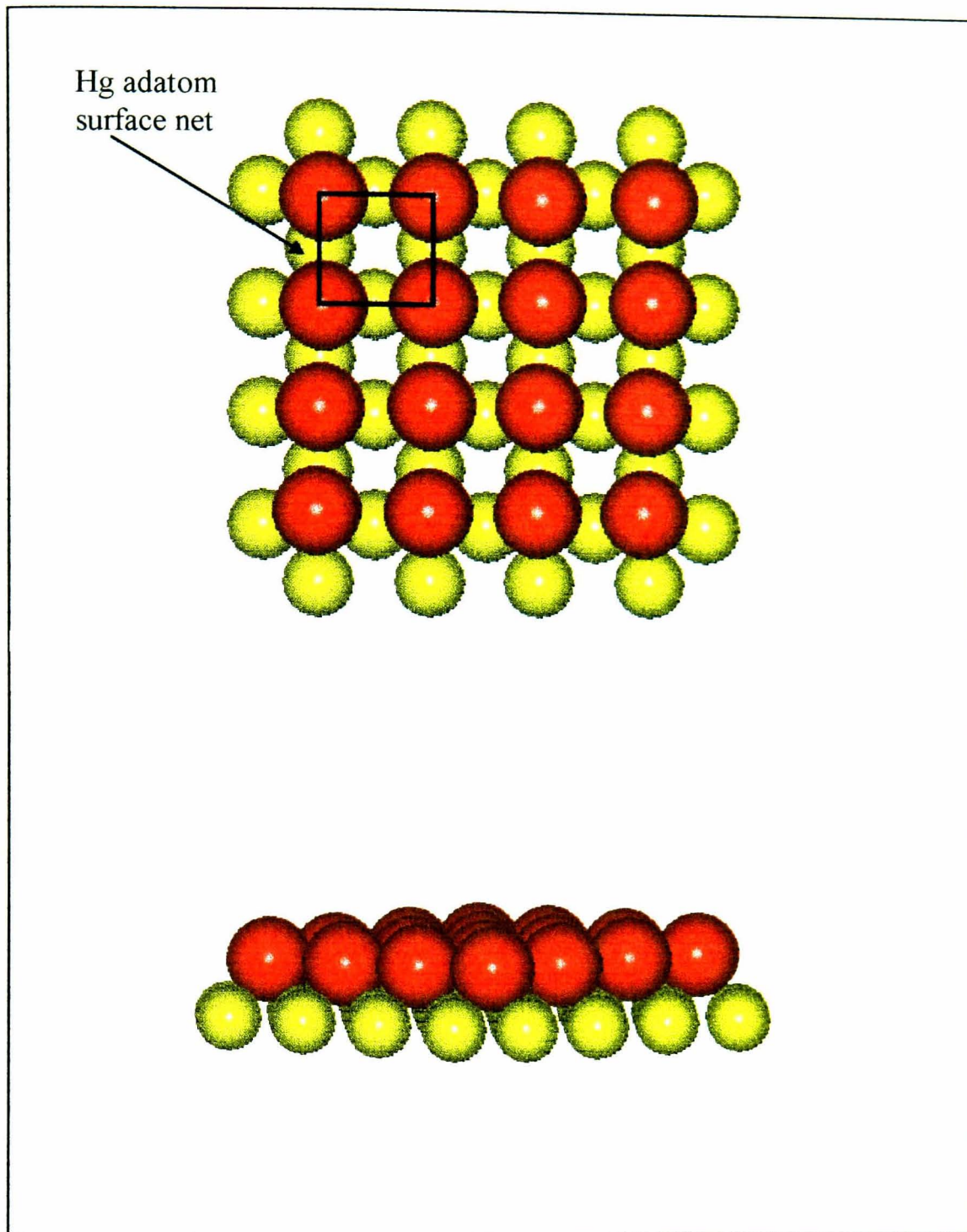


Figure 7.1.1. A schematic diagram of the possible Cu(100)-c(2x2)-Hg-0.50ML real space structure (plan and side views) containing one mercury atom per unit mesh, with the mercury atoms located in four-fold hollow sites. The mercury adatom surface net is also shown. The adlayer is not puckered in this diagram. The yellow and red atoms represent copper and mercury respectively. The diameters of the atoms are relative to each other.

7.1.1 The (200) Reflection NIXSW Data for the c(2x2) Structure

The Argand diagram representation for the theoretical adsorbate height values of the possible sites with respect to the (200) reflection planes is shown in figure 7.1.1.1. along with the vector portrayal of the experimental NIXSW values.

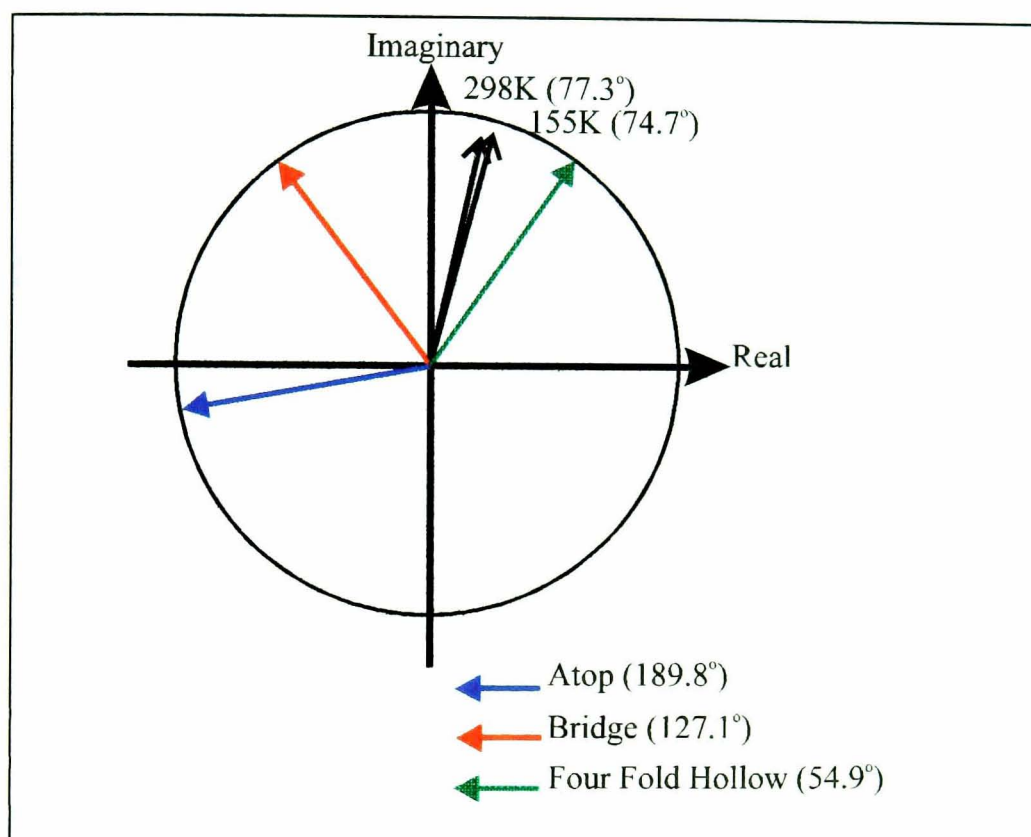


Figure 7.1.1.1. Argand vector diagram showing the vectors for the (200) reflection illustrating the theoretical vectors (coloured arrows) of the atop, bridge, four-fold hollow sites along with the experimental vectors obtained for the Cu(100)/Hg-c(2x2)-0.50ML structure at $T = 298$ K and $T = 155$ K (black arrows). The circle has a radius equivalent to a coherent fraction of 1.0.

Figure 7.1.1.1. illustrates the Argand diagram for the theoretical and experimental vectors obtained for the Cu(100)/Hg-c(2x2)-0.50ML structure with respect to the (200) reflection planes. The experimental vectors are shown with an accurate depiction of the coherent fractions for the respective vectors. The above Argand diagram illustrates that the angle of the experimental data vectors best fits the theoretical adsorption height vector for single site occupation of the four-fold hollow site. However, the theoretical angle is not within the error margins of the experimental data. Such a discrepancy may be due to thermal vibrations of the adsorbate atoms on the copper surface creating a distribution of adsorbate heights with respect to the (200) reflection planes. Furthermore, figure 7.1.1.1. shows that the vector for $T = 155$ K is closer to the real positive axis than the $T = 298$ K vector, thus indicating that the position of the mercury atoms is on average closer to the (200) reflecting planes at low temperatures. This may also be due to the thermal vibrations of the atoms at 298 K being greater than those at 155 K.

The NIXSW technique is not sensitive to the presence (or absence) of the intermediate substrate layers below the surface layer. Removing these substrate layers from the model would not change the NIXSW lineshape. However the nearest neighbour adsorbate-substrate distances for these structures are clearly distinct. A mercury atom in a four-fold hollow site is also positioned directly above copper atom in the second layer of substrate atoms. Therefore the four-fold hollow and atop sites are effectively identical. This ambiguity can be removed when one has an approximate knowledge of the adsorbate atom size and the adsorbate-substrate separation distance. The size of

the mercury and copper atoms prevents the adsorbate from being in the atop site within one substrate layer spacing above the copper surface, as this would create an unfeasibly small Hg-Cu layer spacing. The size of the mercury adatom and copper substrate atoms also dictates that the mercury adatom cannot be placed at an (200) reflection adsorbate height of Δd (1.8075 Å) as it indicates an unreasonably small Hg-Cu bond distance (Hg-Cu bond length = 2.48 Å (Vidali et al. 1990)). Therefore the mercury adatoms must be positioned at a height of $\Delta d + d_{200}$ (Å) above the (100) copper surface atoms (see figure 7.1.1.2.).

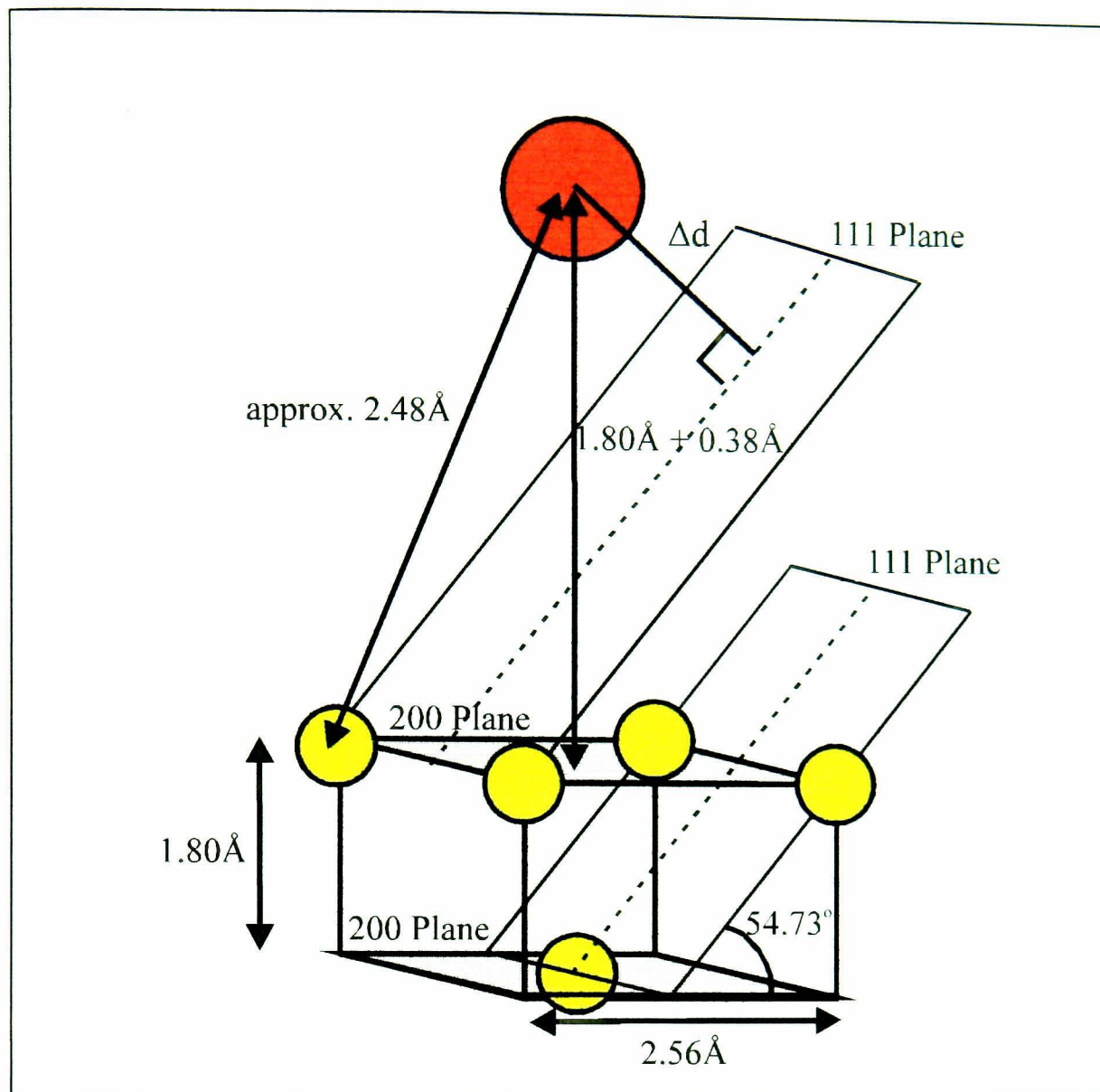


Figure 7.1.1.2. A schematic diagram (not to scale) illustrating a mercury atom sat in a four-fold hollow site directly above a copper atom in the second layer of substrate atoms. The mercury adsorbate atoms (red) and copper substrate atoms (yellow) are of arbitrary radii.

7.1.2 The (111) Reflection NIXSW Data for the c(2x2) Structure

The mercury adatoms must be positioned at a (111) adsorbate height of Δd (Å) as an adsorbate height of $\Delta d + d_{111}$ (2.083 Å) would also produce an unfeasibly large Hg-Cu bond distance compared with the Hg-Cu bond length (2.48 Å, Vidali et al. 1990).

Figure 7.1.2.1. illustrates the Argand diagram for the experimental Cu(100)/Hg-c(2x2)-0.5ML structure at $T = 298$ K and $T = 155$ K with an accurate depiction of the coherent fractions for the respective vectors for the (111) reflection. The comparatively high coherent fraction (0.50 ± 0.10) of the room temperature data implies high degree of order in the adsorbate heights relative to the (111) reflecting planes. The marginally higher coherent fraction of the low temperature data (0.60 ± 0.10) could be due to a reduction in the thermal motion perpendicular to the (111) reflecting planes as the mercury surface structure is “frozen” into sites on the Cu(100) surface. However, the coherent fractions obtained for the (200) reflection are too similar to substantiate this “freezing” of mercury atoms into sites on the Cu(100) surface. The experimental vectors shown in the Argand diagram in figure 7.1.4. also supports mercury adsorption in the four-fold hollow sites on the Cu(100) surface (as shown in figure 7.1.1.). Especially as bridge site adsorption has already been eliminated because the Gaussian NIXSW profile producing a coherent fraction of zero was not seen for the c(2x2)-0.50ML structure. The lower coherent fraction of the (111)

NIXSW profiles compared with that of the (200) profiles could be due to thermal vibrations parallel to the surface (dynamic disorder).

The coherent fractions for the (200) reflection (0.9 ± 0.1) and (111) reflections (0.6 ± 0.1) are very high, thus indicating single site adsorption. The adsorbate heights and high coherent fractions obtained from NIXSW profiles for both reflections can therefore be reconciled with mercury adsorption in the four-fold hollow site (as shown in figure 7.1.1.) of the Cu(100) crystal for the $c(2 \times 2)$ -0.50ML structure.

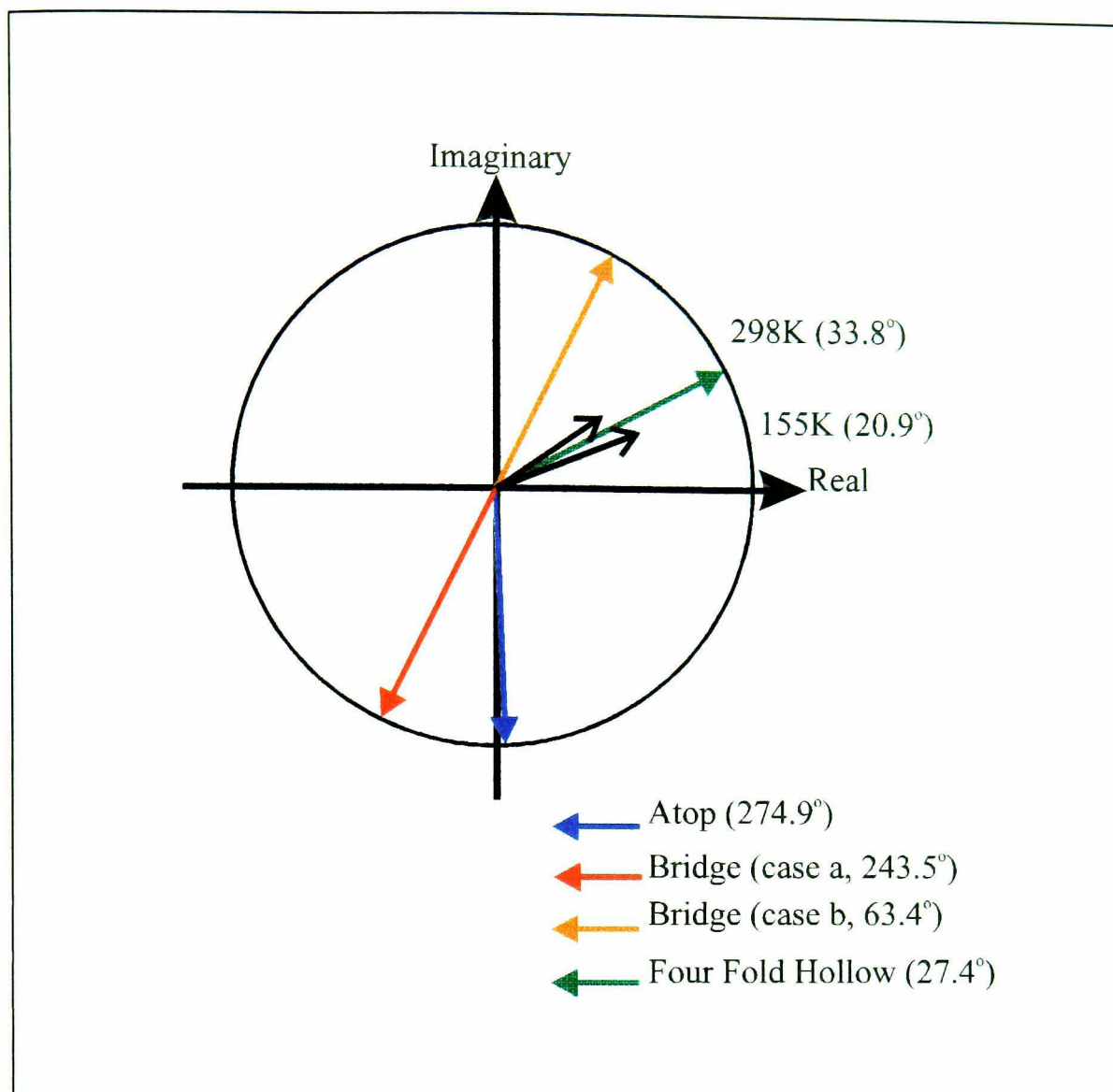


Figure 7.1.2.1. Argand vector diagram for the (111) reflection illustrating the theoretical vectors (coloured arrows) of the atop, bridge (case a. and b.), four-fold hollow sites along with the experimental vectors obtained for the Cu(100)/Hg-c(2x2)-0.50ML structure at $T = 298$ K and $T = 155$ K (black arrows). The circle radius is equivalent to a coherent fraction of 1.0.

7.2 The Cu(100)/Hg-c(4x4)-0.62ML Structure

The peak to peak height ratios of the mercury and copper XPS peaks (0.86 ± 0.23 for 155 K and 0.62 ± 0.02 for 298 K) for the c(4x4)-0.62ML structure are greater than those for the c(2x2)-0.50ML structure (0.54 ± 0.02 for 155 K and 0.50 ± 0.05 for 298 K), thus indicating a higher coverage than the c(2x2)-0.50ML structure. Hutchings et al. (1990) indicated that the c(2x2) and c(4x4) structures were able to coexist. However, we are confident that the LEED patterns and coverages (from peak to peak ratios detailed above) observed indicated only a c(4x4)-0.62ML structure on the copper surface.

Figure 7.2.1. shows an Argand diagram illustrating the theoretical vectors for single site adsorption in atop, bridge and four-fold hollow sites, along with the experimental NIXSW values obtained for the (200) reflection. Clearly, the angle (i.e. the coherent position) of the four-fold hollow site vector (54.9°) is close to that of the experimental vectors obtained for both temperatures ($84.7^\circ \pm 6^\circ$ for 155 K and $77.3^\circ \pm 4^\circ$ for 298 K), but not within the error margins. In fact the room temperature vector is halfway between the bridge (127°) and four-fold hollow (54.9°) vectors. The high coherent fraction for the (200) reflection data also indicates a high degree of order in the adsorbate heights above the (200) planes.

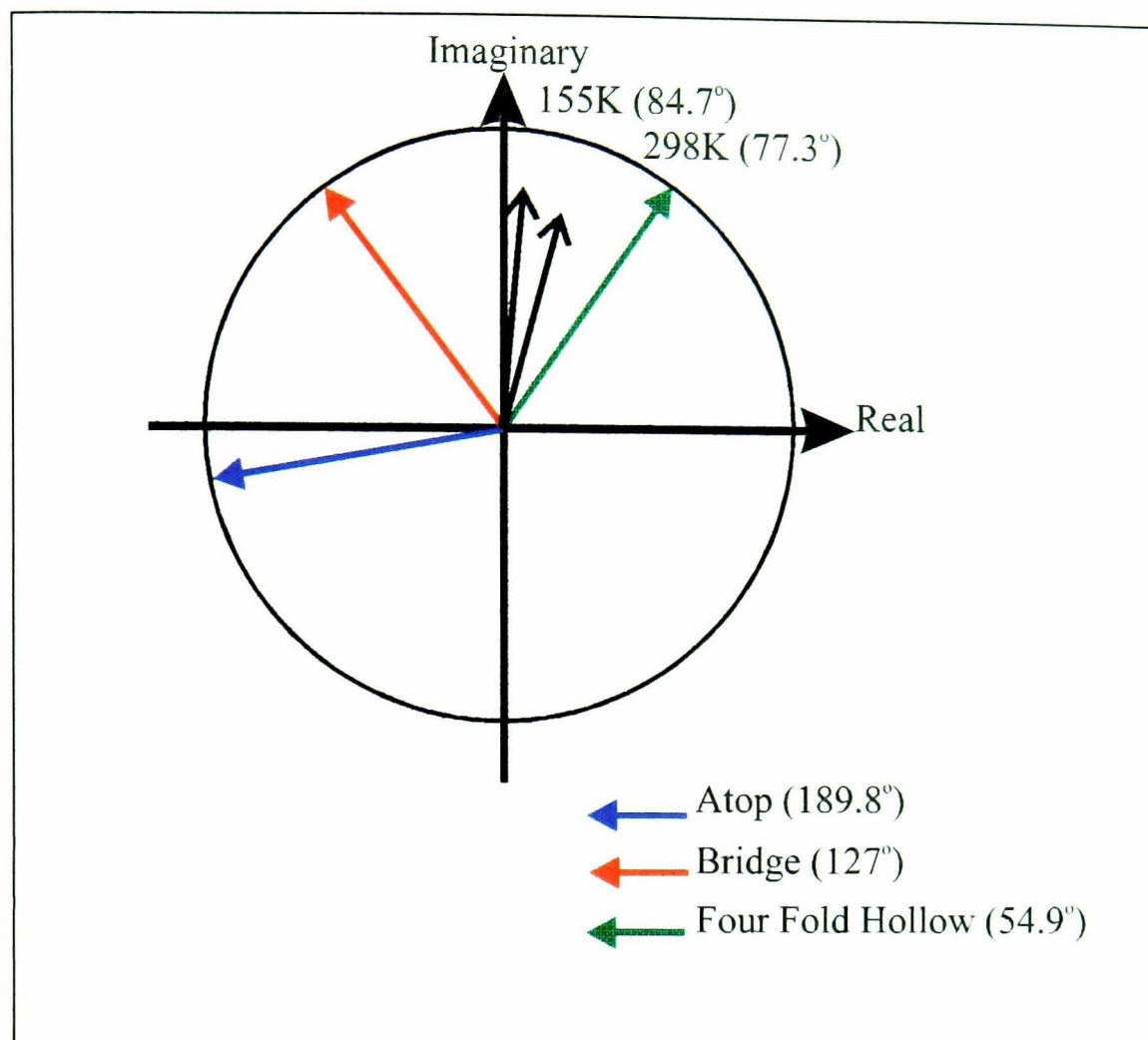


Figure 7.2.1. Argand vector diagram showing the vectors for the (200) reflection illustrating the theoretical vectors (coloured arrows) of the atop, bridge, four-fold hollow sites along with the experimental vectors obtained for the Cu(100)/Hg-c(4x4)-0.62ML structure at $T = 298\text{ K}$ and $T = 155\text{ K}$ (black arrows). The circle radius is equivalent to a coherent fraction of 1.0.

Figure 7.2.2. shows an Argand diagram illustrating the theoretical vectors for single site adsorption in atop, bridge (case a and b) and four-fold hollow sites, along with the experimental NIXSW values obtained for the (111) reflection. The angle (i.e. the coherent position) of the four-fold hollow site vector (27.4°) is identical (within errors) the experimental vectors obtained for both temperatures ($20.9^\circ \pm 8^\circ$ for 255 K and

$25.0^\circ \pm 7^\circ$ for 298 K). Bridge site adsorption has already been eliminated as a Gaussian NIXSW profile producing a coherent fraction of zero was not seen for the $c(4 \times 4)$ -0.62ML structure. The comparatively high coherent fractions combined from the experimental profiles indicate that there is a high degree of order in the adsorbate heights relative to the (111) planes.

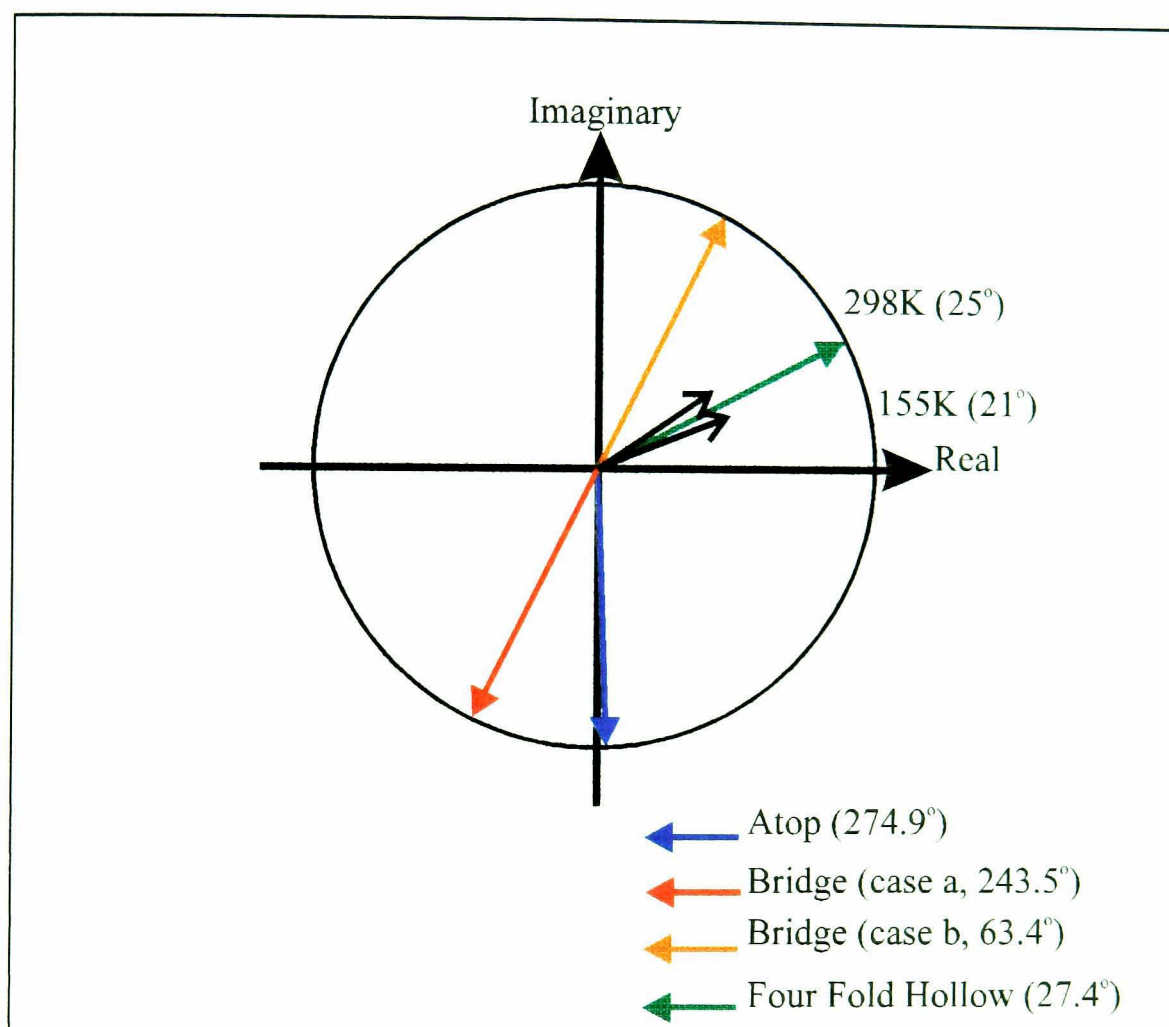


Figure 7.2.2. Argand vector diagram showing the vectors for the (111) reflection illustrating the theoretical vectors (coloured arrows) of the atop, bridge (case a. and b.), four-fold hollow sites along with the experimental vectors obtained for the $\text{Cu}(100)/\text{Hg-}c(4 \times 4)\text{-}0.62\text{ML}$ structure at $T = 298 \text{ K}$ and $T = 155 \text{ K}$ (black arrows). The circle radius is equivalent to a coherent fraction of 1.0.

The Argand diagram for the (111) reflection indicates well-defined adsorption into the high symmetry four-fold hollow sites and the (200) reflection Argand diagram indicates adsorption in either the four-fold hollow or bridge site. Therefore, we are now able to discuss the previous adsorption models for the $c(4\times 4)$ -0.62ML structure.

Several authors (Hutchings et al. 1990, Dowben et al. 1990b, 1991, Kime et al. 1992, Li et al. 1991a, 1992a, Varma et al. 1990 and Vidali et al. 1990) have proposed that the $c(4\times 4)$ -0.62ML structure consists of mercury adatoms forming a coincidence net on the Cu(100) surface. Such a model would consist of a supercell containing five atoms with four in high symmetry sites, and a coverage of 0.62ML. The mercury adsorbate atoms have a nearest neighbour lateral separation of 3.22 Å (Hutchings et al. 1990, Dowben et al. 1990b, 1991, Li et al. 1992a, Varma et al. 1990 and Vidali et al. 1990) relative to the Cu(100) surface lattice constant of 2.55 Å (Dowben et al. 1990b). The coincident mercury square net is rotated by 18.4° with respect to the [100] direction of the copper lattice (Hutchings et al. 1990, Li et al. 1992a). Figure 7.2.3. illustrates the $c(4\times 4)$ -0.62ML mercury coincidence net structure proposed by the above authors.

The $c(4\times 4)$ -0.62ML overlayer structure is expected to be slightly ruffled because the mercury adatoms are partially displaced from their high symmetry four-fold hollow sites. This is because the substrate potential has a strong enough influence to constrain the mercury atoms to occupy well-defined adsorption sites and to impose its square symmetry on the overlayer.

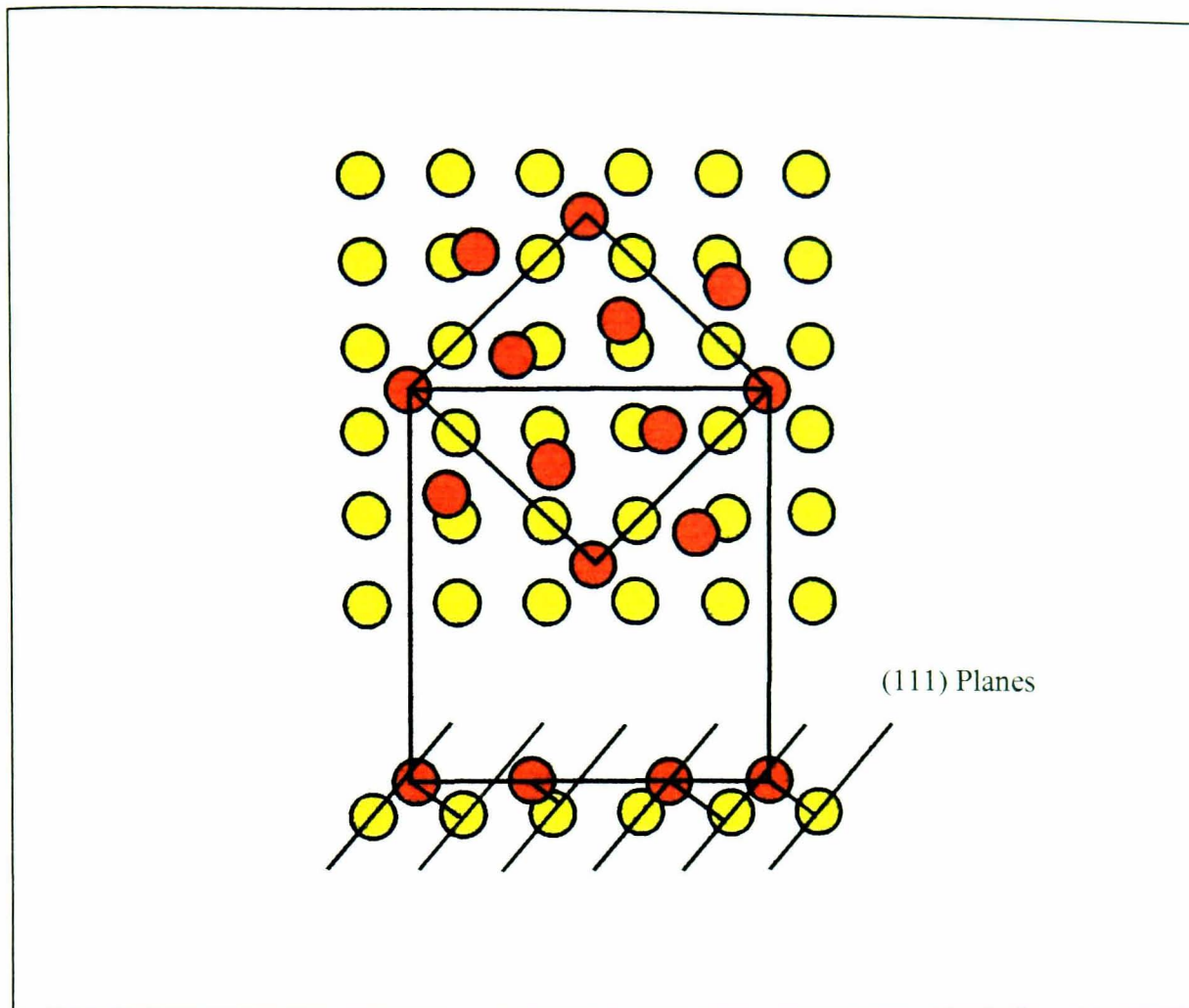


Figure 7.2.3. A schematic diagram of the possible Cu(100)-c(4x4)-Hg-0.62ML real space coincidence net structure proposed by previous studies with the mercury atoms located in four-fold hollow and low symmetry sites. The mercury adatom surface net is also shown. The (111) planes are schematically illustrated on the side view of the structure indicating how these planes relate to the mercury adsorbate atoms' position. The adlayer is not puckered in this diagram. The yellow and red atoms represent copper and mercury respectively. The diameters of the atoms are arbitrary.

As explained in section 2.1.2.2. for any X-Ray standing wavefield in which the reflecting planes are not parallel to the surface, the individual layer spacings of the different adsorption sites for a coincident lattice will involve regular increments that are rational fractions of the bulk layer spacing for this reflection. The vector sum for such a coincident lattice leads to a coherent fraction of zero (Woodruff et al. 1994). However, this prediction would produce a Gaussian NIXSW profile with a positive excursion of approximately 1.48, and hence a coherent fraction of zero which conflicts with our data. Therefore the Argand diagram for the $c(4\times 4)$ -0.62ML structure proposed by the above authors and shown in figure 7.2.3. would be that illustrated in figure 7.2.4. where the vectors sum to zero.

Clearly, this proposed $c(4\times 4)$ -0.62ML coincident mercury adsorbate structure does not fit the data obtained in our NIXSW experiments. We do not obtain a Gaussian NIXSW profile with a coherent fraction of zero in our studies of the $c(4\times 4)$ -0.62ML structure. The NIXSW data reported here for the (111) reflection planes produce a high coherent fraction of 0.5 relative to the (111) reflection. Such a high coherent fraction can only be reconciled with a high degree of order in the adsorbate relative to the (111) reflection planes.

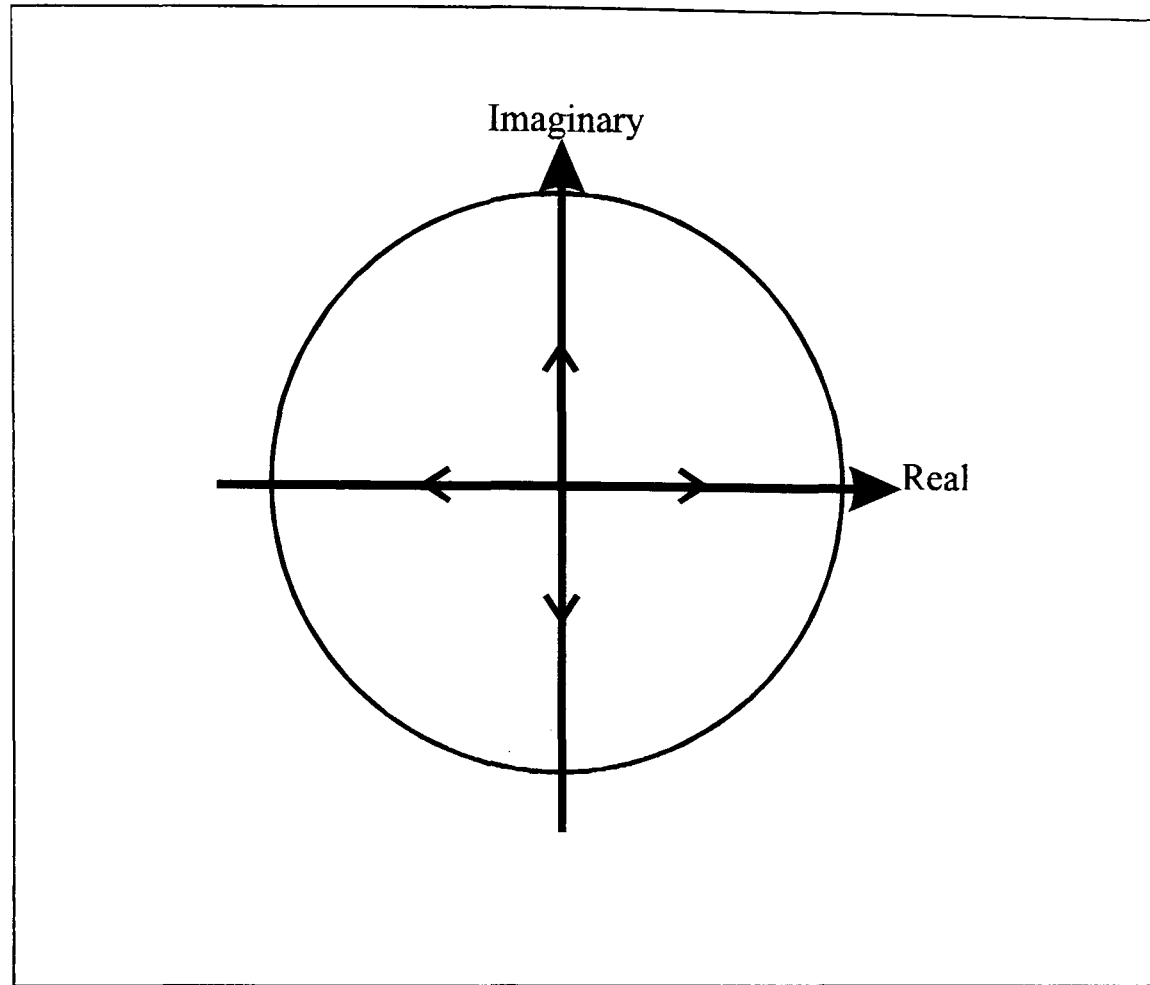


Figure 7.2.4. Argand vector diagram showing the vectors for the (111) reflection illustrating the vectors obtained for the Cu(100)/Hg-c(4x4)-0.62ML coincident net. The coincident net vectors cancel exactly.

A model which is consistent with our data is shown in figure 7.2.5. The red mercury atoms occupy four-fold hollow sites and the violet mercury atoms are positioned slightly off ($\approx 0.45 \text{ \AA}$, see figure 7.2.6) four-fold hollow sites. The adsorbate atoms would be pulled into the high symmetry adsorption sites by the binding energy potential of the surface. The two adjacent adatoms would then be forced into positions with an equal distance between the sites compatible with the adsorbate-adsorbate and adsorbate-substrate bond lengths. The adsorbate atoms therefore have to compromise between these two tendencies if the bond length is different from the site-to-site distance. Therefore, for the $c(4 \times 4)$ -0.62ML mercury adsorbate structure, there would be some atoms in exact four-fold hollow sites and some would reside in sites slightly off the four-fold hollow position (figure 7.2.5). This would produce an adsorbate overlayer consisting of crosses of mercury adatoms. The atoms occupying exact four-fold hollow sites would have four mercury neighbours, whereas the mercury atoms slightly off the four-fold sites would have only one mercury neighbour (within the “crosses”).

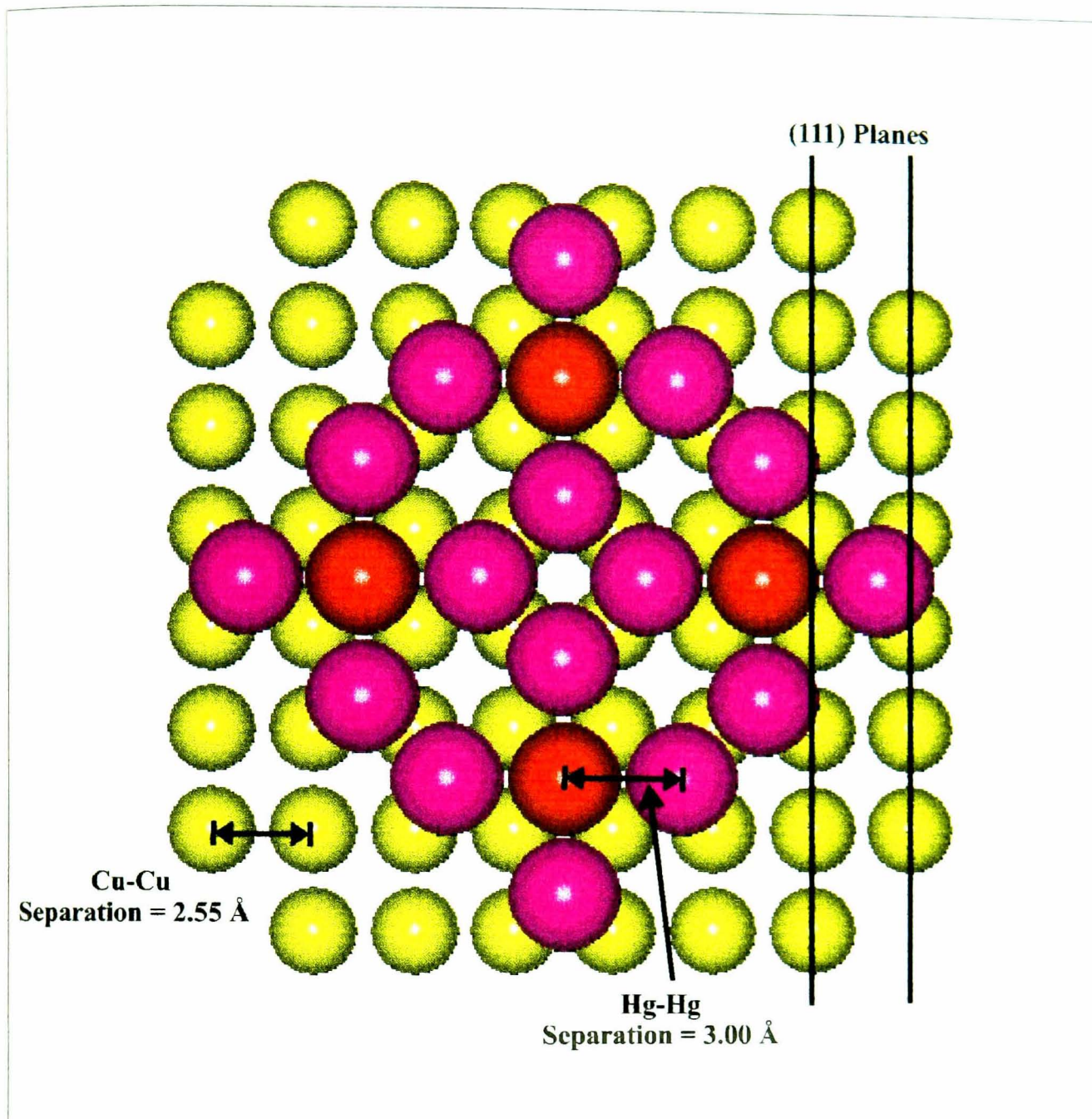


Figure 7.2.5. A schematic diagram of the model Cu(100)-c(4x4)-Hg-0.62ML real space structure consistent with our data by this study. The red mercury atoms located in four-fold hollow and violet mercury atoms in slightly off four-fold hollow sites. The adlayer is not puckered in this diagram. The yellow atoms represent copper. The diameters of the atoms are relative to each other.

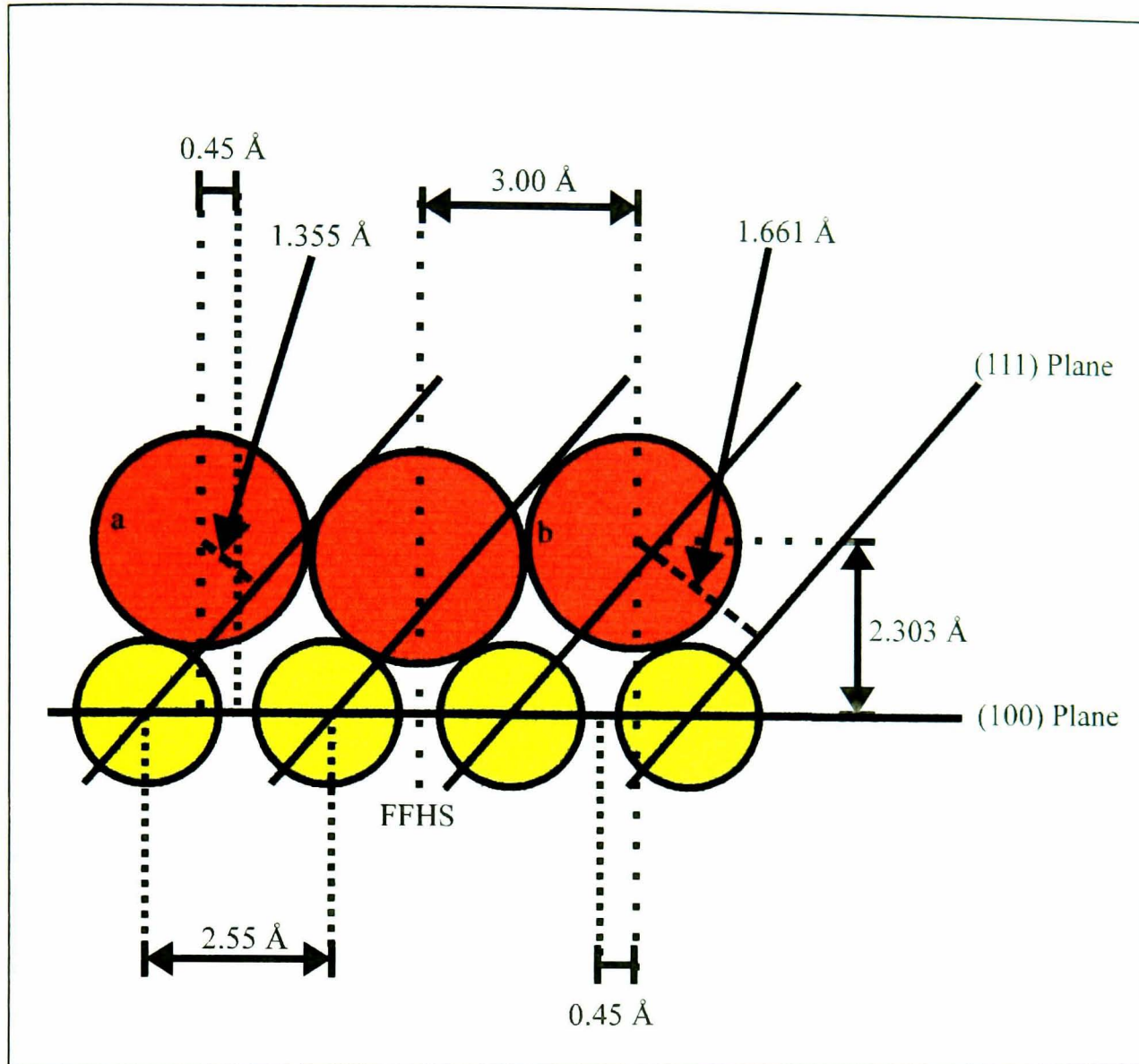


Figure 7.2.6. A schematic diagram illustrating how the coherent position (relative to the (100) and (111) reflection planes) of the mercury adatoms in the four-fold hollow sites (FFHS) and off- four-fold hollow sites can be calculated. The red atoms and yellow atoms represent mercury and copper atoms respectively. The radii of the atoms are arbitrary.

The mercury adsorbate atoms in the aforementioned “cross” structure would all be at a height similar to that of four-fold hollow adsorption relative to the (200) reflection plane. The NIXSW data for the (200) reflection would therefore be indicative of four-fold hollow adsorption. The variation (FFHS = 2.084 Å and Off-FFHS = 2.303 Å) in these (200) adsorption heights would produce a slightly lower coherent fraction than that observed for the c(2x2)-0.50ML structure (in which all the adatoms are in four-fold hollow sites). The Argand diagram in figure 7.2.7 illustrates the resultant vector for the FFHS and off-FFHS sites relative to the (200) reflection planes. Such a vector would equate to a coherent position of 2.204 Å and a coherent fraction of 0.9. These values are remarkably close to the experimental values (coherent position, coherent fraction) of the 298 K (2.196 ± 0.20 Å, 0.80 ± 0.04) and 155 K (2.233 ± 0.03 Å, 0.75 ± 0.05) NIXSW data for the (200) reflection plane.

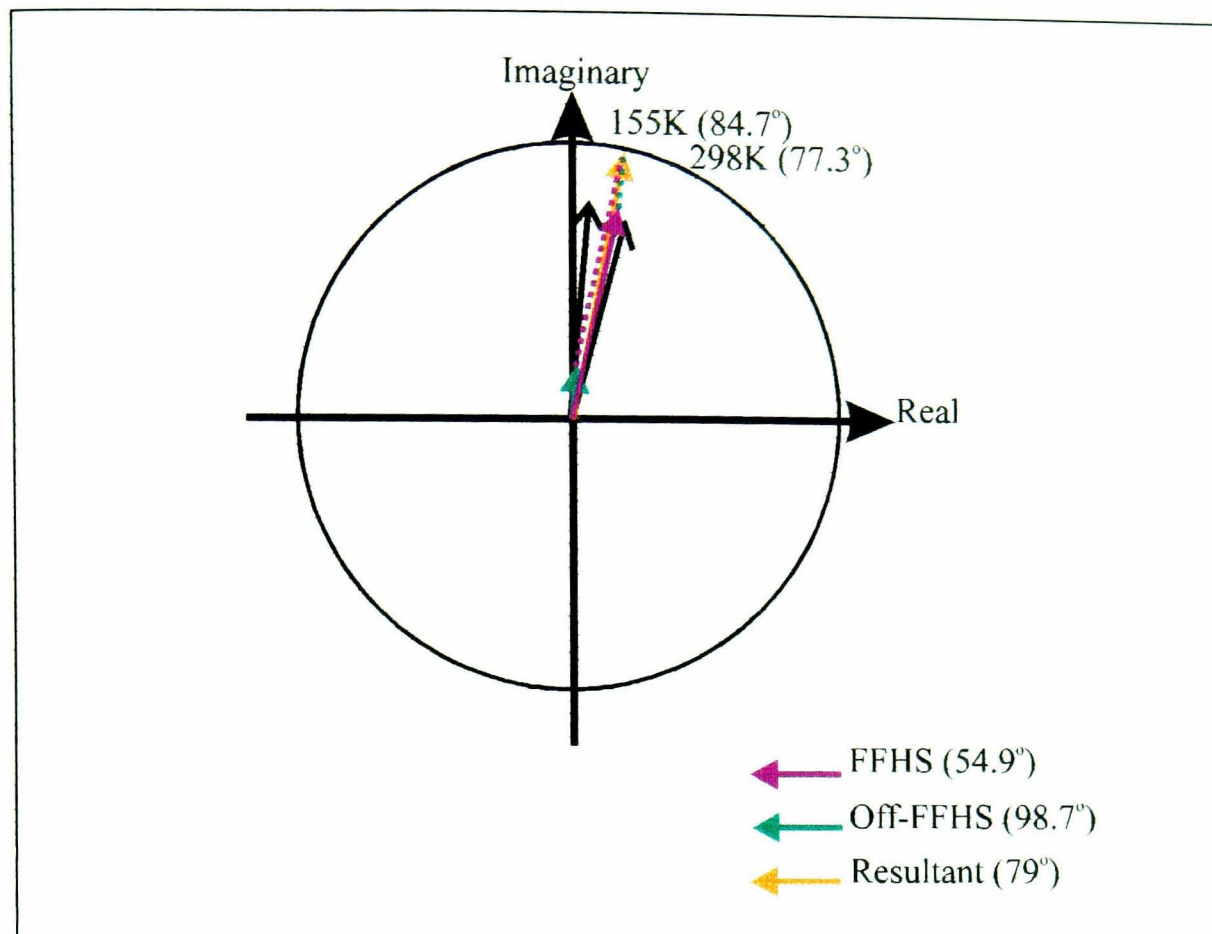


Figure 7.2.7. Argand vector diagram showing the vectors for the (200) reflection illustrating the theoretical vectors (coloured arrows) of the four-fold hollow site (FFHS) and the off-four-fold hollow sites, along with the experimental vectors obtained for the Cu(100)/Hg-c(4x4)-0.62ML structure at $T = 298$ K and $T = 155$ K (black arrows). The circle radius is equivalent to a coherent fraction of 1.0. There are three four-fold hollow sites and two off-four-fold hollow sites per unit cell, therefore the FFHS:off-FFHS ratio is 4:1 for the vector representation.

For the (111) reflection NIXSW data, a low coherent fraction would still be expected because of the various adsorbate heights above the (111) planes (FFHS = 2.246 Å and Off-FFHS = 1.355 Å, 1.661 Å, see figure 7.2.6). This coherent fraction would not be zero as predicted for the coincidence net (111) reflection data. The Argand diagram illustrating the resultant vector for the aforementioned “cross” structure can be seen in figure 7.2.8. The resultant vector represents a coherent position of 2.035 Å and a coherent fraction of 0.47 relative to the (111) reflection planes. The coherent fraction of this resultant vector is identical to that of 0.50 ± 0.10 obtained for the experimental data at both 155 K and 298 K. However, there is a slight discrepancy between the resultant coherent position (2.035 Å) and that of the experimental data (2.208 ± 0.04 Å for 155 K and 2.233 ± 0.04 Å for 298 K). This discrepancy is thought to be due to the high sensitivity of the (111) reflection planes to the lateral position of the adsorbate atom. The adatom’s lateral position chosen in the calculation could be slightly different to that of the actual adsorbate position, thus giving a slightly different coherent position relative to the (111) reflection plane than the experimental data. Nevertheless, the (111) resultant coherent position is close enough to the experimental data to favour the proposed “cross” model.

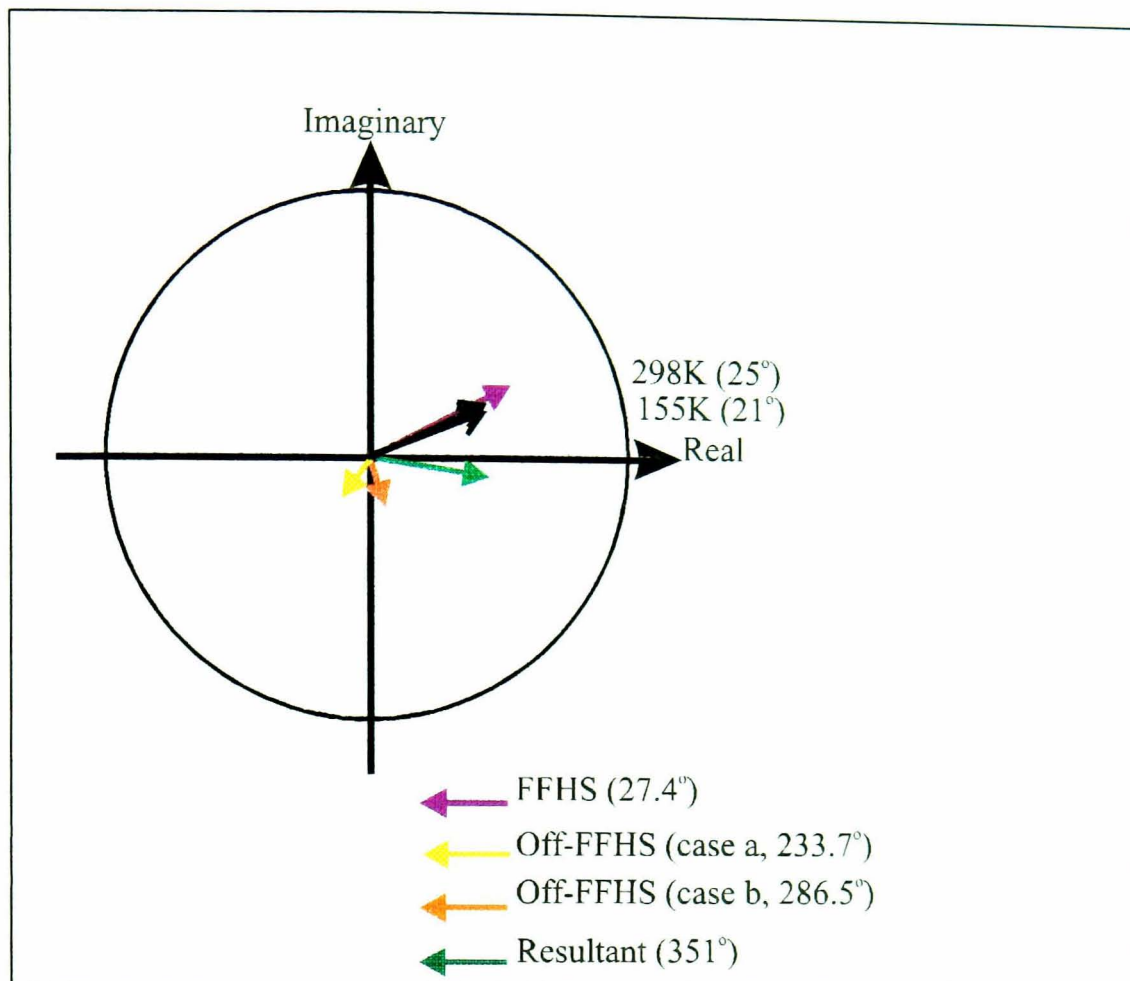


Figure 7.2.8. Argand vector diagram showing the vectors for the (111) reflection illustrating the theoretical vectors (coloured arrows) of the four-fold hollow site (FFHS) and the off-four-fold hollow sites, along with the experimental vectors obtained for the Cu(100)/Hg-c(4x4)-0.62ML structure at $T = 298$ K and $T = 155$ K (black arrows). The circle radius is equivalent to a coherent fraction of 1.0. There are three four-fold hollow sites and two off-four-fold hollow sites (both with a different coherent position) per unit cell, therefore the FFHS:off-FFHS: off-FFHS ratio is 3:1:1 for the vector representation.

The proposed model can provide some insight into the possible $c(4 \times 4)$ -0.62ML structure relative to the Cu(100) substrate surface. However, it may be an extreme version of the structure actually formed on the Cu(100) surface. The structure shown in figure 7.2.5. would provide a very complex LEED pattern. Yet, both the (200) and (111) coherent fractions and adsorbate heights above the respective reflection planes obtained would match those of our experimental data, whereas the coincident net proposed by the previous investigations into this structure can in no way be reconciled with our experimental data.

7.3 The Cu(100)/Hg-(3x3)-0.66ML Structure

The peak to peak height ratio of the mercury and copper XPS peaks for the (3x3)-0.66ML structure (0.59 ± 0.11 for 155 K) indicates a greater coverage than for the c(2x2)-0.50ML and c(4x4)-0.62ML structures.

The (200) and (111) coherent positions ($2.183 \pm 0.025 \text{ \AA}$ and $2.233 \pm 0.035 \text{ \AA}$ respectively) obtained from the fitting of the (3x3)-0.66ML NIXSW profiles indicate four-fold hollow site (2.084 \AA and 2.246 \AA for (200) and (111) reflections respectively) adsorption (Figures 7.3.1. and 7.3.2.). The coherent fractions obtained from the fitting of the NIXSW scans indicates that there is little static or dynamic disorder present. Consequently, one would expect the mercury adatoms to behave in a similar manner to the other structures studied.

The scans carried out for the (200) reflection gave a coherent fraction of $0.90 (\pm 0.05)$. Such a relatively high coherent fraction might be expected for low temperature data, as the adatoms will tend to reside in the shallow energy minima as the thermal motions decrease. Figure 7.3.1. shows the Argand diagram for the Cu(100)/Hg-(3x3)-0.66ML structure at $T = 155 \text{ K}$ for the (200) reflection data, where the theoretical bond lengths are those calculated in section 6.6. The experimental vector ($74.7^\circ \pm 5^\circ$) lies between the theoretical four-fold hollow (54.9°) and bridge (127°) vectors, though it is closer to that of the four-fold hollow site vector.

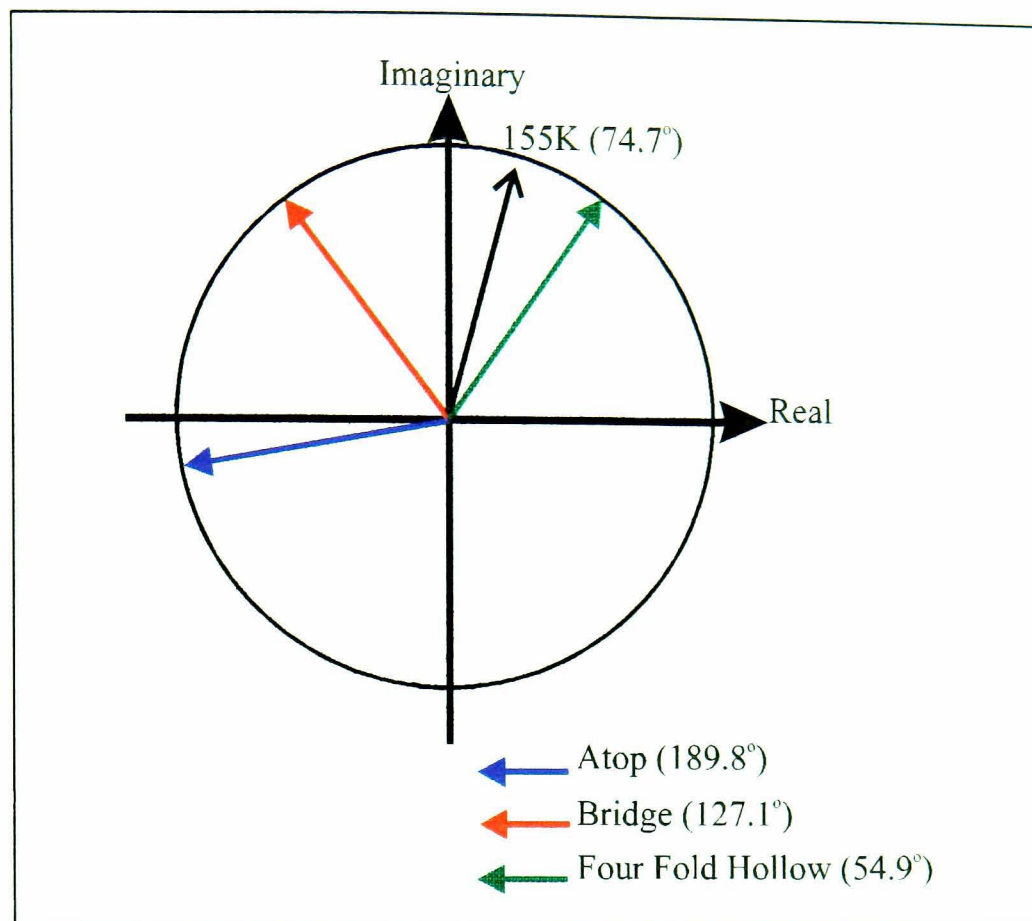


Figure 7.3.1. Argand vector diagram showing the vectors for the (200) reflection illustrating the theoretical vectors (coloured arrows) of the atop, bridge, four-fold hollow sites along with the experimental vector obtained for the Cu(100)/Hg-(3x3)-0.66ML structure at $T = 155$ K (black arrow). The circle radius is equivalent to a coherent fraction of 1.0.

The (111) NIXSW coherent fraction of $0.55 (\pm 0.07)$ once more indicates that there is little static or dynamic disorder present. Figure 7.3.2. shows the Argand diagram for the Cu(100)/Hg-(3x3)-0.66ML structure at $T = 155$ K for the (111) reflection data. The angle (i.e. the coherent position) of the four-fold hollow site vector (27.4°) is close to the experimental vector of $25.0^\circ \pm 6^\circ$. Therefore the coherent position strongly suggests adsorption purely in the four-fold hollow site.

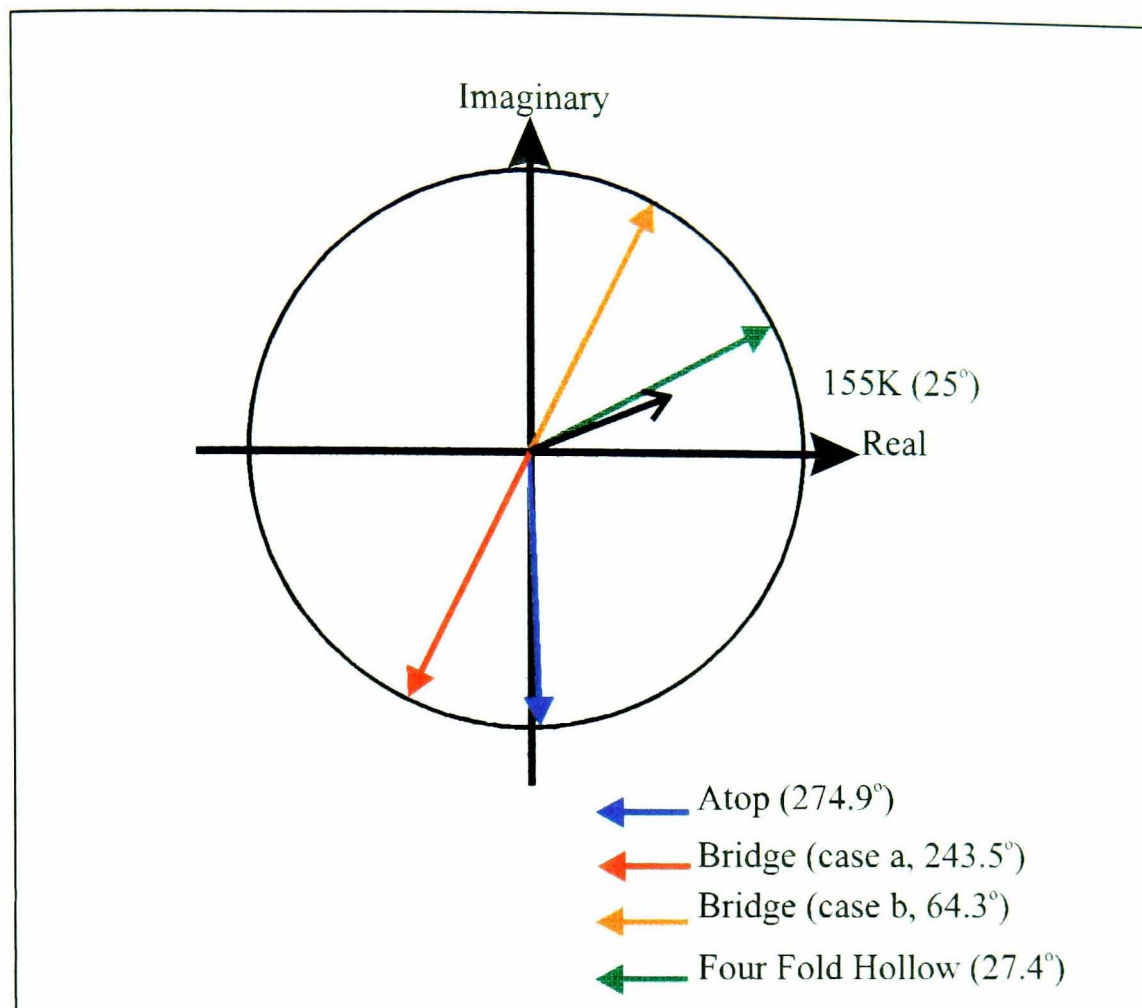


Figure 7.3.2. Argand vector diagram showing the vectors for the (111) reflection illustrating the theoretical vectors (coloured arrows) of the atop, bridge (case a. and b.), four-fold hollow sites along with the experimental vector obtained for the Cu(100)/Hg-(3x3)-0.66ML structure at $T = 155$ K (black arrow). The circle radius is equivalent to a coherent fraction of 1.0.

However, the geometry of the (3x3)-0.66ML mercury adsorbate structure does not permit adsorption purely in the four-fold hollow site. The model previously postulated for the metastable Cu(100)/Hg-(3x3)-0.66ML structure (Dowben et al. 1990b, Li et al. 1991a, 1992a, Kime et al. 1992) places the mercury adatoms equally in four-fold hollow sites and bridge sites. As explained in section 2.1.3.2. the adsorbate heights above the (111) reflection planes for the bridge site have two distinct values.

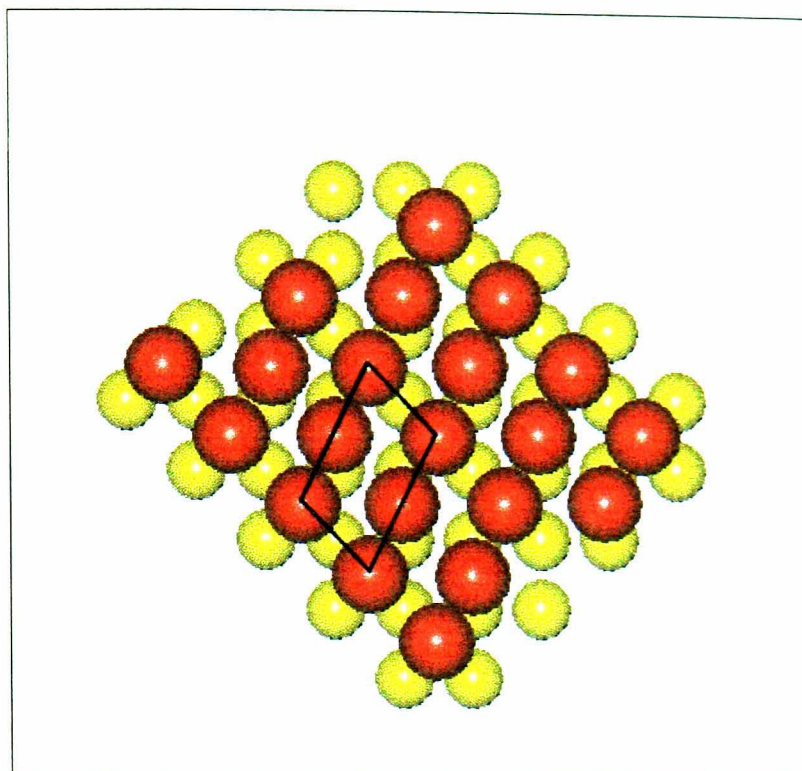


Figure 7.3.3. A schematic diagram of the possible Cu(100)-(3x3)-Hg-0.66ML real space coincidence net structure with the mercury atoms equally located in four-fold hollow and bridge (case a) sites. The mercury adatom surface net is also shown. The adlayer is not puckered in this diagram. The yellow and red atoms represent copper and mercury respectively. The diameters of the atoms are relative to each other.

Therefore, there are two distinct phases of equal four-fold hollow site and bridge adsorption. These phases will be referred to as case (a) and case (b) (from the type of bridge site involved).

Case (a) can be seen in figure 7.3.3. The Argand diagram for equal population of the four-fold hollow site and bridge (case a) site is illustrated in figure 7.3.4. The resultant vector has an angle of 316° (equivalent to a coherent position of 3.92 \AA) and a length equivalent to a coherent fraction of 0.30. Clearly both the adsorbate height and coherent fraction do not match those of the experimental data.

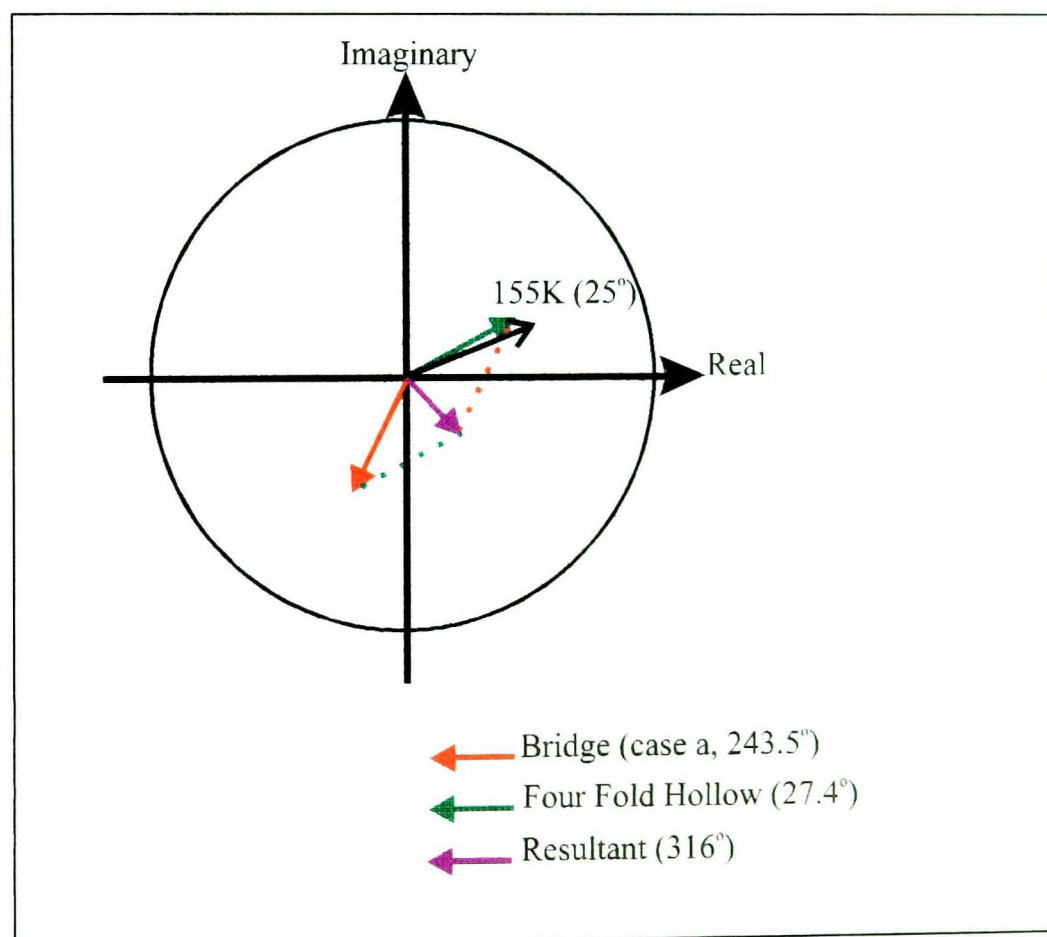


Figure 7.3.4. Argand vector diagram showing the vectors for the (111) reflection illustrating the theoretical vectors (coloured arrows) of the bridge (case a.), four-fold hollow sites and the resultant vector for equal population of these two sites along with the experimental vector obtained for the Cu(100)/Hg-(3x3)-0.66ML structure at $T = 155 \text{ K}$ (black arrow). The circle radius is equivalent to a coherent fraction of 1.0.

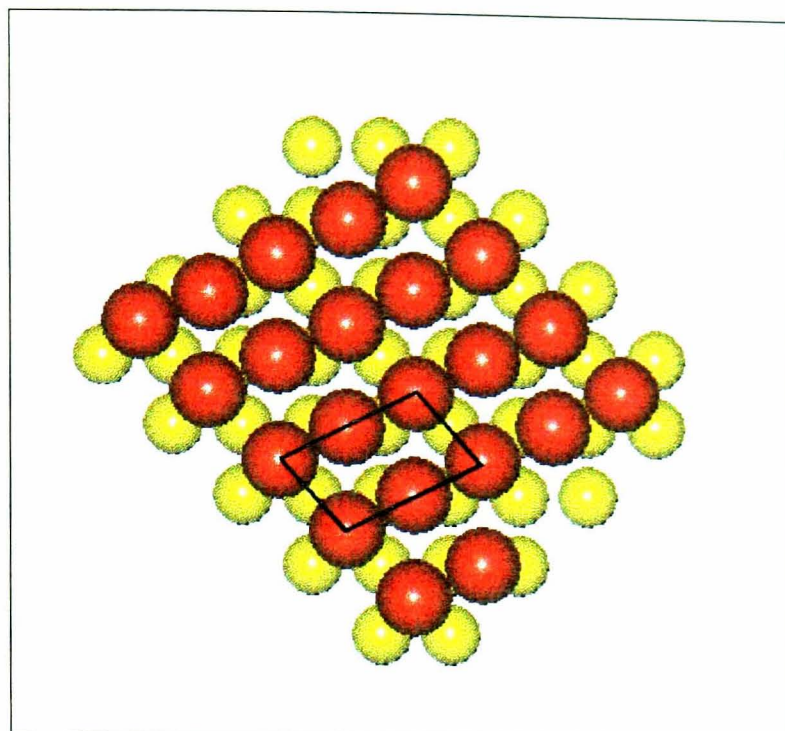


Figure 7.3.5. A schematic diagram of the possible Cu(100)-(3x3)-Hg-0.66ML real space coincidence net structure with the mercury atoms equally located in four-fold hollow and bridge (case b) sites. The mercury adatom surface net is also shown. The adlayer is not puckered in this diagram. The yellow and red atoms represent copper and mercury respectively. The diameters of the atoms are relative to each other.

Case (b) can be seen in figure 7.3.5. The Argand diagram for equal population of the four-fold hollow site and bridge (case b) site is illustrated in figure 7.3.6. The resultant vector has an angle of 45.4° (equivalent to a coherent position of 2.350 \AA) and a length equivalent to a coherent fraction of 0.92. The adsorbate height of 2.350 \AA closely matches the experimental value of $2.233 \pm 0.035 \text{ \AA}$, but the coherent fraction does not match the experimental data.

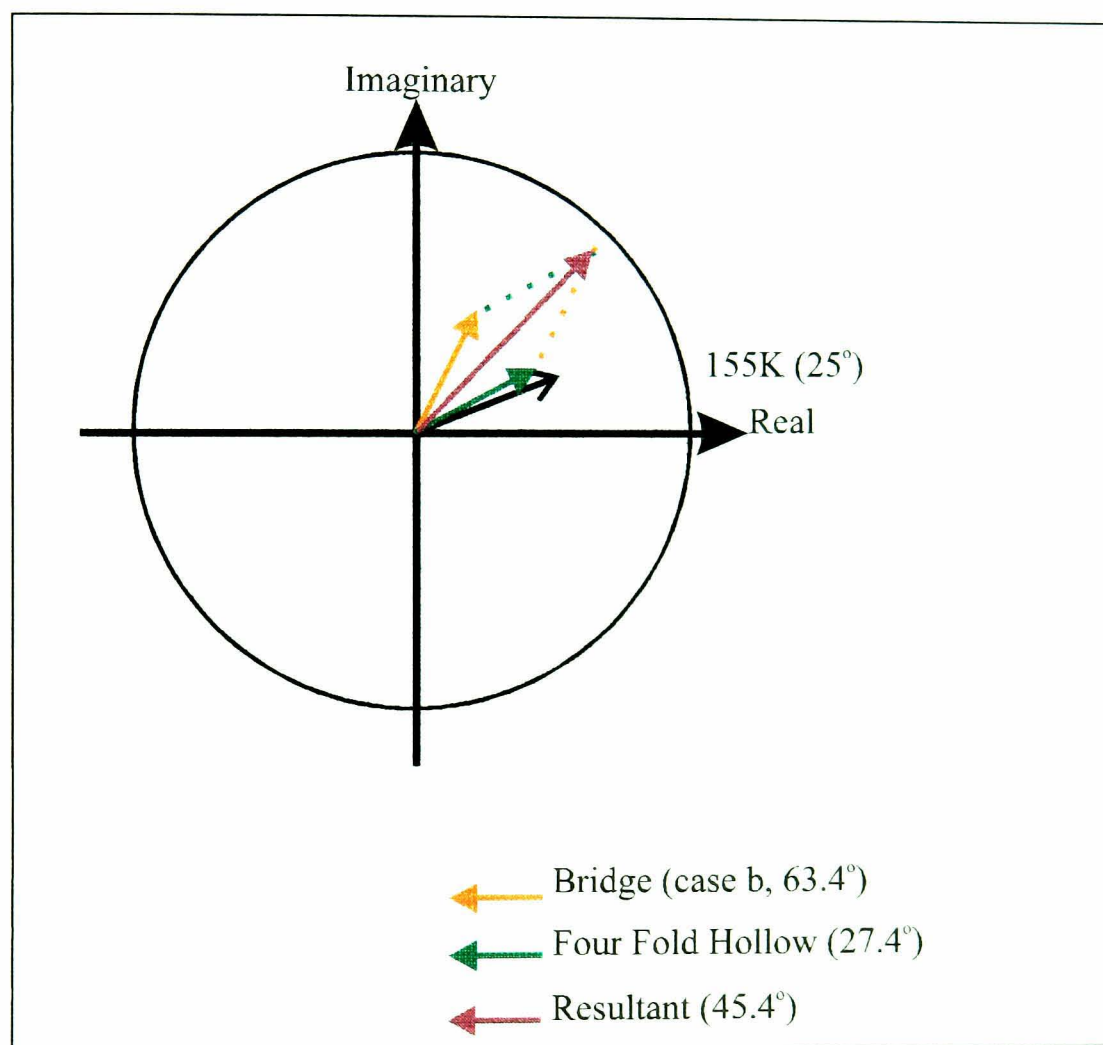


Figure 7.3.6. Argand vector diagram showing the vectors for the (111) reflection illustrating the theoretical vectors (coloured arrows) of the bridge (case b.), four-fold hollow sites and the resultant vector for equal population of these two sites along with the experimental vector obtained for the Cu(100)/Hg-(3x3)-0.66ML structure at $T = 155 \text{ K}$ (black arrow). The circle radius is equivalent to a coherent fraction of 1.0.

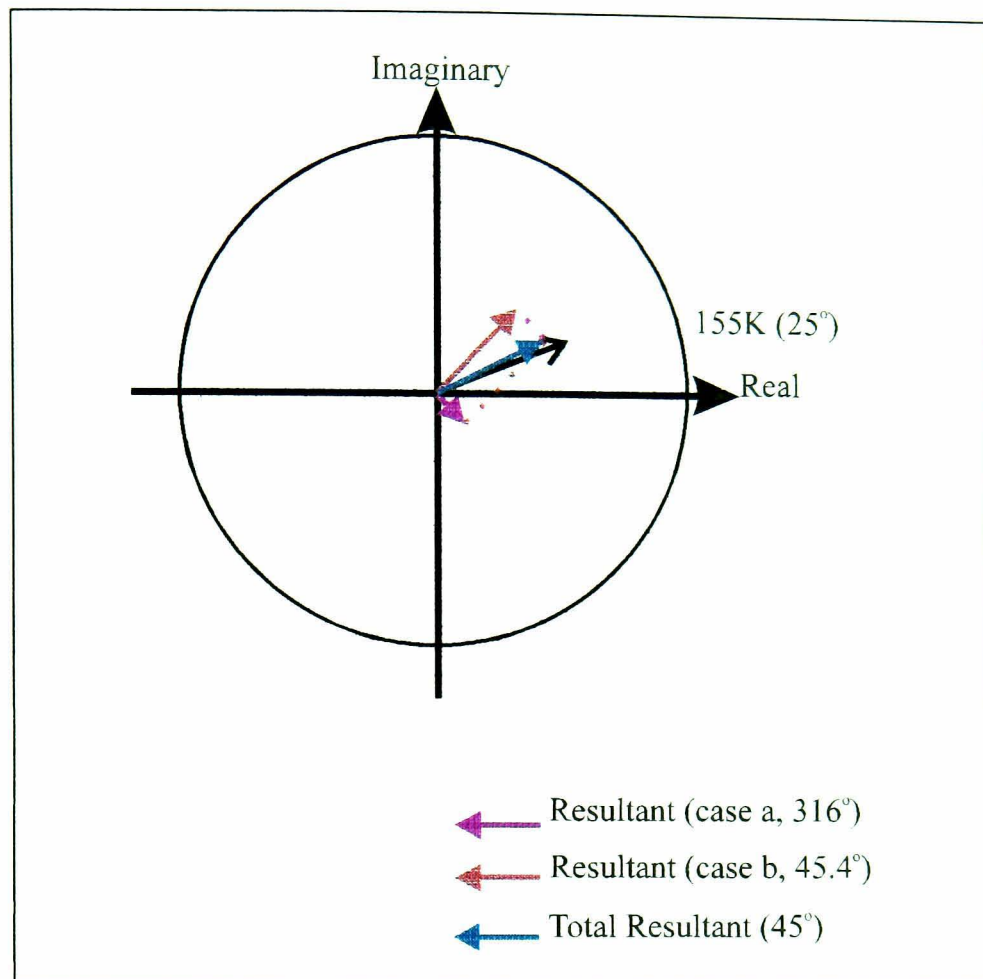


Figure 7.3.7. Argand vector diagram showing the vectors for the (111) reflection illustrating the theoretical resultant vector (coloured arrows) for equal domains of the equal population of the two sites (the bridge (case a.), four-fold hollow sites and the bridge (case b.), four-fold hollow sites) along with the experimental vector obtained for the Cu(100)/Hg-(3x3)-0.66ML structure at $T = 155$ K (black arrow). The circle radius is equivalent to a coherent fraction of 1.0.

However, it is also possible for an equal number of domains of both phase (a) and phase (b) to be present. This situation is represented in an Argand diagram illustrated in figure 7.3.7. The resultant vector has an angle of 45° (equivalent to a coherent position of 2.35 \AA) and a maximum length equivalent to a coherent fraction of 0.5. In this situation, both the adsorbate height and the coherent fraction fit those of the

experimental NIXSW data. This hypothesis is also consistent with the (200) reflection NIXSW data. Therefore, the (3x3)-0.66ML structure consists of domains of both phase (a) and phase (b).

7.4 The Cu(100)/Hg-c(2x6)-0.83ML Structure

The shape and size of the Cu(100)/Hg-c(2x6)-0.83ML structure (200) and (111) NIXSW spectra are quite different from the NIXSW spectra obtained for the other Cu(100)/Hg structures studied. As a result, we would expect rather distinct fitting parameters. The peak-to-peak height ratio (1.70 ± 0.26) of the mercury and copper XPS peaks for the c(2x6)-0.83ML structure is greater than those for the other Cu(100)/Hg structures and indicates a coverage higher than the optimum coverage of approximately 0.83ML.

Figure 7.4.1. shows the Argand diagram for the Cu(100)/Hg-(3x3)-0.66ML structure at $T = 155$ K for the (200) reflection data. The experimental vector ($89.7^\circ \pm 5^\circ$) lies almost halfway between the theoretical four-fold hollow (54.9°) and bridge (127°) vectors. Consequently the (200) coherent position of 2.258 ± 0.025 Å obtained from the fitting of the c(2x6)-0.83ML NIXSW profiles indicate adsorption equally in both bridge and four-fold hollow site adsorption. The coherent fraction for the (200) NIXSW data of approximately 0.4 could also be appropriate for adsorption equally in bridge and four-fold hollow sites. Yet, the coherent fraction (0.9) obtained for the

(3x3)-0.66ML data in which adsorption is thought to occur equally in bridge and four-fold hollow sites is a great deal higher than that of the c(2x6)-0.83ML structure.

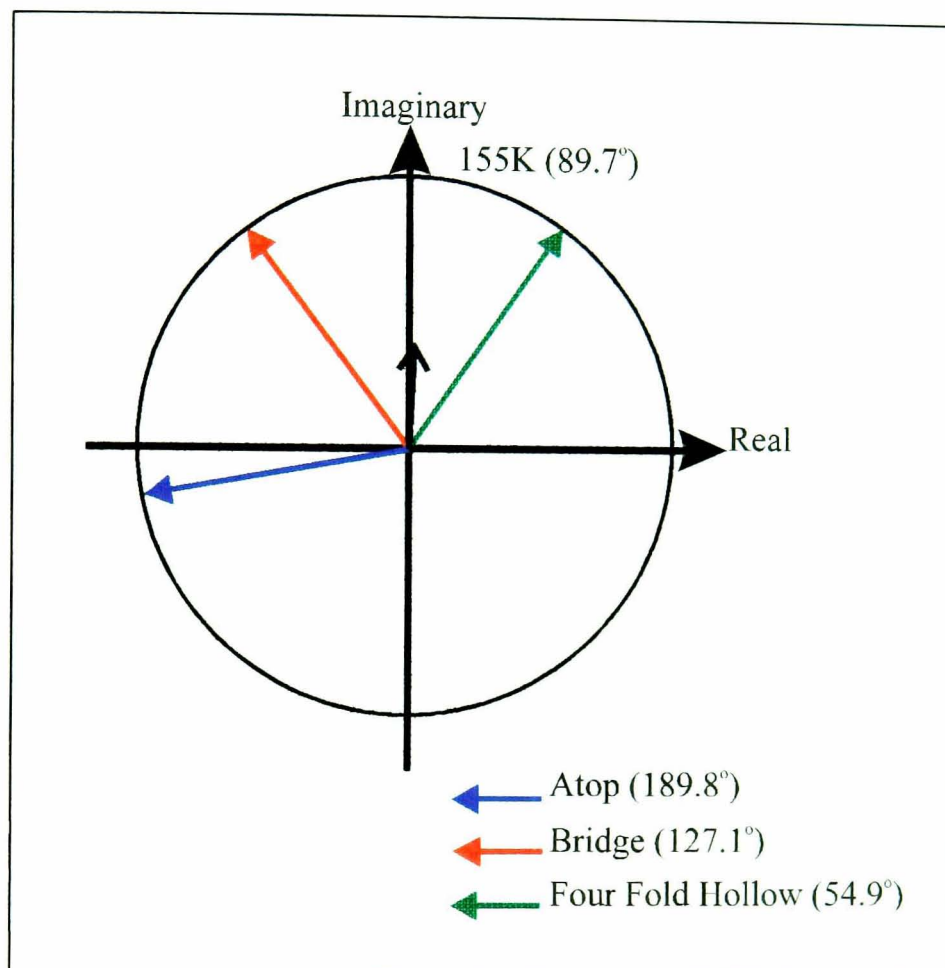


Figure 7.4.1. Argand vector diagram showing the vectors for the (200) reflection illustrating the theoretical vectors (coloured arrows) of the atop, bridge, four-fold hollow sites along with the experimental vector obtained for the Cu(100)/Hg-c(2x6)-0.83ML structure at $T = 155$ K (black arrow). The circle radius is equivalent to a coherent fraction of 1.0.

Figure 7.4.2. shows the Argand diagram for the Cu(100)/Hg-c(2x6)-0.83ML structure at $T = 155$ K for the (111) reflection data. The angle (i.e. the coherent position) of the bridge (case b.) (63.4°) site vector is close to that of the experimental vector ($64^\circ \pm 8^\circ$) obtained. Therefore the coherent position for the (111) NIXSW data could be reconciled with adsorption purely in the bridge (case b.) site. However the very low coherent fraction for the (111) NIXSW profile is not compatible with adsorption in a single site.

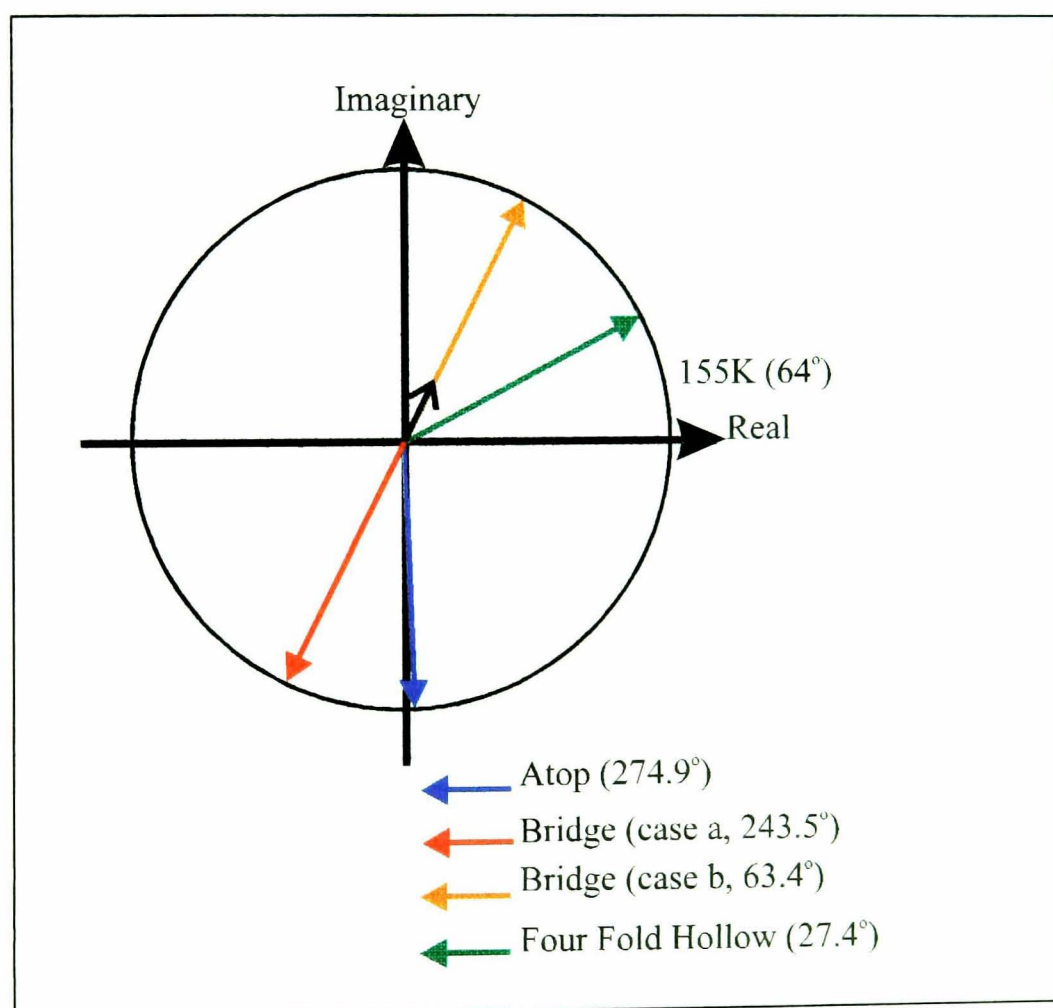


Figure 7.4.2. Argand vector diagram showing the vectors for the (111) reflection illustrating the theoretical vectors (coloured arrows) of the atop, bridge (case a. and b.), four-fold hollow sites along with the experimental vector obtained for the Cu(100)/Hg-c(2x6)-0.83ML structure at $T = 155$ K (black arrow). The circle radius is equivalent to a coherent fraction of 1.0.

The low coherent fractions of both the (200) and (111) NIXSW data (0.39 ± 0.03 and 0.25 ± 0.15 respectively) can only be reconciled with multilayer adsorption, more adsorption sites or by rumpling of the adsorbate layer. Multilayer mercury adsorption on the Cu(100) substrate has been studied by Dowben et al. (1990a, 1990b, 1991), Vidali et al. (1991), Kime et al. (1995), Li et al. (1991b, 1992). Dowben et al. (1990a) observed a Hg-Hg separation close to that of bulk mercury (3.004 \AA) when they adsorbed 2ML of mercury in the form of a $c(2 \times 2)$ structure. Dowben et al. (1990b, 1991) have also observed multilayer adsorption whilst forming the higher coverage $c(4 \times 4)$ structure at 245 K. For this multilayer adsorption they assumed that the second layer adsorption favoured high co-ordination sites. As a result they proposed that the second layer of mercury adatoms formed random domains oriented with mercury atoms occupying the $c(4 \times 4)$ overlayer coincident sites.

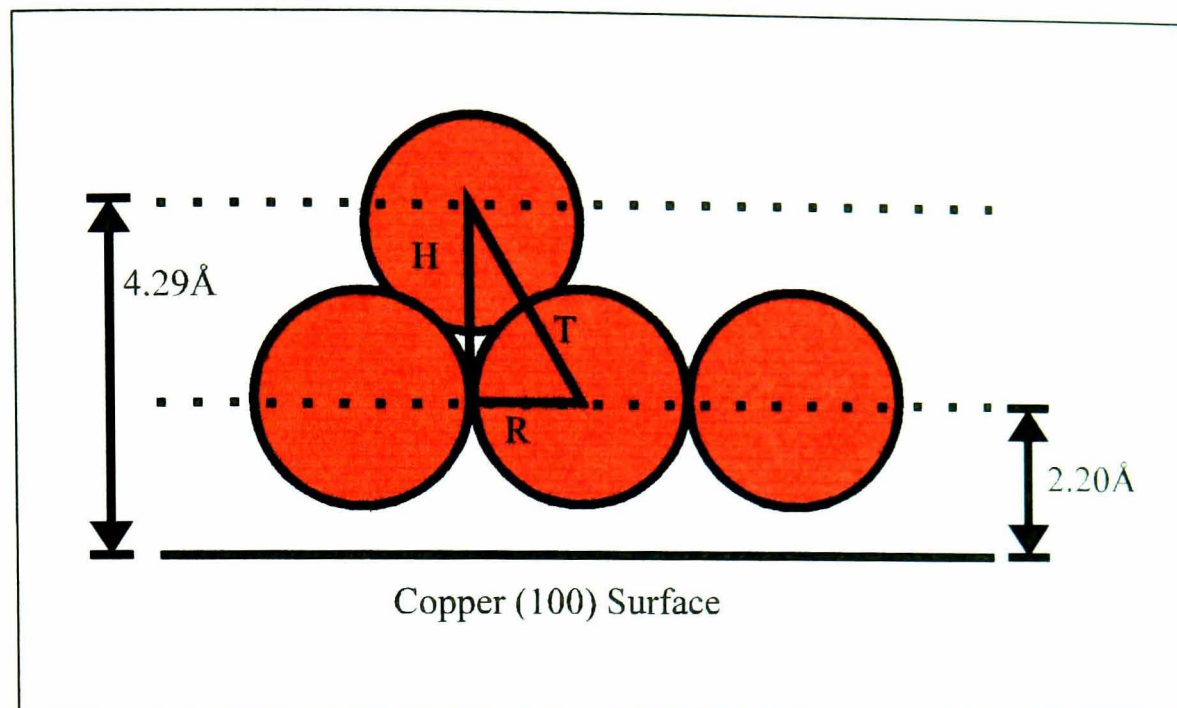


Figure 7.4.3. A schematic diagram illustrating how the height of the second layer of mercury adatoms can be calculated. The calculation is identical to that used in figure 2.1.3.2.2. The mercury atoms are assumed to be hard spheres with a radius of, R (1.48 \AA). The second layer of mercury atoms are positioned at a height, H above the first layer of mercury adatoms.

From the peak to peak ratios for this structure (1.70 ± 0.26) it is obvious that multilayers were formed. Therefore, it is necessary to consider where the next layer of mercury atoms adsorbing and what Argand diagram would such a structure produce. Figure 7.4.3. illustrates how the height of the next layer of mercury adatoms can be calculated. The mercury atoms are assumed to be hard spheres with a radius of 1.48 \AA . The first layer of mercury atoms are assumed to be at a height of 2.20 \AA above the (100) copper surface. This height is similar to the (200) adsorption height obtained for all the previous Cu(100)/Hg structures. Therefore, the second layer of mercury adatoms was calculated to be at a height of 4.29 \AA above the Cu(100) surface. The

(200) adsorption height for the c(2x6) structure was not as large as 4.29 Å. If a partial second layer of mercury adatoms was formed, the (200) adsorbate height would be increased the (200) height is an average of the first and second layer spacings with respect to the (200) layers. The coherent fraction of the (200) reflection data would also be lowered because of the two different heights of mercury adatoms above the (200) layers. However, when a second layer of mercury atoms was adsorbed on top of the c(2x6) structure by Li et al. (1992a) a different LEED pattern was observed. Such a LEED pattern was not observed in our experiments.

Figure 7.4.4. shows the (200) reflection Argand diagram obtained if there is one and a quarter layers of mercury adsorption on the Cu(100) surface. The second layer of mercury adatoms are assumed to adsorb into four-fold hollow sites. The resultant vector has an angle of 91° (equivalent to a resultant NIXSW coherent position of 2.264 Å) and a length equivalent to a coherent fraction of 0.88. The adsorbate height matches the experimental data but the coherent fraction is too high.

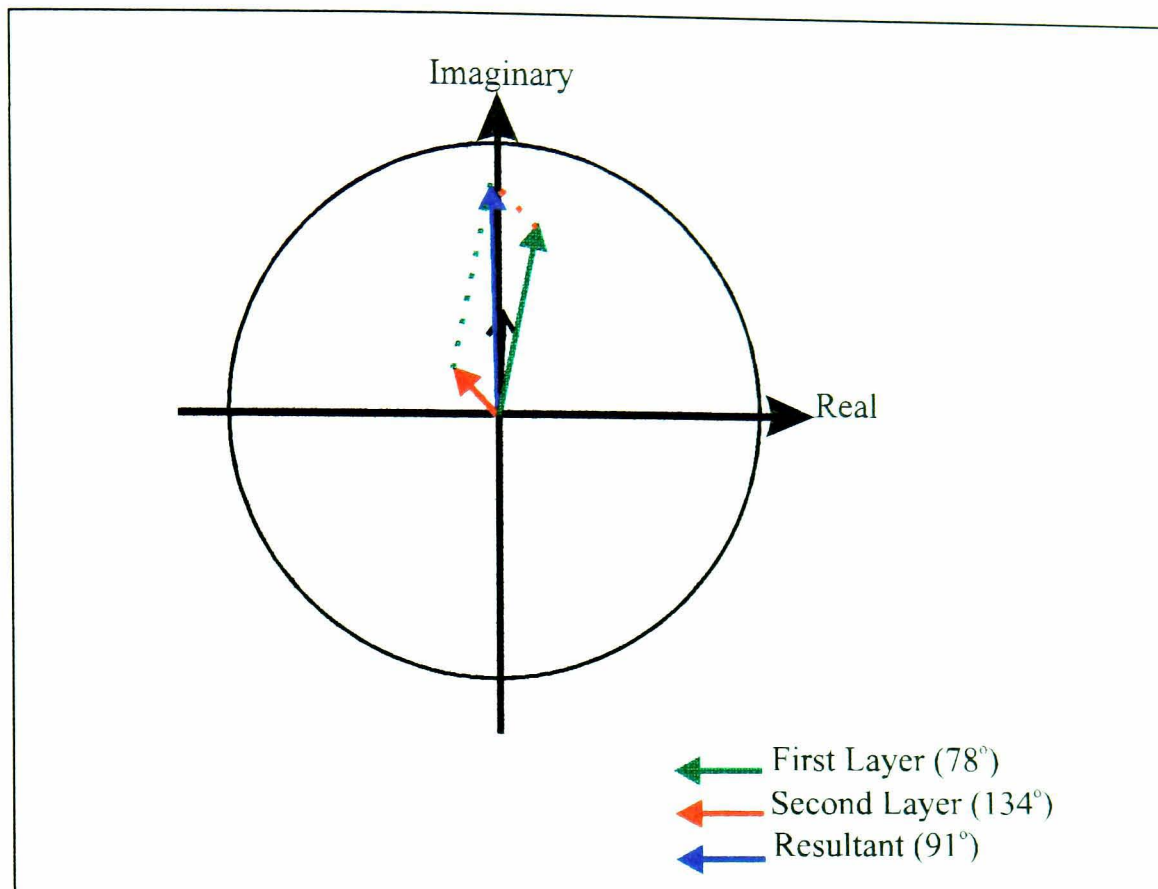


Figure 7.4.4. Argand vector diagram illustrating the vectors for the (200) reflection one and a quarter layers of mercury. It shows the theoretical vectors (coloured arrows) of the first and second mercury adlayers with the experimental vector obtained for the Cu(100)/Hg-c(2x6)-0.83ML structure at $T = 155$ K (black arrow). The circle radius is equivalent to a coherent fraction of 1.0.

Figure 7.4.5. shows the (200) reflection Argand diagram obtained if there is one and a half layers of mercury adsorption on the Cu(100) surface. The resultant vector has an angle of 95° (equivalent to a resultant NIXSW coherent position of 2.284\AA) and a length equivalent to a coherent fraction of 0.91. Neither the adsorbate height nor the coherent fraction closely matches the experimental data.

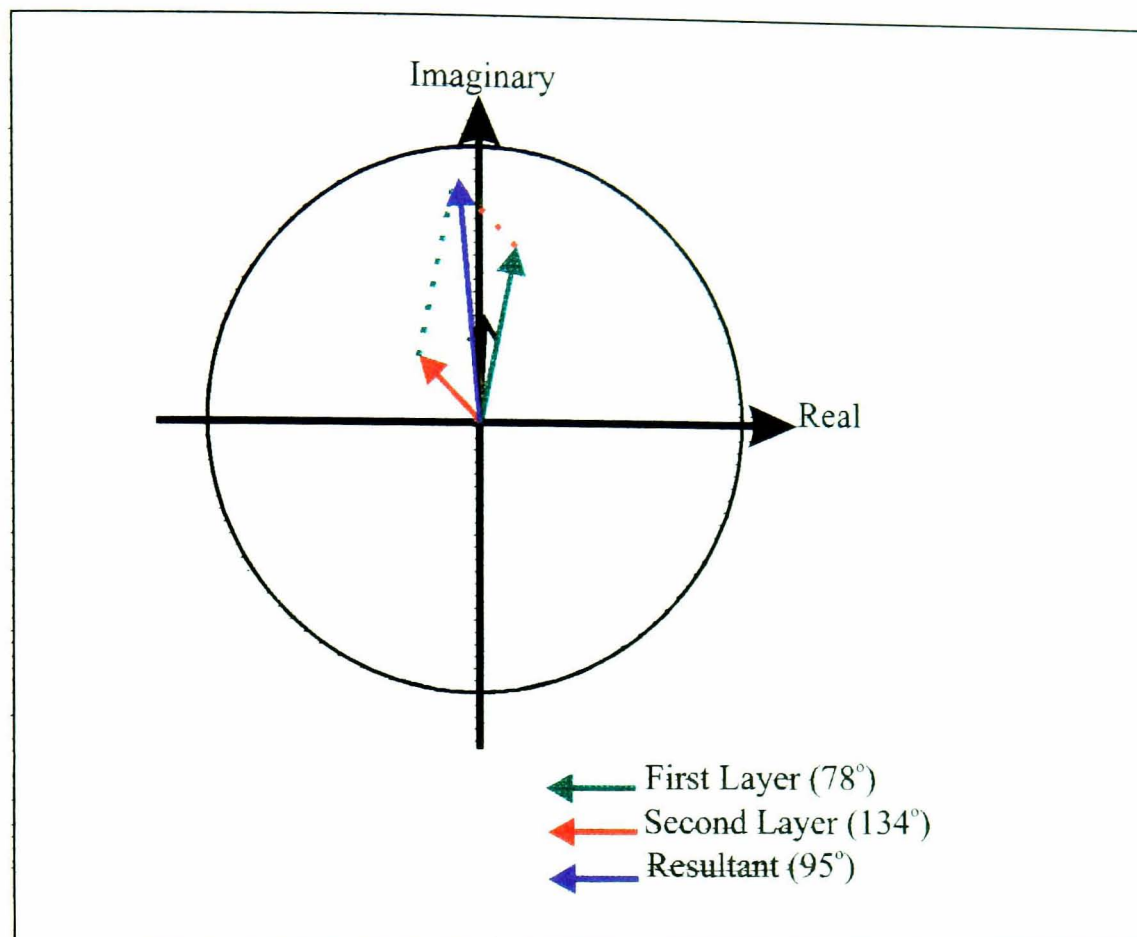


Figure 7.4.5. Argand vector diagram illustrating the vectors for the (200) reflection one and a half layers of mercury. It shows the theoretical vectors (coloured arrows) of the first and second mercury adlayers with the experimental vector obtained for the Cu(100)/Hg-c(2x6)-0.83ML structure at $T = 155$ K (black arrow). The circle radius is equivalent to a coherent fraction of 1.0.

Figure 7.4.6. shows the (200) reflection Argand diagram obtained if there are two layers of mercury adsorption on the Cu(100) surface. The resultant vector has an angle of 107° (equivalent to a resultant NIXSW coherent position of 2.345 \AA) and a length equivalent to a coherent fraction of 0.89. Neither the adsorbate height nor the coherent fraction closely matches the experimental data and this model is not supported by the LEED pattern observed.

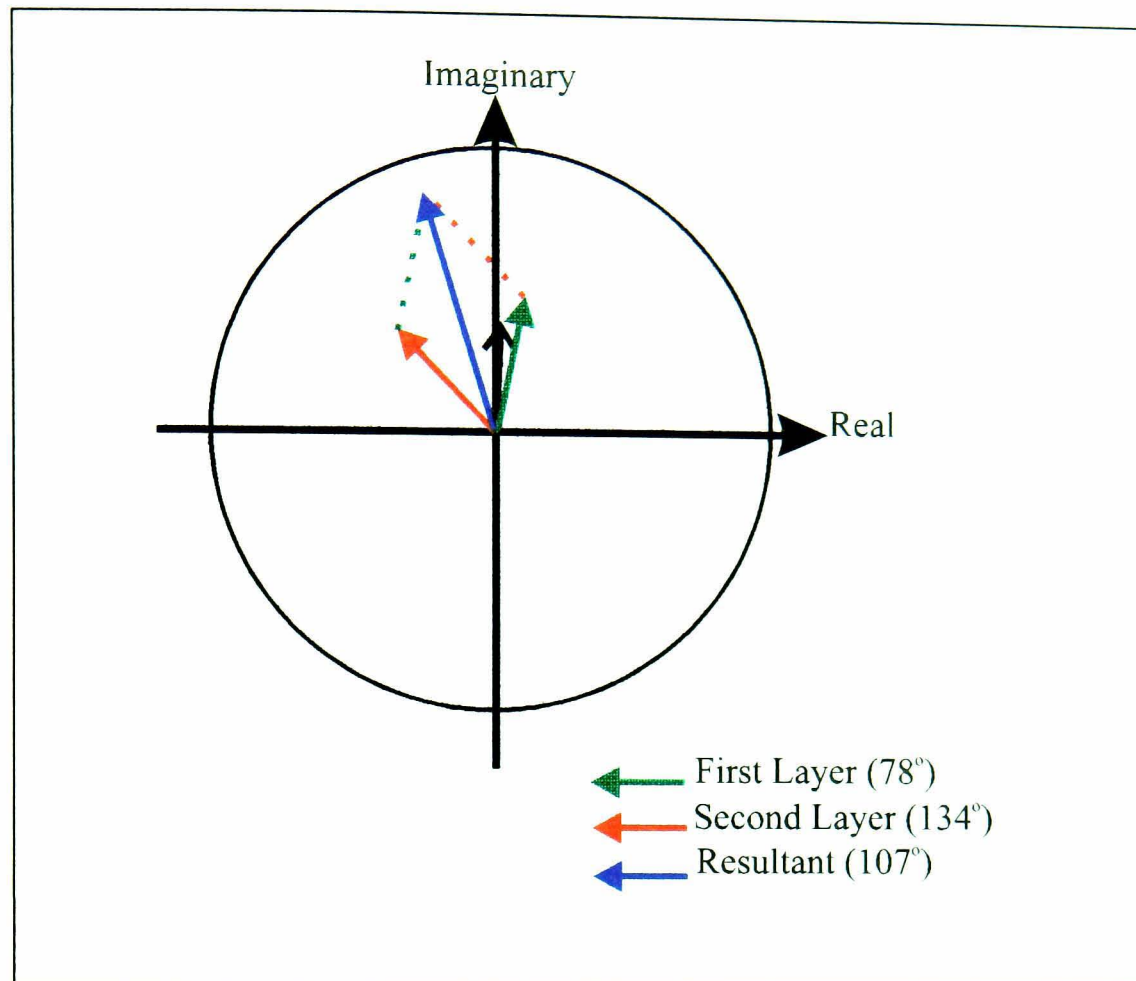


Figure 7.4.6. Argand vector diagram illustrating the vectors for the (200) reflection two layers of mercury. It shows the theoretical vectors (coloured arrows) of the first and second mercury adlayers with the experimental vector obtained for the Cu(100)/Hg-c(2x6)-0.83ML structure at $T = 155$ K (black arrow). The circle radius is equivalent to a coherent fraction of 1.0.

Clearly it can be seen from the above Argand diagrams that the experimental (200) reflection vector for the c(2x6)-0.83ML best fits the theoretical vector for $1\frac{1}{4}$ layers of mercury adsorbed on the Cu(100) surface. However, it is highly probable that a better Argand vector fit would be obtained for less than a quarter of a monolayer adsorbed on top of the first layer of mercury atoms. Therefore one can assume that c(2x6)-

0.83ML structure in this NIXSW study has less than $\frac{1}{4}$ ML of mercury atoms adsorbed on top of it. A quarter of a monolayer of mercury atoms adsorbed on top of a $c(2 \times 6)$ structure should not significantly alter the LEED pattern observed. Any apparent change in such a LEED pattern would be difficult to observe. This would therefore agree with the $c(2 \times 6)$ LEED pattern observed, unlike the different LEED pattern observed by Li et al. (1992a).

Rumpled overlayer mercury structures formed on Cu(100) crystals have been observed by Dowben et al. (1991), Li et al. (1991a, 1992a). The displacement of the mercury adatoms with respect to the Cu(100) surface was thought to be approximately 0.15 Å (Dowben et al. 1991, Li et al. 1991a). Such rumpling has only been observed for the $c(4 \times 4)$ -0.62ML structure, but it is possible that there could be buckling of the higher coverage $c(2 \times 6)$ overlayer. A displacement of 0.15 Å with respect to the (200) reflections planes would produce Argand vectors 30° either side of the experimental (200) vector. This rumpling of the mercury overlayer could also lower the coherent fraction for both the (200) and (111) reflection data.

The $c(2 \times 6)$ -0.83ML structure previously studied (Dowben et al. 1990b, Kime et al. 1992, Li et al. 1991a, 1992a) has lattice constants of 3.07 Å and 2.98 Å which are very close to the lattice constants of bulk mercury at low temperatures consistent with mercury adsorption on nickel (Singh and Jones 1989a). The proposed structure of the $c(2 \times 6)$ -0.83ML adsorbate structure is shown in figure 7.4.7. It is thought that the densely packed $c(2 \times 6)$ -0.83ML structure is a more stable and tightly bound structure

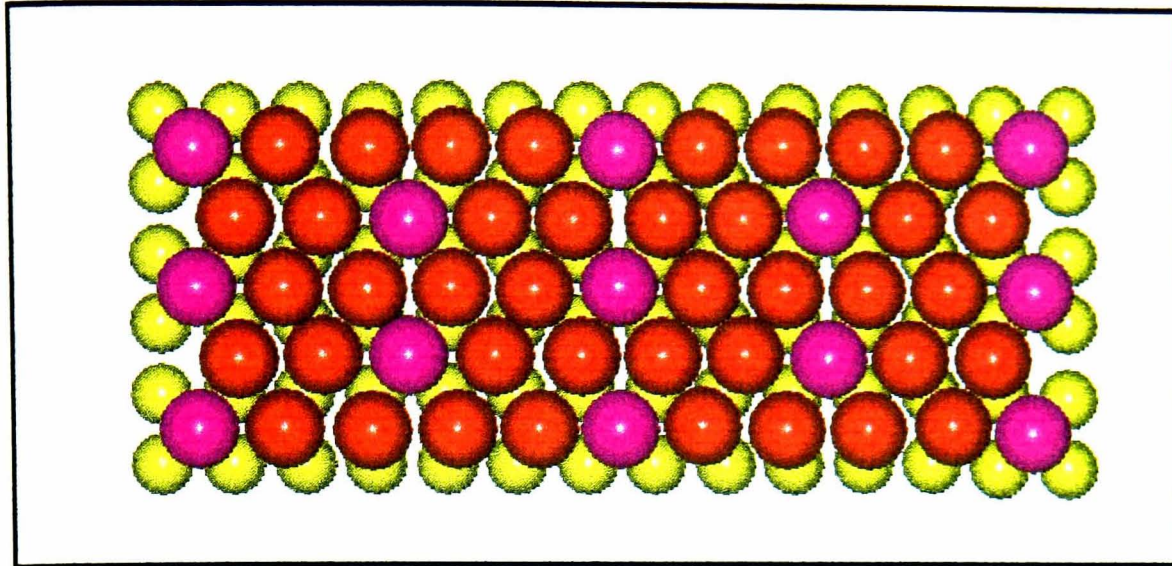


Figure 7.4.7. A schematic diagram of the possible Cu(100)-c(2x6)-Hg-0.83ML real space structure with the violet mercury atoms located in four-fold hollow sites and red mercury atoms in low symmetry sites. The adlayer is not puckered in this diagram. The yellow atoms represent copper. The diameters of the atoms are relative to each other.

than the (3x3)-0.66ML (Kime et al. 1992). For the c(2x6)-0.83ML structure, it is possible to locate two mercury atoms at a four-fold hollow sites which then positions eight mercury atoms in low symmetry sites. With the four possible orientations of this structure relative to the fixed (111) planes, there are then a large number of vectors which need to be summed leading to a small coherent fraction, f_c . Add to this the fraction of a monolayer coverage of second layer mercury atoms and their various orientations to the (111) plane. Consequently, there will be a vast number of theoretical adsorption height vectors all summing to a very low coherent fraction. Such a low coherent fraction has been observed for the c(2x6)-0.83ML (111) NIXSW data. Hence, when one contemplates that there are more than just this one series of possible adsorption sites, subsequent deductions along these lines would become immensely complicated.

7.5 The Cu(100)/Hg Conclusion

It was said in the conclusion of chapter 5 about the Ni(111)/Hg NIXSW data that the factors governing the optimum adsorption site may be more subtle than in a system having larger corrugation. In this chapter the more open Cu(100) surface was used as a substrate for the mercury adsorbate. Quite different results from the Ni(111)/Hg were obtained.

Firstly NIXSW analysis of the lowest coverage Cu(100)/Hg-c(2x2)-0.50ML structure indicated that the mercury atoms adsorbed into the most energetically stable four-fold hollow sites.

The NIXSW analysis of the Cu(100)/Hg-c(4x4)-0.62ML structure proved that the mercury atoms did not form a coincidence net with the substrate as previously thought. A model that best fits our experimental data has been proposed, but this model is not entirely conclusive. In our model, some of the mercury atoms are thought to adsorb again exactly in energetically favourable four-fold hollow sites and some reside in sites slightly off the four-fold hollow position.

The NIXSW analysis of the Cu(100)/Hg-(3x3)-0.66ML structure was previously thought to consist of adsorption half in four-fold hollow sites and half in bridge sites. This study can conclude that the Cu(100)/Hg-(3x3)-0.66ML structure consists of two domains. Each domain contained mercury atoms adsorbed equally in both bridge and four-fold hollow sites. These domains differ only in the type of bridge sites occupied by the mercury adsorbate atoms.

Finally, in the NIXSW study of the highest coverage Cu(100)/Hg-c(2x6)-0.83ML structure, the NIXSW data was found to indicate a more complex adsorption model. We have therefore concluded that a combination of a slightly rumpled overlayer and more than a monolayer of adsorbate atoms would best fit the experimental NIXSW data presented here.

8 Summary

We have performed structural studies of the Hg/Ni(111) and Hg/Cu(100) adsorption systems using the Normal Incidence X-Ray Standing Wavefield technique. The results from these studies have improved our understanding of the behaviour of mercury as an adsorbate and consequently provide an insight into the general adsorption behaviour of metals on metals. The three Hg/Ni(111) structures studied were $(\sqrt{3}\times\sqrt{3})R30^\circ$ -0.33ML, $p(2\times 2)$ -0.5ML and “ $c(2\sqrt{3}\times 2\sqrt{3})R30^\circ$ ”-0.64ML. The four Hg/Cu(100) structures studied were the equilibrium structures, $c(2\times 2)$ -0.50ML and $c(4\times 4)$ -0.62ML and the non-equilibrium structures, (3×3) -0.66ML and $c(2\times 6)$ -0.83ML.

The 298 K and 138 K (111) reflection profiles for the Ni(111)/Hg- $(\sqrt{3}\times\sqrt{3})R30^\circ$ -0.33ML structure gave coherent positions of $2.46\pm 0.20\text{\AA}$ and coherent fractions of approximately 2.7 ± 0.1 . The $(\bar{1}11)$ profiles for the $(\sqrt{3}\times\sqrt{3})R30^\circ$ structure taken at 298 K and 138 K produced coherent positions of $0.40\pm 0.05\text{\AA}$ and $0.10\pm 0.05\text{\AA}$ respectively. The coherent fractions for the $(\sqrt{3}\times\sqrt{3})R30^\circ$ profiles taken at 298 K and 138 K were 0.05 ± 0.05 and 0.35 ± 0.05 respectively.

Both the 298 K and 138 K (111) reflection profiles for the Ni(111)/Hg- $p(2\times 2)$ -0.5ML structure gave coherent positions of $2.43\pm 0.25\text{\AA}$, with coherent fractions of 0.58 ± 0.10 and 0.78 ± 0.10 respectively. The coherent positions for the $(\bar{1}11)$ profiles taken at 298 K

and 138 K were $1.69 \pm 0.12 \text{ \AA}$ and $1.81 \pm 0.12 \text{ \AA}$ respectively, both with a coherent fraction of 0.05 ± 0.05 .

The (111) profile obtained for the “ $c(2\sqrt{3} \times 2\sqrt{3})R30^\circ$ ” structure at 185 K had a coherent position and coherent fraction of $2.35 \pm 0.20 \text{ \AA}$ and 0.46 ± 0.05 respectively. The fit of the $(\bar{1}11)$ profile provided a coherent position of $1.56 \pm 0.10 \text{ \AA}$ and coherent fraction of 0.29 ± 0.05 .

The coherent fractions of the profiles taken for the (111) reflections indicate good order in the substrate and adsorbate atoms perpendicular to the surface for the Hg/Ni(111) structures. However, the low coherent fractions obtained for the $(\bar{1}11)$ reflection data indicate significant disorder parallel to the surface for all phases. Such indications of disorder contradict the ordered adlayer implied by the sharp, bright LEED patterns observed. Furthermore, the coherent positions of the (111) and $(\bar{1}11)$ NIXSW data for all the phases do not conclusively lead to a specific adsorption site. Consequently, a model to resolve the apparent paradox of the LEED patterns implying an ordered adlayer and NIXSW results implying a disordered adsorbate surface for the Hg/Ni(111) adsorption system has been proposed. It is suggested that the mercury adlayer undergoes a low frequency, large amplitude vibration parallel to the surface, thus allowing the crystallinity of the adlayer to be maintained for LEED analysis. Such a large distribution of adsorbate distances relative to the $(\bar{1}11)$ set of planes leads to a low coherent fraction, in agreement

with the $(\bar{1}11)$ NIXSW data. Therefore, the proposed model provides the best explanation of the experimental data obtained.

For mercury adsorption on the more open Cu(100) surface, the results obtained were somewhat different from those obtained for the Ni(111)/Hg adsorption system. Firstly, by studying the lowest coverage Cu(100)/Hg-c(2x2)-0.50ML structure with the NIXSW technique, coherent positions for the (200) and (111) reflections were found to be ≈ 2.20 Å and 2.23 Å respectively at both 155 K and 298 K. From these adsorbate heights and coherent fractions of ≈ 0.9 and ≈ 0.55 for the (200) and (111) reflections respectively, it was concluded that the mercury atoms adsorb in the most energetically stable four-fold hollow sites. Similar four-fold hollow site adsorption has been observed for the c(2x2) adsorbate structure formed by atomic adsorption of elements such as Mn (Wuttig et al. 1993, OBrien et al. 1993, Noh et al. 1994, Hayden et al. 1995) and Pd (Pope et al. 1994, Valden et al. 1994) on the copper (100) surface.

The NIXSW analysis of the Cu(100)/Hg-c(4x4)-0.62ML structure also produced coherent positions of ≈ 2.2 Å for the (200) and (111) reflection data taken at 155 K and 298 K. However, a lower coherent fraction of ≈ 0.8 compared with that for the c(2x2) structure was found for the (200) reflection at both 155 K and 298 K. The coherent fraction of 0.50 for the (111) reflection data proved that the mercury atoms did not form the expected coincidence net, as this would have produced a (111) coherent fraction of zero. A model was therefore proposed, which although not entirely conclusive was the most suitable for

our experimental data. We suggest that whilst some of the mercury atoms do indeed adsorb into the energetically favourable four-fold hollow sites previously suggested, certain mercury atoms reside in sites slightly off the four-fold hollow position due to the size and close proximity of the mercury adatoms.

Using the NIXSW technique at 155 K, we obtained a coherent position of 2.183 ± 0.025 Å and 2.233 ± 0.035 Å for the (200) and (111) reflections respectively for the Cu(100)/Hg-(3x3)-0.66ML structure. The (200) and (111) coherent fractions at 155 K were found to be 0.90 ± 0.05 and 0.55 ± 0.07 respectively. This NIXSW data led to the conclusion that the Cu(100)/Hg-(3x3)-0.66ML structure consists of two domains, each consisting of mercury atoms adsorbed equally in both bridge and four-fold hollow sites. These domains differ only in the type of bridge sites occupied by the mercury adsorbate atoms.

Finally, the NIXSW study of the highest coverage Cu(100)/Hg-c(2x6)-0.83ML structure at 155 K produced coherent positions of 2.258 ± 0.025 Å and 2.458 ± 0.025 Å and coherent fractions of 0.388 ± 0.028 and 0.20 ± 0.07 for the (200) and (111) reflections respectively. The analysis of these fitting parameters indicated a more complex adsorption model. This model combined an uneven overlayer with more than a monolayer of adsorbate atoms.

The combination of a large atom adsorbed on a close packed metal surface produces a surface with a very small degree of geometrical corrugation. Consequently, it may appear that various interactions dominant in the “choice” of ideal adsorption site may be more

subtle than in a system with larger corrugation. In using the Normal Incidence X-Ray Standing Wavefield technique we have been able to show that for surfaces with a larger corrugation, the substrate does influence the adsorbate structures formed. The mercury adsorbate structures formed on the Cu(100) surface were more site specific than those on the less corrugated Ni(111) surface. Therefore, the NIXSW technique has confirmed that mercury adsorbate structures formed on single crystal surfaces are influenced by substrate unit mesh and the adsorbate coverage (i.e. the mercury adsorbate lateral interactions). However, the relative size of the substrate corrugation to the size of the mercury adatom does indicate which of the adsorbate-adsorbate interactions or adsorbate-substrate interactions will have most influence on the adsorbate structures formed. It is surprising to note that the mercury adsorption is more site specific on the copper surface instead of the more reactive nickel substrate.

Many structural studies of mercury adsorbed on other single crystal metal surfaces need to be accomplished, especially those whose substrate net enables mercury to form (1x1) adsorbate structures, such as Ag(100), Fe(100) and W(100). A NIXSW study of mercury adsorbed on these surfaces may determine whether these (1x1) structures formed are site specific (as for the Cu(100) surface) or more mobile (as for the Ni(111) surface). The adsorption behaviour of mercury on semiconductor surfaces has barely been studied (Li et al. 1992, 1993). The use of the Normal Incidence X-Ray Standing Wavefield technique to study such adsorption systems could bring about some very exciting results. A structural study of the higher coverage $p(2 \times 2)$ -0.75ML and non-equilibrium Hg/Ni(111) structures

may determine whether these structures behave similarly to the other mercury structures formed on the Ni(111) surface.

To provide a complete story, theoretical studies of the mercury adsorbate-adsorbate lateral interactions on all the possible substrates would be needed. These theoretical studies would provide more of an insight into how the interplay between the adsorbate-substrate and adsorbate-adsorbate interactions influence the formation of the adsorbate structure.

An experimental technique which may help determine the extent of the mercury adlayer motion could be Scanning-Tunneling-Microscopy (STM). Such a study has been performed on the mercury adsorption on thin epitaxial gold films (Levlin et al. 1996) indicating the island formation of mercury. It would enable the scientist to actually "see" the mercury adlayer on the substrate surface. However, if there is true movement of the adlayer on the Ni(111) surface, the frequency of this motion could produce blurred pictures if the timescale of the STM experiment (approximately 10^2 s) is comparable with that of the vibration of the adlayer (10^{-12} s). However, such a technique could indicate whether the mercury islands are mobile and also whether any domains are formed. It would also be beneficial to use other structural techniques to study mercury adsorption on single crystal metal surfaces and therefore add yet more substance to the results already discussed.

References

- Barber, D.J. and Loudon, R. (1989) *An Introduction to the Properties of Condensed Matter* (Cambridge University Press).
- Batterman B.W.(1964) *Phys. Rev.* **133**, A759.
- Batterman B.W. (1969) *Phys. Rev. Lett.* **22**, 703.
- Berndt, W., Weick, D., Stampfl, C., Bradshaw, A.M., Scheffler, M. (1995) *Surf. Sci.* **330**, 182.
- Biham, O., Chen, L-W. and Vidali, G. (1993) *Surf. Sci.* **287/288**, 815.
- Bradshaw, A.M. (1990) *Faraday Discu. Chem. Soc.* **89**, 1.
- Carlson, T,A, (1975) *Photoelectron and Auger Spectroscopy* (Plenum Press).
- Chen, X., Aeukawa, T., Tain, J., Kono, S. (1995) *Surf. Rev. And Lett.* **2(6)**, 795.
- Cowan P.L., Golovchenko J.A. and Robbins M.F. (1980) *Phys. Rev. Lett.* **44**, 1680.
- Davis, L.E., MacDonald, N.C., P.W. Palmberg, Riach, G.E. and Weber, R.E. (1976) *Handbook of Auger Electron Spectroscopy 2nd ed.* (Physical Electronics Industries, Inc.).
- Donohue, J. (1974) *The Structure of the Elements.* (Wiley, Toronto).
- Dowben, P.A., Kime, Y.J., Varma, S., Onellion, M. and Erskine, J.L. (1987a) *Phys. Rev. B: Condens. Matter.* **36(5)**, 2519.
- Dowben, P.A., Onellion, M. and Kime, Y.J. (1987b) *Scanning Electron Microscopy.* **2**, 177.
- Dowben, P.A., Varma, S., Kime, Y.J., Mueller, D.R. and Onellion, M. (1988) *Z. Phys. Condens. Matter.* **73**, 247.

- Dowben, P.A., Kime, Y.J., LaGraffe, D. and Onellion, M. (1990a) *Surface and Interface Analysis*, **15**, 163.
- Dowben, P.A., Kime, Y.J., Hutchings, C.W., Li, W. and Vidali, G. (1990b) *Surf. Sci.* **230**, 113.
- Dowben, P.A., LaGraffe, D., Li, D., Vidali, G., Zhang, L., Dottl, L. and Onellion, M. (1991) *Phys. Rev. B.* **43**(13), 10677.
- Egelhoff, W.F., Perry, D.L. and Linnett, J.W., *Surf. Sci.* **54**, 670 (1976)
- Etalaimemi, V., Michel, E.G. and Materlik, G. (1993) *Phys. Rev. B*, **48**(16), 12023.
- Evans, J.W. (1989) *Phys. Rev. Lett.* **40**(5), 2868.
- Frost, D.C., McDowell, C.A. and Vroom, D.A (1967) *Chem. Phys. Lett.* **1**, 93.
- Gog, T.H., Harasimowicz, T., Dev, B.N. and Materlik, G. (1994) *Europhys. Lett.* **25**(40), 253.
- Günther C., Günther, S., Kopatzki, E., Hwang, R.Q., Schörder, J., Vrijmoeth, J. and Behm, R.J. (1993) *Ber. Bunsenges. Phys. Chem.* **97**(3), 522.
- Heine, V. and Weaire, D. (1966) *Phys. Rev.* **152**(2), 603.
- Hertel, N., Materlik, G. and Zegenhagen, J. (1985) *Z. Phys. B - Condens. Matter* **58**, 199.
- Hollas, J.M. (1992) *Modern Spectroscopy 2nd Ed.* (John Wiley & Sons, Chicester).
- Hutchings, C.W., Dowben, P.A., Kime, Y.J., Li, W., Karimi, M., Moses, C. and Vidali, G. (1990) *Mat. Res. Soc. Symp. Proc.* **159**, 133.
- Itchkawitz, B.S., Baddorf, A.P., Davis, H.L. and Plummer, E.W. (1992) *Phys. Rev. Lett* **68**, 2488.
- Jones, R.G. and Perry, D.L. (1978) *Surf. Sci.* **71**, 59.

- Jones, R.G. and Perry, D.L. (1979) *Surf. Sci.* **82**, 540.
- Jones, R.G. and Perry, D.L. (1981) *Vacuum.* **31**, 493.
- Jones, R.G. and Tong, A.W.L. (1987) *Surf. Sci.* **188**, 87.
- Kadodwala, M.F., Davis, A.A., Scragg, G., Cowie, B.C.C., Kerkar, M.,
Woodruff, D.P. and Jones, R.G. (1995) *Surf. Sci.* **324**, 122.
- Kadodwala, M.F., Davis, A.A., Scragg, G., Cowie, B.C.C., Kerkar, M.,
Woodruff, D.P. and Jones, R.G. (1996) to be submitted.
- Kerkar M., Fisher D., Woodruff D.P. and Cowie B. (1992a) *Surf. Sci.* **271**, 45.
- Kerkar M., Fisher D., Woodruff D.P., Jones R.G., Diehl R.D. and Cowie B.C.C.
(1992b) *Surf. Sci.* **278**, 246.
- Kerkar, M., Hayden, A.B., Woodruff, D.P., Kadodwala, M. and Jones, R.G. (1992c)
J. Phys. Condens. Matter. **4**, 5043.
- Kerkar, M., Fisher, D., Woodruff, D.P., Jones, R.G., Diehl, R.D., McConville, C.F. and
Cowie, B.C.C. (1992d) *J. Vac. Sci. Technol. A*, **10**(4), 2148
- Kerkar M., Fisher D., Woodruff D.P., Jones R.G., Diehl R.D. and Cowie B.C.C.
(1992e) *Phys. Rev. Lett.* **68**(21), 3204.
- Kerkar M., Walter, W.K., Woodruff D.P., Jones R.G., Ashwin, M.J. and Morgan, C.
(1992f) *Surf. Sci.* **268**,36.
- Kim, B-O., Lee, G., Plummer, E.W., Dowben, P.A. and Liebsch, A. (1995)
Phys. Rev. B **52**(8), 6057.
- Kime, Y.J., Zhang, J. and Dowben, P.A. (1992) *Surf. Sci.* **268**, 98.

- King, D.A. and Woodruff, D.P. (Editors) (1983) *The Chemical Physics of Solid Surfaces and Heterogeneous Catalysis, Vol II. Adsorption at a Solid Surface*. (Elsevier Science Publishing Company, New York).
- Kittel, C. (1986) *Introduction to Solid State Physics*, 6th Ed. (John Wiley & Sons Inc.).
- Li, D., Zhang, J., Lee, S. and Dowben, P.A. (1992b) *Phys. Rev. B* **45**(20), 11876.
- Li, D., Lin, J., Li, W., Lee, S., Vidali, G. and Dowben, P.A. (1993) *Surf. Sci.* **280**, 71.
- Li, W., Lin, J.-S., Karimi, M., Moses, C., Dowben, P.A. and Vidali, G. (1991) *The Structure of Surfaces III*, vol 24, p350 (Ed – S.Y. Tong, M.A. Van Hove, K. Takayanagi, X.D. Xie), (Springer, Berlin).
- Li, W., Lin, J., Karimi, M., Dowben, P.A. and G. Vidali. (1992a) *Phys. Rev. B* **45**(7), 3708.
- Li, W. and G. Vidali. (1993) *Surf. Sci.* **287/288**, 336.
- Lide, D.R. (Editor in Chief) (1992) *CRC Handbook of Chemistry and Physics* (CRC Press, Inc).
- Liu, S., Zhang, Z., Norskov, J and Metiu, H. (1994) *Surf. Sci.* **321**, 161.
- Lüdecke, J., Ettema, A.R.H.F., Driver, S.M., Scragg, G., Kerkar, M., Woodruff, D.P., Cowie, B.C.C., Jones, R.G., Bastow, S.L. (1996) *Surf. Sci.* **366**, 260.
- MacGillavry, C.H., Rieck, G.D. and Lonsdale K.(Editors) (1968), *International Tables For X-ray Crystallography vol II*.
- McDowell, A.A., Norman, D. and West, J.B.(1986) *Rev. Sci. Instr.* **57**, 2667.
- Mizuno, S., Tochiara, H., Kawamura, T. (1993) *Surf. Sci.* **293**, 239.
- Morrison, S.R. (1977) *The Chemical Physics of Surfaces* (Plenum Press, New York).

- Moses, C., Zeng, H., Lin, J.-S., Li, W., Karimi, M., and Vidali, G. (1992) *J. Vac. Sci. Technol.* **A10(4)**, 2377.
- Nielsen, M.M., Burchhardt, J., Adams, D.L. (1994) *Phys. Rev. B.* **50(11)**, 7851.
- Onellion, M., Erskine, J.L., Kime, Y.J., Varma, S. and Dowben, P.A. (1986) *Phys. Rev. B.* **33(12)**, 8833.
- Onellion, M., Kime, Y.J., Dowben, P.A. and Tache, N. (1987) *J. Phys. C: Solid State Phys.* **20**, L633.
- Onellion, M., Dowben, P.A. and Erskine, J.L. (1988) *Phys. Lett. A.* **130(3)**, 171.
- Ohta, T., Sekiyama, H., Kitajima, Y., Kuroda, H., Takahashi, T. and Kikuta, S. (1985) *Jpn. J. Appl. Phys.* **24(6)**, L475.
- Patel J.R., Golovchenko J.A., Freeland P.E. and Gossman H.J. (1987) *Phys. Rev. B.* **36**, 7715.
- Ponec, V., Knor, Z., and Cerny, S. (1974) *Adsorption on Solids* (Butterworths, London).
- Poulsen, P.R., Stensgaard, I. and Besenbacher, F. (1994) *Surf. Sci. Lett.* **310**, L589.
- Prince, N.P., Singh, N.K., Walter, W., Woodruff, D.P. and Jones, R.G. (1989) *J. Phys. Condens. Matter.* **1** SB21
- Prince, N.P., Seymour, D.L., McConville, C.F., Woodruff, D.P., and Jones, R.G. *Surf. Sci.* **230**, 13 (1990a).
- Prince, N.P., Ashwin, M.J., Woodruff, D.P., Singh, N.K., Walter, W. and Jones, R.G. (1990b) *Faraday. Discuss. Chem. Soc.* **89**, 301.
- Puselj, M. and Ban, Z. (1977) *Zeitschrift Für Naturforschung.* **B32**, 479.

- Scragg, G., Cowie, B.C.C., Kerkar, M., Woodruff, D.P., Daimellah, A., Turton, S. and Jones, R.G. (1994) *J. Phys. Condens. Matter*, **6**, 1869.
- Singh, N.K. (1989) *PhD Thesis*, University Of Nottingham.
- Singh, N.K. and Jones, R.G. (1988) *The Structure of Surfaces II*, vol 11, p238, (Ed – J.F. Van Der Veen, M.A. Van Hove), (Springer, Berlin).
- Singh, N.K. and Jones, R.G. (1989a) *Chem. Phys. Lett.* **155**(4,5), 463.
- Singh, N.K. and Jones, R.G. (1989b) *J. Phys. Condens. Matter.* **1**, SB267.
- Singh, N.K. and Jones, R.G. (1990a) *Surf. Sci.* **232**, 229.
- Singh, N.K. and Jones, R.G. (1990b) *Surf. Sci.* **232**, 243.
- Singh, N.K. Woodruff, D.P. and Jones R.G. (1990c) *Surf. Sci. Lett.* **232**, L228.
- Singh, N.K., Dale, P.A.D.M.A., Bullett, D. and Jones, R.G. (1993) *Surf. Sci.* **294**, 333.
- Swanson, L.W., Strayer, R.W. and Davis, L.E. (1968) *Surf. Sci.* **9**, 165.
- Tompkins, F.C. (1978) *Chemisorption of Gases on Metals* (Academic Press, London).
- Varma, S., Kime, Y.J., Dowben, P.A., Onellion, M. and Erskine, J.L. (1986) *Phys. Lett.* **A116**, 66.
- Varma, S., Kime, Y.J., LaGraffe, D., Dowben, P.A., Onellion, M. and Erskine, J.L. (1990) *J. Chem. Phys.* **93**(4), 2819.
- Vidali, G. Hutchings, C.W., Dowben, P.A., Karimi, M. Moses, C. and Foresti, M. (1990) *J. Vac. Sci. Technol.* **A8**(3), 3043.
- Vidali, G. Li, W., Lin, J.-S., and Moses, C. (1991) *Mat. Res. Soc. Symp. Proc.* **208**, 99.
- Weaire, D. (1968a) *J.Phys. C (Proc. Phys. Soc.)* **2**(1), 210.

- Woodruff D.P., Seymour D.L., McConville C.F., Riley C.E., Crapper M.D,
Prince N.P. and Jones R.G. (1987) *Phys. Rev. Lett.* **58**, 1460.
- Woodruff D.P., Seymour D.L., McConville C.F., Riley C.E., Crapper M.D,
Prince N.P. and Jones R.G. (1988a) *Surf. Sci.* **195**, 237.
- Woodruff D.P., Seymour D.L., McConville C.F., Riley C.E., Crapper M.D,
Prince N.P. and Jones R.G. (1988b) *Vacuum.* **38**(4 -5), 428.
- Woodruff D.P. (1993) *Surf. Sci.* **283**, 309.
- Woodruff, D.P., Cowie, B.C.C. and Ettema, A.R.H.F. (1994) *J. Phys:*
Condens Matter **6**, 10633.
- Woodruff, D.P. and Delchar, T.A. (1994) *Modern Techniques Of Surface Science 2nd*
Ed. (Cambridge Solid State Science Series).
- Wright, A.f. and Chrzan, D.C. (1993) *Phys. Rev. Lett* **70**, 1964.
- Zangwill, A. (1992) *Physics at Surfaces.* (Cambridge University Press).
- Zegenhagen, J. (1993) *Surf. Sci. Reports* **18**, 199.
- Zhao, Y.B. and Gomer, R. (1992) *Surf. Sci.* **271**, 85.
- Zhang, J., Li, D. and Dowben, P.A. (1993) *Phys. Lett. A.* **173**, 183.
- Zhang, J., Li, D. and Dowben, P.A. (1994a) *J. Phys. Condens. Matt.* **6**, 33.
- Zhang, J., Li, D. and Dowben, P.A. (1994b) *J. Vac. Sci. Technol. A.* **12**(4), 2190.